
NEW PERSPECTIVES
ON THE CEREBRAL SMALL
VESSELS WITH 7T MRI
Tine Arts

NEW PERSPECTIVES ON THE CEREBRAL SMALL VESSELS WITH 7T MRI

TINE ARTS

New perspectives on the cerebral small vessels with 7T MRI
PhD Thesis, Utrecht University, the Netherlands

Cover and illustrations design	© evelienjagtman.nl
Lay-out	Tine Arts
Printing	Ridderprint | www.ridderprint.nl
ISBN	978-94-6416-803-7

Financial support for the publication of this thesis was generously provided by the Dutch Heart Foundation.

Additional financial support was provided by Chipsoft, Sectra Benelux, and Alzheimer Nederland.

NEW PERSPECTIVES ON THE CEREBRAL SMALL VESSELS WITH 7T MRI

NIEUWE PERSPECTIEVEN OP DE CEREBRALE KLEINE VATEN MET 7T MRI

(met een samenvatting in het Nederlands)

PROEFSCHRIFT

ter verkrijging van de graad van doctor aan de Universiteit Utrecht op gezag van de rector magnificus, prof. dr. H.R.B.M. Kummeling, ingevolge het besluit van het college voor promoties in het openbaar te verdedigen op

woensdag 17 november des ochtends te 10.15

door

TINE ARTS

geboren op 20 juni 1989

te Boxmeer

Promotoren:	Prof. dr. J. Hendrikse
	Prof. dr. G.J. Biessels
Copromotoren:	Dr. ir. J.J.M. Zwanenburg
	Dr. ir. J.C.W. Siero

Voor mijn ouders en mijn zus

"Like branches on a tree we all grow in different directions, yet our roots will forever remain as one"

CONTENTS

Chapter 1	General introduction	11
Part I	**What else is in there?** *Making small perforating artery detection more reliable and employable*	
Chapter 2	Velocity and pulsatility measures in the perforating arteries of the basal ganglia at 3T MRI in reference to 7T MRI	33
Chapter 3	Automated assessment of cerebral arterial perforator function on 7 Tesla MRI	59
Part II	**What is out there?** *Characterizing small vessel hemodynamics in relation to a range of cardiovascular factors*	
Chapter 4	Perforating artery flow velocity and pulsatility with carotid occlusive disease. A 7 Tesla MRI study	89
Chapter 5	Non-invasive assessment of damping of blood flow pulsations in cerebral arteries with 7T MRI	107
Chapter 6	Cerebral perforating artery flow function and pulsatility are largely unaffected by common vascular risk factors	127
Part III	**What is happening?** *Exploring microvascular (dys)function in SVD*	
Chapter 7	Zooming in on cerebral small vessel function in small vessel diseases with 7T MRI: Rationale and design of the "Zoom@ SVDs" study	149
Chapter 8	Novel 7T markers of small vessel function in CADASIL	177
Chapter 9	General discussion	203

Appendices

Nederlandse samenvatting	227
About the author	235
Publications	239
Dankwoord	245

Chapter 1

GENERAL INTRODUCTION

INTRODUCTION

The small vessels in the brain play an essential role in the cerebral blood supply. Disorders concerning the small cerebral vessels are associated with serious medical conditions such as stroke and dementia.[1] Previously, it was not possible to investigate the functioning of these small vessels due to their small size. However, 7 tesla MRI enables us to study the hemodynamics and functioning of the cerebral microvasculature.[2,3] Therefore, the overall goal of this thesis is to make flow measures of the cerebral small vessels more robust and increase their applicability, as well as to explore which factors may be of influence on these metrics, and apply these and other measures of microvascular function in a cohort of patients with small vessel disease (SVD) to investigate small vessel flow in healthy controls and patients. In this thesis, this goal is subdivided in three specific research aims:

- Making small perforating artery detection more reliable and employable
- Charactizing small vessel hemodynamics in relation to a range of cardiovascular factors
- Exploring microvascular (dys)function in SVD

These three specific research aims will be addressed in the three corresponding parts of this thesis.

Part I: What else is in there?

Making small perforating artery detection more reliable and employable

Cerebral vessel imaging

Imaging of the blood vessels in the body is called angiography and currently various techniques exist for blood vessel visualization. Nowadays, brain angiography is mainly achieved with fluoroscopy using x-rays, computed tomography (CT), MRI, transcranial Doppler (TCD), and positron emission tomography (PET) imaging.[4–9] Each of these techniques has its own (dis)advantages and is used for specific purposes. For example, fluoroscopy methods have the advantage that they can image real-time, making it a suitable guide for medical procedures such as stent or catheter placement.[6,8] Computed tomography on the other hand, does not image real-time, but can better show organs and vessels in areas where entities overlap and can acquire high-resolution images.[6] Disadvantages of fluoroscopy and CT techniques are the required use of ionizing radiation

and the necessity of contrast agent injection; both aspects not being without risks.[10–12] PET also involves injection of radiation, but consists of a rapidly decaying radioactive substance into the bloodstream. Due to its high sensitivity to detect metabolites, PET is highly useful to investigate the cerebral metabolism in SVD, for example for the deposition of pathogenic products such as amyloid.[6,13] Though, due to relatively low spatial resolution of PET images a hybrid imaging system is needed to associate functional data with anatomy. However, hybrid systems such as PET/MRI and PET/CT are scarce.[6] Transcranial Doppler can also require contrast agents, but uses ultrasound instead of radiation and is mainly used for blood flow estimations (flow velocity, pulsatility, cerebral blood flow (CBF)) in larger vessels with high temporal resolution. In the brain, this technique mainly aids in the assessment of the carotids, jugular veins and middle and anterior cerebral arteries.[6] A major limitation of transcranial Doppler is that most of the applied ultrasound energy is lost due to absorption and scatter in the temporal bone, which not rarely results in a failed recording.[14] As one can notice, the aforementioned techniques are mainly used to image or assess the larger cerebral vessels or affected regions, and are not suited to investigate the functioning of the small cerebral vessels. However, this does not imply that these techniques cannot be of added value in small vessel research. Concerning other techniques, the fluoroscopy technique named digital subtraction angiography is a widely used technique and actually able to visualize the small arterial cerebral branches.[15,16] However, this method also uses high levels of ionizing radiation, making it unsuitable for research purposes.[17] Because MRI does not use ionizing radiation and does not necessarily require the use of contrast agents, it can more easily be used for research purposes. However, even though MRI techniques such as time-of-flight angiography, arterial spin labeling, cerebrovascular reactivity mapping and phase contrast (PC) imaging are promising for imaging the small cerebral vessels, a high enough SNR is of key importance for sufficient spatial resolution.[18,19] The advance of 7T MRI now offers the ability to non-invasively investigate microvascular function.[2,20,21] 7T has three major advantages over regular field strengths: i) higher signal to noise ratio allowing for measurements with higher spatial or temporal resolution; ii) higher sensitivity to the susceptibility effect of deoxy-hemoglobin associated with the blood oxygenation level-dependent (BOLD) MR signal; and iii) the ability to better distinguish the BOLD signal from the microvasculature from that in larger vessels.[22] This is an important development, since the higher SNR enables us to investigate the cerebral microvasculature at sub-mm resolution as well as at brain tissue level.[23,24] This not only increases our knowledge of SVD pathology, but

can also help unravel how systemic (cardio)vascular disease and normal function relates to the condition of the microvasculature. Furthermore, we can compare functions of the cerebral microvessels and brain tissue, such as blood flow and reactivity, between various populations and it can show to what extent genetic and sporadic variants of SVD are comparable.

In this thesis, we use 2D phase contrast (PC) and blood oxygen level-dependent (BOLD) imaging at 7T MRI to study the functioning of the cerebral microvasculature. Concerning the development of analysis techniques, we focused on improving the post-processing pipeline for 2D PC imaging data.

7 tesla phase contrast MRI for small vessel disease research

MR scanners continues to increase, PC flow measurements are used more often as an (additional) source of quantitative functional information. By imaging a single slice and using a bipolar gradient, a voxelwise calculation of velocities is acquired. It is vital that the velocity encoding parameter, which determines the highest detectable velocity encoded by the sequence, is set to the peak velocity in the vessel to obtain accurate velocity measures. In addition, it is necessary to synchronize the MRI measurements with the cardiac cycle.[27] For this purpose, an electrocardiogram as well as a pulse-oximeter can be used. To obtain time-resolved images, the 2D PC sequence is retrospectively gated. This means that MRI data is collected continuously thoughout the whole cardiac cycle and that during image reconstruction, the data is assigned to multiple positions in the cardiac cycle.[27] The sequence thus produces a number of 2D images, one for each acquired cardiac phase.

By normalizing the voxels' flow velocity over the cardiac cycle the pulsatility can be determined ($[V_{max}-V_{min}]/V_{mean}$).[2] However, because the perforating arteries investigated in this thesis are sub-voxel in size, partial volume averaging can influence the velocity and pulsatility measures. Previous research has shown that it causes a velocity underestimation and a pulsatility overestimation.[2,20,28] Proper background suppression is therefore of high importance, because the better the background is suppressed to have mean zero velocity, the less partial volume averaging and the more accurate the velocity and pulsatility measures will be.[29]

So far, flow measurements of the small cerebral perforating arteries have been performed in the basal ganglia (BG), in which perforating arteries (typical vessel

diameters up to 1mm) receive blood directly from the middle cerebral artery (M1), as well as in the semi-oval center (CSO) in which perforating arteries are relatively smaller (typical vessel diameter 100-200 μm) and receive blood from the cortical segment of the M1 and anterior cerebral artery via medullary arteries (Fig. 1).[30,31] The CSO and BG are used as regions of interest for the detection of perforating arteries because the vessels located in these brain regions penetrate deep into the brain tissue, branch relatively little, are low in density, and have less tight endothelial cell junctions compared to the smaller capillaries. This makes the CSO and BG vulnerable in case of vascular disease, and these regions are therefore known to be affected by SVD.[32–37] Imaging of these small perforating arteries can thus aid in unraveling their role in SVD and in finding SVD biomarkers.

However, small cerebral perforating artery research with large participant cohorts is currently hampered by one major disadvantage of the 2D PC MRI sequence: is it very sensitive to subject motion during scanning.[3,38] This is especially troublesome in patients, which tend to move more and thus have generally less image quality than young, healthy volunteers.[39] In the CSO the consequences of motion are most drastic compared to the BG. In the CSO the main consequences of subject motion are ghosting artefacts, which result in false-positive vessel detection. This makes the velocity and pulsatility measurements of the perforating arteries in the CSO less accurate and calls for the development of an artefact detection algorithm. In **Chapter 2** a robust and time-saving method is presented that aims to select only the perforating arteries outside the ghosting artefacts, which until recently was a manual and thus time-consuming undertaking.

Although the small cerebral vessels can now be imaged in-vivo and flow can be measured quickly and robustly, small cerebral vessels have only been imaged using a 2D PC imaging sequence on 7T MRI. However, compared to 7T MRI scanners, 3T MRI scanners are much more widely available in hospitals and institutions. The ability to image the perforating arteries on 3T MRI would therefore considerably increase the employability of the velocity and pulsatility metrics of the perforating arteries. Nevertheless, 3T MRI has a lower signal-to-noise ratio than 7T MRI[40], which implies that 3T MRI will only be able to detect the relatively large perforating arteries with higher flow velocities. It is currently unknown how the velocity and pulsatility metrics compare to those measured by 7T MRI. Therefore, in **Chapter 3**, the small cerebral perforating arteries are imaged

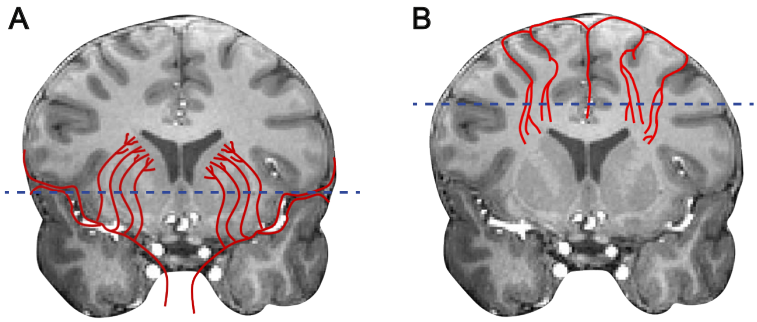

FIGURE 1. Perforating arteries depicted in red in the semi-oval centre (A) and the basal ganglia (B). The 2D phase contrast slice planning is indicated by the blue dotted line and aims to have a perpendicular orientation relative to the perforating artery blood flow.

using 3T and 7T MRI and the agreement of the velocity and pulsatility measures between the two scanning modalities is investigated. Results showed that it is indeed feasible to detect perforating arteries in the BG at 3T MRI. However, the decreased SNR at 3T MRI compared to 7T MRI, makes 3T a factor of five less sensitive for detecting these perforating arteries. As we have access to a 7T MRI scanner, we will utilize its benefits and focus on 7T data acquisition for the remainder of this thesis.

Part II: What is out there?

Characterizing small vessel hemodynamics in relation to a range of cardiovascular factors

In this part of the thesis we investigate cerebral perforating artery flow as part of this bigger whole, and from the perspective of the small perforarting arteries we ask ourselves "What is out there?" The cerebral perforating arteries investigated in this thesis do not function on their own, but are part of an intricate network of interconnected blood vessels.[41–43] As blood is pumped away from the heart it travels through the aorta and to the internal carotid arteries, which in turn lead to the circle of Willis. The circle of Willis distributes the blood over various intracranial arteries which then branch into smaller vessels on the surface of the brain. These so-called pial arteries branch extensively into smaller arterioles, which penetrate into the parenchyma of the brain and terminate in a vast capillary bed.[44] The vessels in this intricate network of interconnected blood vessels all have their own vascular properties and show a complex interrelation with structural and hemodynamic properties of the entire cardiovascular system. In addition, cardiovascular risk factors have known associations with perforating arteries.[45,46] At

the same time, various feedback mechanisms exist to control the CBF and pressure in response to cardiovascular alterations and risk factors.[47–49] Here, we aim to characterize small perforating artery flow in relation to a range of cardiovascular factors with known small vessel associations, and with that we explore whether disturbed hemodynamics in the small arteries can be measured and what the results may imply. Therefore, we investigate small perforating artery flow in response to a stenotic or occluded carotid artery, explore the phenomenon of damping in the small cerebral arteries in relation to proximal measures of pressure and arterial stiffness, and assess small vessel flow dependence on cardiovascular risk factors.

The large vessels responsible for the main blood supply of the cerebral perforating arteries in the CSO and BG are the internal carotid arteries.[41] In patients with carotid occlusive disease (COD), the carotid arteries are stenotic or blocked. It is known that COD is characterized by hemodynamic impairments, such as decreased CBF and CVR, and lower perfusion pressure.[50–56] These impairments are reflected in ischemic symptoms and patients with COD also express low-flow infarcts, mainly in the borderzone areas of the brain, including the CSO and BG.[50,52,56–58] Moreover, patients with COD also express lesions typically attributed to SVD.[58] It is therefore of interest to investigate if small vessels hemodynamics, in particular in cerebral perforating arteries, is affected in patients with COD. Thus, in **Chapter 4** we compare flow velocity and pulsatility in the cerebral perforating arteries of the CSO and BG between patients with COD and matched controls, as well as interheispherically in patientsn with unilateral COD. In addition, we investigate if perforating artery flow measures are related to lesions typically attributed to SVD.

Damping of flow pulsations originating at the heart occurs on many levels along the cardiovascular tree, and aims to protect the vessels from an excess of pulsatile energy and averts vascular damage.[3,4] Large arteries such as the aorta and those of the circle of Willis play a large role in pressure damping. However, it is also believed that the smaller cerebral arteries beyond the circle of Willis are involved in damping of flow pulsations.[5–7] Therefore, in **Chapter 5** we explore the phenomenon of damping of pressure pulsations distal from the first segment of the M1 up to the small perforating arteries, with velocity pulsatility as a proxy for pressure pulsatility. Damping is assessed in association with proximal measures of pressure and arterial stiffness, i.e. left ventricular stroke volume, mean arterial pressure, pulse pressure, and aortic pulse wave velocity.

Previous studies indicate that alterations in the vessel wall of large vessels, such as endothelial failure, arterial stiffness and arteriosclerosis, affect blood flow in those vessels. It is also known from pathological studies that similar alterations in the vessel wall of the cerebral perforating arteries are associated with traditional vascular risk factors.[45,59-63] This raises the question whether traditional vascular risk factors relate to flow in the small perforating arteries. Therefore, in **Chapter 6** we investigate whether traditional vascular risk factors (hypertension, diabetes, hyperlipidemia, and smoking) are associated with perforating artery flow velocity and pulsatility in the CSO and BG. In Fig. 2 a schematic overview of the chapter discussed in this part of the thesis is shown.

Part III: What is happening?
Exploring microvascular (dys)function in SVD

Cerebral small vessel disease

SVD is a widespread condition that affects the small arteries, arterioles, venules and capillaries of the brain.[37] It is the main cause of cognitive decline and stroke and involved in approximately half of all dementia cases.[1,37] Features of cerebral SVD as seen using conventional MRI include small subcortical infarcts, lacunes, white matter hyperintensities, enlarged perivascular spaces and microbleeds (Fig. 2).[64] SVD can be asymptomatic, but often presents as a stroke or cognitive impairment and appears to be driven by a complex mix of genetic as well as cardiovascular risk factors such as age and hypertension.[37,65] MRI conspicuous pathology and symptoms often reflect the result as well as the end-stage of SVD, rather than the anomalies in the cerebral small vessels themselves that occur in an earlier stage of the disease.[37,66] This makes determination and understanding of the early disease stages difficult. In addition, although it is known that SVD is associated with various vascular risk factors, the pathological mechanisms that lead to arteriolar impairment and how these result in brain pathology remains unclear. The same is true for the contribution of SVD lesions to the neurological or cognitive symptoms.[1]

The knowledge gap in cerebral small vessel disease

It is likely that features of SVD have already developed over many years when they become clinically evident. It is suggested that the main mechanism underlying SVD-related brain lesions is ischemia, resulting from arteriolar narrowing or occlusion.[1,67] This narrowing or occlusion of the arteries causes an insufficient supply of metabolites and oxygen to the brain tissue, evoking remodeling of the tissue and eventually tissue

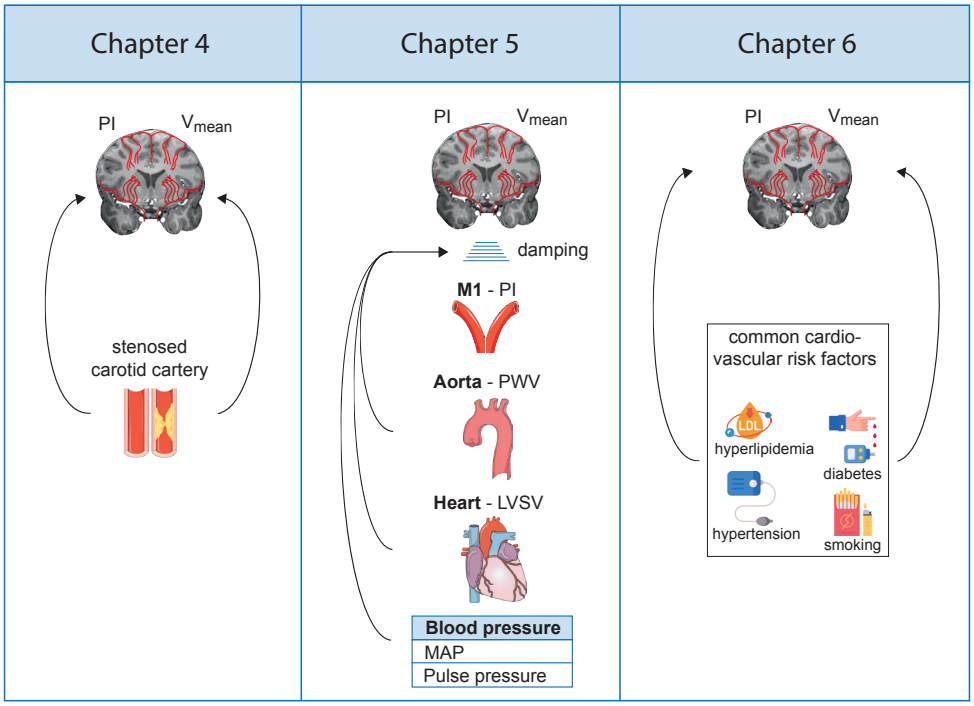

FIGURE 2. Overview of the studies discussed in part II of this thesis. PI = pulsatility index; V_{mean} = mean blood flow velocity; LVSV = left ventricular stroke volume; MAP = mean arterial pressure; PWV = pulse wave velocity.

death.[1,67] However, arteriolar narrowing or occlusion are probably also more late-stage events and do not describe the early stage pathology. Research into a different potential pathological pathway suggests that a process is started in the microvascular endothelium.[1] Endothelium consists of cells lining the interior surface of blood vessels and lymphatic vessels, separating the circulating blood and lymph from the vessel wall and surrounding tissue.[1,68] Endothelium is therefore a key part of the blood-brain-barrier,[69] enabling vessels to regulate the movement of ions, molecules and cells between the blood and the brain.[70] The loss of endothelium function would result in leakage of plasma components and the migration of cells, which enter the vessel wall (and subsequently the brain tissue). This can result in damage to the arteriolar smooth muscle cells making them thicker and stiffer, reducing their autoregulatory function. The loss of autoregulatory function means that these vessels are less able to dilate and contract and are therefore less protected against large fluctuations in arterial pressure and can cause CBF instability. This may result in more vascular damage.[1,71] Animal

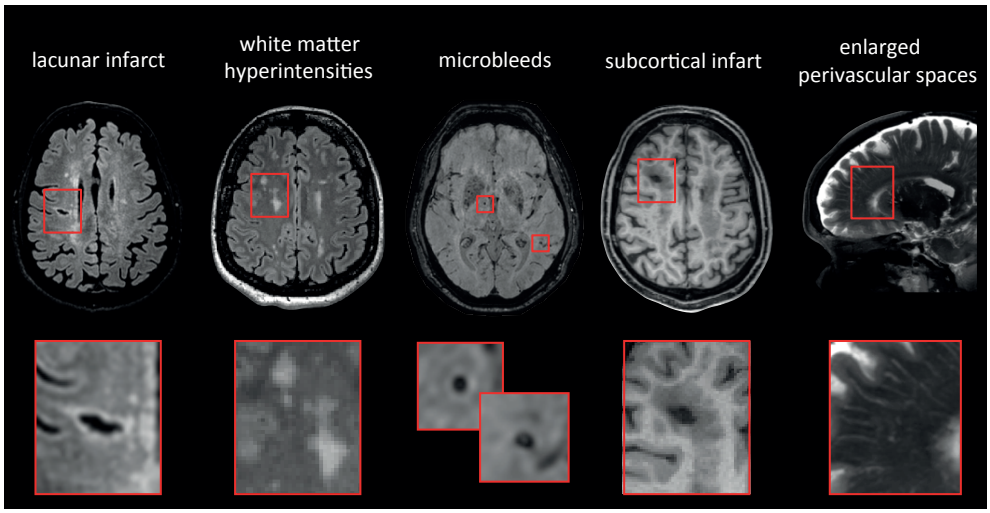

FIGURE 3. Lesions associated with cerebral small vessel disease as seen on MRI.

models confirm these hypotheses, showing a decrease in cerebrovascular reactivity, alterations of blood flow velocity and pulsatility in the microvasculature,[72,73] impairment of vasodilatory responses,[74,75] lumen narrowing in the arterioles, and an increase in the blood-brain barrier permeability.[76,77] However, these animal models cannot be directly translated to humans, because they lack the effect of ageing on the vessels[78] and because the vascular topology in animals is different from that in humans.

Regarding risk factors, age, hypertension, diabetes, hyperlipidemia, smoking and arterial fibrillation are known to significantly increase the risk of dementia.[79,80] Recurrent stroke is one of the strongest predictors of dementia onset.[81] However, it is still unclear via which mechanisms the currently known risk factors lead to SVD.[1,82] Also, discrepancies exist between the prevalence of SVD markers in various populations.[83,84] The cerebral microvasculature is known to be the substrate of onset of SVD, however, until recently it was not possible to visualize or investigate the small vessels non-invasively in humans; the size of the microvessels was simply too small to allow for this. Therefore, the mechanisms underlying SVD are mainly investigated either post-mortem or in animal models.[75,85] Although this can provide useful insights, post-mortem research is unable to look at the hemodynamics and functioning of the small vessels, and animal research is challenging to translate to humans. Due to this knowledge gap, no causative treatment for SVDs is available and management of SVDs is currently limited to the treatment of these risk factors, which is far from sufficient to halt or prevent SVDs. To

develop treatments, we need to increase our knowledge of the processes and pathology occurring in the cerebral microvasculature. In-vivo research of the small cerebral vessels in humans is therefore indispensable. By imaging and assessing the functioning of the microvasculature in a patient cohort affected by SVD, we aim to understand the role of the small perforating arteries in SVD. So in this part the thesis we ask "What is happening"?

In **Chapter 7**, the rationale and the design of ZOOM@SVDs is described. ZOOM@SVDs is one of the clinical studies included in the research program "Small vessel diseases in a mechanistic perspective: Targets for Intervention – Affected pathways and mechanistic exploitation for prevention of stroke and dementia"; acronym SVDs@target, which is funded by the Horizon 2020 scheme of the European Research Council. It focuses on small cerebral vessels at the level of the individual blood vessels and at brain tissue level using 7T MRI. This is investigated in patients with sporadic SVDs as well as in patients with monogenic (hereditary) SVD. Even though SVD is mostly a sporadic disease, a small minority of cases are attributable to monogenic variants of SVD.[78,86] One monogenic variant is called CADASIL (Cerebral Autosomal Dominant Arteriopathy with Subcortical Infarcts and Leukoencephelopathy; see textbox for more information), and while it is characterized by different symptoms and an earlier onset of symptoms than sporadic SVD, they closely resemble one another on a neuropathological and clinical level.[78,86] Due to this resemblance, research into CADASIL has immediate relevance to sporadic SVD.

Chapter 8 focuses on the CADASIL cohort and examines which aspects of cerebrovascular function, as seen with 7T MRI, are affected in patients with CADASIL compared to healthy controls. Three metrics reflecting the function of the microvessels are investigated: i) blood flow velocity and pulsatility index in cerebral perforating arteries; ii) cerebrovascular reactivity in response to a vasoactive stimulus; and iii) cerebrovascular reactivity through neurovascular coupling in response to a neuronal stimulus. This study aims to capture small vessel dysfunction in patients with CADASIL, and adresses i) which measures of small vessel function on 7T MRI are affected in patients with CADASIL relative to controls; and ii) how small vessel dysfunction on 7T MRI related with disease severity in patients with CADASIL.

Finally, **Chapter 9** will reflect on the findings presented in this thesis and discuss what I believe to be valuable future research for further development of the 2D PC MR imaging

technique and BOLD measurements at 7T MRI. Further, I will elaborate how these complementary techniquescan aid in gaining more knowledge about the cerebral small vessels and obtaining a better understanding of SVD.

CADASIL

CADASIL was discovered as a monogenic variant of small vessel disease in 1991 and in 1993 is was discovered that the NOTCH-3 gene on chromosome 19 is primarily accountable for the development of the syndrome. This chromosome is responsible for the maturation and function of small vessels in the body. Currently, patients are diagnosed via genetic testing or with a skin biopsy.[72–74] With a minimum prevalence of 2 and 5 in 100.000 it is the most common heritable cause of stroke and vascular dementia worldwide[75,76] and individuals carrying this pathogenic variant have a a ~100% risk of developing the disease.[48,71] Contrary to sporadic SVDs, CADASIL is characterized by an earlier onset of stroke events and a more frequent occurrence of migraine with aura.[48,71] Treatment is currently mainly aimed at cardiovascular risk reduction.[71]

REFERENCES

1. Wardlaw, J. M., Smith, C. & Dichgans, M. Mechanisms underlying sporadic cerebral small vessel disease : insights from neuroimaging. Lancet Neurol. 12, 70060–7 (2013).
2. Bouvy, W. H. et al. Assessment of blood flow velocity and pulsatility in cerebral perforating arteries with 7-T quantitative flow MRI. NMR Biomed. 29, 1295–1304 (2016).
3. Geurts, L., Biessels, G. J., Luijten, P. & Zwanenburg, J. Better and faster velocity pulsatility assessment in cerebral white matter perforating arteries with 7T quantitative flow MRI through improved slice profile, acquisition scheme, and postprocessing. Magn. Reson. Med. 79, 1473–1482 (2018).
4. Grochowski, C. & Staśkiewicz, G. Ultra high field TOF-MRA: A method to visualize small cerebral vessels. 7 T TOF-MRA sequence parameters on different MRI scanners – Literature review. Neurol. Neurochir. Pol. 51, 411–418 (2017).
5. Demchuk, A. M., Menon, B. K. & Goyal, M. Comparing vessel imaging: Noncontrast computed tomography/computed tomographic angiography should be the new minimum standard in acute disabling stroke. Stroke 47, 273–281 (2016).
6. Laviña, B. Brain vascular imaging techniques. Int. J. Mol. Sci. 18, (2017).
7. Peters, T. M. Image-guidance for surgical procedures. Phys. Med. Biol. 14, 505–540 (2006).
8. Lakhan, S. E., Kaplan, A., Laird, C. & Leiter, Y. The interventionalism of medicine: Interventional radiology, cardiology, and neuroradiology. Int. Arch. Med. 2, 1–6 (2009).
9. Zimmer, L. & Luxen, A. PET radiotracers for molecular imaging in the brain: Past, present and future. Neuroimage 61, 363–370 (2012).
10. Power, S. P. et al. Computed tomography and patient risk: Facts, perceptions and uncertainties. World J. Radiol. 8, 902 (2016).
11. Koenig, T. R., Wolff, D., Mettler, F. A. & Wagner, L. K. Skin injuries from fluoroscopically guided procedures: Part I, characteristics of radiation injury. Am. J. Roentgenol. 177, 3–11 (2001).
12. Christiansen, C. X-ray contrast media - An overview. Toxicology 209, 185–187 (2005).
13. Heiss, W. D. The additional value of PET in the assessment of cerebral small vessel disease. J. Nucl. Med. 59, 1660–1664 (2018).
14. Eden, A. Effect of emitted power on waveform intensity in transcranial doppler. Stroke 25, 523–524 (1994).
15. Kammerer, S., Mueller-Eschner, M., Berkefeld, J. & Tritt, S. Time-resolved 3D Rotational Angiography (4D DSA) of the Lenticulostriate Arteries: Display of Normal Anatomic

Variants and Collaterals in Cases with Chronic Obstruction of the MCA. Clin. Neuroradiol. 27, 451–457 (2017).
16. Chen, Y. C. et al. Correlation between the number of lenticulostriate arteries and imaging of cerebral small vessel disease. Front. Neurol. 10, 1–8 (2019).
17. Miller, D. L. et al. Radiation doses in interventional radiology procedures: The RAD-IR study part I: Overall measures of dose. J. Vasc. Interv. Radiol. 14, 711–727 (2003).
18. Tang, H. et al. Accelerated time-of-flight magnetic resonance angiography with sparse undersampling and iterative reconstruction for the evaluation of intracranial arteries. Korean J. Radiol. 20, 265–274 (2019).
19. Farhat, N. S., Theiss, R., Santini, T., Ibrahim, T. S. & Aizenstein, H. J. Neuroimaging of Small Vessel Disease in Late-Life Depression. Adv. Exp. Med. Biol. 1192, 95–115 (2019).
20. Geurts, L., Biessels, G. J., Luijten, P. & Zwanenburg, J. Better and faster velocity pulsatility assessment in cerebral white matter perforating arteries with 7T quantitative flow MRI through improved slice profile, acquisition scheme, and postprocessing. Magn. Reson. Med. 79, 1473–1482 (2018).
21. Geurts, L. J. et al. Vascular reactivity in small cerebral perforating arteries with 7 T phase contrast MRI – A proof of concept study. Neuroimage 172, 470–477 (2018).
22. Siero, J. C. W., Bhogal, A. & Jansma, J. M. Blood oxygenation level-dependent/ Functional Magnetic Resonance Imaging: Underpinnings, Practice, and Perspectives. PET Clin. 8, 329–344 (2013).
23. Ocali, O. & Atalar, E. Ultimate Intrinsic Signal-to-Noise Ratio in MRI F ~ B. 462–473.
24. Pohmann, R., Speck, O. & Scheffler, K. Signal-to-noise ratio and MR tissue parameters in human brain imaging at 3, 7, and 9.4 tesla using current receive coil arrays. Magn. Reson. Med. 75, 801–809 (2016).
25. O'Donnel, M. NMR blood flow imaging using multiecho, phase contrast sequences. Med. Phys. 12, 59–64 (1985).
26. Carr, H. Y. & Purcell, E. M. Effects of Diffusion on Free Precession in Nuclear Magnetic Resonance Experiments*t. (1954).
27. Lotz, J., Meier, C., Leppert, A. & Galanski, M. Cardiovascular flow measurement with phase-contrast MR imaging: Basic facts and implementation. Radiographics 22, 651–671 (2002).
28. Hoogeveen, R. M., Bakker, C. J. G. & Viergever, M. A. MR phase-contrast flow measurement with limited spatial resolution in small vessels: Value of model-based image analysis. Magn. Reson. Med. 41, 520–528 (1999).
29. Hoogeveen, R. M., Bakker, C. J. G. & Viergever, M. A. Limits to the accuracy of vessel

diameter measurement in MR angiography. J. Magn. Reson. Imaging 8, 1228–1235 (1998).
30. Del Bene, A., Makin, S. D. J., Doubal, F. N., Inzitari, D. & Wardlaw, J. M. Variation in risk factors for recent small subcortical infarcts with infarct size, shape, and location. Stroke 44, 3000–3006 (2013).
31. Moody, D. M., Bell, M. A. & Challa, V. R. Features of the Cerebral Vascular Pattern That Predict Vulnerability to Perfusion or Oxygenation Deficiency: An Anatomic Study. Am. J. Neuroradiol. 11, 431–439 (1990).
32. Wardlaw, J. M., Smith, C. & Dichgans, M. Mechanisms of sporadic cerebral small vessel disease: Insights from neuroimaging. The Lancet Neurology vol. 12 483–497 (2013).
33. Fisher, C. M. The arterial lesions underlying lacunes. Acta Neuropathol. 12, 1–15 (1969).
34. Scuteri, A., Nilsson, P. M., Tzourio, C., Redon, J. & Laurent, S. Microvascular brain damage with aging and hypertension: Pathophysiological consideration and clinical implications. J. Hypertens. 29, 1469–1477 (2011).
35. Blair, G. W., Hernandez, M. V., Thrippleton, M. J., Doubal, F. N. & Wardlaw, J. M. Advanced Neuroimaging of Cerebral Small Vessel Disease. Current Treatment Options in Cardiovascular Medicine vol. 19 (2017).
36. Wardlaw, J. M., Smith, C. & Dichgans, M. Mechanisms of sporadic cerebral small vessel disease: Insights from neuroimaging. Lancet Neurol. 12, 483–497 (2013).
37. Pantoni, L. Cerebral small vessel disease: from pathogenesis and clinical characteristics to therapeutic challenges. Lancet Neurol. 9, 689–701 (2010).
38. Geurts, L. J., Luijten, P. R., Klijn, C. J. M., Zwanenburg, J. J. M. & Biessels, G. J. Higher Pulsatility in Cerebral Perforating Arteries in Patients With Small Vessel Disease Related Stroke, a 7T MRI Study. Stroke 50, 62–68 (2018).
39. Zeng, L.-L. et al. Neurobiological basis of head motion in brain imaging. Proc. Natl. Acad. Sci. 111, 6058–6062 (2014).
40. Schenck, J., Kelley, D. A. C. & Marinelli, L. Instrumentations: magnets, coils and hardware. in Magnetic Resonance Imaging of the Brain and Spine 2–24 (Lippincott Williams & Wilkins, 2009).
41. Purves, D. et al. Neuroscience. (Sinauer Associates Inc., 2001).
42. Chandra, A., Li, W., Stone, C., Geng, X. & Ding, Y. The cerebral circulation and cerebrovascular disease I: Anatomy. Brain circulation, 3(2), 45. Brain Circ. 3, 45–56 (2017).
43. Djulejić, V. et al. Common features of the cerebral perforating arteries and their clinical significance. Acta Neurochir. (Wien). 157, 743–754 (2015).
44. Edvinsson, L. & Krause, D. N. Cerebral Blood Flow and Metabolism. in 1–521 (Lippincott,

Williams & Wilkins, 2002).

45. Granger, D. N., Rodrigues, S. F., Yildirim, A. & Senchenkova, E. Y. Microvascular responses to cardiovascular risk factors. Microcirculation (2010) doi:10.1111/j.1549-8719.2009.00015.x.
46. Pase, M. P., Grima, N. A., Stough, C. K., Scholey, A. & Pipingas, A. Cardiovascular disease risk and cerebral blood flow velocity. Stroke (2012) doi:10.1161/STROKEAHA.112.666727.
47. Guyton, A. C. Blood pressure control - Special role of the kidneys and body fluids. Science (80-.). 252, 1813–1816 (1991).
48. Delicce, A. V, Basit, H. & Makaryus, A. N. Physiology, Frank-Starling Law. In: StatPearls. Treasure Island (FL): StatPearls Publishing; 2020. (StatPearls Publishing LLC, 2020).
49. Cipolla, M. J. Control of Cerebral Blood Flow. in The Cerebral Circulation (Morgan & Claypool Life Sciences, 2010).
50. Hendrikse, J., Hartkamp, M. J., Hillen, B., Mali, W. P. T. M. & Van Der Grond, J. Collateral Ability of the Circle of Willis in Patients With Unilateral Internal Carotid Artery Occlusion Border Zone Infarcts and Clinical Symptoms. Stroke 32, 2768–2773 (2001).
51. Powers, W. J., Press, G. A., Grubb, R. L., Gado, M. & Raichle, M. E. The effect of hemodynamically significant carotid artery disease on the hemodynamic status of the cerebral circulation. Ann. Intern. Med. 106, 27–35 (1987).
52. Leblanc, R., Yamamoto, Y. L., Tyler, J. L. & Hakim, A. Hemodynamic and Metabolic Effects of Extracranial Carotid Disease. J. Neurol. Sci 16, 51–57 (1989).
53. Bokkers, R. P. H. et al. Arterial spin-labeling MR imaging measurements of timing parameters in patients with a carotid artery occlusion. Am. J. Neuroradiol. 29, 1698–1703 (2008).
54. Yamauchi, H., Fukuyama, H., Nagahama, Y., Katsumi, Y. & Okazawa, H. Cerebral hematocrit decreases with hemodynamic compromise in carotid artery occlusion: A PET study. Stroke 29, 98–103 (1998).
55. Kluytmans, M., Van Der Grond, J. & Viergever, M. A. Gray matter and white matter perfusion imaging in patients with severe carotid artery lesions. Radiology 209, 675–682 (1998).
56. Leoni, R. F. et al. Assessing Cerebrovascular Reactivity in Carotid Steno-Occlusive Disease Using MRI BOLD and ASL Techniques. Radiol. Res. Pract. 2012, 1–10 (2012).
57. Krapf, H., Widder, B. & Skalej, M. Small rosarylike infarctions in the centrum ovale suggest hemodynamic failure. Am. J. Neuroradiol. 19, 1479–1484 (1998).
58. Klijn, C. J. M., Kappelle, L. J., Tulleken, C. A. F. & Van Gijn, J. Symptomatic carotid artery occlusion: A reappraisal of hemodynamic factors. Stroke vol. 28 2084–2093 (1997).

59. Nichols, W. W., O'Rourke, M. F., Vlachopoulos, C., Hoeks, A. P. & Reneman, R. S. McDonald's blood flow in arteries theoretical, experimental and clinical principles. McDonald's Blood Flow in Arteries, Sixth Edition: Theoretical, Experimental and Clinical Principles (2011). doi:10.1016/0306-3623(92)90079-y.
60. Webb, A. J. S. et al. Increased Cerebral Arterial Pulsatility in Patients With Leukoaraiosis Arterial Stiffness Enhances Transmission of Aortic Pulsatility. 43, 2631–2636 (2012).
61. Bai, C. H., Chen, J. R., Chiu, H. C. & Pan, W. H. Lower blood flow velocity, higher resistance index, and larger diameter of extracranial carotid arteries are associated with ischemic stroke independently of carotid atherosclerosis and cardiovascular risk factors. J. Clin. Ultrasound 35, 322–330 (2007).
62. S., A., D.M.O., P., L.J., K. & A., A. Risk of vascular events after nondisabling small and large vessel cerebral ischemia. Cerebrovasc. Dis. 36, 190–195 (2013).
63. Petrie, J. R., Guzik, T. J. & Touyz, R. M. Diabetes, Hypertension, and Cardiovascular Disease: Clinical Insights and Vascular Mechanisms. Canadian Journal of Cardiology 34(5): 575-584 (2018) doi:10.1016/j.cjca.2017.12.005.
64. Wardlaw, J. M. et al. Neuroimaging standards for research into small vessel disease and its contribution to ageing and neurodegeneration. The Lancet Neurology vol. 12 822–838 (2013).
65. Wardlaw, J. M. et al. Neuroimaging standards for research into small vessel disease and its contribution to ageing and neurodegeneration. Lancet Neurol. 12, 822–838 (2013).
66. Iadecola, C. The Pathobiology of Vascular Dementia. Neuron vol. 80 844–866 (2013).
67. Shi, Y. & Wardlaw, J. M. Update on cerebral small vessel disease: A dynamic whole-brain disease. Stroke and Vascular Neurology vol. 1 83–92 (2016).
68. Hakim, A. M. Small vessel disease. Front. Neurol. 10, (2019).
69. Bechmann, I., Galea, I. & Perry, V. H. What is the blood-brain barrier (not)? Trends Immunol. 28, 5–11 (2007).
70. Benson, P. F. & Joseph, M. C. The Blood-Brain Barrier. Dev. Med. Child Neurol. 3, 510–514 (1961).
71. Stevenson, S. F., Doubal, F. N., Shuler, K. & Wardlaw, J. M. A Systematic Review of Dynamic Cerebral and Peripheral Endothelial Function in Lacunar Stroke Versus Controls. Stroke 41, (2010).
72. Jandke, S. et al. The association between hypertensive arteriopathy and cerebral amyloid angiopathy in spontaneously hypertensive stroke-prone rats. Brain Pathol. 28, 844–859 (2018).
73. Schreiber, S. et al. The pathologic cascade of cerebrovascular lesions in SHRSP: Is

erythrocyte accumulation an early phase. J. Cereb. Blood Flow Metab. 32, 278–290 (2012).

74. Iadecola, C. et al. SOD1 rescues cerebral endothelial dysfunction in mice overexpressing amyloid precursor protein. Nat. Neurosci. 2, 157–161 (1999).
75. Dabertrand, F. et al. Potassium channelopathy-like defect underlies early-stage cerebrovascular dysfunction in a genetic model of small vessel disease. Proc. Natl. Acad. Sci. 112, E796–E805 (2015).
76. Faraci, F. M. Protecting against vascular disease in brain. Am. J. Physiol. - Hear. Circ. Physiol. 300, 1566–1582 (2011).
77. Faraco, G. & Iadecola, C. Hypertension: A harbinger of stroke and dementia. Hypertension 62, 810–817 (2013).
78. Joutel, A. & Faraci, F. M. Cerebral Small Vessel Disease (SVD): insights and opportunities from mouse models of collagen IV-related SVD and CADASIL. Stroke 45, (2014).
79. Sahathevan, R., Brodtmann, A. & Donnan, G. A. Dementia, stroke, and vascular risk factors; a review. Int. J. Stroke 7, 61–73 (2012).
80. Staals, J., Makin, S. D. J., Doubal, F. N., Dennis, M. S. & Wardlaw, J. M. Stroke subtype, vascular risk factors, and total MRI brain small-vessel disease burden. Neurology 83, 1228–1234 (2014).
81. Pendlebury, S. T. & Rothwell, P. M. Prevalence, incidence, and factors associated with pre-stroke and post-stroke dementia: a systematic review and meta-analysis. Lancet Neurol. 8, 1006–1018 (2009).
82. Zwanenburg, J. J. M. & Van Osch, M. J. P. Targeting cerebral small vessel disease with MRI. Stroke 48, 3175–3182 (2017).
83. Shu, J. et al. Clinical and neuroimaging disparity between Chinese and German patients with cerebral small vessel disease: a comparative study. Sci. Rep. 9, 1–7 (2019).
84. Mok, V. et al. Race-ethnicity and cerebral small vessel disease—comparison between Chinese and White populations. Int. J. Stroke 9 Suppl A100, 36–42 (2014).
85. Joutel, A. et al. Cerebrovascular dysfunction and microcirculation rarefaction precede white matter lesions in a mouse genetic model of cerebral ischemic small vessel disease. J. Clin. Invest. 120, (2010).
86. Chabriat, H., Joutel, A., Dichgans, M., Tournier-Lasserve, E. & Bousser, M. G. CADASIL. The Lancet Neurology vol. 8 643–653 (2009).
87. Tournier-Lasserve, E., Iba-Zizen, M. T., Romero, N. & Bousser, M. G. Autosomal dominant syndrome with strokelike episodes and leukoencephalopathy. Stroke 22, 1297–1302 (1991).

88. Tournier-Lasserve, E. et al. Cerebral autosomal dominant arteriopathy with subcortical infarcts and leukoencephalopathy maps to chromosome 19q12. Nat. Genet. 3, 256–259 (1993).
89. Domenga, V. et al. Notch3 is required for arterial identity and maturation of vascular smooth muscle cells. Genes Dev. 18, 2730–2735 (2004).
90. Razvi, S. S. M., Davidson, R., Bone, I. & Muir, K. The prevalence of cerebral autosomal dominant arteriopathy with subcortical infarcts and leucoencepnalopathy (CADASIL) in the west of Scotland. J. Neurol. Neurosurg. Psychiatry 76, 739–741 (2005).
91. Narayan, S. K., Gorman, G., Kalaria, R. N., Ford, G. A. & Chinnery, P. F. The Minimum Prevalence of CADASIL in Northeast England. Neurology 78, 1025–1027 (2012).

Part 1

WHAT ELSE IS IN THERE?

MAKING SMALL PERFORATING ARTERY DETECTION MORE RELIABLE AND EMPLOYABLE

Chapter 2

VELOCITY AND PULSATILITY MEASURES IN THE PERFORATING ARTERIES OF THE BASAL GANGLIA AT 3T MRI IN REFERENCE TO 7T MRI

T. Arts, T.A. Meijs, H.B. Grotenhuis, M. Voskuil, J.C.W. Siero, G.J. Biessels, J.J.M. Zwanenburg

Frontiers in Neuroscience, 15, 665480 (2021)

ABSTRACT

Background and purpose: Cerebral perforating artery flow velocity and pulsatility can be measured at 7 tesla (T) MRI. Enabling these metrics on more widely available 3T systems would make them more employable. It is currently unknown whether these measurements can be performed at 3T MRI due to the lower signal-to-noise ratio. Therefore, this study investigates if perforating artery flow velocity and pulsatility in the basal ganglia (BG) can be measured at 3T and assess the agreement with 7T MRI as reference.

Methods: Twenty-nine subjects were included, of which 14 patients with aortic coarctation (median age 29 years [21-72]) and 15 controls (median age 27 years [22-64]). Using a cardiac-gated 2D phase-contrast MRI sequence BG perforating arteries were imaged at 3T and 7T MRI and perforating artery density ($N_{density}$, #/cm^2), flow velocity (V_{mean}, cm/s) and pulsatility index (PI) were determined. Agreement between MRI modalities was assessed using correlation and difference plots with linear regression. A p-value ≤ 0.05 indicated statistical significance.

Results: Perforating artery flow velocity and pulsatility can be measured at 3T MRI ($N_{density}$=0.21±0.11; V_{mean}=6.04±1.27; PI=0.49±0.19), although values differed from 7T MRI measurements ($N_{density}$=0.95±0.21; V_{mean}=3.89±0.56; PI=0.28±0.08). The number of detected arteries was lower at 3T (5±3) than 7T MRI (24±6), indicating that 3T MRI is on average a factor 4.8 less sensitive to detect cerebral perforating arteries. Comparison with 7T MRI showed some agreement in $N_{density}$, but little to no agreement for V_{mean} and PI. Equalizing the modalities' sensitivity by comparing the detected arteries on 7T MRI with the highest velocity with all vessels detected on 3T MRI, showed some improvement in agreement for PI, but not for V_{mean}.

Conclusion: Cerebral perforating artery flow velocity and pulsatility can be measured at 3T MRI, although an approximately fivefold sample size is needed at 3T relative to 7T MRI for a given effect size, and the measurements should be performed with equal scanner field strength and protocol.

INTRODUCTION

Cerebral perforating arteries are small branches of the main cerebral arteries that supply blood to the deep gray and white matter brain regions. Dysfunction of these perforating arteries plays a major role in cerebral small vessel disease.[1,2] These perforating arteries can be imaged using 7 tesla (T) magnetic resonance imaging (MRI) with a retrospectively gated 2D phase-contrast sequence.[3–5] Previous literature has shown that this sequence enables us to reliably measure the perforating artery flow metrics, i.e. blood-flow velocity and pulsatility.[4] However, compared to 7T MRI scanners, 3T MRI scanners are more widely available in research institutions and hospitals. The ability to image the perforating arteries and measure their flow on 3T MRI would therefore considerably increase the employability of these metrics. However, the signal-to-noise ratio (SNR) of 3T MRI is lower than that of 7T MRI[6], which means that 3T MRI will only be able to detect the relatively large perforating arteries with higher flow velocities. Therefore, in this study we investigate if flow velocity and pulsatility in the perforating arteries of the basal ganglia (BG) can be measured at 3T MRI and assess the agreement with 7T MRI measurements as reference. Also, we will explore whether the subset of perforating arteries detected at 7T MRI with the highest velocities are representative for the perforating arteries detected at 3T MRI. As a region of interest we chose the level of the basal ganglia (BG), as perforating arteries in this region are relatively large (up to 1 mm in diameter), which increases the likelihood of being detected with 3T MRI.

METHODS AND MATERIALS

Image acquisition

Images for the technical comparison between 3T and 7T MRI were obtained from a larger, clinical study in which brain lesions and hemodynamics were studied in 14 patients with coarctation of the aorta (CoA) and 15 control subjects with no history of cardiovascular disease, neurological disease, or intellectual disability. The study was approved by our institutional review board. All subjects provided written informed consent. Patients with CoA were included when they had previously undergone surgical repair of CoA. Prior stent implantation for native or recurrent CoA was an exclusion criterion due to potential artefacts. General exclusion criteria comprised current pregnancy and the presence of a contraindication for undergoing MRI. Subjects were scanned on a Philips Ingenia Elition 3T scanner with a 20-channel Head-Neck-Spine coil and on a Philips Achieva 7T MRI

scanner using a 32-channel receive head coil (Nova Medical, Wilmington, USA)(Philips Healthcare, Best, The Netherlands). For the controls, 3T and 7T scanning sessions were performed on the same day, in random order. Patients' 3T and 7T MRI scans were often performed on different days (n=10, ranging from 96 to 227 days apart). On 7T MRI, small cerebral perforating arteries in the BG were imaged using a previously described retrospectively gated 2D phase-contrast (PC) sequence.[3] The 3T MRI 2D PC protocol was in principle the same as the 7T protocol, both with an acquired in-plane resolution of 0.3x0.3 mm^2, reconstructed to 0.2x0.2 mm^2 in-plane resolution. Scan parameters of the 3T and 7T PC scans can be found in Table 1. A peripheral pulse oximeter was used for retrospective gating and cushions were placed besides the subject's head to minimize head movement during scanning. The scan was planned manually, with a target slice location at the bottom of the corpus callosum (see Fig. 1A). At 3T MRI, scanning was performed by the clinical technician on duty, and was therefore not always the same scanner operator for each subject. At 7T MRI, scanning was performed by the same scanner operator.

Image processing

2D PC scans were visually checked for sufficient quality, which meant that severe artefacts due to motion or large pulsating vessels should be absent. Scans with poor image quality were excluded from analysis.

The region of interest (ROI) was manually drawn around the BG (see Fig. 1), using the magnitude 2D PC image. The anterior zone of this ROI was demarcated by the anterior end of the insula, the posterior zone by the posterior end of the thalamus, and the lateral zone by the claustrum.[4] Small cerebral perforators in the BG were detected as previously published using Matlab[3](R2016b, The MathWorks, Natick, MA), which includes the following steps: First, a phase correction was applied on the background to make the mean velocity of tissue 0 cm/s by median filtering the time-averaged velocity map and subtracting it from the velocity map of each cardiac time point. Then, the velocity SNR was calculated from an estimation of the magnitude SNR. Further, given the velocity SNR, the two-sided 95% velocity confidence intervals (CIs) were estimated for the mean blood flow velocity (V_{mean}) to enable consistent selection of vessels with significant positive flow (i.e. non-zero, positive V_{mean} with a statistical significance of 0.05). All voxels inside the BG mask without 0 cm/s within their CI of V_{mean} and hyperintense signal in the magnitude image were considered significant. Only positive

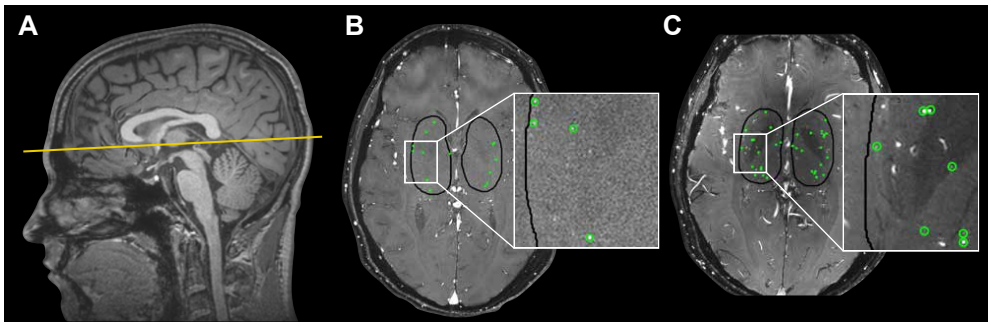

FIGURE 1. (A) The 2D phase contrast slice in the basal ganglia (BG) is located at the bottom of the corpus callosum (solid line). (B-C) Cerebral perforating arteries detected in the BG with 3 tesla (T) MRI (B) and 7T MRI (C) and included in the analysis are circled in green. Cerebral perforating arteries excluded from analysis due to a non-perpendicular orientation or close proximity to other perforating arteries (<1.2mm) are circled in red. Note that for this subject all detected vessels at 3T were sufficient for inclusion. Also note the inhomogeneity in the background suppression at 7T (darker central area), which is induced by the well-known inhomogeneity of the radiofrequency B1+ transmit field (resulting in spatially varying flip angle) at 7T MRI.[14]

TABLE 1. Parameters of the 2D phase contrast sequence of 3 and 7 tesla MRI

	3 tesla/7 tesla
FOV, mm (RLxAP)	250 x 250/180*
SENSE factor (AP direction)	1.5/1*
Acquired voxel size, mm**	0.3 x 0.3 x 2.0
Flip angle, °	50
Venc, cm/s	20
TR, ms	28.2/28
TE, ms	14.5/14.7-15.1
TFE factor	3/2***
Acquired temporal resolution (ms)	169/112
Reconstructed time points	9-10/13
Scan time, min:s†	3:27/5:28

Abbreviations: FOV= field of view; RL= right-left, AP= anterior-posterior; Venc= encoded velocity; TR= repetition time; TE= echo time; TFE= turbo field echo. † Scan time for a heart rate of 52 bpm. *The acquired matrix (FOV/voxel size/SENSE factor), which determines the scan time and affects the signal-to-noise ratio, is practically equal between 3T and 7T. **Reconstructed to 0.2 x 0.2 mm2 in-plane resolution. ***The TFE factor determines the acquired temporal resolution (which is 2*TFE*TR); the 3T implementation didn't allow for a lower TFE factor than 3.

velocities with hyperintense magnitude signal were included to ensure that veins were not included in the selected vessels. Every group of neighboring significant voxels was defined as belonging to the same perforating artery and the voxel with the highest mean velocity of such a group was taken as representative for the perforating artery and used to calculate the flow measures. Perforating arteries in the BG with a non-perpendicular orientation to the scanning plane were excluded. This was performed by taking the perforating artery voxel and assessing the shape of the collection of surrounding high-intensity voxels. If the ratio of the largest axis length to the smallest axis length was more than a set threshold (2 in our case), the shape was determined to be elliptical and the small perforating artery was excluded. In addition, perforating arteries within 1.2 mm distance from each other were excluded from analysis as these are mostly multiple detections located on larger and/or non-perpendicular vessels. In Fig. 1 the slice orientation and delineation of the BG as well as detected perforating arteries at 3T and 7T MRI are shown.

Quantitative measures

Analysis of the 3T as well as the 7T PC data resulted in a perforating artery density (number of detected perforators/cm^2, $N_{density}$). For each detected perforator, an average blood-flow velocity (V_{mean}, cm/s), was obtained. The mean blood-flow velocity curve per subject was determined by averaging over all perforators. To calculate the pulsatility index (PI), the perforating arteries' velocity curves were first normalized and then averaged. PI was calculated from the resulting mean normalized velocity curve with the following formula

$$PI = (V_{max} - V_{min})/V_{mean} \quad [1]$$

where V_{min}, V_{max} and V_{mean}, respectively, are the minimum, maximum and mean of the mean normalized velocity curve (due to the normalization procedure V_{mean} equals 1.0).

Statistical analysis

The agreement between $N_{density}$, V_{mean} and PI at 7T and 3T MRI was quantified and visually shown using correlation plots combined with linear regression as well as difference plots combined with linear regression.[7-9] The next sections briefly provide background information on correlation plots and difference plots, after which the details of the methods to compare the 3T and 7T results are described.

Correlation plots

The correlation plots combined with linear regression determine the coefficient of determination (r^2), the latter with an associated *p*-value, providing information regarding the coefficient's significance. In case of significance, the coefficient of determination shows the amount of shared inter-subject variance between 7T MRI and 3T MRI results. If significance is absent, shared inter-subject variance is lost in the noise.

Difference plots

Difference plots in absolute units (i.e. Bland Altman plots or absolute difference plots)[8,10] provide information about how the inter-method variance compares to the inter-subject variance. A large inter-method variance compared to the mean values suggests that the measurement noise dominates over the inter-subject variance, resulting in limited agreement between the methods. However, a small inter-method variance compared to the mean values implies a high level of agreement between the two methods. By using Bland Altman plots with linear regression and a resulting *p*-value, a possible significant proportional bias (*p*-value≤0.05) can be studied between the differences and the measured values. Proportional bias indicates that the difference of the measured values of the two modalities scales with the average of the two values, i.e. the differences are (partly) predicted by the mean values. In case of a significant proportional bias, the bias is further investigated to assess its characteristics. To this end, the difference plots are presented in percentage unit differences (i.e. Pollock plots or relative difference plots)[9] and likewise combined with linear regression. If significant proportional bias exists in the absolute difference plots, but not in the relative difference plots, it can be concluded that the bias between 3T and 7T MRI is mainly linear. However, if significant proportional bias is present in the absolute difference plots as well as in the relative difference plots, also considerable non-linear sources of error are present. Measurement error is therefore not constant in an absolute or relative sense, strongly limiting the agreement.[7]

3T-7T comparison using correlation and difference plots

First, we determined whether significant differences existed between patients and controls in $N_{density}$, V_{mean} and PI at 7T MRI using an unpaired Student's t-test. A *p*-value≤0.05 was considered statistically significant. Significant differences at 7T MRI would allow us to further evaluate the 3T MRI for its ability to detect a certain effect size. Further, correlation and difference plots were constructed for all detected perforating

arteries on 3T and 7T MRI, and linear regression was applied. A secondary analysis was performed in which the bias caused by the higher sensitivity of the 7T MRI was minimized. This was done with two matching approaches: i) matching by number, in which the number of analyzed vessels was made equal per subject between 3T and 7T MRI by selecting the *N* vessels at 7T with the highest velocities, with *N* the number of vessels detected at 3T MRI; ii) matching by location, by visually matching 3T and 7T MRI vessels on anatomical location. For both approaches correlation and difference plots were constructed. However, concerning matching by location, 2D PC planning of 3T and 7T MRI was sufficiently similar for matching in only 11 of 28 subjects. In these 11 subjects, a total of 17 matched pairs were found (range 1-4 per subject). This limited number of suitable subjects and matches resulted in limited power. Therefore, in this study, vessel matching by anatomical location was not seen as a suitable approach to compare small vessel flow measures across two scanning modalities. The results of this approach are shown in Supplementary Material A.

Statistical analyses were performed in IBM SPSS (IBM Corp., v22.0, NY, USA) and GraphPad Prism (GraphPad Software, v5.03, CA, USA).

RESULTS

The 3T 2D PC scan of one patient exhibited excessive motion artifacts, therefore this subject was excluded from analyses. Data of the remaining 13 patients (median age 29 years [range 21-72 years]) and 15 controls (median age 27 years [range 22-64 years]) were included.

At 3T as well as at 7T MRI, cerebral perforating arteries were detected for each subject. At 7T MRI, perforating artery measurements of patients did not significantly differ from those of controls (see Supplementary Material B). As group differences in perforating artery measures could therefore not be used to compare 3T and 7T MRI, the subject groups were pooled for the remaining analyses.

The number of detected perforating arteries ($N_{detected}$) at 3T MRI and 7T MRI was (mean±standard deviation) 5±3 and 24±6, respectively.

Agreement between 7T and 3T MRI perforating artery flow measures, using all detected perforating arteries

3T MRI detected less perforating arteries with low velocities compared to 7T MRI, as can be seen from the velocity distribution in Fig. 2. For higher velocities, the number of detected perforating arteries became more similar between 3T and 7T MRI for a given velocity.

The mean and standard deviations of $N_{density}$, V_{mean} and PI are given in Table 2. The correlation and absolute and relative difference plots for these variables are shown in Fig. 3. For $N_{density}$, the coefficient of determination r^2 of the correlation showed a weak but significant correlation (r^2=0.17, p=0.02). For V_{mean} (p=0.34) and PI (p=0.97) no significant coefficient of determination was seen in the correlation plots.

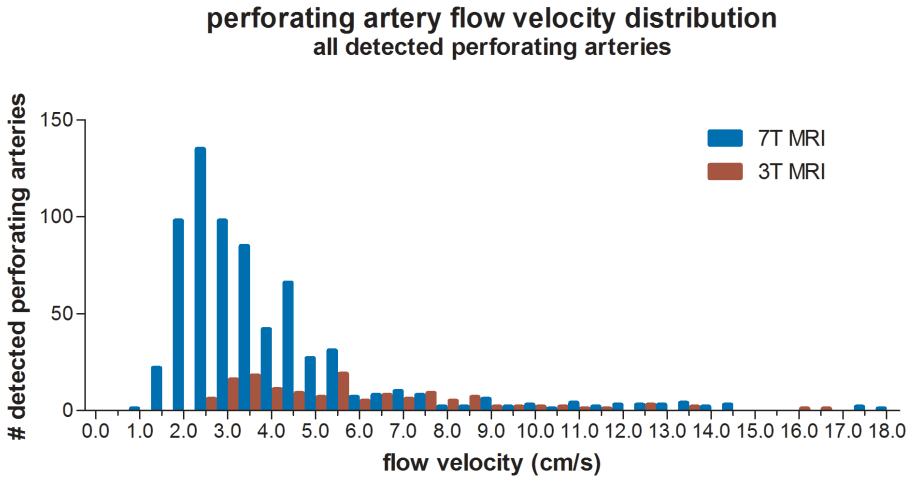

FIGURE 2. Histogram showing the velocity distribution of all detected perforating arteries on 3 tesla (T) and 7T MRI of all subjects.

TABLE 2. Perforating artery flow at 3 and 7 tesla MRI using all detected perforating arteries

	3 tesla (n=28)	7 tesla (n=29)
$N_{density}$ (#/cm^2)	0.21±0.11	0.95±0.21
V_{mean} (cm/s)	6.04±1.27	3.89±0.56
PI	0.49±0.19	0.28±0.08

Results are presented as mean±standard deviation. Abbreviations: $N_{density}$= number of detected perforating arteries/cm^2; V_{mean}= mean blood-flow velocity; PI= pulsatility index.

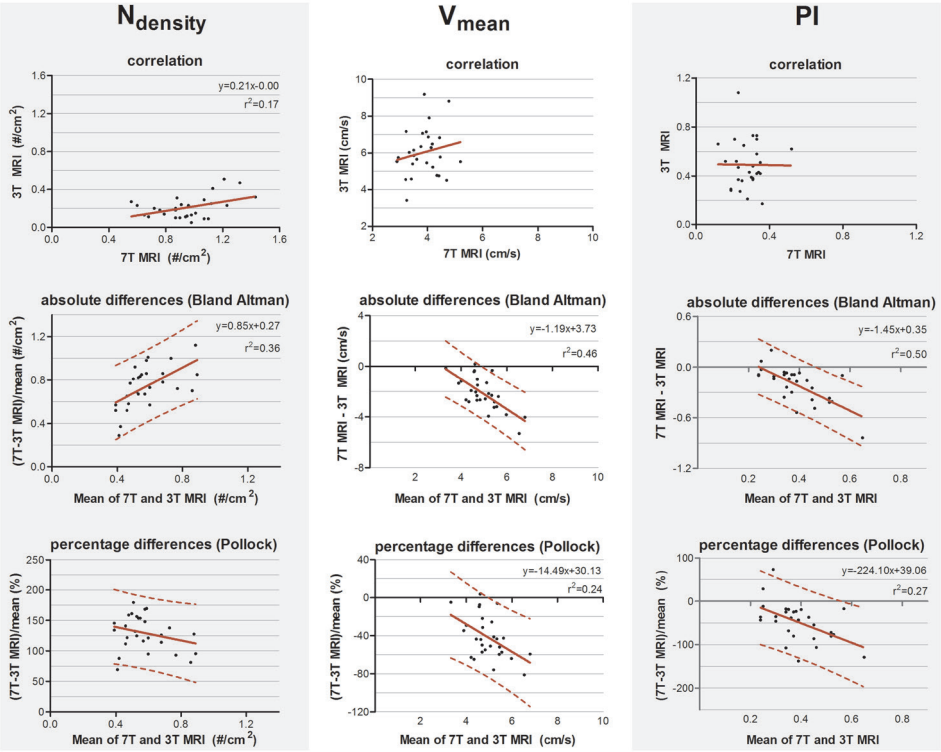

FIGURE 3. Top row: Correlation plots of the number of detected perforating arteries/cm² ($N_{density}$), the mean blood flow velocity (V_{mean}) and pulsatility (PI) measured at 3 tesla (T) and 7T MRI. The line resulting from linear regression is given by the solid line. In case of a significant correlation the equation of the regression line is given. Middle and bottom row: difference plots in absolute units (Bland Altman) and in percentage units (Pollock), respectively, for Ndensity, Vmean and PI. The regression line (i.e. bias) (solid line) and the limits of agreement (dotted lines) are shown. In case of a significant linear regression, the equation of the regression line is presented.

For $N_{density}$, V_{mean} and PI, the inter-method variances were equal or even larger compared to the average values (see Bland Altman plots, Fig. 3). For $N_{density}$, linear regression of the Bland Altman plots showed a significant linear bias (r^2=0.36, p=0.001) indicating that the difference between the measured values scales with the average of the measured values. This was also true for V_{mean} (r^2= 0.46, p<0.001) and PI (r^2= 0.50, p<0.001).

For $N_{density}$, linear regression of the relative differences against the mean no longer showed a significant proportionality of the bias (p=0.16,) indicating that the earlier detected dependency of the absolute differences on the measured value, is mainly linear bias. However, V_{mean} and PI still showed a significant proportional bias in the relative difference plots (r^2=0.24, p=0.01 and (r^2=0.27, p=0.005, respectively).

Agreement between 3T and 7T MRI perforating artery flow measures in case of matched perforating artery detection sensitivity

The velocity distribution of all detected perforating arteries on 3T MRI and the detected perforating arteries with highest velocities on 7T MRI (matching the number of 7T arteries to the number detected on 3T to avoid the bias induced by the higher sensitivity on 7T MRI) is shown in Fig. 4. A more equal velocity distribution of the perforating arteries between 7T and 3T MRI can be seen. However, a paired Student's t-test still showed a significant difference between the two scanning modalities in V_{mean} (p<0.001) and PI (p=0.03).

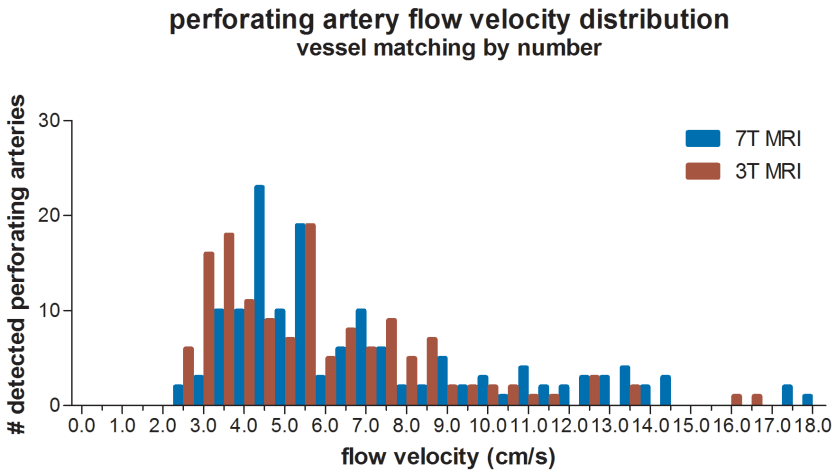

FIGURE 4. Histogram showing the velocity distribution of all detected vessels of 3 tesla (T) MRI vs. 7T MRI, where for 7T for each individual only the N vessels with highest velocities were taken (N refers to the number of vessels detected on 3T MRI for a given subject), in order to equalize the sensitivity to detect cerebral perforating arteries for both modalities.

TABLE 3. Perforating artery flow at 3 and 7 tesla MRI in case of vessel matching by number

	3 tesla (n=28)	7 tesla (n=28)
V_{mean} (cm/s)	6.04±1.27	7.85±2.44
PI	0.49±0.19	0.41±0.18

Results are presented as mean±standard deviation. Abbreviations: V_{mean}= mean blood-flow velocity; PI= pulsatility index.

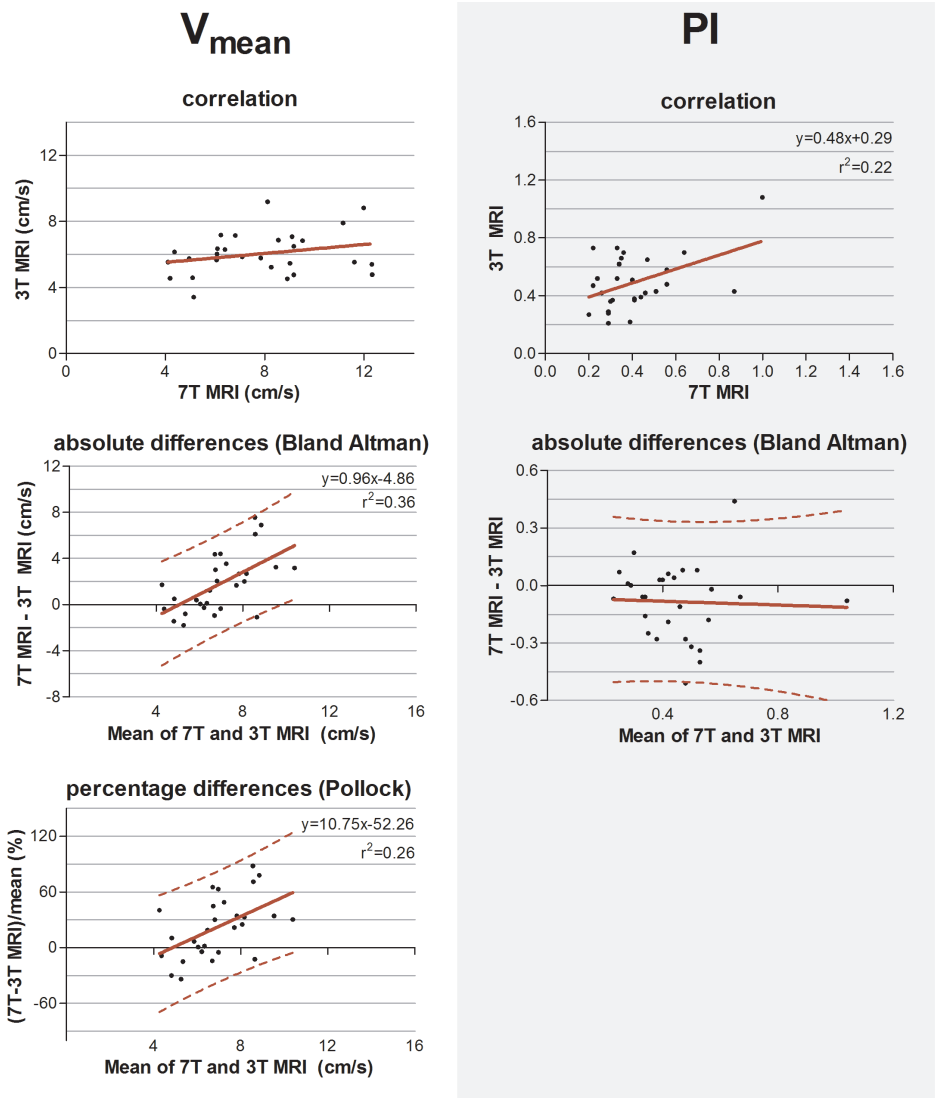

FIGURE 5. Top row: Correlation plots of the mean blood flow velocity (V_{mean}) and pulsatility index (PI) determined of all detected perforating arteries at 3 tesla (T) and of the detected perforating arteries with highest velocities at 7T MRI. The line resulting from linear regression is given by the solid line. In case of a significant correlation the equation of the regression line is given. Middle and bottom row: difference plots in absolute units (Bland Altman) and in percentage units (Pollock), respectively, for Vmean and PI. The regression line (i.e. bias) (solid line) and the limits of agreement (dotted lines) are shown. In case of a significant linear correlation, the equation of the regression line is presented. If proportional bias is absent in the Bland Altman plots, no Pollock plot is shown.

The measured values and standard deviations of V_{mean} and PI, of 7T and 3T MRI are given in Table 3. The correlation and absolute and relative difference plots for these variables are shown in Fig. 5. Linear regression revealed no
significant correlation for V_{mean} (p=0.17), contrary to PI, for which the coefficient of determination was significant (r^2=0.22, p=0.01), indicating that some of the variation in PI on 3T MRI was explained by variation of PI on 7T MRI.

For V_{mean}, the Bland Altman plot shows large inter-method variance compared to inter-subject variance. For PI, however, the two variances were quite equal. Linear regression of the Bland Altman plots for V_{mean} showed a significant linear bias (linear regression in the Bland Altman plot; r^2=0.36, p<0.001). This bias was still present in the Pollock plots (r^2=0.26, p=0.01), indicating that the measurement error is not merely linear in an absolute or relative sense. PI showed no significant linear bias (linear regression in the Bland Altman plot; p=0.84).

DISCUSSION

This study shows that perforating artery flow velocity and pulsatility can be measured at 3T MRI at the level of the BG, though the values found on 3T MRI differed from those obtained at 7T MRI. Comparison of all detected vessels on 7T and 3T MRI suggests agreement in $N_{density}$, but little to no agreement for V_{mean} and PI. When equalizing the modalities' sensitivity by comparing the detected vessels on 7T MRI with the highest velocities with all vessels detected on 3T MRI, we find an improved agreement for PI, but not for V_{mean}. From the fact that the standard deviations of V_{mean} and PI are about twice as large at 3T as at 7T MRI, while only one-fifth of the number of vessels is detected per cm^2 (Table 2 vs Table 3), we conclude that the measurement noise strongly dominates any physiological inter-subject differences and temporal intra-subject variability in the current measurements: the contribution of both physiological inter-subject differences and intra-subject temporal variability to these standard deviations would not scale with the number of detected vessels. Large group sizes are therefore required for sufficient power to detect differences in perforating artery conditions in, for example, disease. Below, we will discuss the observations in light of the differences in sensitivity between 3T and 7T MRI, 2D PC slice planning differences, and in light of the known measurement errors that exist due to the fact that these perforators have diameters typically smaller than the voxel size of the measurements. These measurement errors depend on 3T

and 7T MRI specific details, and thus vary with field strength, which further limits the agreement. It is therefore important to be thoughtful regarding the study design, and to use an equal MRI scanner strength and protocol in future clinical studies.

Sensitivity

As illustrated in Fig. 6, the higher SNR at 7T MRI makes the 2D PC at 7T sensitive to smaller, more downstream vessel segments compared to 3T. This has two consequences: a) more detected vessels at 7T MRI and b) lower velocities at 7T, since the additional vessels at 7T are smaller vessels. Both consequences were recognized when all detected vessels were included in the analysis. The tendency of 7T MRI to reflect on average smaller vessels also explains the negative trend in the difference plot of V_{mean} when all vessels are included. Whereas the 7T mean velocity is relatively stable due to a high prevalence of small vessels with low velocity (see Fig. 2), the 3T mean velocity is quickly dominated by a few relatively large vessels (velocity 'outliers' in the relatively flat histogram), which explains why an average higher velocity is accompanied by a higher difference in V_{mean} between 3T and 7T. Similar behavior as for V_{mean} is seen for the PI as well, as larger vessels also have larger pulsatility.

Contrast differences due to partial volume effects

Since the diameters of the majority of the detected perforating arteries are lower than the voxel size, partial volume effects cause non-linear errors in the measured velocities and the derived pulsatilities. Partial volume effects lead to an underestimation of the velocity and an overestimation of the pulsatility, as has been described and quantified by simulations in previous work.[4,11] Since we used the same acquired resolution for 3T and 7T MRI, the 7T measurements are more affected by partial volume effects due to a larger vessel diameter-voxel size mismatch (see Fig. 6), as they include more distal/smaller vessels. This dissimilarity can explain the non-linear behavior of the differences between 3T and 7T as reflected by the relative difference (Pollock) plots when all vessels were included in the analysis. One could expect that the influence of partial volume effects would be minimized in the secondary analysis, where we discarded the vessels with the lowest velocities from the 7T measurements. By doing this, we focused on a similar segment of the vascular tree and, thus, to similar velocities and partial volume fractions. However, partial volume effects on the velocity not only depend on the volume fraction in the voxel that is occupied by the vessel, but also on tissue and imaging parameters, such as the longitudinal relaxation time T_1 and the flip angle. At 7T,

the tissue T1 values are generally longer, which leads to better background suppression for a given flip angle, and, thus to less velocity underestimation compared to a similar vessel and partial volume fraction at 3T. The velocity histogram for the analysis with matched vessel detection sensitivity and thus matched vessel numbers indicates that the partial volume effect indeed appears to be worse at 3T, as we see more vessels with low velocities (<4cm/s) at 3T. This explains the positive trend in the difference plot for V_{mean} for the analysis with matched detection sensitivity, as higher mean velocities on the x-axis of the Bland-Altman plot now are mainly due to higher 7T velocities, and cause, thus, a positive difference between the 7T and 3T MRI measurements. The fact that the PI no longer shows a linear bias in the difference plot for the analysis with matched vessel detection sensitivity, suggests that this analysis indeed effectively focuses on a similar segment of the vascular tree and that the remaining underestimation of the velocities due to the partial volume effects drops out in the calculation of PI.

The values found in this study for $N_{detected}$, V_{mean} and PI at 7T MRI are lower than those found in earlier studies.[3,4] This may be attributable to the exclusion of non-perpendicular perforating arteries in the basal ganglia, which are often larger perforating arteries with higher velocities and pulsatilities. Also, the mean age of our subject group is lower, which could result in lower PI values.[12]

Consequences of the field strength dependence

The results presented in this paper show that the measurements of perforator velocity and pulsatility are strongly field strength dependent. This does not mean that impaired flow or pulsatility of the microvessels cannot be detected using 3T MRI but does show the importance of acquiring data on scanners of equal field strength and with equal scanning parameters when comparing subject cohorts.

The fact that measurement noise strongly dominates any natural inter-subject differences and temporal physiological variations, together with the observation that on 3T MRI almost one-fifth of the number of vessels is detected per cm^2 compared to 7T MRI, implies that at 3T MRI one would need a subject cohort almost five times larger as needed at 7T MRI to detect a given effect size. However, this is only true under the assumption that the perforating arteries detected on 3T MRI are physiologically similar to those detected on 7T MRI. To the best of our knowledge, it is currently unknown to what extent cerebral small vessel disease affects the larger perforating arteries visible at 3T compared to the smaller artery segments to which 7T MRI is more sensitive.

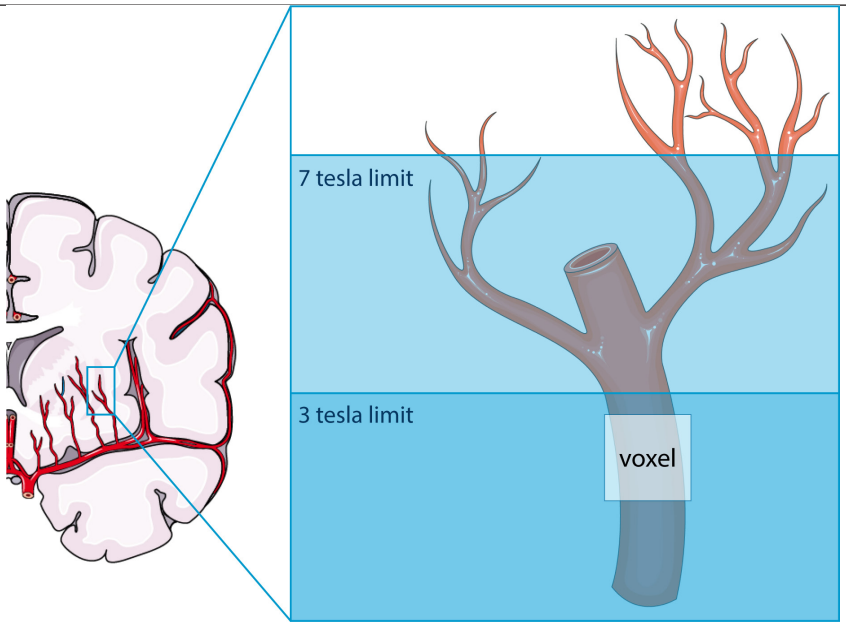

FIGURE 6. Schematic representation of the difference in sensitivity between 3 tesla (T) and 7T MRI for assessing flow and pulsatility in the perforating arteries in the basal ganglia. Both modalities can only detect the proverbial tip of the iceberg, albeit that this tip is larger at 7T than at 3T MRI. The voxel shown indicates the presence of partial volume effects, which are thus different between 3T and 7T MRI due to the difference in the proverbial tip of the iceberg. This image was created using Servier Medical Art templates, which are licensed under a Creative Commons Attribution 3.0 Unported License; https://smart.servier.com.

Limitations

This study also has a few limitations. First, planning of the 2D PC slice was done manually, on 3T as well as 7T MRI, by different scanner operators. This may have caused slight differences in the slice location. This, together with physiological intra-subject variation and subject repositioning, was the main reason why vessel matching by location of the 3T and 7T acquisition was feasible in only a limited number of subjects, yielding only a total of 17 matched vessels. In addition, a direct vessel-to-vessel comparison does not allow to average over vessels. As a result, measurement noise remains in the flow measures, which further complicates vessel-to-vessel flow comparison. This is particularly true for the pulsatility index as discussed in more depth before.[13] Therefore, in this study, vessel matching by anatomical location was not seen as a suitable approach to compare small vessel flow measures across two scanning modalities. Nonetheless, differences in the agreement between the approach to match vessels by number (using scans with similar and deviant 2D PC planning) and by location (using only scans with similar 3T and 7T

planning) show that planning dissimilarities contribute considerably to the agreement between the scanning modalities. Despite the fact that the 2D PC slice planning was protocolled, slice planning variation was still present. This was particularly true at 3T MRI, where the planning was performed by different clinical technicians. Therefore, the MRI data acquisition as performed in this study is representative for daily clinical practice.

A second limitation concerns the lower temporal resolution of the 3T MRI protocol compared to the 7T MRI protocol. As the 3T MRI study was integrated in the clinical workflow, it required the use of the vendor supplied scanner control software prohibiting the use of higher temporal resolutions (minimum TFE factor of 3, see Table 1). Lower temporal resolution leads to flattening of the velocity curve, and thus to underestimation of the PI. Even at 7T, the temporal resolution was limited.[3] It seems that a further reduction of the temporal resolution in the current 3T protocol had limited effect on PI, as 3T MRI PI values were not systematically lower than the 7T MRI PI values for the matched analysis (Fig. 5).

Third, as performed on 7T MRI in previous literature,[3] 3T MRI 2D PC repeatability studies should be completed. Knowing the uncertainty from repeated measurements of the velocity and pulsatility, will allow calculation of the sample sizes needed for future clinical studies. Given the fact that the measurement noise apparently dominates inter-subject variance in the current 3T MRI results as argued above, the reported inter-subject standard deviation of Table 2 may serve as preliminary uncertainty metrics for power calculations.

A final limitation is that no significant differences were present between patients and control subjects at 7T MRI, limiting the dynamical range of our subject cohort. However, pooling these subject groups did increase our sample size.

A strength of this study is the fact that the majority of included subjects was scanned on the same day, with the 3T and 7T MRI performed close together in time. This minimalizes the intra-subject variability. Also, the 3T and 7T scanning sessions were performed in random order. This diminishes bias due to, for example, more subject nervousness and accompanying motion during the first scanning session compared to the second scanning session.

Conclusion

In this study it was shown that cerebral perforating artery velocity and pulsatility measurements can be performed at 3T MRI, paving the way for more microvascular

flow research in relation to cerebrovascular disease. Although 3T MRI shows little agreement with 7T MRI concerning the perforating artery flow measurements, these differences can be explained from the fact that both field strengths can measure only the proverbial tip of the iceberg of the perforating arteries, resulting in scanner-dependent biases. Consequently, future clinical studies should use equal scanning protocol and field strength for all participants. The lower sensitivity of 3T MRI to detect perforating arteries warrants the use of larger cohorts for detecting a given effect size, compared to a similar study at 7T. The drawback of the larger sample sizes may however be compensated by the much larger availability and lower scanning costs of 3T MRI.

REFERENCES

1. Wardlaw, J. M., Smith, C. & Dichgans, M. Mechanisms underlying sporadic cerebral small vessel disease : insights from neuroimaging. Lancet Neurol. 12, 70060–7 (2013).
2. Wardlaw, J. M., Smith, C. & Dichgans, M. Small vessel disease: mechanisms and clinical implications. Lancet Neurol. 18, 684–696 (2019).
3. Geurts, L., Biessels, G. J., Luijten, P. & Zwanenburg, J. Better and faster velocity pulsatility assessment in cerebral white matter perforating arteries with 7T quantitative flow MRI through improved slice profile, acquisition scheme, and postprocessing. Magn. Reson. Med. 79, 1473–1482 (2018).
4. Bouvy, W. H. et al. Assessment of blood flow velocity and pulsatility in cerebral perforating arteries with 7-T quantitative flow MRI. NMR Biomed. 29, 1295–1304 (2016).
5. Guralnik, J. M. et al. A Short Physical Performance Battery Assessing Lower Extremity Function: Association With Self-Reported Disability and Prediction of Mortality and Nursing Home Admission. J. Gerontol. 49, M85–M94 (1994).
6. Schenck, J., Kelley, D. A. C. & Marinelli, L. Instrumentations: magnets, coils and hardware. in Magnetic Resonance Imaging of the Brain and Spine 2–24 (Lippincott Williams & Wilkins, 2009).
7. Giavarina, D. Understanding Bland Altman analysis. Biochem. Medica 25, 141–151 (2015).
8. J. Martin Bland, D. G. A. Statistical methods for assessing agreement between two methods of clinical measurement. Lancet 1, 307–310 (1986).
9. Pollock, M. A. et al. Method comparison-a different approach. Ann. Clin. Biochem. 29, 556–560 (1992).
10. Bland, M. J. & Altman, G. Comparing methods of measurement: why plotting difference against standard method is misleading. Lancet 346, 1085–1087 (1995).
11. Geurts, L. J. et al. Vascular reactivity in small cerebral perforating arteries with 7 T phase contrast MRI – A proof of concept study. Neuroimage 172, 470–477 (2018).
12. Zarrinkoob, L. et al. Aging alters the dampening of pulsatile blood flow in cerebral arteries. J. Cereb. Blood Flow Metab. 36, 1519–1527 (2016).
13. Arts, T., Siero, J. C. W., Biessels, G. J. & Zwanenburg, J. J. M. Automated Assessment of Cerebral Arterial Perforator Function on 7T MRI. J. Magn. Reson. Imaging 53, 234–241 (2021).
14. Van De Moortele, P. F. et al. B1 destructive interferences and spatial phase patterns at 7 T with a head transceiver array coil. Magn. Reson. Med. 54, 1503–1518 (2005).

Supplements

Supplementary material A

In Table A1 the measured values and standard deviations of the mean blood flow velocity (V_{mean}) and the pulsatility index (PI), of 7 tesla (T) and 3T MRI, are given, after visually matching vessels by anatomical location. A paired Student's t-test showed no significant difference between the two scanning modalities in V_{mean} (p=0.49) or PI (p=0.17).

The correlation and absolute difference plots for these variables are shown in Fig. A1. For V_{mean} (p=0.07) as well as PI (p=0.26) no significant coefficient of determination was seen in the correlation plots. Bland Altman plots show that for V_{mean} and PI the inter-method variances were larger than the average values (see Bland Altman plots), implying limited agreement between modalities. However, for V_{mean} and PI the Bland Altman plots showed no significant linear bias, indicating that the difference between the measures values does not scale with the average of the measured values.

Results of this approach, i.e. visually matching vessels by anatomical location, suggest more agreement compared to the approach of matching vessels by number. Unlike for matching by number, no differences were seen in V_{mean} and PI between field strengths, nor linear biases in the Bland-Altman plots. This is likely due to two reasons. First, matching by location compares the same vessel across scanning modalities, making the vessel size equal at 3T and 7T MRI. Therefore, partial volume differences can only result from T1 differences, and not from partial volume fraction. In fact, the impact of T1 differences even appears to be small, since it would result in more velocity underestimation at 3T MRI compared to 7T MRI which is not evident in Table A1. Second, vessel matching can only be achieved in case of sufficiently similar planning of the 2D phase contrast (PC) slice at 3T and 7T MRI. So, differences between 3T and 7T MRI due to planning dissimilarities are absent.

However, an important remark should be made regarding the noise in these resulting measurements. This was firstly due to 2D PC planning differences, yielding only a total of 17 matched vessels in 11 out of 28 subject. Second, this direct vessel-to-vessel comparison resulted in noisy flow measures, particularly for PI as shown in previous research.[13] Therefore, vessel matching by anatomical location was not seen as a highly suitable approach to compare small vessel flow measures across two scanning modalities.

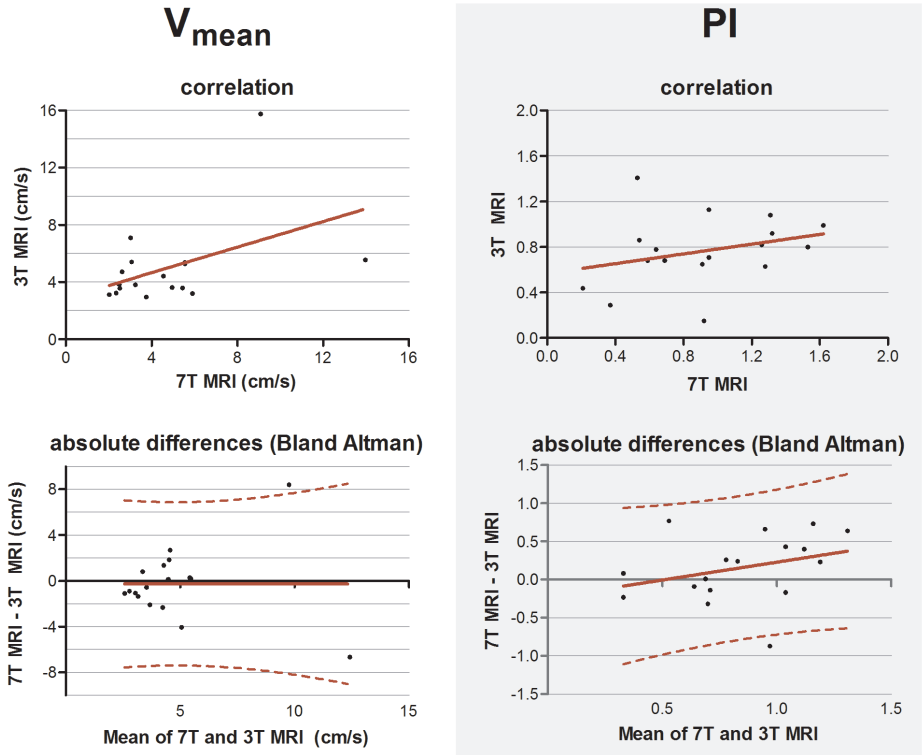

FIGURE A1. Top row: Correlation plots of the mean blood flow velocity (V_{mean}) and pulsatility index (PI) measured at 3 tesla (T) and 7T MRI. The line resulting from linear regression is given by the solid line. Middle and bottom row: difference plots in absolute units (Bland Altman) for V_{mean} and PI. Because proportional bias is absent in the Bland Altman plots, no Pollock plots are shown. The regression line (i.e. bias) (solid line) and the limits of agreement (dotted lines) are shown.

TABLE A1. Perforating artery flow at 3 and 7 tesla MRI in case of vessel matching by location

	3 tesla (n=28)	7 tesla (n=28)
V_{mean} (cm/s)	4.97±2.91	4.72±2.91
PI	0.77±0.30	0.92±0.40

Results are presented as mean±standard deviation. Abbreviations: V_{mean}= mean blood-flow velocity; PI= pulsatility index.

Supplementary material B

TABLE B1. Perforating artery flow measures at 7 tesla MRI of patients and controls

	Patients (n=13)	Controls (n=15)	*p*-value
$N_{density}$	0.97±0.18	0.93±0.23	0.60
V_{mean}	3.91±0.59	3.87±0.54	0.85
PI	0.27±0.09	0.29±0.06	0.17

Results are presented as mean±standard deviation. ***P***-values are determined using an unpaired Student's t-test and $p \leq 0.05$ was considered statistically significant. Abbreviations: $N_{density}$= number of detected perforating arteries/cm^2; V_{mean}= mean blood-flow velocity; PI= pulsatility index.

Chapter 3

AUTOMATED ASSESSMENT OF CEREBRAL ARTERIAL PERFORATOR FUNCTION ON 7 TESLA MRI

T. Arts, J.C.W. Siero, G.J. Biessels, J.J.M. Zwanenburg.

Journal of Magnetic Resonance Imaging, 53, 234-241 (2021)

ABSTRACT

Background and purpose: Blood flow velocity and pulsatility of small cerebral perforating arteries can be measured using 7 tesla (T) quantitative 2D phase contrast (PC) MRI. However, ghosting artifacts arising from subject movement and pulsating large arteries cause false positives when applying a previously published perforator detection method. The aim of this research was to develop a robust, automated method to exclude perforators located in ghosting artifacts.

Methods: Fifteen patients with vascular cognitive impairment or carotid occlusive disease and 10 healthy controls were included. All subject underwent a 2D PC cardiac gated sequence at 7T MRI. Cerebral perforators were automatically excluded from ghosting regions, which were defined as bands in the phase-encoding direction of large arteries. As reference, perforators were manually excluded by two raters (T.A., J.J.M.Z.), based on perforator location with respect to visible ghosting artifacts. The performance of both censoring methods was assessed for the number of ($N_{included}$), mean velocity (V_{mean}), and pulsatility index (PI) of the included perforators.

Results: The automated censoring method showed a moderate to good ICC (95% CI) vs. manual censoring for $N_{included}$ (0.73 [0.58–0.87]) and V_{mean} (0.90 [0.84–0.96]), and a moderate ICC for PI (0.57 [0.37–0.76]). The test–retest reliability of the manual censoring method was considerably lower than the interrater and intrarater reliability, indicating that scanner noise dominates the uncertainty of the analysis.

Conclusion: The proposed automated censoring method can reliably exclude small perforators affected by ghosting artifacts.

INTRODUCTION

Cerebral small vessel disease is a widespread condition which affects the small arteries, arterioles, venules and capillaries of the brain and is the main cause of cognitive decline and stroke.[1] Also, it is involved in approximately half of all dementia cases.[2] However, insight into the exact processes that lead to cerebral small vessel disease is limited, and this hampers the development of effective treatment. Therefore, measuring the flow properties of the small cerebral perforating arteries may improve our understanding of cerebral hemodynamics[3] and may be of use for treatment assessment.
It is possible to measure the hemodynamics of the cerebral perforating arteries using a cardiac-gated 2D phase contrast (2D PC) MRI sequence at 7 tesla (T).[4,5] This method utilizes the increased signal-to-noise ratio (SNR) of 7T MRI and the fact that the relatively low blood flow velocities in these small perforators (100-300 μm) allow for a very low readout bandwidth, which further enhances the SNR to a level that makes the flow velocity measureable in the perforators. The method yields the mean velocity (V_{mean}) during the cardiac cycle and the pulsatility index (PI) of the blood flow in the perforators of deep white matter (WM), specifically the centrum semi-ovale (CSO). In this brain region vessels are located that penetrate deep into the brain tissue, branch relatively little and are low in density. This makes the CSO vulnerable in case of diseased vessels such as in SVDs and is therefore a region of interest to assess perforator flow.[6–9]

Previous results showed good repeatability in these metrics in older subjects;[4] however, the processing procedure is hampered by ghosting artifacts arising from subject movement and pulsations from large cerebral arteries[5]. Ghosts in the phase encoding direction (Fig. 1) reflect phase inconsistencies in the multishot acquisition, which are due to subject movement and intershot variation in blood flow pulsations of large cerebral vessels in combination with the low encoding velocity.[10,11] Ghosting artifacts are visible in data from healthy subjects but are more prominent in data from elderly patients, who tend to move more during the examination.[12]

To reduce false-positive perforator detection, perforators initially detected in these artifact regions should be excluded. Currently, this censoring step is done manually.[5] While manual censoring is manageable for small datasets, it becomes time-consuming for large datasets, particularly when data from elderly patients is involved. Besides, manual procedures make the censoring process subjective and reduce the precision

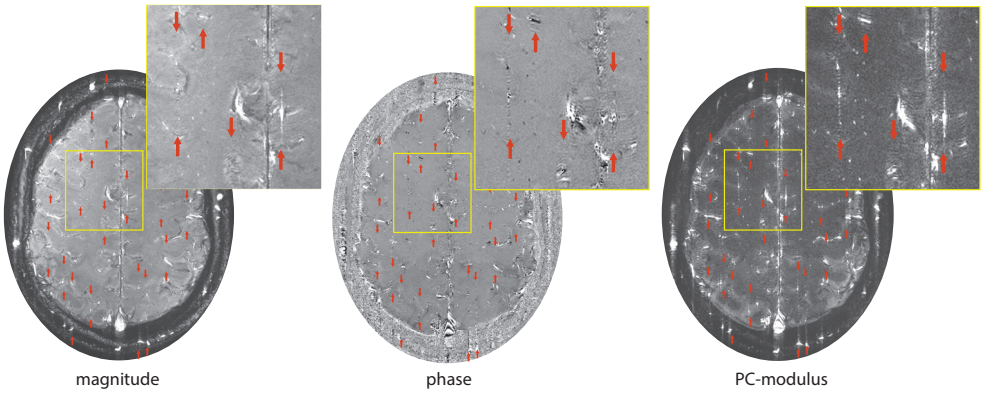

FIGURE 1. Magnitude, phase, and phase contrast (PC)-modulus images. Ghosting artifacts (between the arrowheads) are apparent in the phase-encoding direction, mainly in the phase and PC-modulus images.

in calculated measures describing perforator hemodynamics. Therefore, the main goal of this work was to develop a robust, automated censoring method for fast exclusion of small perforating arteries in artifact regions in the CSO.

METHODS

Image acquisition

Our proposed method was evaluated using data from an ongoing study approved by our local institutional review board, and all subjects provided informed consent. The mixed subject group consisted of 20 patients with either vascular cognitive impairment (Mini Mental State Examination ≥20) or carotid occlusive disease (according to most recent clinical guidelines) and 10 healthy controls (recruited through advertising leaflets in the hospital or spouses of patients). Subjects were required to be aged over 50 and were excluded in case of a contraindication for MRI. Of the 20 patients, five were excluded from analysis due to poor scan quality caused by excessive movement during scanning (n = 2), severe patient discomfort (n = 1), scanner issues (n = 1), or a noisy peripheral pulse unit signal resulting in poor triggering for retrospective gating (n = 1). Of the healthy controls, no one was excluded (aged 68±8, mean ± standard deviation). Of the 15 included patients (aged 69±8, mean ± standard deviation), five were diagnosed with cognitive impairment and 10 with carotid occlusive disease.

Images were acquired on a 7T Philips Achieva MRI system (Philips Healthcare, Best, the Netherlands) with a 32-channel receive head coil (Nova Medical, Wilmington, MA). A 3D T1-

weighted image (T1WI) was acquired for WM segmentation with an isotropic resolution of 1.0 mm^3 and whole brain coverage[4]. The CSO was scanned using a previously described retrospectively gated 2D PC sequence[4]. Scan parameters included the following: field of view = 250 x 250 mm^2, acquired voxel size = 0.3 x 0.3 x 2.0 mm^3 (interpolated to 0.2 x 0.2 mm^2 in-plane resolution), flip angle = 50-90° (increasing flip angle across the slice using tilted optimized non-saturating excitation), sensitivity encoding = 1.5, velocity encoding = 4 cm/s, and 14 reconstructed cardiac phases (for one participant 12 cardiac phases were acquired due to a lower heart rate during scanning). Scan duration was 4 min for a heart rate of 78 bpm (range: 3 min 10 s – 4 min 35 s). The repetition time (TR) and echo time depend on the angle of the planned slice and ranged from 28.8-30.2 ms and 16.6-17.7 ms, respectively. For every cardiac time point, two velocity encoding cycles were acquired (i.e., two phase encoding steps per heartbeat or turbo field-echo factor = 2), leading to an acquired temporal resolution of 4*TR (~118 ms). The scan was planned manually, with a target slice location 15 mm superior to the top of the corpus callosum (see Fig. 2). To minimize motion, cushions were placed beside the head of the scanned subject during all scans. For test-retest assessment, this 2D PC scan was performed twice in succession without repositioning.

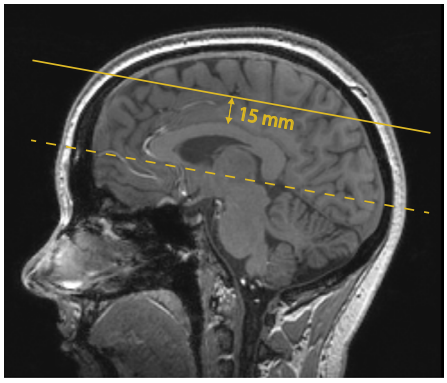

FIGURE 2. Planning of the 2D PC slice in the centrum semi-ovale projected on the T1-weighted image. The dashed line is aligned with the bottom of the corpus callosum, indicating the angle of the slice. The slice is then located 15 mm superior to the top of the corpus callosum (solid line).

Automated small perforator selection

WM masks of the CSO were generated using the 3D T1WI with a white matter probability threshold of 0.75 (SPM12, Wellcome Trust Centre for Neuroimaging). For each 2D PC scan (ie, two per subject), the mask was manually corrected in case of improper segmentation due to either failure of the segmentation algorithm (four subjects, ie, eight masks) or considerable subject shift between the T1WI and the 2D PC scans (four subjects, ie, eight masks). Only the central white matter pixels were included that were

more than 80 pixels away from the outside contour of the 2D PC brain slice mask (a 2D PC pixel equals 0.2 mm).

An initial, uncensored perforator selection was performed within the WM mask using a previously published method[4,13] that includes the following steps. First, the background was phase corrected to make the mean velocity of tissue 0 cm/s by median filtering the velocity map and subtracting it from the velocity map of each cardiac time point. Then, the velocity SNR was calculated from an estimation of the magnitude SNR to enable consistent selection of vessels with significant flow. Further, the two-sided 95% velocity confidence intervals (CIs) were estimated for V_{mean}, for which, which is consistent with a statistical significance of 0.05. Finally, perforators were identified based on significant V_{mean}. All voxels inside the WM mask without 0 cm/s within their CI of V_{mean} were considered significant, and every group of neighboring significant voxels was defined as belonging to the same perforator. Only perforators with downward flow, thus negative V_{mean}, were included; and for every group, the voxel with the highest absolute V_{mean} was taken as the perforator.

Manual censoring

Two raters (Rater 1: TA, 2 years experience; Rater 2: JJMZ, 14 years experience) visually determined the presence and extent of ghosting paths from both the 2D PC magnitude and phase images and manually selected perforators located in ghosting regions for exclusion (Fig. 3). The intrarater reliability was assessed by performing manual exclusions by Rater 1 at two time points, two months apart. Interrater reliability was determined by having Rater 2 perform the manual exclusions at one time point.

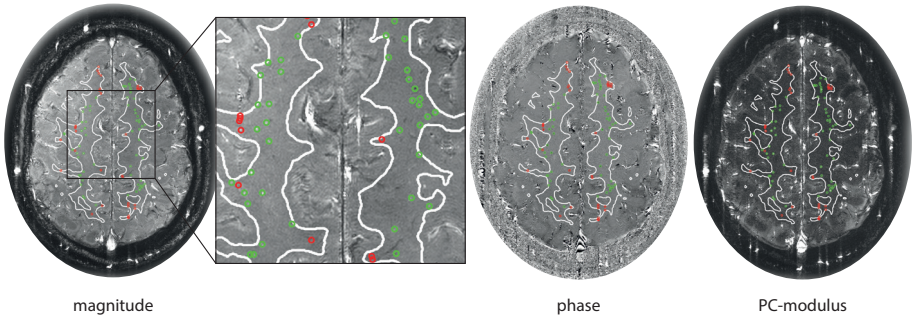

FIGURE 3. Example of the manual censoring method. Detected perforators located inside ghosting artifacts are circled in red, perforators located outside ghosting artifacts are circled in green, projected on the magnitude, phase, and PC-modulus image.

Automated censoring

The automated censoring method was applied with the following steps, which are illustrated in Fig. 4:

1. Correct for spatial intensity variation in the mean (over the cardiac cycle) magnitude PC image by applying a median filter (window 70 x 70 pixels) and subtracting the median filtered magnitude image from the original mean magnitude image.
2. Automatically identify large blood vessels by applying a relative intensity threshold on the PC magnitude image. This threshold was defined by sorting the voxels' intensity values from high to low and selecting the top 0.3% of that sorting. Only voxel clusters consisting of more than two voxels were taken into account to not misidentify small perforators as large vessels.
3. Dilate these clusters in the readout direction, and extend them in the phase encoding direction (direction in which ghosts occur) to create vertical stripes, partially overlapping the WM mask. Clusters ≥80 voxels were dilated by 2 pixels and extended by 200 pixels in the phase encoding direction. Smaller clusters were dilated by 1 pixel and extended by 110 pixels in the phase encoding direction.
4. Determine which small perforators are located outside the stripes (included perforators) and which are located on the stripes (excluded perforators).

Quantitative measures

Both censoring methods resulted in a number of perforators, $N_{included}$, in the WM of the CSO for each subject and scan. For each perforator, an average velocity of the blood was obtained. Averaging over all perforators resulted in a mean blood flow velocity per subject (V_{mean}). To calculate the pulsatility index, the perforators' velocity curves were first normalized and subsequently averaged. The PI was calculated from the resulting mean normalized velocity curve with the following formula:

$$PI = (V_{max} - V_{min})/V_{mean}.$$

Concerning the relative magnitude of the ghosting artifact regions, we evaluated the percentages of how much of the original WM mask is defined as ghosting artifact regions after applying the automated censoring method.

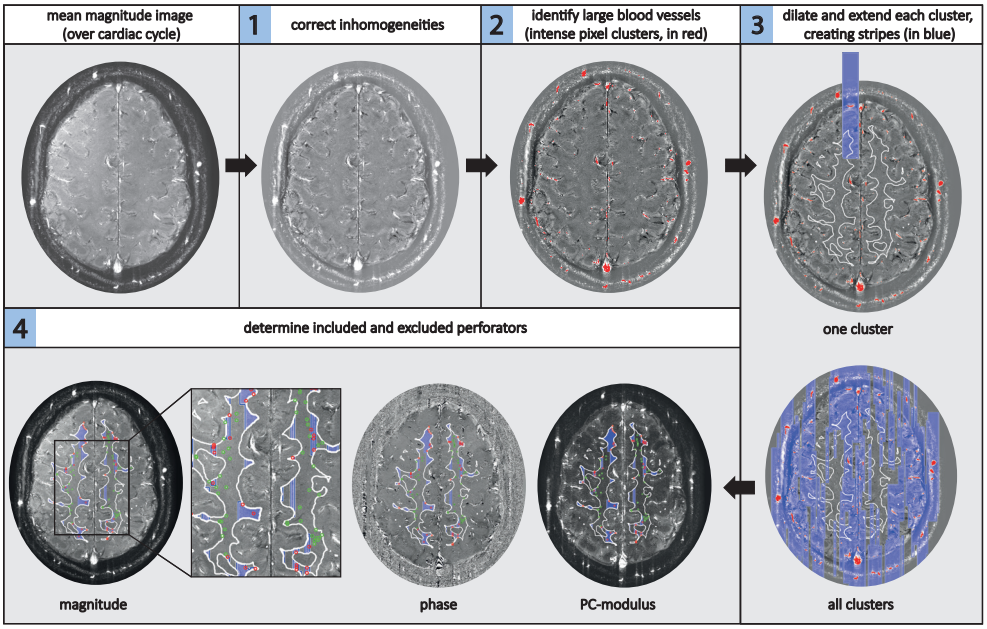

FIGURE 4. Overview of the automated censoring method. Steps 1–4, as described in the Materials and Methods under the heading Automated Censoring. In step 1, spatial inhomogeneities are corrected. In step 2, the automatically identified large arteries of more than two voxels are shown in red on the detrended and filtered image. In step 3, the vertical stripes created are shown in blue, first for one cluster, then for all clusters. The white matter mask contour is shown in white on the magnitude image. In step 4, the included perforators are circled in green (located outside the stripes) and the excluded perforators are circled in red (located on theripes) on the magnitude, phase, and PC-modulus image.

Statistical tests

A within-method reliability assessment enabled us to assess the reliability of the automated censoring method and the manual censoring method for $N_{included}$, V_{mean} and PI. Further, a between-method comparison allowed us to measure the closeness of agreement between the measured values, i.e. $N_{included}$, V_{mean} and PI, of the two censoring methods.

Within-method reliability assessment

For the automated as well as the manual censoring methods test-retest reliability of $N_{included}$, V_{mean} and PI was determined on the first compared to the second scan using intraclass correlation coefficients (ICCs) and their 95% CIs derived from a single measurement two-way mixed-effects model using the SPSS statistical package

(Chicago, IL). Both absolute agreement and consistency were tested. In addition, for the manual censoring method, ICCs and their 95% CIs of intrarater (T.A.) and interrater (T.A. versus J.J.M.Z.) reliability were determined on the first scan, again using a single measurement two-way mixed-effects model with absolute agreement for intrarater comparisons and consistency for interrater comparisons.[14]. An ICC > 0.90 was defined as "excellent", an ICC between 0.75-0.90 as "good", an ICC between 0.5-0.75 as "moderate" and an ICC < 0.5 was considered "poor".[14]

Between-method comparison

ICC values were also determined to compare the results of the automated and manual censoring (rater T.A.) methods for the measures $N_{included}$, V_{mean} and PI. For this comparison, a multi-level statistical analysis was performed using SAS software with the NLMIXED procedure (Non-Linear MIXED model procedure, SAS v. 9.4, SAS Institute, Cary, NC), comparing the automated and manual censoring method while taking into account the repeated measures, ie, scan 1 and scan 2.

For scan 1 we registered the time needed for rating of the perforators for the manual censoring method for all subjects and both raters. These times were then averaged over all subjects and both raters to obtain a mean manual rating time per subject. The automated method was a push-of-a-button method and thus required no timing assessment.

RESULTS

No significant differences were found between patients and controls for the automated or manual censoring method, for $N_{included}$ ($P = 0.68$; $P = 0.36$), V_{mean} ($P = 0.22$; $P = 0.41$) and PI ($P = 0.50$; $P = 0.19$) using an unpaired Student's t-test where a P-value < 0.05 was considered statistically significant. Also, the mean velocity curves over the cardiac cycle (normalized and non-normalized) did not significantly differ between both groups for both methods. Therefore, patient and control groups were pooled. Analyses separated by group, as well as representative velocity traces of a patient and a control subject with P-values resulting from significance testing per cardiac phase, are included in Supplementary Material A.

Within-method reliability assessment

Table 1 shows the ICCs and 95% CIs of the automated and manual censoring methods for test-retest reliability assessment, and the ICCs and their 95% CIs for the manual intrarater and interrater reliability assessment. For the automated, as well as the manual censoring method, the ICC values showed good to excellent reliability for $N_{included}$ and V_{mean}, for test-retest reliability. PI showed moderate to good reliability. Comparing the reliability of both methods, the automated censoring method had equal or higher ICCs compared to the manual censoring method.[14] Bland Altman plots of these results can be found in Supplementary Material B.

Between-method comparison

Table 2 shows the outcome measure values for $N_{included}$, V_{mean} and PI for scan 1 and scan 2 and the ICC values and their 95% CIs for the comparison between the automated and manual censoring method. The ICC (95% CI) values of $N_{included}$ (0.73 [0.58-0.87]), as well as V_{mean} (0.90 [0.84-0.96]), showed moderate to good agreement between the two methods. PI showed moderate agreement (0.57 [0.37-0.76]).[14]

After WM segmentation and possible mask adjustments, it took 6.0 ± 1.9 minutes (mean ± standard deviation) per subject to manually select perforators outside ghosting artifacts. The automated censoring method did not cost time.

The WM regions defined as ghosting artifact by the automated censoring method comprised 65 ± 15% (mean ± standard deviation) of the original WM region (assessed on scan 1).

DISCUSSION

We have shown that automated censoring of small cerebral perforators affected by ghosting artifacts gives similar values for Nincluded, Vmean and PI with equal or improved reliability compared to manual censoring. Because the automated method runs without user input, and thus does not occupy the user, it is faster, saving on average six minutes per subject compared to the manual method. Also, the automated method is inherently objective, as it removes any potential rater bias.

Comparison between the automated and manual censoring methods showed moderate to good ICC for $N_{included}$ and V_{mean}. PI showed moderate ICC, but the value was similar to

the ICC of the test-retest reliability analysis with the automated method. This indicates that variation in PI between methods is comparable to that between scans and, thus, is dominated by the noise of the measurements rather than by differences in performance between the two analysis methods.
Because the PI calculation is relatively sensitive to noise,[13] two calculation methods for determining the PI were compared. For the first method, the PIs of all detected perforators were calculated first, after which these PIs were averaged to obtain a single PI for each subject. For the second method, all normalized velocity curves were averaged first, after which the PI was calculated. The second method showed to be least sensitive to noise and was therefore used in this study. Simulation results for both PI calculation methods can be found in Supplementary Material C.

For manual censoring, the ICC values for the intrarater comparison were excellent and generally higher than the test-retest and interrater ICCs. Additionally, the variation between scans was higher than the variation between raters for all outcome measures. Together, this indicates that the uncertainty is mainly due to the noise in the images.
The automated censoring method showed better or equal test-retest reliability than the manual censoring method for all outcome measures, confirming the objective and consistent nature of the automated method. Although the rater applying the manual censoring method can mostly distinguish between perforators in- and outside ghosting paths, the vertical extent of a ghosting path is not always clear, making it difficult to objectively judge perforators in areas where the ghost extinguishes. However, for the automated method, varying the areas defined as ghosting regions had little effect on the outcome measures $N_{included}$, V_{mean} and PI (Supplementary Material D). We therefore expect that for the manual censoring method the subjective judgement of where the ghost extinguishes also has limited effect on $N_{included,}$ V_{mean} and PI.

The mean velocity and pulsatility values reported in this paper are in agreement with earlier studies.[4,13] As expected, the number of perforators included for the Vmean and PI calculations, $N_{included}$, is less than in the aforementioned studies because in this study only perforators located outside ghosting artifacts are included. However, the number of included perforators is high enough for reliable PI measurements, as shown by the simulation results in Supplementary Material C.

It is important to note that the method of censoring may affect $N^{included}$, V^{mean} and PI. Therefore, when analyzing small perforator PC MRI data, attention should be paid to

TABLE 1. Reliability of the automated and manual censoring methods (ICC (95% CI)) for 25 subjects

		$N_{included}$	V_{mean}	PI
Test-retest	*Automated censoring*			
	Consistency	0.90(0.79-0.96)	0.90(0.78-0.95)	0.66(0.36-0.83)
	Absolute agreement	0.91(0.80-0.96)	0.90(0.79-0.96)	0.66(0.37-0.83)
	Manual censoring, Rater 1			
	Consistency	0.84(0.67-0.93)	0.87(0.74-0.94)	0.50(0.14-0.74)
	Absolute agreement	0.84(0.67-0.93)	0.88(0.74-0.95)	0.48(0.13-0.73)
Intrarater	*Manual censoring, Rater 1**			
	Absolute agreement	0.99(0.97-0.99)	0.99(0.99-1.0)	0.87(0.73-0.94)
Interrater	*Manual censoring Rater 1 vs. Rater 2**			
	Consistency	0.94(0.93-0.99)	0.96(0.92-0.98)	0.88(0.86-0.97)

Abbreviations: ICC= intraclass correlation coefficient; CI= confidence interval; $N_{included}$= number of included perforators; V_{mean}= mean velocity during the cardiac cycle; PI= pulsatility index. *The intrarater and interrater ICCs are based on the first of the repeated phase contrast scans for the manual censoring method.

TABLE 2. Comparison between the automated and manual censoring methods for 25 subjects

	$N_{included}$ ± SD		V_{mean} (cm/s) ± SD		PI ± SD	
	scan 1	*scan 2*	*scan 1*	*scan 2*	*scan 1*	*scan 2*
Automated censoring	33±18	33±24	0.71±0.15	0.70±0.13	0.43±0.17	0.45±0.13
Manual censoring	38±19	36±21	0.69±0.11	0.69±0.13	0.40±0.14	0.45±0.14
Multi-level ICC (95% CI) based on both scans	0.73 (0.58-0.87)		0.90 (0.84-0.96)		0.57 (0.37-0.76)	

Data are reported as mean± standard deviations (SD). ICC= intraclass correlation coefficient; CI= confidence interval; $N_{included}$= number of included perforators; V_{mean}= mean velocity during the cardiac cycle; PI= pulsatility index; ICC= intraclass correlation coefficient; CI= confidence interval.

what method is used for small perforator censoring and the method must be the same for all included subjects.

This automated method also permits assessment of perforator density, because not only the number of perforators located outside ghosting artifacts is known ($N_{included}$), but the size of the analyzed area is also known, because the automated method distinguishes between WM regions with and without ghosting artifacts. This is not the case for the manual method for which ghosting regions are not quantitatively/spatially defined. For both methods, it is the case that the mask size, and thus also $N_{included}$, highly depends on the severity and amount of the ghosting artifacts present in a PC image. Therefore, comparing $N_{included}$ between groups may introduce some bias.

The presented automated method allows for the measurement of the hemodynamics of small cerebral perforators in an objective and fast manner, which may improve our understanding of the functioning of the microvasculature and its role in cognitive impairment and dementia.[15] It is known that vessels become stiffer with aging, reducing the dampening of the pressure wave as blood travels to the perforators. This results in an increased pulse pressure and microvascular remodeling and a decrease in regional autoregulation.[16–19] This could damage the capillaries and tissue.[16] Jefferson et al[20] found reductions in regional cerebral blood flow (CBF) despite autoregulation being preserved in central arterial stiffening. Because the exact mechanisms involved in cerebral vascular impairment are still unknown, velocity and pulsatility measures of the small perforators can be of great value to determine how damage to these perforators relates to vascular brain injuries such as microbleeds, infarcts and decreased WM integrity and shed light on the changes occurring in patients with vascular cognitive impairment.

Limitations

First, the stringency of our automated censoring method depends on parameter settings (the intensity threshold for large vessel identification as well as the length and width of the stripes) and affects how many and which perforators are included. The parameter settings used in this paper were chosen empirically to visually match the automatically censored perforators and the manually censored perforators as closely as possible for a subset of the data. However, systematically varying these parameters around the empirically chosen value and assessing the resulting changes showed only little effect on $N_{included}$, V_{mean} and PI (Supplementary Material D).

Second, our automated censoring method still requires a manual processing step: the WM mask, as segmented by SPM12, needs manual adjustments when necessary. If the mask is not properly adjusted, this can lead to false-positive or false-negative perforator detection, making the results less accurate. It is particularly important to exclude sulci from the mask to avoid false inclusion of the vessels that run over the cortex. Therefore, a user check and potential corrections on the WM mask remain a required step. Note that this is required for both the manual and the automated censoring methods.

Also, given the subvoxel size of the perforators detected in this study, partial volume averaging is an issue in velocity quantification. We have previously shown that partial volume averaging results in underestimation of flow velocity and overestimation of pulsatility.[13] Therefore, if changes occur in V_{mean} and PI, we cannot distinguish to what extent this is due to actual changes in velocity or changes in perforator diameter. Nonetheless, changes in velocity and pulsatility do indicate perforator changes, but assumptions regarding vessel diameter are needed for further interpretation.
Additionally, we did not reposition the subject in between the two PC scans, which would have been a more thorough test-retest reliability assessment. However, this was not performed because 1) noise due to planning of the PC slice is very limited compared to thermal and physiological noise, as we have previously shown,[4] 2) repositioning and replanning would add additional variation between the repeated scans that could possibly mask subtle differences in performance between the analysis methods, and 3) repositioning would make the scanning session substantially longer and increase the burden for the participant.

Moreover, subject motion remains a major cause of artifacts in the PC image acquisition used in this study. Our method accounts for ghosting artifacts resulting from nonexcessive motion, but other motion-related artifacts such as blurring can still result in inaccurate velocity and pulsatility measurements.

Further, the number of included subjects was limited, particularly when a comparison between patients and controls would have been the focus. However, for assessing the performance of the censoring methods, we were able to pool the data of the patients and controls, and assess the performance of the methods on a fair number of subjects. Finally, in this study the manual censoring method was used as a reference method, which is not a gold standard. Up to now, no gold standard exists to distinguish between perforators affected and unaffected by ghosting artifacts.

Conclusion

We have shown that it is feasible to automatically detect small cerebral perforators affected by ghosting artifacts in 2D PC images with a method that is reliable, more objective, and faster compared to manual selection. Our proposed method may provide more accurate quantitative measures of cerebral microcirculation for the study of small vessel disease.

ACKNOWLEDGEMENTS

We thank Laurien P. Onkenhout and Hilde van den Brink for assistance in collecting the data used in this study. We thank Dr. Peter Zuithoff of the Julius Center for assistance with the statistical analyses of the results.

REFERENCES

1. Pantoni, L. Cerebral small vessel disease: from pathogenesis and clinical characteristics to therapeutic challenges. Lancet Neurol. 9, 689–701 (2010).
2. Wardlaw, J. M., Smith, C. & Dichgans, M. Mechanisms underlying sporadic cerebral small vessel disease : insights from neuroimaging. Lancet Neurol. 12, 70060–7 (2013).
3. Zwanenburg, J. J. M. & Van Osch, M. J. P. Targeting cerebral small vessel disease with MRI. Stroke 48, 3175–3182 (2017).
4. Geurts, L., Biessels, G. J., Luijten, P. & Zwanenburg, J. Better and faster velocity pulsatility assessment in cerebral white matter perforating arteries with 7T quantitative flow MRI through improved slice profile, acquisition scheme, and postprocessing. Magn. Reson. Med. 79, 1473–1482 (2018).
5. Geurts, L. J., Luijten, P. R., Klijn, C. J. M., Zwanenburg, J. J. M. & Biessels, G. J. Higher Pulsatility in Cerebral Perforating Arteries in Patients With Small Vessel Disease Related Stroke, a 7T MRI Study. Stroke 50, 62–68 (2018).
6. Wardlaw, J. M., Smith, C. & Dichgans, M. Mechanisms of sporadic cerebral small vessel disease: Insights from neuroimaging. The Lancet Neurology vol. 12 483–497 (2013).
7. Fisher, C. M. The arterial lesions underlying lacunes. Acta Neuropathol. 12, 1–15 (1969).
8. Scuteri, A., Nilsson, P. M., Tzourio, C., Redon, J. & Laurent, S. Microvascular brain damage with aging and hypertension: Pathophysiological consideration and clinical implications. J. Hypertens. 29, 1469–1477 (2011).
9. Blair, G. W., Hernandez, M. V., Thrippleton, M. J., Doubal, F. N. & Wardlaw, J. M. Advanced Neuroimaging of Cerebral Small Vessel Disease. Current Treatment Options in Cardiovascular Medicine vol. 19 (2017).
10. Schultz, C. L., Alfidi, R. J., Dennis Nelson, A., Kopiwoda, S. Y. & Mark Clampitt, M. E. The Effect of Motion on Two-dimensional Fourier Transformation Magnetic Resonance Images. Radiology 152, 117–121 (1984).
11. Axel, L., Summers, R. M., #{149}, B. A. & Kressel, H. Y. Respiratory Effects In Two-Dimensional Fourier Transform MR Imaging. Radiology 160, 795–801 (1986).
12. Zeng, L.-L. et al. Neurobiological basis of head motion in brain imaging. Proc. Natl. Acad. Sci. 111, 6058–6062 (2014).
13. Bouvy, W. H. et al. Assessment of blood flow velocity and pulsatility in cerebral perforating arteries with 7-T quantitative flow MRI. NMR Biomed. 29, 1295–1304 (2016).
14. Koo, T. K. & Li, M. Y. A Guideline of Selecting and Reporting Intraclass Correlation

Coefficients for Reliability Research. J. Chiropr. Med. 15, 155–163 (2016).
15. Gorelick, P. et al. Vascular Contributions to Cognitive Impairment and Dementia. Stroke 42, 2672–2713 (2011).
16. Mitchell, G. F. Effects of central arterial aging on the structure and function of the peripheral vasculature: implications for end-organ damage. J. Appl. Physiol. 105, 1652–1660 (2008).
17. Najjar, S. S., Scuteri, A. & Lakatta, E. G. Arterial aging: Is it an immutable cardiovascular risk factor? Hypertension vol. 46 454–462 (2005).
18. Stevenson, S. F., Doubal, F. N., Shuler, K. & Wardlaw, J. M. A Systematic Review of Dynamic Cerebral and Peripheral Endothelial Function in Lacunar Stroke Versus Controls. Stroke 41, (2010).
19. Lakatta, E. G. Cardiovascular regulatory mechanisms in advanced age. Physiological Reviews vol. 73 413–465 (1993).
20. Jefferson, A. L. et al. Higher aortic stiffness is related to lower cerebral blood flow and preserved cerebrovascular reactivity in older adults. Circulation 138, 1951–1962 (2018).

Supplements

Supplementary material A

Fig. A1 shows no significant differences between both groups in the mean velocity curves over the cardiac cycle. In Fig. A2 the mean velocity traces of a representative control and patient subject are given including a velocity trace of a cerebral perforator of that subject. Table A1 shows that no significant differences exist between the patient and control group, for $N_{included}$, V_{mean} as well as PI.

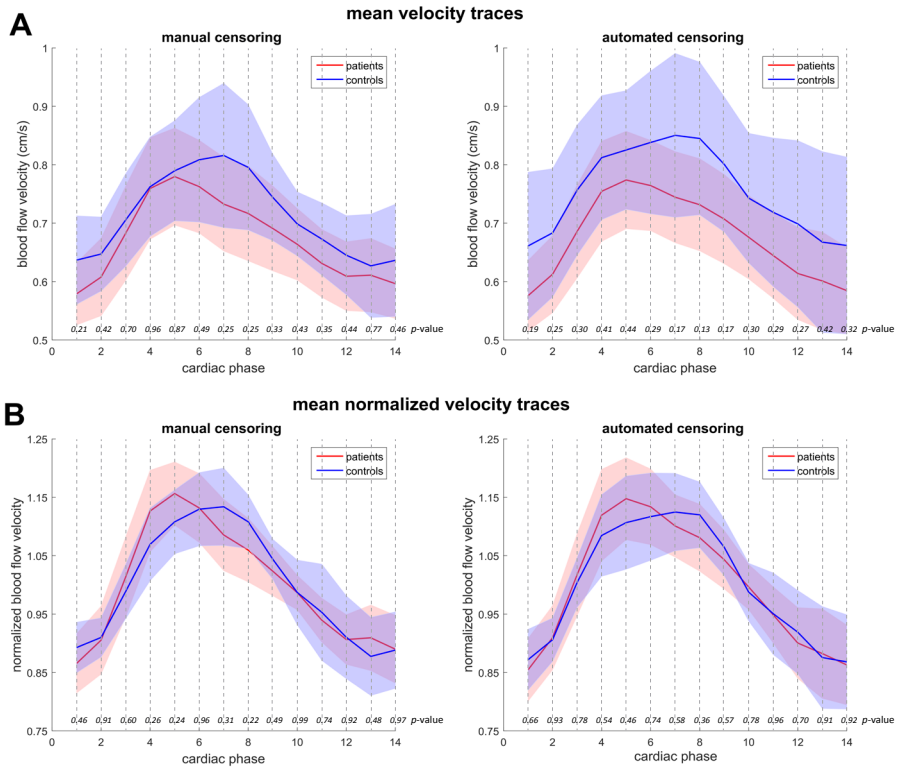

FIGURE A1. Comparison of the mean velocity traces (A) and mean normalized (division by the mean) velocity traces (B) between the patients (red curves) and controls (blue curves), for the manual censoring method (left) and the automated censoring method (right). Subject velocity traces are interpolated to the maximum number of occurring cardiac phases. Shaded regions indicate ± 2*standard error of the mean. Manual censoring results are based on the first rating of rater 1 at the first time point and the data used is based on scan 1. A statistically significant difference ($p < 0.05$) between patients and controls was tested for each cardiac phase using an independent Student's t-test. P-values are given in italics.

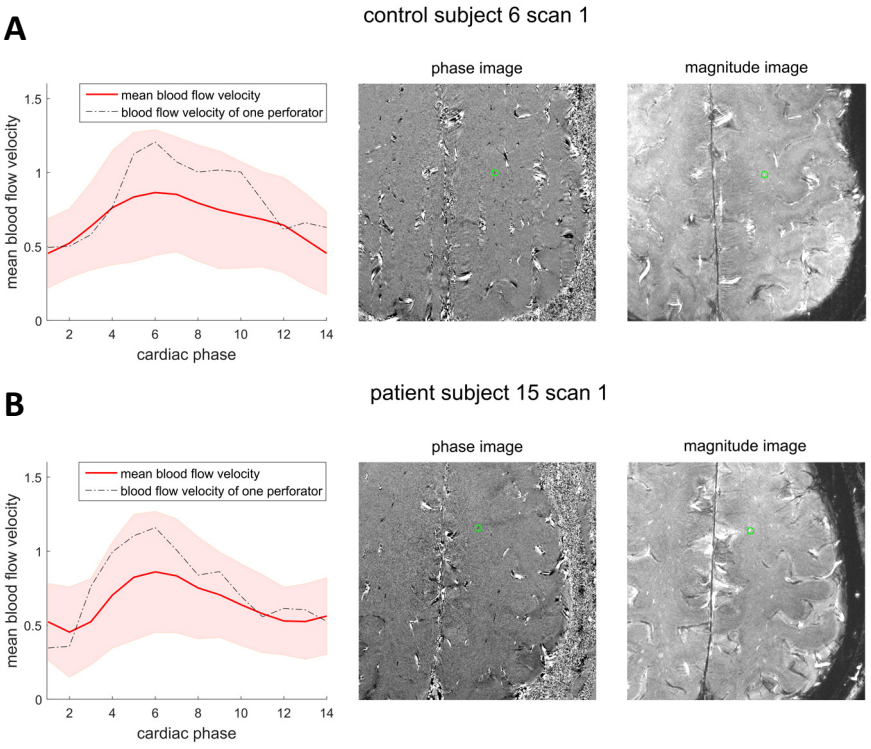

FIGURE A2. Mean velocity traces ± standard deviation of a representative subject from the control group (A) and a representative subject from the patient group (B). In addition, the trace of an individual perforator is given and the concerning perforator is circled in green on the phase and magnitude images of the 2D phase contrast scan (shown for cardiac phase #7).

TABLE A1. Average values, standard deviations and p-values of $N_{included}$, V_{mean} and PI for comparison between the patient group and control group

	$N_{included}$			V_{mean}			PI		
	patients	*controls*	*p-value*	*patients*	*controls*	*p-value*	*patients*	*controls*	*p-value*
Automated censoring	31±20	35±15	0.68	0.68±0.12	0.75±0.17	0.22	0.45±0.16	0.40±0.18	0.50
Manual censoring	35±17	42±20	0.36	0.67±0.11	0.71±0.11	0.41	0.43±0.14	0.36±0.12	0.19

P-values are calculated using an unpaired Student's t-test and a *p*-value < 0.05 was considered statistically significant. Outcomes are based on the first scan of 15 patients and 10 controls. Manual censoring results are based on the first rating of rater 1. $N_{included}$= number of included perforators; V_{mean}= mean velocity during the cardiac cycle; PI= pulsatility index.

Supplementary material B

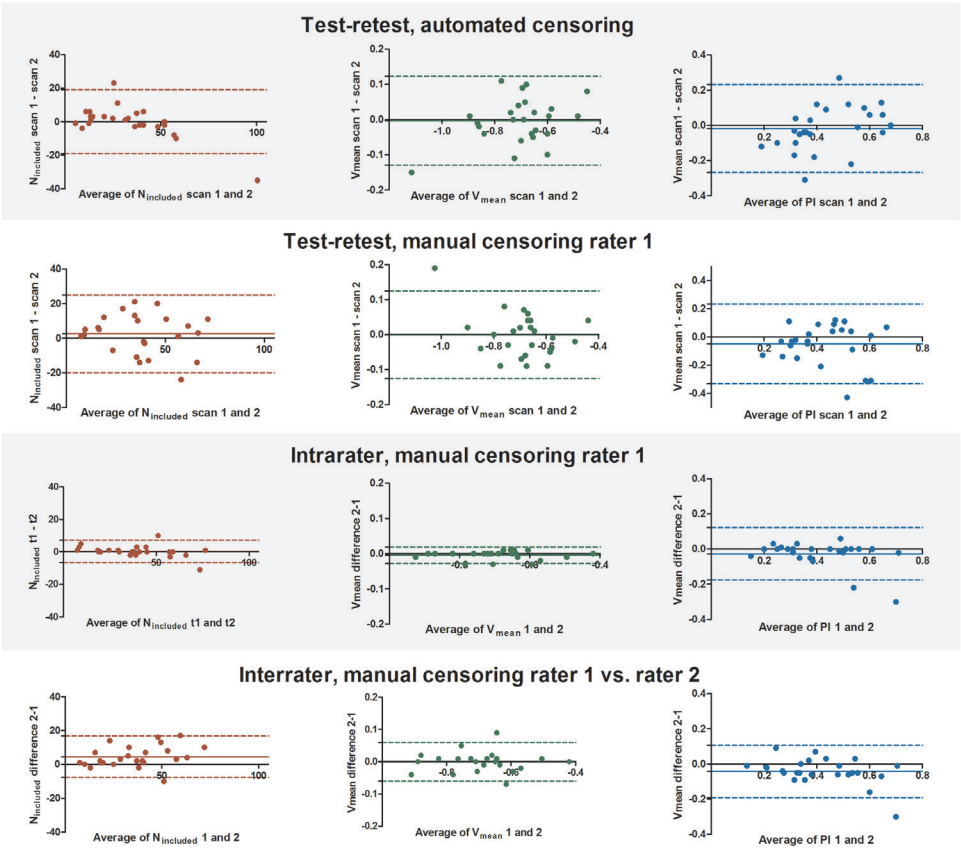

FIGURE B1. Bland-Altman plots showing the method reliability of the automated and the manual censoring method for test-retest, intrarater and interrater comparison. For the manual censoring method the interscan correlation of rater 1 and the correlation of rater 1 vs. rater 2 are based on the first of the repetitive scans. The test-retest correlation of rater 1 is based on both scans. Outcomes are based on 25 subjects. $N_{included}$= number of included perforators; V_{mean}= mean velocity over the cardiac cycle; PI= pulsatility index; t1= time point of first rating of rater 1, scan 1; t2= time point of second rating of rater 1, scan 1.

Supplementary material C

Two methods for calculating PI were compared:

Method 1: Averaging after PI calculation: Determine V_{max}, V_{min} and V_{mean} of each detected perforator's normalized velocity curve and calculate PI of each perforator. Averaging all PI's results in a PI for each participant.
Method 2: Averaging before PI calculation: Average the normalized velocity curves of all perforators, and obtain V_{max}, V_{min} and V_{mean} from this averaged curve to calculate a subject's PI.

Monte Carlo simulations were performed to determine what measure of PI was least sensitive to noise, mimicking the velocity curve for twenty perforators and fifteen cardiac phases. Fourteen SNR values ranging between 2 and 8.5 were used for the magnitude signal of the perforators. For all simulations, a single true value for V_{mean} and PI was used: V_{mean} = 1.0 cm/s and PI = 0.4. Thousand velocity simulations were performed, each with randomly assigned noise, σ_V, where

$$\sigma_V = \sigma_{phase} \cdot (Venc/\pi) \qquad \text{and} \qquad \sigma_{phase} = 1/SNR_{magnitude}$$

Simulation results for the two calculation methods for PI are depicted in Fig. C1. For $N = 1$ PI of both methods behaves equally as a function of magnitude SNR, since no averaging occurs. For $N > 1$ for method 1, calculating PI of each perforator before averaging, will only narrow the 95% confidence interval, while its behavior with changing SNR remains the same (data not shown). For method 2, calculating PI from an average velocity curve, the overestimation of PI is greatly reduced in the entire SNR range when compared to method 1. Method 2 was therefore used for PI calculations in this study. The mean SNR ± 2*SD (5.8 ± 2.5) of our data is also shown in Fig. C1. This SNR is the SNR at the locations of the included perforators, averaged over all included perforators and all scans.

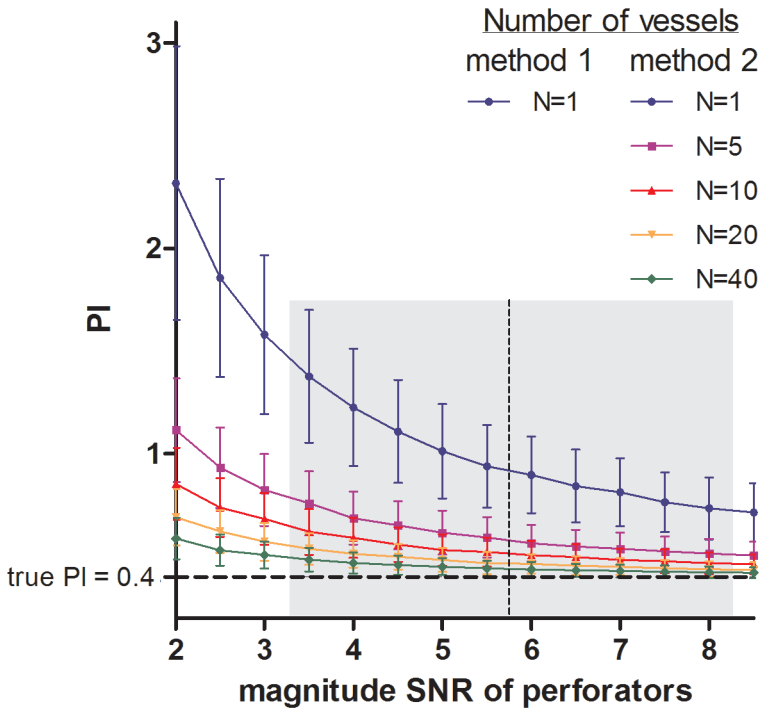

FIGURE C1. PI simulation results and standard deviations (SD), for various numbers of included perforators *N* for method 1 and method 2. The dotted horizontal line indicates the true PI value of 0.4. The mean SNR of the perforators selected in this study (5.8) is indicated by the vertical dotted line and its 2*SD range (3.25-8.27) is indicated by the grey filled area. On average, 33 (range: 5 - 118) vessels are detected with the automated method in this study. PI= pulsatility index.

Supplementary material D

Fig. D1 shows that variation in the six parameters involved in the automated censoring method have only little impact on the outcome measures and the variation in the outcome measures remains within mean ± 2*standard error range.

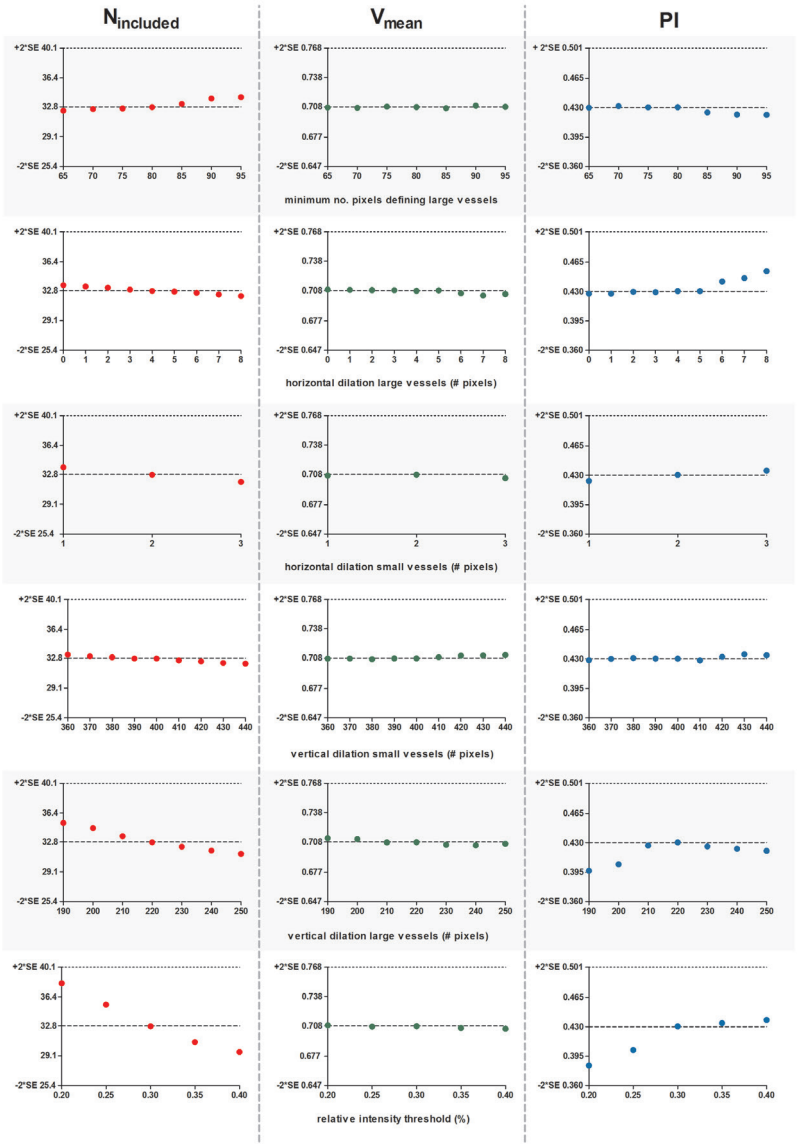

FIGURE D1. Plots showing the impact of variation in the six parameters involved in the automated censoring method on the outcome measures $N_{included}$, V_{mean} and PI. All results are based on the first of the repetitive scans.

Part II

WHAT IS OUT THERE?

CHARACTERIZING SMALL VESSEL HEMODYNAMICS IN RELATION TO A RANGE OF CARDIOVASCULAR FACTORS

Chapter 4

PERFORATING ARTERY FLOW VELOCITY AND PULSATILITY IN PATIENTS WITH CAROTID OCCLUSIVE DISEASE. A 7 TESLA MRI STUDY.

T. Arts*, L.P. Onkenhout*, D. Ferro, E.A. Oudeman, M.J.P. van Osch, J.J.M. Zwanenburg, J. Hendrikse, L.J. Kappelle, G.J. Biessels. On behalf of the Heart-Brain Connection Consortium.

*these authors contributed equally to this manuscript.

Submitted in Cerebral Circulation - Cognition & Behavior

ABSTRACT

Background and purpose: Patients with carotid occlusive disease (COD) express altered haemodynamics in the post-occlusive vasculature and lesions commonly attributed to cerebral small vessel disease (SVD). We addressed the question if cerebral perforating artery flow measures, using a novel 7T MRI technique, are altered and related to SVD lesion burden in patients with COD.

Methods: 21 patients were included with a uni- (18) or bilateral (3) carotid occlusion (64±7 years) and 19 controls (65±10 years). Mean flow velocity and pulsatility in the perforating arteries in the semi-oval centre (CSO) and basal ganglia (BG), measured with a 2D phase contrast 7T MRI sequence, were compared between patients and controls, and between hemispheres in patients with unilateral COD. In patients, relations were assessed between perforating artery flow measures and SVD burden score and white matter hyperintensity (WMH) volume.

Results: CSO perforating artery flow velocity was lower in patients than controls, albeit non-significant (mean difference [95% confidence interval] 0.08 cm/s [0.00–0.16]; p =0.053), but pulsatility was similar (0.07 [-0.04–0.18]; p =0.23). BG flow velocity and pulsatility did not differ between patients and controls (velocity=0.28 cm/s [-0.32–0.88]; p =0.34; pulsatility=0.00 [-0.10–0.11]; p =0.97). Patients with unilateral COD showed no significant interhemispherical flow differences. Though non-significant, within patients lower CSO (p =0.06) and BG (p =0.11) flow velocity related to larger WMH volume.

Conclusion: Our findings suggest that COD may be associated with abnormal cerebral perforating artery flow and that this relates to SVD lesion burden in these patients, although our observations need corroboration in larger study populations.

INTRODUCTION

Patients with uni- or bilateral carotid occlusive disease (COD) are known to express post-occlusive haemodynamic abnormalities in the cerebral vasculature. These include a lower perfusion pressure in the absence of sufficient collaterals,[1,2] as well as abnormalities in cerebral blood flow (CBF) and cerebrovascular response (CVR).[3–7] Furthermore, patients may develop low-flow infarcts, mainly in border zone areas of the brain, the deep white matter (WM) of the semi-oval centre (CSO), and the gray matter of the basal ganglia (BG).[1,3,7–9] Moreover, patients with COD can also express lesions typically attributed to small vessel disease (SVD), such as lacunar infarcts and white matter hyperintensities (WMH).[9] This raises the question if haemodynamics of small vessels, in particular in perforating arteries, are also affected in patients with COD.

With the advance of 7 tesla (T) MRI we are now able to measure blood flow velocity and pulsatility in the small perforating arteries of the brain.[10,11] In this study, we assessed if perforating artery flow measures are altered in patients with COD. We compared flow velocity and pulsatility in the cerebral perforating arteries in the CSO and BG between patients with COD and matched controls, as well as interhemispherically in patients with unilateral COD. In addition, we investigated if perforating artery flow measures are related to lesions typically attributed to SVD.

METHODS

Study population

Participants of the Heart Brain Connection study were included and all participants provided written informed consent prior to enrolment in the study.[12] We included participants with asymptomatic or symptomatic > 80% stenosis of the internal carotid artery (ICA) who were not eligible for a carotid endarterectomy, as well as patients with an occlusion of the ICA. Patients with an ICA occlusion should not have had a brain infarct or transient ischemic attack in the three months prior to inclusion. Subjects in the control group had no history of COD. All participants were aged > 50 years and independent in daily life. On the first study visit all participants underwent clinical assessment of sociodemographic factors and cardiovascular risk factors, extensive neuropsychological testing and assessment of daily functioning and psychiatric measures. Furthermore, a venous blood sample was drawn to assess biomarkers and

a cardiac (at 3T MRI) and brain MRI (at 3T and 7T MRI) was performed. After two years, participants underwent the same protocol of clinical assessment, neuropsychological testing and assessment of daily functioning and psychiatric measurement, as well as 3T brain MRI.[13] In this study MRI data obtained during the first visit was used, of which 3T and 7T MRI scans were successfully completed in 27 patients with COD and 20 controls.

The Heart-Brain Connection study was approved by the Medical Ethics Committee of the Leiden UMC (LUMC) and local boards of the participating UMCs (LUMC, Maastricht UMC, Utrecht UMC and VU UMC).[13] The study was conducted in accordance with the declaration of Helsinki and the Medical Research Involving Human Subjects Act (WMO).

Clinical characteristics

For the patients with COD the side of the stenosis or occlusion was recorded and whether the stenosis or occlusion had been symptomatic, which was defined as a transient ischemic attack (TIA) or ischemic stroke. This was based on medical records and questionnaires. Possible stenosis or occlusions in other cervical arteries (i.e. left and right internal carotid arteries and left and right vertebral arteries) were recorded from medical records as well.

Vascular risk factors were recorded for patients and reference participants. Hypertension was determined by measurement on two study visits. Each study visit systolic and diastolic blood pressure were measured on each arm twice, at least one minute apart. Mean systolic and diastolic blood pressure were averaged out of four measurements on two study visits. The criteria for hypertension were: the use of blood pressure medication, or a mean systolic blood pressure above 140mmHg or a mean diastolic blood pressure higher than 90mmHg. The criteria for hyperlipidemia were: the use of cholesterol lowering medication, or a diagnosis of hyperlipidemia by a physician based on earlier blood cholesterol and LDL levels (even if a patient did not use medication, but for example would adhere to a diet) or a present LDL above 3,5mmol/L. The present LDL cholesterol level (mmol/L) was determined from a blood sample taken from the participant the first study visit. The criteria for diabetes were: the use of antidiabetic medication, or a diagnosis of diabetes by a physician (even if a patient did not use medication, but for example would adhere to a diet) based on glucose levels or on previous or present HbA1c levels above 53 mmol/mol. The present HbA1c level (mmol/mol) was determined from a blood sample taken from the participant at the first

study visit. Both current or previous smoking was noted, as well as the number of years of smoking, years stopped and amount of smoked cigarettes/cigars per day.

Image acquisition

2D phase contrast (PC) acquisitions aimed at small perforating arteries in the semioval centre (CSO) and the basal ganglia (BG) were performed on 7T MRI (Philips) as previously described.[10,14] Slice planning and scanning parameters of the 2D PC scans are shown in the Table 1 and Fig. 1. In addition, 2D-Qflow measurements at the first branch of both left and right middle cerebral arteries (MCA, M1) were acquired. A peripheral pulse oximeter was used for retrospective gating and cushions were placed beside the subject's head to minimize head movement during scanning.

Image processing

First segment of the middle cerebral artery (M1)

Velocity (cm/s) and pulsatility measurements at the first segment of both left and right middle cerebral arteries were acquired on 7T MRI (0.5x0.5mm resolution, Venc=120cm/s) using a 2D-Qflow sequence. Contouring of the M1 was done semi-automatically using MeVisLab (v3.1.1, VS2017, MeVis Medical Solutions AG, DE) and M1 flow velocity was defined as the average over the contoured lumen. Pulsatility was derived from the velocity (V) using the following formula

$$\text{pulsatility} = (V_{max} - V_{min})/V_{mean} \quad [1]$$

where V_{max}, V_{min} and V_{mean} are the maximum, minimum and mean flow velocity respectively. Flow velocity and pulsatility measures of left and right M1 were averaged. During data analysis we learned that the echo time of the M1 2D-Qflow was too long, resulting in flow voids. Participants with flow voids covering a large part of the contoured lumen were excluded.

Cerebral perforating arteries

2D PC scans were first visually checked for sufficient quality; scans with poor image quality due to severe subject movement were excluded from analysis.

Perforating artery flow measures were assessed in the two regions of interest using a 2D WM mask at the CSO and a manual delineation of the BG, both excluding infarcts. WM

masks and lacunar infarcts in these regions were delineated from 3T MRI T1-weighted and FLAIR images using the Quantib Brain Segmentation Tool and the FMRIB Software Library (FSL version 6.0.1, Oxford, UK). The lacunar infarct masks were dilated with a 3x3mm kernel. Only the central white matter (further than 16 mm away from the outside of the PC brain slice) was included because the poor gray/white matter contrast in these regions on the PC image makes it difficult to recognize a mismatch between the WM mask and the underlying anatomy. Small perforating arteries in the CSO and BG were detected as previously published[10,11], also automatically excluding CSO perforating arteries located in ghosting artifact regions[15] and perforating arteries in the BG oriented non-perpendicularly to the scanning plane. In addition, apparent perforating arteries located within a 1.2mm radius from each other were excluded, as these are mostly multiple detections located on larger and/or non-perpendicular vessels.

The perforating artery density, mean blood flow velocity and pulsatility were assessed separately for the BG and CSO. The cerebral perforating artery density is defined as the number of perforating arteries per cm^2 of the mask. Averaging over all perforating arteries results in the mean blood flow velocity. To calculate the pulsatility the perforating arteries' velocity curves are first normalized by division with V_{mean} and averaged before the pulsatility is calculated using formula [1] (due to the normalization procedure V_{mean} equals 1.0).

SVD manifestations

Automated delineation of WMH was based a previous method using a FLAIR scan.[16] Visual assessment of lacunar infarcts, microbleeds, enlarged perivascular spaces, and WMH grade was performed by a neuroradiologist. SVD burden score ranged 0-4, and was based on i) presence of one or more lacunar infarcts (1 point), ii) microbleeds present (1 point), iii) moderately to severely enlarged perivascular spaces in basal ganglia (1 point), iv) Fazekas 3 (1 point), according to an established scale.[17,18] To limit the number of correlational analyses perforating artery flow measures were primarily related to WMH volume and the SVD burden score.

Statistical analysis

Demographics and vascular risk factors were compared between patients and controls with unadjusted independent t-test or Chi square test for proportions. Perforating artery flow measures were compared between the groups with ANOVA, in secondary

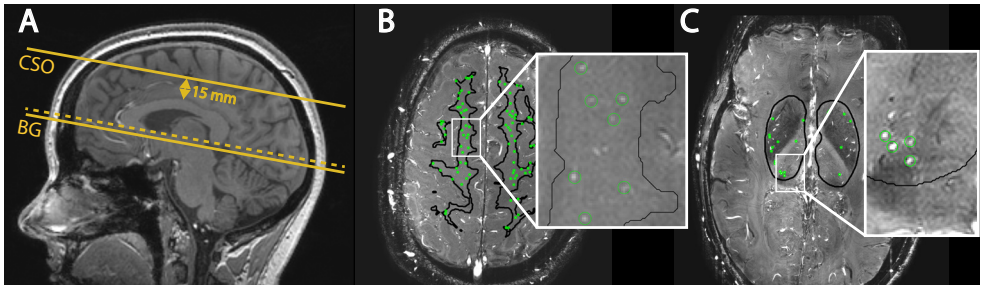

FIGURE 1. Slice planning of the phase contrast (PC) images and detected perforating arteries. (A) Location of the 2D PC slice in the semi-oval centre (CSO), located 15 mm above the corpus callosum, and in the basal ganglia (BG) located at the level of the anterior commissure. Slice angulation is associated with the bottom of the corpus callosum (dotted line). (B) Cerebral perforatorating arteries detected in the CSO are circled in green. (C) Cerebral perforating arteries detected in the BG are circled in green.

analyses also adjusted for age, sex and hypertension. In patients with unilateral COD, flow measures were compared between hemispheres with paired samples t-tests. In the patients, the relation between perforating artery flow measures and SVD manifestations was assessed with Spearman correlation. All data analyses were executed in IBM SPSS statistics (v. 22, SPSS Inc., Chicago, IL) and a p-value ≤0.05 was considered statistically significant.

RESULTS

Of 27 patients with COD and 20 controls, 21 patients (mean age 64±7 years) and 19 controls (mean age 65±10 years) had sufficient 2D PC scan quality at the CSO or BG level, and these 40 subjects constituted the study population (characteristics in Table 2). The reason for low quality scans were artifacts resulting from subject movement during scanning (see Fig. 2). All included 21 patients had occlusions, of which 18 had a unilateral and three a bilateral occlusion.

Sixteen patients and four controls were diagnosed with hypertension (Table 2). Four patients were diabetic. Fifteen patients were symptomatic, of which eleven with ischemic stroke, and fifteen with TIA.

M1 velocity and pulsatility measures could be obtained of 18 patients and 19 controls. Exclusion was necessary because of erroneous slice planning or flow voids. M1 flow velocity was not significantly different between patients with COD (34.1±10.8 cm/s) and controls (34.9±7.8 cm/s)(mean difference [95% CI]=0.8 cm/s [-5.5 – 7.1], p=0.39). The

TABLE 1. Imaging parameters of the 2D phase contrast (PC) sequence in CSO and BG

	2D PC CSO/BG
FOV, mm (RLxAP)	250x250/250x169
Slices	1
Acquired voxel size, mm*	0.3x0.3x2.0
Flip angle**, °	50-90/60
Venc, cm/s	4/20
TR, ms	28.5-29.6/28
TE, ms	16.1-17.3/14.7-15.0
TFE factor	2
Sense factor (AP direction)	1.5/1
Acquired time points	10-15/11-15
Scan time, min:s**	3:30/3:32

**scantime for a heart rate of 80 bpm

Imaging parameters of the 2D phase contrast sequence in the semi-oval centre (CSO) and basal ganglia (BG). Abbreviations: PC= phase contrast; FOV= field of view; RL= right-left, AP= anterior-posterior; V_{enc}= encoded velocity; TR= repetition time; TE= echo time; TFE= turbo field echo. *Reconstructed to 0.2x0.2 mm^2 in-plane resolution. ** Ramped flip angle along the flow direction (perpendicular to the slice) to mitigate saturation effects.

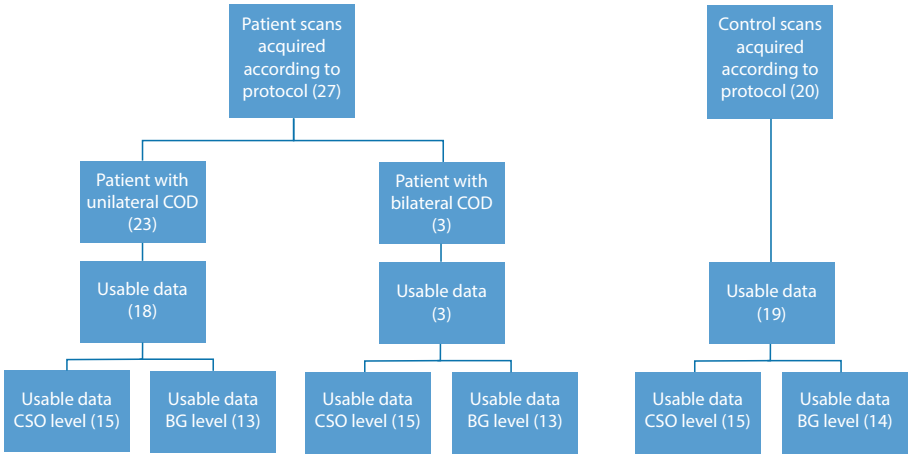

FIGURE 2. Flow chart showing the number of excluded phase contrast scans for patients and controls.

same was found for pulsatility between patients (0.79±0.25) and controls (0.65 ± 0.32) (0.14 [-0.04 – 0.31], p=0.12). In patients with COD no differences were found for M1 velocity between the ipsilateral (34.8±10.9 cm/s) and contralateral hemisphere (36.2±8.8 cm/s)

(1.38 cm/s [-4.92 – 7.69], p=0.65). M1 pulsatility was significantly lower in the ipsilateral hemisphere (0.74±0.26) compared to the contralateral hemisphere (0.82±0.27)(0.08 [-0.00 – 0.16], p=0.049).

Perforating artery flow measures of patients with COD vs. controls

In the CSO, Ndensity and pulsatility of the perforating arteries were similar in patients with COD as compared to controls, but flow velocity tended to be lower in patients (mean difference [95%CI]: 0.08 cm/s [0.00 – 0.16], p=0.053). In the BG, $N_{density}$, flow velocity and pulsatility were similar between patients and controls (Table 3). Adjustment for age, sex and hypertension did not influence these results.

Perforating artery flow measures between hemispheres of patients with COD

In the 18 patients with unilateral COD there were no differences in Ndensity or the perforating artery flow measures between hemispheres in the CSO (Table 4). In the BG, perforating artery flow velocity and $N_{density}$ also did not differ between hemispheres. However, BG perforating artery pulsatility tended to be lower in the ipsilateral than the contralateral hemisphere (0.11 [-0.00 – 0.22], p=0.08).

SVD manifestations and relations with perforating artery flow measures

Compared to controls, patients with COD showed significantly more lacunar infarcts (patients=1[0;2]; controls=0[0;0]; p=<0.001) and tended to have a higher WMH volume (patients=0.54 ml [0.28;1.7]; controls=0.27 ml [0.11;0.73]; p=0.11). The number of microbleeds (p=0.41) and SVD burden score p=0.25) did not differ significantly between patients and controls (Table 2).

Within patients, no significant relations between perforating artery flow measures and SVD manifestations were found, although a lower CSO flow velocity (r=-0.56; p=0.06) and BG flow velocity (r=-0.43; p=0.11) tended to be related to larger WMH volume (Table 5).

DISCUSSION

In this exploratory study we found that several measures of cerebral perforating artery flow were unaffected in patients with COD, although there were indications of reduced perforating artery flow velocity at the level of the CSO. Lower CSO artery flow velocity

TABLE 2. Demographics and vascular risk factors in patients with COD vs. controls

	COD	controls	*p*
Demographics			
Age	64±7	65±10	0.74
Sex (male)	15 (71)	9 (47)	0.12
Unilateral ACI occlusion	18 (86)	n.a.	
Vascular risk factors			
Hypertension	16 (76)	4 (21)	**<0.01***
Hypercholesterolemia	19 (90)	6 (32)	**<0.01***
Diabetes mellitus	5 (23)	0 (0)	**<0.01***
Current smoking	6 (29)	2 (11)	0.08
History of reported TIA	15 (71)	0 (0)	**<0.01***
History of reported stroke	11 (52)	0 (0)	**<0.01***
Small vessel disease manifestations			
SVD burden score [0-4]	1 [0; 2]	0 [0; 1]	0.25
WMH volume (ml)	0.54 [0.28; 1.7]	0.27 [0.11; 0.73]	0.11
Lacunar infarct (number present)	1 [0; 2]	0 [0; 0]	**0.00**
Microbleed (number present)	0 [0; 0]	0 [0; 0]	0.41

Demographics are listed of 21 patients with carotid occlusive disease (COD) and 19 controls, unless indicated otherwise. Data presented as group mean ± standard deviation or n (%). Age and $N_{detected}$ were compared with a Student's t-test, all other demographic and vascular risk factor comparisons with a Chi square test. Small vessel manifestations are compared using a Mann Whitney U analysis, and results are presented as median [quartile: 25% ; 75%]. Abbreviations: COD= carotid occlusive disease; ACI=internal carotid artery; SVD= small vessel disease; WMH= white matter hyperintensity.

also tended to be associated with larger WMH volume in these patients and the same was found for artery flow velocity at the BG level.

Observed values for CSO perforating artery flow velocity and pulsatility of our controls correspond with previous findings in elderly healthy participants.[10,11] This is also true for the pulsatility values of perforating arteries in the BG.[10,11] BG flow velocities are slightly lower, likely due to the exclusion of non-perpendicular perforating arteries at this level in the current study. These are often larger vessels with higher velocities. A relatively large number of subjects was excluded due to poor scan quality resulting from subject movement during scanning (patients: 33% in CSO and 21% in BG; controls: 25% in CSO and 18% in BG). A previous study about perforating artery flow reported lower exclusion numbers due to subject motion (patients: 18% in CSO and 0% in BG; controls: 0% in CSO and 8% in BG).[14] The difference may result from the slightly higher mean age of our cohort

TABLE 3. Cerebral perforating artery flow in COD patients and controls

	COD	controls	mean difference [95% CI]	*p#*
$N_{detected}$ CSO	40 ± 22 (n=18)	33 ± 24 (n=15)	-7.5 [-23.6 – 8.7]	0.35
$N_{detected}$ BG	16 ± 3 (n=15)	17 ± 6 (n=14)	0.56 [-2.9 – 4.1]	0.74
$N_{density}$ CSO (#/cm^2)	2.3 ± 0.91 (n=18)	2.6 ± 1.0 (n=15)	0.32 [-0.22 – 0.85]	0.61
$N_{density}$ BG (#/cm^2)	0.69 ± 0.18 (n=15)	0.69 ± 0.26 (n=14)	0.00 [-0.14 – 0.14]	0.93
Flow velocity CSO (cm/s)	0.66 ± 0.12 (n=18)	0.74 ± 0.11 (n=15)	0.08 [0.00 – 0.16]	0.053
Flow velocity BG (cm/s)	3.45 ± 0.66 (n=15)	3.73 ± 0.90 (n=14)	0.28 [-0.32 – 0.88]	0.34
Pulsatility CSO	0.40 ± 0.16 (n=18)	0.47 ± 0.15 (n=15)	0.07 [-0.04 – 0.18]	0.23
Pulsatility BG	0.41 ± 0.13 (n=15)	0.41 ± 0.14 (n=14)	0.00 [-0.10 – 0.11]	0.97

Data are presented as group mean ± standard deviation. # ANOVA test. Abbreviations: COD= carotid occlusive disease; $N_{detected}$= the number of detected perforating arteries; $N_{density}$= number of detected erebral perforating arteries/ cm^2; CSO= semioval centre; BG= basal ganglia; CI= confidence interval.

TABLE 4. Cerebral perforating artery flow in the hemisphere ipsilateral and contralateral to the carotid occlusion

	hemisphere ipsilateral to the occlusion	hemisphere contralateral to the occlusion	mean difference [95% CI]	*p#*
$N_{density}$ CSO (#/cm^2)	2.09 ± 1.01 (n=15)	2.57 ± 1.15 (n=15)	0.48 [-0.06 - 1.02]	0.08
$N_{density}$ BG (#/cm^2)	0.79 ± 0.35 (n=13)	0.60 ± 0.19 (n=13)	-0.19 [-0.44 - 0.06]	0.20
Flow velocity CSO (cm/s)	0.63 ± 0.18 (n=15)	0.66 ± 0.12 (n=15)	0.03 [-0.04 - 0.11]	0.41
Flow velocity BG (cm/s)	3.49 ± 0.82 (n=13)	3.47 ± 0.73 (n=13)	-0.02 [-0.46 - 0.42]	0.92
Pulsatility CSO	0.50 ± 0.23 (n=15)	0.46 ± 0.19 (n=15)	- 0.04 [-0.19 - 0.11]	0.57
Pulsatility BG	0.44 ± 0.12 (n=13)	0.56 ± 0.17 (n=13)	0.11 [-0.00 - 0.22]	0.08

Results are shown for 18 patients with unilateral carotid occlusive disease. Data are presented as group mean ± standard deviation. # paired samples t-test. Abbreviations: $N_{density}$= number of detected cerebral perforating arteries/cm^2; CSO= semioval centre; BG= basal ganglia; CI= confidence interval.

TABLE 5. Relations between cerebral perforating artery flow and visible manifestation of small vessel disease

	Pulsatility CSO	Flow velocity CSO	Pulsatility BG	Flow velocity BG
SVD burden score	r = -0.06; p = 0.83	r = -0.37; p = 0.17	r = 0.09; p = 0.77	r = 0.08; p = 0.80
WMH volume (ml)	r = -0.30; p = 0.23	r = -0.56; p = 0.06	r = 0.05; p = 0.85	r = -0.43; p = 0.11

r= Spearman correlation coefficient. Abbreviations: CSO= semioval centre; BG= basal ganglia; SVD= small vessel disease; WMH= white matter hyperintensity.

(64 vs. 59 years for patients; 65 vs. 61 years for controls), and this has been noted before in studies of perforating artery flow in older subjects.[10] This is a known phenomenon for older people which tend to move more during MRI scanning than younger people.[19] The burden of SVD manifestations in our patients with COD was somewhat lower than previously described.[20–22] This may be caused by the lower age of our included patients and the fact that they are still independent in daily life, suggesting a patient cohort with relatively normal and stable haemodynamic function.

COD is characterized by haemodynamic impairments, such as decreased CBF and CVR, and lower perfusion pressure in the absence of sufficient collaterals.[1-7] These haemodynamic impairments can vary between COD patients, depending on the degree of collateral flow and on the patient's haemodynamic stability, and is also reflected in ischemic symptoms. PET, MRI and transcranial Doppler measurements have shown that haemodynamic impairments are typically most pronounced in border zone areas, including the CSO and BG.[3–6] In patients with COD, these regions also frequently present with low-flow infarcts (i.e. rosary-like infarctions) and WMH.[8,9] Previous research has shown that haemodynamic alterations as well as cerebral lesions are more common in the CSO than in other border zone regions.[3–6,23] These previous findings agree with lower flow velocity in the CSO perforating arteries in patients with COD and its relation with WMH volume as observed in the present study. Hemispherical differences concerning haemodynamic impairments and lesion occurrence and severity in patients with COD are not unambiguously shown in literature.[9] This agrees with the current finding that apart from lower M1 pulsatility, no differences between hemispheres were found in haemodynamic parameters of flow.

Our results suggest that haemodynamic changes occur in the distal small perforating arteries of CSO border zone areas, which likely reflect the vulnerability of these regions in patients with COD, despite the fact that our patients otherwise appeared to be relatively haemodynamically stable, being asymptomatic for the past period and also having normal flow in proximal arteries. Nevertheless, the haemodynamic changes in the small perforating arteries may be clinically relevant also in this setting as reflected in the relation with WMH volume. In light of these observations the question arises whether lower perforating artery flow and subcortical ischemic lesions in patients with COD are a direct consequence of haemodynamic changes at the level of the carotid artery, or rather reflect co-occurring SVD. The latter can be due to shared risk factors

between atherosclerosis and SVD.[9,24] Our research cannot distinguish between these two possibilities, but does indicate that haemodynamic changes in small perforating arteries contribute to overall brain damage in patients with COD.

Some limitations of our study need to be considered. First, the perforating arteries assessed in this study have sub-voxel sizes, indicating the presence of partial volume effects which generally lead to underestimation of the velocity and an overestimation of the pulsatility.[10] However, it appears unlikely that partial volume effect drive our results, because a drop in perfusion pressure and CBF has been shown to result in vasodilation in an attempt to maintain CBF.[25] Therefore, in patients with COD, partial volume effects are expected to be less, leading to less velocity underestimation. Nevertheless, despite less velocity underestimation, results indicate lower flow velocities in patients with COD. Furthermore, the statistical power of this study was limited. Therefore, we could only detect relations with medium or large effect. Limited power was due to i) the challenging acquisition of good quality 7T MRI data of the cerebral perforating arteries due a motion sensitive 2D CP sequence, reflected in the relatively small sample size included in the analysis; ii) the perforating artery flow measurements have a relatively large amount of noise, introducing measurement uncertainty; and iii) the inclusion of a reasonably haemodynamically stable subject cohort, reflected by the absence of symptoms three months prior to inclusion. In haemodynamically less stable subjects larger effects are expected to be found.

Conclusion

Our observations in a group of patients with COD without recent ischemic symptoms, indicate that although several measures of cerebral perforating artery flow were unaffected, there were indications of reduced perforating artery flow velocity, particularly in the watershed areas, and reduced perforating artery flow velocity tended to be related to a higher burden of subcortical ischemic injury. This suggests that the small perforating arteries contribute to damage and possibly also to clinical outcome in patients with COD. This offers value to future research into the small cerebral perforating arteries in larger cohorts and preferably longitudinal studies.

ACKNOWLEDGEMENTS

We thank K.M. van Hespen for his technical assistance in MRI data analysis.

REFERENCES

1. Hendrikse, J., Hartkamp, M. J., Hillen, B., Mali, W. P. T. M. & Van Der Grond, J. Collateral Ability of the Circle of Willis in Patients With Unilateral Internal Carotid Artery Occlusion Border Zone Infarcts and Clinical Symptoms. Stroke 32, 2768–2773 (2001).
2. Powers, W. J., Press, G. A., Grubb, R. L., Gado, M. & Raichle, M. E. The effect of hemodynamically significant carotid artery disease on the hemodynamic status of the cerebral circulation. Ann. Intern. Med. 106, 27–35 (1987).
3. Leblanc, R., Yamamoto, Y. L., Tyler, J. L. & Hakim, A. Hemodynamic and Metabolic Effects of Extracranial Carotid Disease. J. Neurol. Sci 16, 51–57 (1989).
4. Bokkers, R. P. H. et al. Arterial spin-labeling MR imaging measurements of timing parameters in patients with a carotid artery occlusion. Am. J. Neuroradiol. 29, 1698–1703 (2008).
5. Yamauchi, H., Fukuyama, H., Nagahama, Y., Katsumi, Y. & Okazawa, H. Cerebral hematocrit decreases with hemodynamic compromise in carotid artery occlusion: A PET study. Stroke 29, 98–103 (1998).
6. Kluytmans, M., Van Der Grond, J. & Viergever, M. A. Gray matter and white matter perfusion imaging in patients with severe carotid artery lesions. Radiology 209, 675–682 (1998).
7. Leoni, R. F. et al. Assessing Cerebrovascular Reactivity in Carotid Steno-Occlusive Disease Using MRI BOLD and ASL Techniques. Radiol. Res. Pract. 2012, 1–10 (2012).
8. Krapf, H., Widder, B. & Skalej, M. Small rosarylike infarctions in the centrum ovale suggest hemodynamic failure. Am. J. Neuroradiol. 19, 1479–1484 (1998).
9. Klijn, C. J. M., Kappelle, L. J., Tulleken, C. A. F. & Van Gijn, J. Symptomatic carotid artery occlusion: A reappraisal of hemodynamic factors. Stroke vol. 28 2084–2093 (1997).
10. Geurts, L., Biessels, G. J., Luijten, P. & Zwanenburg, J. Better and faster velocity pulsatility assessment in cerebral white matter perforating arteries with 7T quantitative flow MRI through improved slice profile, acquisition scheme, and postprocessing. Magn. Reson. Med. 79, 1473–1482 (2018).
11. Bouvy, W. H. et al. Assessment of blood flow velocity and pulsatility in cerebral perforating arteries with 7-T quantitative flow MRI. NMR Biomed. 29, 1295–1304 (2016).
12. Van Buchem, M. A. et al. The heart-brain connection: A multidisciplinary approach targeting a missing link in the pathophysiology of vascular cognitive impairment. J. Alzheimer's Dis. 42, S443–S451 (2014).

13. Hooghiemstra, A. M. et al. The Missing Link in the Pathophysiology of Vascular Cognitive Impairment: Design of the Heart-Brain Study. Cerebrovasc. Dis. Extra 7, 140–152 (2017).
14. Geurts, L. J., Luijten, P. R., Klijn, C. J. M., Zwanenburg, J. J. M. & Biessels, G. J. Higher Pulsatility in Cerebral Perforating Arteries in Patients With Small Vessel Disease Related Stroke, a 7T MRI Study. Stroke 50, 62–68 (2018).
15. Arts, T., Siero, J., Biessels, G. J. & Zwanenburg, J. Method for vessel selection effects the outcome and reproducibility of velocity and pulsatility measures in cerebral penetrating arteries. in Annual Meeting of the International Society of Magnetic Resonance #3264 (2019).
16. de Boer, R. et al. White matter lesion extension to automatic brain tissue segmentation on MRI. Neuroimage 45, 1151–1161 (2009).
17. Wardlaw, J. M. et al. Neuroimaging standards for research into small vessel disease and its contribution to ageing and neurodegeneration. The Lancet Neurology vol. 12 822–838 (2013).
18. Staals, J. et al. Total MRI load of cerebral small vessel disease and cognitive ability in older people. Neurobiol. Aging 36, 2806–2811 (2015).
19. Pardoe, H. R., Kucharsky Hiess, R. & Kuzniecky, R. Motion and morphometry in clinical and nonclinical populations. Neuroimage 135, 177–185 (2016).
20. Enzinger, C. et al. High-grade internal carotid artery stenosis and chronic brain damage: A volumetric magnetic resonance imaging study. Cerebrovasc. Dis. 30, 540–546 (2010).
21. Ammirati, E. et al. Relation between characteristics of carotid atherosclerotic plaques and brain white matter hyperintensities in asymptomatic patients. Sci. Rep. 7, 1–11 (2017).
22. Lin, M. P. et al. Collateral Recruitment Is Impaired by Cerebral Small Vessel Disease. Stroke 51, 1404–1410 (2020).
23. Nakano, S., Yokogami, K., Ohta, H., Goya, T. & Wakisaka, S. CT-defined large subcortical infarcts: Correlation of location with site of cerebrovascular occlusive disease. Am. J. Neuroradiol. 16, 1581–1585 (1995).
24. Wardlaw, J. M., Smith, C. & Dichgans, M. Mechanisms underlying sporadic cerebral small vessel disease : insights from neuroimaging. Lancet Neurol. 12, 70060–7 (2013).
25. Gordon, A. L., Goode, S., Souza, O. D', Auer, D. P. & Munshi, S. K. Cerebral misery perfusion diagnosed using hypercapnic blood-oxygenation-level-dependent contrast functional magnetic resonance imaging: a case report. J. Med. Case Rep. 4, (2010).

Chapter 5

NON-INVASIVE ASSESSMENT OF DAMPING OF BLOOD FLOW PULSATIONS IN CEREBRAL ARTERIES WITH 7T MRI

T. Arts, L.P. Onkenhout, R. Amier, R. van der Geest, T. van Harten, L.J. Kappelle, S. Kuipers, M.P. van Osch, J.J.M. Zwanenburg, E.T. van Bavel, G.J. Biessels. On behalf of the Heart-Brain Connection Consortium

Submitted in Journal of Magnetic Resonance Imaging

ABSTRACT

Background and purpose: Damping of pressure pulsations created by the beating heart occurs in large arteries such as the aorta and cerebropetal arteries, but also beyond that, up to the small arteries and microcirculation. Since recently, velocity pulsatility in the small cerebral arteries can be measured. This enables investigation of the phenomenon of damping of flow pulsations from the first segment of the middle cerebral artery (M1) up to the small perforating arteries, with velocity pulsatility as a proxy for pressure pulsatility.

Methods: Using phase contrast MRI, velocity pulsatilities of the M1 and of small perforating arteries in the basal ganglia (BG) and semi-oval center (CSO) were measured in thirty-eight participants aged above 50 without history of heart failure, carotid occlusive disease or cognitive impairment. We used the damping index between the M1 and perforating arteries as a damping indicator (velocity pulsatilityM1/velocity pulsatilityCSO/BG). Left ventricular stroke volume, mean arterial pressure, pulse pressure (PP), and aortic pulse wave velocity (PWV) were used as proximal measures of pressure and arterial stiffness, and related to velocity pulsatility in the M1 and in the perforating arteries, and the damping index of the CSO and BG.

Results: PP and PWV were positively related to M1 velocity pulsatility ($p=0.03$ and $p=0.02$, respectively). By contrast, PWV was negatively related ($p=0.01$) to CSO velocity pulsatility, and PP was unrelated. PP and PWV were not related to BG velocity pulsatility. Positive associations for PWV and PP were found with the CSO damping index ($p<0.001$ and $p=0.02$, respectively).

Conclusion: Results indicate damping of velocity pulsatility between the M1 and small cerebral perforating arteries. Findings may differ in young healthy subjects, and in people with cardiovascular disease. This is subject for further research.

INTRODUCTION

Blood supply to the brain originates in the left ventricle of the heart and is conducted through the cardiovascular tree, propagated by pressure pulsations created by the beating heart.[1,2] The attenuation of these pressure pulsations as they travel towards the microcirculation is called damping, and prevents excessive pulsatile energy from reaching this microcirculation and averts cerebral damage.[3,4] Therefore, better insight into the damping of pressure pulsations carries value in health and disease.[4] Damping of pressure pulsations occurs in the large arteries such as the aorta, carotid arteries, and the circle of Willis (CoW), but also beyond the CoW, up to the small arteries and the microcirculation.[5–7] Nowadays, with 7 tesla (T) MRI, it has become possible to measure blood velocity pulsatility in the small cerebral perforating arteries. In this study we study the phenomenon of damping of flow pulsations from the first segment of the middle cerebral artery (MCA, M1) up to the small perforating arteries, using velocity pulsatility as a proxy for pressure pulsatility. To this end, we first assess the presence of damping between the M1 and the perforating arteries, which is expressed as a damping index, and, second, investigate relations between proximal measures of pressure and arterial stiffness, and the measured damping index.

METHODS

Data availability

The data that support the findings in this study are available from the corresponding author upon reasonable request.

Study population and study visits

We included participants of the reference group of the Heart Brain Connection study[8] who were recruited through advertising leaflets in the hospital or were spouses of patients participating in the same program. All participants were aged > 50 years, and had no history of heart failure, carotid occlusive disease or cognitive impairment. The Heart-Brain Connection study was approved by the Medical Ethics Committee of the Leiden UMC (LUMC) and local boards of the participating UMCs (LUMC, Maastricht UMC, Utrecht UMC and VU UMC).[8] This study was conducted in accordance with the declaration of Helsinki and the Medical Research Involving Human Subjects Act (WMO). All included participants provided written informed consent. On the first study visit

all participants underwent clinical assessment of sociodemographic factors and cardiovascular risk factors, extensive neuropsychological testing and assessment of daily functioning and psychiatric measures. Furthermore, a venous blood sample was drawn to assess biomarkers and cardiac (3T MRI) and brain MRI (3T and 7T MRI) were performed. After two years, participants underwent the same protocol of clinical assessment, neuropsychological testing and assessment of daily functioning and psychiatric measurement, as well as 3T brain MRI.[8] In this study MRI data obtained during visit one was used, of which 3T and 7T MRI scans were successfully completed in 38 subjects.

MRI scanners

3T and 7T MRI data was acquired at the Leiden UMC and UMC Utrecht. 3T MRI data was acquired on a Philips Ingenia MRI scanner with an 8-channel receive head coil at the UMC Utrecht and a 32-channel head coil at the Leiden UMC (Philips, Best, The Netherlands). At both institutions, 7T MRI data was acquired on a Philips Achieva MRI system with a 32-channel receive head coil (Nova Medical, Wilmington, MA). 7T MRI data was acquired approximately three months after the 3T scanning session.

Data acquisition and processing: Intracranial pulsatility measures

First segment of the middle cerebral artery (M1)

Velocity (cm/s) and pulsatility measurements at the first segment of both left and right MCA (M1) were acquired on 7T MRI (0.5x0.5mm^2 resolution, Venc=120cm/s, TR/TE=18.5/7.7 ms, flip angle=60°, Sense factor=1, scan duration=114s for a heart rate of 60 bpm) using a 2D-Qflow sequence. A peripheral pulse unit was used for retrospective gating and cushions were placed beside the subject's head to minimize head movement during scanning. Contouring of the M1 was done semi-automatically using MeVisLab (v3.1.1, VS2017, MeVis Medical Solutions AG, DE) and M1 velocity pulsatility was calculated using the flow velocity, where flow velocity was defined as the average over the contoured lumen. Blood flow velocity pulsatility was derived from the velocity curve using the following formula

$$\text{pulsatility} = (V_{max} - V_{min})/V_{mean} \quad [1]$$

where V_{max}, V_{min} and V_{mean} are the maximum, minimum and mean flow velocity respectively. Pulsatility values of left and right M1 were averaged. During data analysis we learned that the echo time in the protocol of the 2D-Qflow in the M1 was unfortunately too long,

which resulted in the presence of flow voids. Participants with flow voids accompanied by visible noise in the velocity trace were excluded.

Cerebral perforating artery flow velocity and pulsatility

2D PC scans were first visually checked for sufficient quality; scans with poor image quality due to subject movement during scanning were excluded from analysis.

2D phase contrast (PC) acquisitions aimed at small perforating arteries in the CSO and the BG were performed on 7T MRI using a previously published sequence (Philips, 0.3x0.3x2.0mm resolution, CSO Venc=4cm/s, BG Venc=20cm/s)[9,10] (Fig. 1). Similar to the Qflow acquisition, a peripheral pulse oximiter was used for retrospective gating and cushions were placed beside the subject's head to minimize head movement during scanning. Perforating artery flow was assessed in the two regions of interest using an automatically delineated white matter mask at the CSO and a manually delineated 2D mask at the BG, both excluding infarcts. These white matter and infarct masks were automatically delineated from 3 Tesla MRI T1-weighted image (T1WI) and FLAIR images using the Quantib Brain Segmentation Tool. The infarct masks were dilated with a 3x3mm kernel. Registration of the masks to 7T PC space was achieved using the transformation of the 3T T1WI to the 7T T1WI with the FMRIB Software Library (FSL version 6.0.1., Oxford, UK). Only the central white matter (beyond 16mm of the rim of the brain on the PC brain slice) was included because the poor gray/white matter contrast in these regions on the PC image makes it difficult to recognize a mismatch between the white matter mask and the underlying anatomy. Cerebral perforating arteries in the CSO and BG were detected as previously published[9,10], also automatically excluding CSO perforating arteries located in ghosting artefact regions[11] and perforating arteries in the BG oriented non-perpendicularly to the scanning plane. In addition, apparent perforating arteries located within a 1.2mm radius from each other were excluded, as these are mostly 'false detections' located on larger and non-perpendicular vessels.
For each detected perforating artery, an average blood-flow velocity was obtained. The mean blood-flow velocity curve per subject was determined by averaging over all perforating arteries. To calculate the velocity pulsatility, the perforating artery's velocity curves were first normalized by division by the mean and then averaged. The velocity pulsatility was subsequently calculated with equation [1](note: due to the normalization procedure V_{mean} equals 1.0). Perforating artery count within the regions of interest was expressed as a density (number of perforating arteries/cm^2 mask, $N_{density}$).

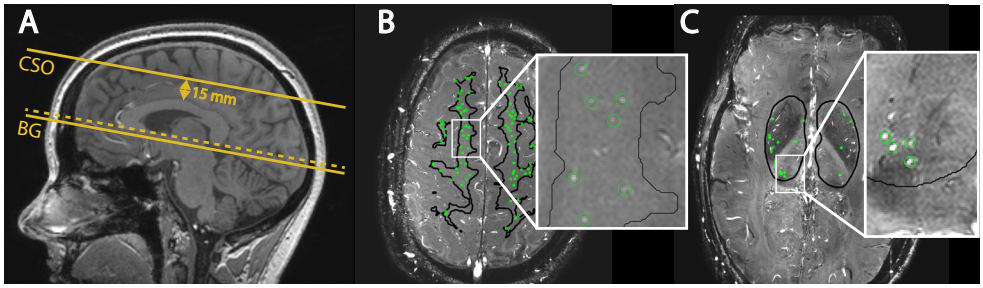

FIGURE 1. Slice planning of the phase contrast (PC) images and detected perforating arteries. (A) Location of the 2D PC slice in the semi-oval centre (CSO), located 15 mm above the corpus callosum, and in the basal ganglia (BG) located at the level of the anterior commissure. Slice angulation is associated with the bottom of the corpus callosum (dotted line). (B) Cerebral perforating arteries detected in the CSO are circled in green. (C) Cerebral perforating arteries detected in the BG are circled in green.

Damping index

The damping index was defined using the following formula:[12]

$$\text{Damping index} = \text{velocity pulsatility}_{M1}/\text{velocity pulsatility}_{CSO/BG}$$

This damping index reflects the amount of damping between the M1 and cerebral perforating arteries using one measure (a damping index > 1.0 represents damping, while a damping index < 1.0 reflects an increase in velocity pulsatility rather than damping).

Data acquisition and processing: proximal measures of pressure and arterial stiffness

Left ventricular stroke volume

Left ventricular stroke volume (LVSV; ml) was used as a pressure measure as the arterial pulse pressure (PP) wave results from systolic ejection of blood from the left ventricle which is followed by diastolic arterial dissipation of the LVSV.[13,14] LVSV was measured with 3T MRI using a breath hold short-axis multi-slice cine balanced SSFP sequence (1.5x1.6x8.0mm resolution). Forty heart phases were acquired.[8] Analysis was done using MASS research software (v2018-EXP, Leiden, the Netherlands) and consisted of the following steps: (i) using cine mode visualization of the images, the end-diastolic and end-systolic phases were determined. End-diastolic was defined as the phase of maximum left ventricular cavity and end-systolic as the phase of minimum left ventricular cavity volume; (ii) using the semi-automated contour detection of MASS, left ventricular endocardial contours were generated for the imaging slices from apex

to base in the end-diastolic and end-systolic phases; (iii) left ventricular end-diastolic volume and left ventricular end-systolic volume were derived; (iv) LVSV (=left ventricular end-diastolic volume – left ventricular end-systolic volume) was calculated.

Blood pressure

To determine mean arterial pressure (MAP; mmHg) and PP (mmHg), systolic and diastolic blood pressure (in mmHg) were acquired in a standardized way. Each visit the patient was asked to sit for five minutes, after which the blood pressure was measured on each arm and repeated at least one minute later. Systolic and diastolic blood pressure were acquired by averaging the second measurements of the two study visits. The mean arterial pressure was calculated with the following formula:

$$MAP = (2 * \text{diastolic blood pressure} + \text{systolic blood pressure})/3$$

PP was calculated by taking the difference between mean systolic and diastolic blood pressure.

Aortic pulse wave velocity (PWV)

The aortic arch was imaged on 3T MRI using a multi-slice 3D T1-weighted gradient echo acquisition in oblique sagittal orientation (reconstructed into 15 slices with a voxel size of 1.76x1.76x5.0mm). Additionally, a 2D phase contrast velocity mapping sequence was acquired intersecting both ascending and descending aorta at the level of the pulmonary artery bifurcation (2.5x2.5x8.0mm^3 resolution, TR/TE=4.7/2.8 ms, flip angle=10°, Venc=150cm/s, scan duration=107s for a heart rate of 60 bpm, temporal resolution is 5 ms). The number of acquired cardiac phases depended on the heart rate.[8] Quantification of PWV from these acquisitions was performed using a fully automated method as previously described.[15] In brief, the aortic arch was segmented, from which the 3D aortic center lumen line was derived. The two intersection points of the centerline with the velocity mapping slice were used as seed points for automated segmentation of the ascending and descending aorta and time velocity curves were derived for both ascending and descending aorta. The pulse wave transit time from ascending to descending aorta was derived using the half-max method and the travelled distance from ascending to descending aorta was measured along the computed centerline. PWV was subsequently derived according to the following formula:

$$PWV = l/\Delta t$$

Where *l* is the distance along the centerline between the ascending and descending aorta cross-section and Δ*t* the difference in pulse-wave arrival time. Aortic PWV is measured in m/s.[15]

Statistical analysis

The relations between proximal measures of pressure and arterial stiffness, velocity pulsatility in the M1 and in the small cerebral perforating arteries, as well as relations with the damping indices were evaluated with linear regression analyses. To facilitate comparison between pulsatility, pressure and arterial stiffness measures along the cardiovascular tree, all data is presented as standardized beta (B [95%CI]). All data analyses were performed in IBM SPSS statistics (IBM Corp., v22.0, NY, USA). A *p*-value ≤0.05 was considered statistically significant.

RESULTS

2D PC scan quality was sufficient in 33 of 38 subjects, of which 28 and 26 subjects had sufficient scan quality in the CSO and BG, respectively. Included participants were aged 65±8 years (mean±standard deviation), and 55% were men. None had diabetes, 26% had hypertension, and 8% had a history of cardiovascular disease (i.e. stroke, TIA or ischemic heart disease). Cardiac measures, as well as blood pressure and vascular measures are presented in Table 1.

TABLE 1. Cardiac measures, blood pressure and vascular measures

Demographics	
Age (years)	65±8
Sex (male)	18 (55)
Vascular risk factors	
Hypertension	9 (26)
Hypercholesterolemia	10 (29)
Diabetes mellitus	0 (0)
Current smoking	2 (6)
History of reported TIA	1 (3)
History of reported ischemic stroke	0 (0)
Cardiac	
Left ventricular stroke volume (ml)	91.3±20

Blood pressure	
Systolic blood pressure (mmHg)	135±19
Diastolic blood pressure (mmHg)	81±11
MAP (mmHg)	99.8±13.3
Pulse pressure (mmHg)	54.6±14.3
Aorta	
Pulse wave velocity (m/s)	8.2±2.9
Middle cerebral artery (M1) (n=28)	
Velocity (cm/s)	35±7.5
Pulsatility	0.76±0.17
Cerebral perforating arteries	
Basal ganglia (BG; n=26)	
$N_{density}$ (# perforating arteries/cm^2)	0.66±0.22
Velocity (cm/s)	3.8±0.80
Pulsatility	0.40±0.14
Semi-oval center (CSO; n=28)	
$N_{density}$ (# perforating arteries/cm^2)	2.6±1.0
Velocity (cm/s)	0.7±0.12
Pulsatility	0.42±0.13
Damping index	
Between M1 and CSO	2.0±0.93
Between M1 and BG	2.1±0.81

Data presented as group mean±SD or n (%). N=33 unless otherwise indicated. MAP= mean arterial pressure.

Velocity pulsatility in the M1 was higher compared to the velocity pulsatility in the perforating arteries of the CSO and BG. This resulted in the damping index between the M1 and CSO (i.e. CSO damping index) and between the M1 and BG (i.e. BG damping index) to be larger than 1.0 in all but one subject, (in whom the measured damping index was 0.94). The CSO and BG damping indices were similar. These results are shown in Table 1. PP and aortic PWV were positively related to M1 velocity pulsatility (0.47 [0.06, 0.87], p=0.03 and 0.49 [0.08, 0.90], p=0.02, respectively). By contrast, aortic PWV was negatively related to CSO velocity pulsatility (-0.47 [-0.83, -0.10], p=0.01) and PP was

TABLE 2. Relations between proximal measures of perfusion pressure and arterial stiffness, flow pulsatility in the middle cerebral artery and in the small cerebral perforating arteries

	M1 pulsatility (n=28)	*p*	BG pulsatility (n=26)	*p*	BG damping index (n=26)	*p*	CSO pulsatility (n=28)	*p*	CSO damping index (n=28)	*p*
LVSV (ml)	0.07 [-0.40, 0.55]	0.75	0.06 [-0.37, 0.49]	0.78	-0.26 [-0.71, 0.19]	0.24	-0.18 [-0.59, 0.24]	0.39	0.01 [-0.45, 0.46]	0.98
MAP (mmHg)	-0.10 [-0.55, 0.35]	0.65	-0.23 [-0.61, 0.16]	0.23	0.17 [-0.31, 0.64]	0.47	-0.18 [-0.55, 0.20]	0.34	0.07 [-0.37, 0.51]	0.76
PP (mmHg)	0.47 [0.06, 0.87]	0.03	0.23 [-0.18, 0.65]	0.25	0.32 [-0.14, 0.77]	0.16	-0.21 [-0.60, 0.18]	0.28	0.49 [0.10, 0.88]	0.02*
Aortic PWV (m/s)	0.49 [0.08, 0.90]	0.02	0.09 [-0.34, 0.52]	0.68	0.20 [-0.25, 0.66]	0.37	-0.47 [-0.83, -0.10]	0.01*	0.71 [0.40, 1.02]	0.00*
M1 pulsatility	——	——	0.30 [-0.23, 0.82]	0.25	——	——	0.10 [-0.41, 0.61]	0.68	——	——

Data are presented as standardized regression coefficients (B) with 95% CI. A *p*-value ≤ 0.05 was considered significant and marked*. Statistical results were obtained using linear regression analysis. LVSV= left ventricular stroke volume; MAP= mean arterial pressure; PP= pulse pressure; PWV= pulse wave velocity; M1= first segment of the middle cerebral artery; BG= basal ganglia; CSO= semi-oval centre.

not related to CSO velocity pulsatility (-0.21 [-0.60, 0.18], p=0.28). PP and aortic PWV were also not related to BG velocity pulsatility (0.23 [-0.18, 0.65], p=0.25 and 0.09 [-0.34, 0.52], p=0.68, respectively). A significant association was found between aortic PWV and the CSO damping index (0.71 [0.40, 1.02], p<0.001), and the same was seen for PP and the CSO damping index (0.49 [-0.10, 0.88], p=0.02). Results of the relations between proximal measures of pressure and arterial stiffness, velocity pulsatility in the M1 and in the small cerebral perforating arteries are shown in Table 2.

DISCUSSION

This study shows the presence of damping between the M1 and perforating arteries in the BG and CSO, which is evident from the damping indices, which are larger than 1.0. Variable damping behavior is suggested, given the positive relations between proximal measures of pressure and arterial stiffness with the pulsatility in the M1, and lacking or negative relations with pulsatility in the more distal perforating arteries in the CSO and BG. This is furthermore implied by the positive relations between proximal measures of pressure and arterial stiffness with the damping index between M1 and CSO. Thus, these findings not only indicate the presence of damping between the M1 and the perforating arteries of the CSO and BG, but also suggest that the damping is variable between subjects in a way that distal damping is increased when proximal pressure and arterial stiffness increases.

The values found in our cohort for the velocity pulsatility in the M1 match well with those found in the literature, which range between 0.56 and 0.97 for controls without stroke or white matter hyperintensities of various ages.[9,16–21] Velocity pulsatility in the cerebral perforating arteries is less studied. The values reported here agree with those reported previously.[9,22] Schnerr et al. reported a PI for the lenticulostriate arteries of 0.46 for younger subjects (mean age 25 years) and 0.69 for older subjects (mean age 75 years), which is higher than our values.[17] This may partly be explained by the fact that Schnerr et al. analyzed only the relatively large perforating arteries close to the MCA with a mean perforating artery diameter of 1.7mm. This is also reflected in the lower damping index found by the authors between those vascular segments (1.31±0.30 vs. 2.1±0.81 in this study). The proximal measures of pressure and arterial stiffness assessed in this study were similar to those reported in literature.[19,23–26] Slight differences were likely due to the fact that we included participants with variable levels of risk factors and vascular

events, which assured us of the required variation in the measures of proximal pressure and arterial stiffness.

The relations found between proximal measures and pulsatility and damping indices in the CSO and BG indicate variable damping behavior, in which damping appears to increase with increased proximal 'stress', thus mitigating the effect on the pulsatility in the microcirculation. The suggestion of the existence of mechanisms that mitigate pressures traveling towards the microcirculation is not new, though techniques to measure flow pulsations in the small cerebral vessels were previously lacking.[27] Nevertheless, we can only speculate about the potential mechanisms underlying the negative relation of PWV with CSO velocity pulsatility. Increased PWV indicates increased aortic stiffness, but it is also suggested to indicate arterial stiffness in other cerebral vascular beds.[28] Arterial stiffness affects propagation and reflection characteristics of pressure waves of the arterial tree[4]. It may be that due to these changes in reflection, for example in the pial arteries which feed the CSO and not the BG, cancellation of forward and backward travelling waves occurs, decreasing CSO pulsatility. However, Mitchell et al. suggest a more proximal role for wave reflections. The research states that an increase in aortic stiffness as compared with the carotid arteries results in a reduction of wave reflections at the interface of the aorta and carotid arteries, which would increase pulsatile energy towards the microcirculation, contrary to our findings. In the BG positive relations of PP and PWV with M1 and lacking relations with BG pulsatility suggest damping, though, counterintuitively, relations between PP and PWV with the BG damping index are not found. This may be due to the fact that the pulsatility measures are relatively noisy, which is known from earlier studies. Division of two pulsatility measures, i.e. the damping index, increases the level of noise. It may thus be that a possibly present (weak) relation with the BG damping index is lost in the noise. Also, relations of PP and PWV with M1 pulsatility are borderline significant, which reflects some individual inconsistency in how M1 pulsatility changes in relation to changes in PP and PWV. This inconsistency may also cause that a relation with the BG damping index is too weak to be measured. Nevertheless, results suggest 'compensatory' damping between the M1 and CSO perforating arteries to be stronger compared to damping between the M1 and BG perforating arteries. This difference may be due to the fact that the small perforating arteries of the CSO are several branches further away from the M1 compared to the relatively adjacent BG. In addition, pathology and pathological degeneration of the perforating arteries in the BG and CSO are different, which is

reflected by the fact that arteriolar and tissue damage in the BG advances that in the CSO, and is more severe.[29] Finally, it is known that blood supply to the CSO, contrary to that of the BG, occurs via the pial arteries originating from the MCA,[30,31] and that pial arteries attenuate pressure and flow pulsatility prior to their arrival in downstream tissues.[32]

Research into the damping of flow pulsations travelling from the heart towards the cerebral vasculature is not new. Damping of flow pulsations is known to be associated with arterial compliance, i.e. the ability of elastic vessels to stretch and recoil and, with that, absorb pulsatile energy and protect the cerebral vasculature. Concerning compliance in the cardiovascular tree, it is believed that the aorta plays a primary role, as well as reflection at the relatively stiff muscular arteries, and the geometry of the CoW, which makes it serve as a pressure damper.[19,33] Standard physiology textbooks also reserve an important role in compliance for the cerebral small arteries and arterioles, located just proximal of the capillaries.[5–7] These vessels are lined with a smooth muscle cell layer enabling active alterations in compliance by changes in tone or wall structure.[34,35] While research into cerebral damping of flow pulsations is not new, research into damping of flow pulsations distal from the CoW is scarce. Earlier research into cerebral pulsatility and damping mainly focused on the larger arteries such as the carotid arteries, basilar artery, and the anterior, posterior and MCA.[7,36] Recently, velocity pulsatility of smaller cerebral arteries was performed with 4D flow MRI and by averaging over many planes and vessels.[37] This enabled the assessment of distal cerebral arteries originating from cerebral cortical arteries. However, this method was unable to assess vessels with diameters smaller than approx. 1mm, and assessment of regional vessel flow is difficult and time-consuming. Nonetheless, this study did find a cerebral arterial pulsatility increase as a function of age. A similar finding was observed in the large perforating arteries assessed by Schnerr et al.,[17] revealing an increase in pulsatility and a decrease in damping factor with age. These studies are in agreement with the belief that pulsatile energy in the small cerebral arteries increases with age, and contributes to the development of small vessel disease and manifestation such as white matter hyperintensities and cognitive decline. Research into brain pulsatility with NIRS also showed a higher pulsatility in older compared to younger adults. In addition, NIRS brain pulsatility in relation to cortical thickness (near-infraread spectroscopy) implied autoregulation mechanisms to damp and regulate pulsatility distal from the internal carotids.[38] With this work we extended the current literature on pulsatility damping to

damping beyond the CoW up to the level of the perforating arteries in the white matter of the semi-oval center. In addition, we have shown that with 2D PC imaging at 7T MRI damping of the cerebral small vessels can be investigated. This paved the way for future research of damping of cerebral pressure pulsations in other cohorts, such as young healthy subjects or subjects with cardiovascular disease due to a potentially decreased ability to dampen pressure pulsations in the cardiovascular tree.
A few limitations need to be considered. First, the PC sequence is relatively sensitive for motion during scanning. This can result in severe motion artifacts, and give unreliable velocity and pulsatility measurements. This lead to a considerable number of subjects to be excluded from small perforating artery analysis for the CSO level and BG level. This high exclusion rate is also known from earlier studies[10,22] and so far no quality assessment method has been developed to objectively exclude PC images from analysis. We therefore relied on an experienced observer to decide whether quality was sufficient. Although data of the elderly and diseased is more likely to be excluded due to severe motion artifacts, we believe that heterogeneity of our cohort, i.e. with multiple and variable levels of risk factors and vascular events, makes exclusion bias unlikely. A second limitation is that the perforating artery detection method inherently has a detection threshold, making perforating arteries with flow velocities below this threshold undetectable. Such floor-effects may in particular affect the CSO measures due to smaller perforating arteries and thus lower signal-to-noise compared to the measures in the BG. Third, for the M1 2D-Qflow a too long echo time resulting in flow voids caused exclusions of Qflow scans. Therefore, seven subjects had only either left or right M1 measurements, with no possibility of averaging both measurements. However, all study participants are healthy controls and we therefore expect no large differences between left and right M1 flow pulsatility. A final limitation relates to the fact that the perforating artery pulsatility measure is relatively noisy. Therefore, the absence of a correlation between a certain measure and the somewhat noisy perforating artery pulsatility does not necessarily mean that an effect between these two measures is inexistent. It is therefore important that in the future the 2D PC perforating artery pulsatility measures are supplemented with other pulsatility measurements, such as near-infrared spectroscopy, and more prospective studies are performed.

In this research we have non-invasively investigated damping between the M1 and the small cerebral perforating arteries, and its behavior in relation to proximal pressure pulsations. The results presented in this paper show the presence of damping between

the M1 and small cerebral perforating arteries of the CSO and BG, as well as variable damping behavior in relation to changes in proximal pressure and arterial stiffness. Future research should explore whether findings differ in other cohorts.

ACKNOWLEDGEMENTS

We thank K.M. van Hespen for his technical assistance in MRI data analysis.

REFERENCES

1. Chandra A, Li W, Stone C, Geng X, Ding Y. The cerebral circulation and cerebrovascular disease I: Anatomy. Brain circulation, 3(2), 45. Brain Circ. 2017;3(2):45-56. doi:10.4103/bc.bc
2. Djulejić V, Marinković S, Milić V, et al. Common features of the cerebral perforating arteries and their clinical significance. Acta Neurochir (Wien). 2015;157(5):743-754. doi:10.1007/s00701-015-2378-8
3. Mitchell GF, Van Buchem MA, Sigurdsson S, et al. Arterial stiffness, pressure and flow pulsatility and brain structure and function: The Age, Gene/Environment Susceptibility-Reykjavik Study. Brain. 2011;134(11):3398-3407. doi:10.1093/brain/awr253
4. Van De Vosse FN, Stergiopulos N. Pulse wave propagation in the arterial tree. Annu Rev Fluid Mech. 2011;43:467-499. doi:10.1146/annurev-fluid-122109-160730
5. Hall JE, Hall ME. Guyton and Hall Textbook of Medical Physiology. 13th ed. (WBSaunders, ed.).; 2015.
6. Safar ME, O'Rourke M. Handbook of Hypertension. In: 1st ed. Elsevier; 2006.
7. Holmgren M, Wåhlin A, Dunås T, Malm J, Eklund A. Assessment of Cerebral Blood Flow Pulsatility and Cerebral Arterial Compliance With 4D Flow MRI. J Magn Reson Imaging. 2019;51(5):1516-1525. doi:10.1002/jmri.26978
8. Hooghiemstra AM, Bertens AS, Leeuwis AE, et al. The Missing Link in the Pathophysiology of Vascular Cognitive Impairment: Design of the Heart-Brain Study. Cerebrovasc Dis Extra. 2017;7(3):140-152. doi:10.1159/000480738
9. Bouvy WH, Geurts LJ, Kuijf HJ, et al. Assessment of blood flow velocity and pulsatility in cerebral perforating arteries with 7-T quantitative flow MRI. NMR Biomed. 2016;29(9):1295-1304. doi:10.1002/nbm.3306
10. Geurts L, Biessels GJ, Luijten P, Zwanenburg J. Better and faster velocity pulsatility assessment in cerebral white matter perforating arteries with 7T quantitative flow MRI through improved slice profile, acquisition scheme, and postprocessing. Magn Reson Med. 2018;79(3):1473-1482. doi:10.1002/mrm.26821
11. Arts T, Siero JCW, Biessels GJ, Zwanenburg JJM. Automated Assessment of Cerebral Arterial Perforator Function on 7T MRI. J Magn Reson Imaging. 2021;53(1):234-241. doi:10.1002/jmri.27304
12. Gosling RG, King DH. Arterial assessment by Doppler-shift ultrasound. Proc R Soc Med. 1974;67:447-449.
13. Esper SA, Pinsky MR. Arterial waveform analysis. Best Pract Res Clin Anaesthesiol.

2014;28(4):363-380. doi:10.1016/j.bpa.2014.08.002

14. Bighamian R, Hahn JO. Relationship between stroke volume and pulse pressure during blood volume perturbation: A mathematical analysis. Biomed Res Int. 2014;2014. doi:10.1155/2014/459269
15. Shahzad R, Shankar A, Amier R, et al. Quantification of aortic pulse wave velocity from a population based cohort: A fully automatic method. J Cardiovasc Magn Reson. 2019;21(1):1-14. doi:10.1186/s12968-019-0530-y
16. Zarrinkoob L, Ambarki K, Wahlin A, et al. Aging alters the dampening of pulsatile blood flow in cerebral arteries. J Cereb Blood Flow Metab. 2016;36(9):1519-1527. doi:10.1177/0271678X16629486
17. Schnerr RS, Jansen JFA, Uludag K, et al. Pulsatility of lenticulostriate arteries assessed by 7 Tesla flow MRI-Measurement, reproducibility, and applicability to aging effect. Front Physiol. 2017;8(NOV):1-10. doi:10.3389/fphys.2017.00961
18. Warnert EAH, Verbree J, Wise RG, Van Osch MJP. Using high-field magnetic resonance imaging to estimate distensibility of the middle cerebral artery. Neurodegener Dis. 2016;16(5-6):407-410. doi:10.1159/000446397
19. Lefferts WK, DeBlois JP, Augustine JA, Keller AP, Heffernan KS. Age, sex, and the vascular contributors to cerebral pulsatility and pulsatile damping. J Appl Physiol. 2020;129(5):1092-1101. doi:10.1152/japplphysiol.00500.2020
20. Biedert S, Förstl H, Hewer W. Multiinfarct Dementia vs Alzheimer's Disease: Sonographic Criteria. Angiology. 1995;46(2):129-135. doi:10.1177/000331979504600206
21. Mok V, Ding D, Fu J, et al. Transcranial doppler ultrasound for screening cerebral small vessel disease: A community study. Stroke. 2012;43(10):2791-2793. doi:10.1161/STROKEAHA.112.665711
22. Geurts LJ, Luijten PR, Klijn CJM, Zwanenburg JJM, Biessels GJ. Higher Pulsatility in Cerebral Perforating Arteries in Patients With Small Vessel Disease Related Stroke, a 7T MRI Study. Stroke. 2018;50(1):62-68. doi:10.1161/strokeaha.118.022516
23. Cattermole GN, Leung PYM, Ho GYL, et al. The normal ranges of cardiovascular parameters measured using the ultrasonic cardiac output monitor. Physiol Rep. 2017;5(6):1-9. doi:10.14814/phy2.13195
24. Zhou B, Bentham J, Di Cesare M, et al. Worldwide trends in blood pressure from 1975 to 2015: a pooled analysis of 1479 population-based measurement studies with 19.1 million participants. Lancet. 2017;389(10064):37-55. doi:10.1016/S0140-6736(16)31919-5
25. Mattace-Raso FUS, Hofman A, Verwoert GC, et al. Determinants of pulse wave velocity in healthy people and in the presence of cardiovascular risk factors: 'Establishing normal

and reference values.' Eur Heart J. 2010;31(19):2338-2350. doi:10.1093/eurheartj/ehq165
26. Bognoni L, Cecelja M, Hussain T, et al. Pulse Wave Velocity Comparing Estimated and Direct Measures of Path Length in Older Women. Artery Res. 2020;26(4):236-241. doi:10.2991/artres.k.200819.001
27. Faraci FM, Heistad DD. Regulation of large cerebral arteries and cerebral microsvascular pressure. Circ Res. Published online 1990. doi:10.1161/01.RES.66.1.8
28. Laurent S, Cockcroft J, Van Bortel L, et al. Expert consensus document on arterial stiffness: methodological issues and clinical applications on behalf of the European Network for Non-invasive Investigation of Large Arteries. doi:10.1093/eurheartj/ehl312
29. Wardlaw JM, Smith C, Dichgans M. Mechanisms underlying sporadic cerebral small vessel disease : insights from neuroimaging. Lancet Neurol. 2013;12(5):70060-70067. doi:10.1016/S1474-4422(13)70060-7
30. Bogousslavsky J, Regli F. Centrum ovale infarcts. Neurology. 1992;42(10). doi:https://doi.org/10.1212/WNL.42.10.1992
31. Moody1 DM, Bell MA, Challa VR. Features of the Cerebral Vascular Pattern That Predict Vulnerability to Perfusion or Oxygenation Deficiency: An Anatomic Study.
32. Cooper LL, Mitchell GF. Aortic Stiffness, Cerebrovascular Dysfunction, and Memory. Pulse. 2016;4(2-3):69-77. doi:10.1159/000448176
33. Vrselja Z, Brkic H, Mrdenovic S, Radic R, Curic G. Function of circle of Willis. J Cereb Blood Flow Metab. 2014;34(4):578-584. doi:10.1038/jcbfm.2014.7
34. Correia MLG, Haynes WG. Arterial Compliance and Endothelial Function. Curr Diab Rep. 2007;7(4):269-275. doi:10.1007/s11892-007-0043-1
35. Rhodin J. Handbook of Physiology: The Cardiovascular System. (Bohr D, Somlyo A, Sparks JH, Grieger S, eds.). The Williams and Wilkins Company; 1980.
36. Birnefeld J, Wåhlin . Anders, Eklund A, Malm J. Cerebral arterial pulsatility is associated with features of small vessel disease in patients with acute stroke and TIA: a 4D flow MRI study. J Neurol. 2020;267:721-730. doi:10.1007/s00415-019-09620-6
37. Vikner T, Nyberg L, Holmgren M, Malm J, Eklund A, Wåhlin A. Characterizing pulsatility in distal cerebral arteries using 4D flow MRI. J Cereb Blood Flow Metab. 2020;40(12):2429-2440. doi:10.1177/0271678X19886667
38. Mohammadi H, Peng K, Kassab A, et al. Journal Pre-proof Cortical Thinning is Associated with Brain Pulsatility in Older Adults: An MRI and NIRS Study. Published online 2021. doi:10.1016/j.neurobiolaging.2021.05.002

Chapter 6

CEREBRAL PERFORATING ARTERY FLOW FUNCTION AND PULSATILITY ARE LARGELY UNAFFECTED BY COMMON VASCULAR RISK FACTORS

L.P Onkenhout, T. Arts, D. Ferro, S. Kuipers, E.A. Oudeman, T. van Harten, M.J.P. van Osch, J.J.M. Zwanenburg, J. Hendrikse, G.J. Biessels, L.J. Kapelle. On behalf of the Heart-Brain Connection Consortium

In preparation for submission in the Journal of Cerebral Blood Flow and Metabolism

ABSTRACT

Background and purpose: Cerebral perforating arteries are distal arterial branches that supply the deep regions of the brain. Recently, it became possible to measure blood flow velocity and pulsatility in these small arteries. It is unknown if these measures are affected by vascular risk factors.

Methods: We measured perforating artery flow with a 2D phase contrast 7T MRI at the level of the semi-oval center and the basal ganglia (BG) in seventy participants who participated in the heart brain connection study with either carotid occlusive disease (COD), vascular cognitive impairment (VCI), or no cerebrovascular disease. Vascular risk factors included hypertension, diabetes, hyperlipidemia and smoking.

Results: There was a trend between increased diastolic blood pressure and reduction of flow velocity ($p=0.052$) and pulsatility ($p=0.045$) at the BG level. With all other individual vascular risk factors we did not find this relationship, nor in case of more than one vascular risk factor present. Results were similar in stratified analyses for patients with and without a history of cardiovascular disease, or only COD or VCI.

Conclusion: We conclude that cerebral perforating artery flow velocity and pulsatility are largely independent of the presence of common vascular risk factors in a population with a mixed vascular burden.

INTRODUCTION

Cerebral perforating arteries are distal arterial branches that supply blood to the deep regions of the brain.[1] In healthy people, flow in cerebral perforating arteries is kept stable by the vasomotor response, but in elderly people or in participants with cerebrovascular disease this protective reflex may fail.[2,3] Recently, it has become possible to visualize the cerebral perforating arteries and to perform flow velocity measures with 7 Tesla (T) MRI,[3-6] but it is largely unknown which factors can affect flow in these perforating arteries.

From autopsy studies we know that the perforating arteries may remodel in the presence of vascular risk factors, due to increased oxidative stress, endothelial damage and apoptosis, inflammation and vasomotor dysfunction (Fig. 1). These may cause impaired vascular dilation resulting in increased pulsatility. In large vessels this phenomenon is a well-known early marker of vascular pathology, even before structural changes to the vascular wall are visible in both pathology as in vivo imaging.[7-9]

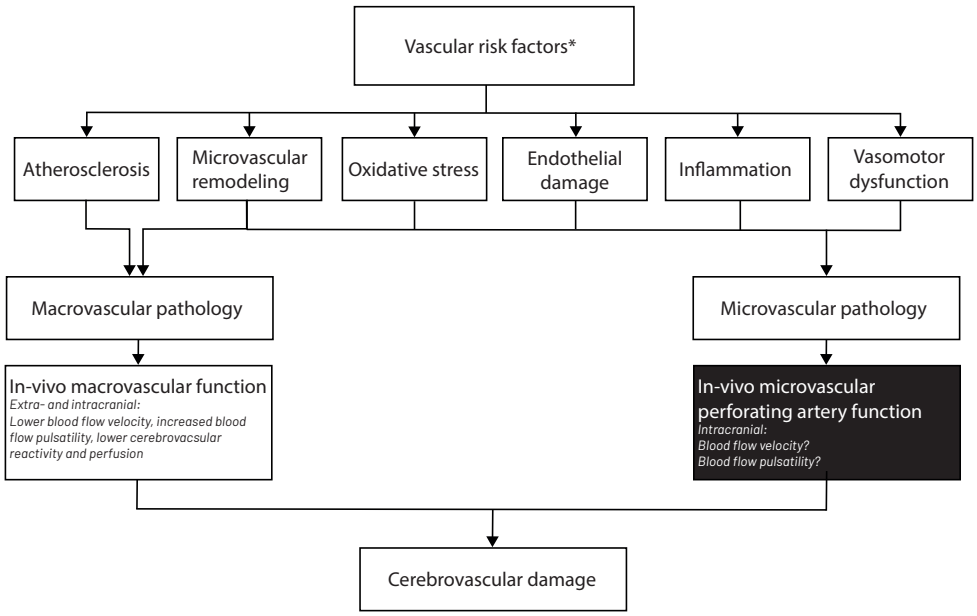

FIGURE 1. Vascular risk factors and vascular processes associated with cerebrovascular disease, with perforating artery function being a black box. *Vascular risk factors: hypertension, type 2 diabetes, hyperlipidemia, smoking.

It is well known that vascular risk factors are associated with a decrease in blood flow velocity and an increased pulsatility in large intracranial vessels. [10–12] Moreover, vascular risk factors have been associated with divergent effects on cerebrovascular reactivity and perfusion in the brain.[11,13] Single risk factors such as hypertension are associated with a decrease, however each risk factor independently contributes with variable effects.[14,15] Whether the relations between flow velocity and pulsatility and vascular risk factors also exist in the small perforating arteries is unknown. The aim of the current study is to investigate the relation between concurrent presence and levels of traditional vascular risk factors (hypertension, diabetes, hyperlipidemia and smoking) and both flow velocity and pulsatility in cerebral perforating arteries.

METHODS

Study population

We analyzed data from participants of the Heart-Brain Connection (HBC) study.[16] We choose this population because of its variable (cardio-)vascular burden and because of the extensive magnetic resonance imaging data. The HBC study investigates relationships between (cardio)vascular risk factors, the hemodynamic status of the heart and the brain, and cognitive impairment in four participant categories (carotid occlusive disease [COD], vascular cognitive impairment [VCI] or heart failure) and in a reference group.

For the present study, patients with COD (n=24) or VCI (n=10) and participants of the reference group (n=36) were selected. Perforating artery flow measurements were performed with 7T-MRI. In this population COD was defined as an occlusion of the internal carotid artery as assessed with magnetic resonance angiography. For VCI, inclusion criteria were cognitive complaints, a Clinical Dementia Rating scale score of ≤1, and a Mini-Mental State Examination score of ≥20 (i.e., we included patients with subjective cognitive decline, mild cognitive impairment, or mild dementia), combined with moderate to severe vascular brain injury, namely white matter lesion (Fazekas >1) and/or (lacunar) infarct(s) and/or intracerebral (micro-) hemorrhage(s); or mild white matter lesions (Fazekas=1) combined with the presence of vascular risk factors. The participants in reference group did not have a history COD or VCI. Group-specific inclusion and exclusion criteria for the overall HBC study have been described in detail previously. [16] This study was approved by our institutional review board. The study was

conducted in accordance with the declaration of Helsinki and the medical Research Involving Human Subjects Act (WMO).

Vascular risk factors

Blood pressure

Systolic and diastolic blood pressure (in mmHg) were acquired in a standardized way. During the study visit the patient was asked to sit for five minutes, after which the blood pressure was measured on each arm and repeated at least one minute later. Mean systolic and diastolic blood pressure was averaged out of four measurements during the study visits. The criteria for hypertension were: the use of antihypertensive medication, a mean systolic blood pressure above 140 mmHg or a mean diastolic blood pressure above 90 mmHg.

Type 2 Diabetes

The criteria for type 2 diabetes were: the use of antidiabetic medication, or a diagnosis of diabetes by a physician (even if a patient did not use medication, but for example would adhere to a diet) based on glucose levels or on HbA1c levels above 53 mmol/mol.

Hyperlipidemia

The criteria for hyperlipidemia were: the use of cholesterol lowering medication, or a diagnosis of hyperlipidemia by a physician based on earlier blood cholesterol and LDL levels (even if a patient did not use medication, but for example would adhere to a diet) or a present LDL above 3.5 mmol/L.

Smoking

Both current and a history of smoking was noted, as well as the number of packyears.

7 tesla MRI data acquisition and processing

7Tesla MRI data were acquired on a Philips Achieva MRI system in Leiden or Utrecht, The Netherlands. Flow velocity and pulsatility in cerebral perforating arteries were measured at two levels: the semi oval center (CSO) and the basal ganglia (BG).[17]

Cerebral perforating artery flow velocity and pulsatility

2D phase contrast (PC) acquisitions aimed at small perforating arteries in an axial slice

at the level of the CSO (approx. 100-300µm) and the BG (approx. 200-800µm) were performed on 7T MRI using a previously published sequence (Philips, 0.3x0.3x2.0 mm^3 resolution, CSO Venc=4cm/s, BG Venc=20cm/s).[4,5] (Suppl. Table 1 and Fig. 2). A peripheral pulse oximeter was used for retrospective gating and cushions were placed beside the subject's head to minimize head movement during scanning.

Perforating artery flow was assessed within a 2D white matter mask at the CSO level and a manually delineated 2D mask at the BG level, both excluding infarcts. White matter masks and infarcts in these regions were delineated from 3T MRI T1-weighted and FLAIR images with the Quantib Brain Segmentation Tool (FSL version 6.0.1, Oxford, UK). Registration of these masks to 7T space was done with FMRIB Software Library (FSL version 6.0.1, Oxford, UK). The infarct masks were dilated with a 3x3 mm kernel. Only the central white matter (further than 16 mm away from the outer rim of the brain on the PC slice) was included because the poor gray/white matter contrast in these regions on the PC image makes it difficult to recognize inclusion of gray matter into the white matter mask.[18]

Cerebral perforating arteries in the CSO and BG were detected as previously published,[4,5] also automatically excluding CSO perforating arteries located in regions with ghosting artefacts[19] and perforating arteries in the BG oriented non-perpendicularly to the scanning plane. In addition, apparent perforating arteries located within a 1.2 mm radius from each other were excluded, as these are mostly 'false detections' located on larger and non-perpendicular vessels.

Blood flow velocity (cm/s) and pulsatility ($(V_{max}-V_{min})/V_{mean}$, based on the normalized velocity curves) were assessed in the cerebral perforating arteries. Perforating artery count within the regions of interest was expressed as a density (number of perforating arteries/cm^2 mask, $N_{density}$).

Statistical analysis

Data are presented as mean ± SD or proportions, as appropriate. The relations between the vascular risk factors and perforating artery flow and pulsatility were assessed with linear regression analyses, adjusted for age and sex, and presented as an as unstandardized beta (B [95% confidence interval (CI)]) for dichotomous risk factors measures (i.e. hypertension, type 2 diabetes, hyperlipidemia and current or previous smoker), and as standardized beta (B [95% confidence interval (CI)]) for continuous risk

factor measures, (i.e. systolic – and diastolic blood pressure, HbA1c and LDL cholesterol). Additional analyses addressed the presence of one or more risk factors (0 versus ≥1 and 0 versus ≥ 2; independent of the type of risk factor). To rule out that our findings are driven by a clinical manifestation of vascular pathology in a sensitivity analyses we performed three stratified analyses: excluding 37 participants with a (previous) diagnosis of clinically manifest vascular disease (defined as: transient ischemic attack ischemic stroke or both; cardiovascular disease defined as: angina pectoris, ischemic heart disease, dotter treatment, bypass or peripheral arterial disease), only COD, and only VCI.

Data analyses were performed in IBM SPSS statistics (v. 22, SPSS Inc., Chicago, IL). A p-value ≤0.05 was considered statistically significant.

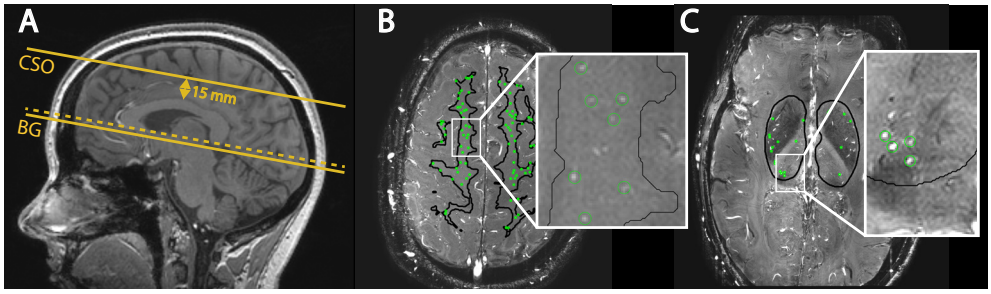

FIGURE 2. (A) Location of the 2D PC slice in the semi-oval centre (CSO), located 15 mm above the corpus callosum. The basal ganglia (BG) 2D PC slice is located at the level of anterior commissure. Slice angulation is associated with the bottom of the corpus callosum (dotted line). (B) Cerebral perforating arteries detected in the CSO circled in green. (C) Cerebral perforating arteries detected in the BG circled in green.

RESULTS

Ninety-five participants qualified and provided written informed consent. After exclusion of participants with unusable 7 tesla MRI data at the level of both the CSO and the BG, due to either participant movement during scanning or to erroneous slice planning, data of seventy participants (mean age 65±8 years; 63% male) remained. MRI scans of ten participants were excluded from analysis at the CSO level due to subject motion. At the BG level MRI scans of 19 participants could not be analyzed; seven due to subject motion and twelve due to erroneous slice planning. Information about vascular risk factors was complete in all participants. Fifty-three percent of participants had hypertension, 59% had hyperlipidemia, 10% had diabetes, 14% were current smokers and 59% had a history of smoking (Table 1).

TABLE 1. Demographics, MRI features and vascular risk factors

	N =70
Demographics	
Age (years)	65 ± 8
Sex (male)	44 (63)
COD	24 (34.3)
VCI	10 (14.3)
Controls	36 (51.4)
MRI features	
Pulsatility CSO (N=60)	0.43 ± 0.16
Pulsatility BG (N=51)	0.42 ± 0.14
Flow velocity CSO (cm/s)(N=60)	0.71 ± 0.16
Flow velocity BG (cm/s)(N=51)	3.7 ± 0.75
Number of perforating arteries detected CSO (N=60)	36 ± 20
Number of perforating arteries detected BG (N=51)	16 ± 5
$N_{density}$ CSO (# perforating arteries/cm^2)(N=60)	2.4 ± 1.0
$N_{density}$ BG (# perforating arteries/cm^2)(N=51)	0.7 ± 0.2
Vascular risk factors and history	
Hypertension	37 (53)
Systolic blood pressure (mmHg)	146 ± 21
Diastolic blood pressure (mmHg)	83 ± 10
Hyperlipidemia	41 (59)
LDL cholesterol (mmol/L)	3.1 ± 1.0
Diabetes mellitus II	7 (10)
HbA1c (mmol/mol)	38 ± 5.9
Current smoking / packyears	10 (14) / 31 ± 16
History of smoking / packyears	41 (59) / 24 ± 23
History of cerebral vascular disease	30 (43)
History of cardiovascular disease	16 (23)

Abbreviations: COD= carotid occlusive disease; VCI= vascular cognitive impairment; CSO= semi-oval centre; BG= basal ganglia. Data are presented as: mean ± standard deviation; N (%); cerebral vascular disease defined as: transient ischemic attack ischemic stroke or both; cardiovascular disease defined as: angina pectoris, ischemic heart disease, dotter treatment, bypass or peripheral arterial disease.

At the CSO and at the BG level the mean number of detected cerebral perforating arteries was 36±20 and 16±5, respectively. None of the vascular risk factors were related with the density of perforating arteries at both the CSO and BG level. No consistent relations were found between presence of any of the vascular risk factors and either flow pulsatility or velocity at the CSO or BG level (Table 2). At the BG a small effect with

TABLE 2. Relationship between vascular risk factors and cerebral perforating artery flow

	Pulsatility CSO N=60	p	Pulsatility BG N=51	p	Flow velocity CSO (cm/s) N=60	p	Flow velocity BG (cm/s) N=51	p
Hypertension †	-0.02 PI [-0.10 – 0.06]	0.63	0.00 PI [-0.08 – 0.08]	0.96	-0.01 cm/s [-0.09 – 0.08]	0.88	-0.32 cm/s [-0.72 – 0.07]	0.11
Systolic blood pressure	-0.14 [-0.41 – 0.13]	0.30	-0.03 [-0.33 – 0.28]	0.87	-0.03 [-0.31 – 0.25]	0.84	-0.22 [-0.50 – 0.07]	0.14
Diastolic blood pressure	-0.19 [-0.44 – 0.07]	016	-0.29 [-0.57 – -0.01]	0.045*	0.05 [-0.22 – 0.32]	0.70	-0.26 [-0.52 – 0.00]	0.052
Diabetes Mellitus II †	0.02 PI [-0.13 – 0.18]	0.75	0.10 PI [-0.03 – 0.23]	0.12	-0.09 cm/s [-0.25 – 0.07]	0.24	-0.04 cm/s [-0.72 – 0.64]	0.90
HbA1c	0.17 [-0.09 – 0.43]	0.19	-0.01 [-0.30 – 0.29]	0.95	0.04 [-0.23 – 0.31	0.76	0.02 [-0.25 – 0.30]	0.86
Hyperlipidemia †	0.02 PI [-0.06 – 0.10]	0.63	0.03 PI [-0.05 – 0.11]	0.48	-0.04 cm/s [-0.13 – 0.05]	0.39	-0.26 cm/s [-0.68 – 0.17]	0.23
LDL cholesterol	0.02 [-0.25 – 0.28]	0.87	-0.19 [-0.50 – 0.12]	0.22	-0.08 [-0.35 – 0.20]	0.58	0.18 [-0.11 – 0.47]	0.21
Current or previous smoker †	-0.00 PI [-0.12 – 0.12]	0.96	0.03 PI [-0.07 – 0.12]	0.59	-0.11 cm/s [-0.23 – 0.02]	0.09	-0.17 cm/s [-0.67 – 0.33]	0.50

Abbreviations: CSO= semi-oval centre; BG= basal ganglia. Continuous data are presented as standardized Beta [95% confidence interval]. † = dichotomous data, are presented as unstandardized Beta [95%CI]. All data are corrected for age and sex. *p ≤ 0.05 was considered significant.

TABLE 3. Relationship between the presence of one or more vascular risk factor(s) and cerebral perforating artery flow

	Pulsatility CSO N=60	p	Pulsatility BG N=51	p	Flow velocity CSO (cm/s) N=60	p	Flow velocity BG (cm/s) N=51	p
Presence of one risk factor	-0.01 PI [-0.13 – 0.11]	0.82	-0.03 PI [-0.15 – 0.09]	0.57	-0.05 cm/s [-0.18 – 0.08]	0.42	-0.07 cm/s [-0.68 – 0.53]	0.83
Presence of two or more risk factors	0.01 PI [-0.08 – 0.09]	0.06	0.00 PI [-0.08 – 0.09]	0.93	-0.04 cm/s [-0.13 – 0.05]	0.37	-0.35 cm/s [-0.79 – 0.09]	0.12

Abbreviations: CSO= semi-oval centre; BG= basal ganglia. Data on presence of risk factor are dichotomous and presented as unstandardized Beta [95% confidence interval]. All data are corrected for age and sex. *p ≤ 0.05 was considered significant.

boundary significance was found between increase (per 1 mmHg) in diastolic blood pressure and lower cerebral perforator pulsatility (standardized beta: -0,29, 95%CI: -0,57 - -0,01; p=0,045). Moreover, we did find a trend between increased systolic and diastolic blood pressure and reduction of flow velocity at the BG level (standardized beta: -0,26. 95%CI: -0,52 – 0,00; p=0.052).

In additional analyses we did not find any relation between the presence of one or more vascular risk factors (regardless of type) and measurements of perforating artery flow and although when looking at the presence of two or more risk factors, BG flow velocity shows the same trend as mentioned above (Table 3). All three sensitivity analyses showed similar results as the main analysis. Moreover, a stratified analyses looking at only COD and only VCI did not alter the results.

DISCUSSION

Cerebral perforating artery flow velocity and pulsatility on 7T MRI have been presented as new measures of cerebral small vessel functioning.[3] We investigated if traditional vascular risk factors are related to these flow measures. We could not demonstrate consistent relations between measures of flow in cerebral perforating arteries and the presence or level of individual vascular risk factors, although there is a trend between hypertension and a reduction of flow velocity and pulsatility at the BG level which is partially significant.
Earlier studies on cerebral blood flow in relation to vascular risk factors have shown that vascular risk factors attributing to arterial stiffening were associated with decreased flow velocity and increased pulsatility.[13–16] To the best of our knowledge ours is the first study to examine this relation with flow in cerebral perforating arteries.

Our observed values for perforating artery flow velocity and pulsatility in the CSO and BG are in agreement with previous literature in which elderly participants were studied.[4–6] The number of detected perforating arteries in our study is lower than previously reported, probably due to the exclusion of non-perpendicular perforating arteries in the BG and the exclusion of perforating arteries located in ghosting regions in the CSO. The exclusion of non-perpendicular perforating arteries at the level of the BG also explains why velocities in that region are slightly lower; non-perpendicular perforating arteries are mostly larger vessels with higher blood flow velocities.

We can only speculate about explanations for our findings. Arterial stiffening, atherosclerosis and damage to the endothelium are all known to be risk factor-induced pathologies, [1,7,17–21] substantiating the initial thought that vascular risk factors could be related to cerebral perforating artery flow measures. Hypertension is known to induce adaptive changes in cerebral arteries such as hypertrophy in smooth muscle cells, impaired endothelial function, increase of the vascular wall thickness due to hyperplasia and vascular stiffening and atherosclerosis.[17–20] Yet, literature on animals suggests that hypertrophy of cerebral perforating arteries may reduce stiffening in compensation.[20,22] A second explanation may be that we investigated a population that received strict cardiovascular risk management and thus limiting the effect of hypertension showing some effect but not consistently. Finally, it could be that hypertension activates autoregulation mechanisms to stabilize cerebral blood flow.[17,20,23] Autoregulation of flow is present in many vascular beds, but is particularly well developed in the brain.[24] Autoregulation mechanisms involve neurovascular coupling which is driven by endothelium signaling in which endothelium secretes vasodilation and vasoconstriction substances to ensure appropriate cerebral blood flow.[25] Since hyperlipidemia, diabetes and smoking are also associated with endothelial dysfunction,[26–28] it is likely that the lack of relations between these risk factors and perforating artery flow measures is also due to unaffected autoregulation of cerebral blood flow.

The somewhat different findings for the CSO and BG level may be due to the fact that the small perforating arteries at the CSO level are smaller than the relatively more proximally located arteries at the BG level. Therefore, at the CSO level the blood has had a longer trajectory to carry out the autoregulation mechanisms showing it's effect in these distal arteries.

Some limitations of our study need to be considered. First, during scanning the PC sequence is relatively sensitive for motion. This may result in motion artifacts and, as such, in unreliable velocity and pulsatility measurements. Therefore a number of MRI scans could not be assessed due to movement artefacts, even though the participants were instructed to lie as still as possible. These drop-out numbers are known from previous similar studies on 7T MRI and unfortunately inherent to the complexity and sensitivity of the scanning method.[5,3] Since the dropout was more or less evenly distributed in the different participant group, this probably did not cause selection bias. Second, the heterogeneity of our population could affect our findings as their underlying pathology is different, for example in participants with severe atherosclerotic large

vessel disease, or in those with cerebral small vessel disease. However, additional analyses performed in the sensitivity analysis did not show influence of our results.
An important strength of this study is the relatively large sample size of participants who underwent a 7T MRI. Secondly, we measured cerebral perforating artery flow at two brain levels, i.e. the CSO and BG, which are both fed by different arteries, allowing us to distinguish between these two brain regions.

In conclusion, this study shows that blood flow velocity and pulsatility of cerebral perforating arteries are largely independent of the presence or level of vascular risk factors in a population above the age of 50 years with mixed vascular burden. However a small effect on flow pulsatility and velocity at the level of BG is still possible. Our results suggest that flow-stabilizing mechanisms are able to largely maintain stable cerebral perforating artery flow independent of the presence of vascular risk factors.

REFERENCES

1. Chandra, A., Li, W., Stone, C., Geng, X. & Ding, Y. The cerebral circulation and cerebrovascular disease I: Anatomy. Brain circulation, 3(2), 45. Brain Circ. 3, 45–56 (2017).
2. Wardlaw, J. M., Smith, C. & Dichgans, M. Mechanisms of sporadic cerebral small vessel disease: Insights from neuroimaging. The Lancet Neurology vol. 12 483–497 (2013).
3. Geurts, L. J., Luijten, P. R., Klijn, C. J. M., Zwanenburg, J. J. M. & Biessels, G. J. Higher Pulsatility in Cerebral Perforating Arteries in Patients With Small Vessel Disease Related Stroke, a 7T MRI Study. Stroke 50, 62–68 (2018).
4. Bouvy, W. H. et al. Assessment of blood flow velocity and pulsatility in cerebral perforating arteries with 7-T quantitative flow MRI. NMR Biomed. 29, 1295–1304 (2016).
5. Geurts, L., Biessels, G. J., Luijten, P. & Zwanenburg, J. Better and faster velocity pulsatility assessment in cerebral white matter perforating arteries with 7T quantitative flow MRI through improved slice profile, acquisition scheme, and postprocessing. Magn. Reson. Med. 79, 1473–1482 (2018).
6. Schnerr, R. S. et al. Pulsatility of lenticulostriate arteries assessed by 7 Tesla flow MRI-Measurement, reproducibility, and applicability to aging effect. Front. Physiol. 8, 1–10 (2017).
7. Granger, D. N., Rodrigues, S. F., Yildirim, A. & Senchenkova, E. Y. Microvascular responses to cardiovascular risk factors. Microcirculation (2010) doi:10.1111/j.1549-8719.2009.00015.x.
8. Nichols, W. W., O'Rourke, M. F., Vlachopoulos, C., Hoeks, A. P. & Reneman, R. S. McDonald's blood flow in arteries theoretical, experimental and clinical principles. McDonald's Blood Flow in Arteries, Sixth Edition: Theoretical, Experimental and Clinical Principles (2011). doi:10.1016/0306-3623(92)90079-y.
9. Hooghiemstra, A. M. et al. The Missing Link in the Pathophysiology of Vascular Cognitive Impairment: Design of the Heart-Brain Study. Cerebrovasc. Dis. Extra 7, 140–152 (2017).
10. Van Buchem, M. A. et al. The heart-brain connection: A multidisciplinary approach targeting a missing link in the pathophysiology of vascular cognitive impairment. J. Alzheimer's Dis. 42, S443–S451 (2014).
11. Arts, T., Siero, J. C. W., Biessels, G. J. & Zwanenburg, J. J. M. Automated Assessment of Cerebral Arterial Perforator Function on 7T MRI. J. Magn. Reson. Imaging 53, 234–241 (2021).
12. Avolio, A. & Schiffrin, E. L. Are central hemodynamic parameters better prognostic

markers than peripheral blood pressure in stroke? Artery Res. (2018) doi:10.1016/j.artres.2018.10.015.

13. Pase, M. P., Grima, N. A., Stough, C. K., Scholey, A. & Pipingas, A. Cardiovascular disease risk and cerebral blood flow velocity. Stroke (2012) doi:10.1161/STROKEAHA.112.666727.
14. Jefferson, A. L. et al. Higher aortic stiffness is related to lower cerebral blood flow and preserved cerebrovascular reactivity in older adults. Circulation 138, 1951–1962 (2018).
15. Cho, S. J., Sohn, Y. H., Kim, G. W. & Kim, J. S. Blood flow velocity changes in the middle cerebral artery as an index of the chronicity of hypertension. J. Neurol. Sci. (1997) doi:10.1016/S0022-510X(97)05391-4.
16. A., K., J., G., B., G., B., W. & T., G. Is blood flow in the middle cerebral artery determined by systemic arterial stiffness? Blood Pressure (2009).
17. Neumann, S. et al. Cerebral blood flow response to simulated hypovolemia in essential hypertension a magnetic resonance imaging study. Hypertension (2019) doi:10.1161/HYPERTENSIONAHA.119.13229.
18. Iadecola, C. & Gottesman, R. F. Neurovascular and Cognitive Dysfunction in Hypertension. Circ. Res. (2019) doi:10.1161/circresaha.118.313260.
19. Iadecola, C. & Davisson, R. L. Hypertension and Cerebrovascular Dysfunction. Cell Metabolism (2008) doi:10.1016/j.cmet.2008.03.010.
20. Smulyan, H., Lieber, A. & Safar, M. E. Hypertension, Diabetes Type II, and their association: Role of arterial stiffness. Am. J. Hypertens. (2016) doi:10.1093/ajh/hpv107.
21. Pires, P. W., Dams Ramos, C. M., Matin, N. & Dorrance, A. M. The effects of hypertension on the cerebral circulation. American Journal of Physiology - Heart and Circulatory Physiology (2013) doi:10.1152/ajpheart.00490.2012.
22. Baumbach, G. L., Sigmund, C. D. & Faraci, F. M. Cerebral arteriolar structure in mice overexpressing human renin and angiotensinogen. Hypertension (2003) doi:10.1161/01.HYP.0000042427.05390.5C.
23. Faraci, F. M. & Heistad, D. D. Regulation of large cerebral arteries and cerebral microsvascular pressure. Circulation Research (1990) doi:10.1161/01.RES.66.1.8.
24. Cipolla, M. J. The Cerebral Circulation. (Morgan & Claypool Life Sciences, 2010). doi:10.4199/C00005ED1V01Y200912ISP002.
25. Silverman, A. & Petersen, N. H. Physiology, Cerebral Autoregulation. StatPearls (2020).
26. Valenzuela-Garcia, L. F. et al. Lack of correlation between the optimal glycaemic control and coronary micro vascular dysfunction in patients with diabetes mellitus: A cross sectional study. Cardiovasc. Diabetol. (2015) doi:10.1186/s12933-015-0269-1.
27. Pruzin, J. J., Nelson, P. T., Abner, E. L. & Arvanitakis, Z. Review: Relationship of type 2

diabetes to human brain pathology. Neuropathology and Applied Neurobiology (2018) doi:10.1111/nan.12476.

28. Lekakis, J. et al. Effects of acute cigarette smoking on endothelium-dependent arterial dilatation in normal subjects. Am. J. Cardiol. (1998) doi:10.1016/S0002-9149(98)00098-8.

Supplements

Supplementary material

SUPPLEMENTAL TABLE 1. Imaging parameters of the 2D phase contrast (PC) sequence in CSO and BG

	2D PC CSO/BG
FOV, mm (RLxAP)	250x250/250x169
Slices	1
Acquired voxel size, mm*	0.3x0.3x2.0
Flip angle**, °	50-90/60
Venc, cm/s	4/20
TR, ms	28.5-29.6/28
TE, ms	16.1-17.3/14.7-15.0
TFE factor	2
Sense factor (AP direction)	1.5/1
Acquired time points	10-15/11-15
Scan time, min:s**	3:30/3:32
**scantime for a heart rate of 80 bpm	

Imaging parameters of the 2D phase contrast sequence in the semi-oval centre (CSO) and basal ganglia (BG). Abbreviations: PC= phase contrast; FOV= field of view; RL= right-left, AP= anterior-posterior; V_{enc}= encoded velocity; TR= repetition time; TE= echo time; TFE= turbo field echo. *Reconstructed to 0.2x0.2 mm^2 in-plane resolution. ** Ramped flip angle along the flow direction (perpendicular to the slice) to mitigate saturation effects.

Part III

WHAT IS HAPPENING?

EXPLORING MICROVASCULAR (DYS)FUNCTION IN SVD

Chapter 7

ZOOMING IN ON CEREBRAL SMALL VESSEL FUNCTION IN SMALL VESSEL DISEASES WITH 7T MRI: RATIONALE AND DESIGN OF THE "ZOOM@SVDS" STUDY

H. van den Brink*, A. Kopczak*, T. Arts*, L.P. Onkenhout, J.C.W. Siero, J.J.M. Zwanenburg, M. Duering, G.W. Blair, F. Doubal, M.S. Stringer, M.J. Thrippleton, H.J. Kuijf, A. de Luca, J. Hendrikse, J.M. Wardlaw, M. Dichgans, G.J. Biessels. On behalf of the SVDs@target group.

*these authors contributed equally to this manuscript.

Published in CCCB (2021)

ABSTRACT

Background and purpose: Cerebral small vessel diseases (SVDs) are a major cause of stroke and dementia. Yet, specific treatment strategies are lacking in part because of a limited understanding of the underlying disease processes. There is therefore an urgent need to study SVDs at their core, the small vessels themselves. This paper presents the rationale and design of the ZOOM@SVDs study, which aims to establish measures of cerebral small vessel dysfunction on 7T MRI as novel disease markers of SVDs.

Methods: ZOOM@SVDs is a prospective observational cohort study with two years follow-up. ZOOM@SVDs recruits participants with Cerebral Autosomal Dominant Arteriopathy with Subcortical Infarcts and Leukoencephalopathy (CADASIL, N=20), sporadic SVDs (N=60), and healthy controls (N=40). Participants undergo 7T brain MRI to assess different aspects of small vessel function including small vessel reactivity, cerebral perforating artery flow, and pulsatility. Extensive work-up at baseline and follow-up further includes clinical and neuropsychological assessment as well as 3T brain MRI to assess conventional SVD imaging markers. Measures of small vessel dysfunction are compared between patients and controls, and related to the severity of clinical and conventional MRI manifestations of SVDs.

Conclusion: ZOOM@SVDs will deliver novel markers of cerebral small vessel function in patients with monogenic and sporadic forms of SVDs, and establish their relation with disease burden and progression. These small vessel markers can support etiological studies in SVDs and may serve as surrogate outcome measures in future clinical trials to show target engagement of drugs directed at the small vessels.

ABBREVIATIONS

ASL: Arterial Spin Labeling
BOLD: Blood Oxygenation Level-Dependent
CADASIL: Cerebral Autosomal Dominant Arteriopathy with Leukoencephalopathy and Subcortical Infarcts
CDR: Clinical Dementia Rating scale
CERAD+: Consortium to Establish a Disease Registry for Alzheimer's Disease Plus battery
CES-D: Center for Epidemiologic Studies Depression Scale
CO2: Carbon Dioxide
CSF: Cerebrospinal Fluid
DTI: Diffusion Tensor Imaging
EPIC: European Prospective Investigation into Cancer and Nutrition
EtCO2: End-tidal Carbon Dioxide
fMRI: Functional Magnetic Resonance Imaging
FLAIR: Fluid Attenuated Inversion Recovery
FOV: Field Of View
FWHM: Full-Width-at-Half-Maximum
GE: Gradient Echo
GM: Grey Matter
GPRS: General Packet Radio Service
HRF: Hemodynamic Response Function
LMU: Ludwig-Maximilians-Universität
MMSE: Mini-Mental State Examination
NAWM: Normal Appearing White Matter
NIHSS: National Institute for Health Stroke Scale
PI: Pulsatility Index
ROI: Region Of Interest
SPPB: Short Physical Performance Battery
SVDs: Small Vessel Diseases
SWI: Susceptibility Weighted Imaging
TE: Echo Time
TI: Inversion Time
TR: Repetition Time

TSE: Turbo Spin Echo
UMCU: University Medical Center Utrecht
Vmax: Maximum velocity
Vmin: Minimum velocity
Vmean: Mean velocity
WM: White Matter
WMH: White Matter Hyperintensity

INTRODUCTION

Cerebral small vessel diseases (SVDs) affect small arteries, capillaries and small veins in the brain.[1] SVDs account for most hemorrhagic strokes, a quarter of ischemic strokes, and at least 40% of dementia cases, alone or in combination with neurodegenerative pathology[1]. Roughly 70% of 65-year-old individuals and almost all 90-year-olds exhibit manifestations of SVDs on brain imaging[2]. Despite this profound impact, there is no specific treatment for SVDs with proven efficacy. Current management is limited to treatment of risk factors, foremost hypertension, which is clearly of fundamental importance, but is not sufficient to halt SVDs and their consequences. Better insight into the mechanisms underlying SVDs is urgently needed to support the development of targeted treatments.

Over the years there has been major progress in the development of SVD biomarkers. These include visible manifestations on MRI (i.e. lacunes, white matter hyperintensities, microbleeds, enlarged perivascular spaces[3]), more subtle microstructural white matter changes (measured with diffusion tensor imaging[4–6]) and blood-based biomarkers of neuro-axonal damage (serum neurofilament light[7]). All of these biomarkers primarily reflect SVDs-related parenchymal injury. This injury relates to important functional outcomes, in particular cognitive decline and dementia, but is essentially a downstream consequence of a disease that originates in the small cerebral vessels. In these vessels, SVDs manifest as loss of smooth muscle cells, fibrinoid necrosis, narrowing of the lumen, and thickening of the vessel wall.[1,8] This impacts vessel function, as observed in pial and parenchymal arteries in experimental animal models of both hereditary and sporadic forms of SVDs.[9,10] Emerging techniques at 7T MRI provide noninvasive measures of cerebral small vessel function in humans.[11] These measures allow SVDs to be studied at their core, the small vessels themselves, and have important potential as biomarker of SVDs to help unravel the pathophysiology and serve as surrogate outcome measures in treatment studies.

This paper presents the rationale and design of ZOOM@SVDs, part of the SVDs@target research program (see textbox). ZOOM@SVDs explores (1) which aspects of small vessel function on 7T brain MRI are affected in patients with Cerebral Autosomal Dominant Arteriopathy with Subcortical Infarcts and Leukoencephalopathy (CADASIL) and in patients with symptomatic sporadic SVD, and (2) how small vessel function relates to SVD severity at baseline and disease progression after two years.

SVDs@target (Small vessel diseases in a mechanistic perspective: Targets for Intervention – Affected pathways and mechanistic exploitation for prevention of stroke and dementia) (www.svds-at-target.eu). The program is funded by Horizon 2020 and includes three clinical studies: ZOOM@SVDs (current paper), INVESTIGATE-SVDs, and TREAT-SVDs. This textbox provides a summary on INVESTIGATE-SVDs and TREAT-SVDs.

INVESTIGATE-SVDs (Imaging NeuroVascular, Endothelial and STructural InteGrity in prepAration to TrEat Small Vessel Diseases.): PI Prof JM Wardlaw, Centre for Clinical Brain Sciences Edinburgh. INVESTIGATE-SVDs is a three-centre (Edinburgh, Maastricht, Munich) observational study in 45 patients with sporadic SVDs and in 30 patients with CADASIL. The main objective is to advance knowledge of SVD pathophysiology by assessing the relationship between blood brain barrier integrity, cerebrovascular reactivity to CO_2, intracranial vascular and CSF pulsatility, blood pressure and its variability and clinical and structural features of SVD.

TREAT-SVDs (EffecTs of Amlodipine and other Blood PREssure Lowering Agents on Microvascular FuncTion in Small Vessel Diseases): PI Prof M Dichgans, Institute for Stroke and Dementia Research, Ludwig-Maximilians-Universität, Munich
TREAT-SVDs is a five-centre (Edinburgh, Maastricht, Munich, Oxford, Utrecht), randomized, open-label, crossover trial in 75 patients with sporadic SVDs and 30 patients with CADASIL. The primary objective is to test the hypothesis that the calcium channel blocker amlodipine has a beneficial effect on small vessel function in patients with symptomatic SVDs when compared to either the Angiotensin II type 1 receptor blocker losartan or the beta-blocker atenolol. The secondary objective is to test the hypothesis that losartan has a beneficial effect on small vessel function compared to atenolol.

METHODS

Study design

ZOOM@SVDs is a prospective observational cohort study with a follow-up measurement after two years. The study is a collaboration between the University Medical Center Utrecht (UMCU) in the Netherlands and the Institute for Stroke and Dementia Research at Ludwig-Maximilians-Universität (LMU), Munich, Germany. At the UMCU, 60 patients

with symptomatic sporadic SVD and 30 age and sex-matched controls are recruited. At the LMU, 20 patients with CADASIL and 10 age and sex-matched controls are recruited. Participants attend two baseline visits and one follow-up visit after two years, see Table 1 for an overview of the data collection per visit. The 7T MRI scan for all participants is performed at the UMCU. All other assessments for the patients with CADASIL and their controls are performed at the LMU.

TABLE 1. Overview of data collection per visit

	Baseline visit 1	Baseline visit 2	Follow-up
	Day 1	Day 8-28	2 years
Informed consent	X		
Clinical assessment	X		X
Blood sampling	X		
Neuropsychological assessment	X		X
7-day blood pressure monitoring	X		
3T brain MRI	X		X
7T brain MRI		X	

Ethical approval

The Medical Ethics Review Committees of the UMCU and the LMU both approved the study (under number NL62090.041.17 and 17-088 respectively). The study is registered in the Nederlands Trial Register (under number NTR6265) and is conducted in accordance with the declaration of Helsinki and the European law of General Data Protection Regulation. Written informed consent is obtained from all participants prior to enrollment in the study.

Participants

Patients with symptomatic sporadic SVDs (N=60) are recruited from the stroke, rehabilitation and memory clinics of the UMCU, and from referring neighboring clinics (Diakonessenhuis Zeist and Utrecht). Patients with a diagnosis of CADASIL (N=20), either confirmed by molecular genetic testing of the *NOTCH3* gene or by skin biopsy, are recruited through the Institute for Stroke and Dementia Research at the LMU. The institute is a tertiary national referral center for patients with CADASIL in Germany. Controls are recruited among partners or relatives of the patients, and through flyer advertisement. Table 2 lists specific participant inclusion and exclusion criteria.

TABLE 2. Inclusion and exclusion criteria for patients with sporadic SVDs, CADASIL and healthy controls.

General selection criteria for all groups	
Inclusion criteria	***Exclusion criteria***
• Age 18 years or older • Capacity to give written informed consent • Independent in activities of daily living (Modified Rankin score ≤ 3)	• Pregnant or breastfeeding women and women of childbearing age not taking contraception • Contraindication to MRI or unable to undergo MRI protocol due to physical condition • Other major neurological or psychiatric conditions affecting the brain and interfering with the study design (e.g. multiple sclerosis, Parkinson's disease) • Life expectancy <2 years
Additional selection criteria specific to patients with sporadic SVDs	
Inclusion criteria	***Exclusion criteria***
A diagnosis of CADASIL established by molecular genetic testing of the NOTCH3 gene (presence of an archetypical, cysteine-affecting mutation) or the presence of granular osmiophilic material in ultrastructural, electron microscopy analysis of skin biopsy. NB: thus both symptomatic and asymptomatic patients are included.	Not appicable
Additional selection criteria specific to controls	
Inclusion criteria	***Exclusion criteria***

No additional inclusion criteria applicable	• A history of stroke or of cognitive complaints for which the person has previously sought medical advice • So-called "silent" SVDs defined as confluent white matter hyperintensities (Fazekas ≥ 2) or lacunes on the 3T brain MRI scan on baseline visit 1

Baseline assessment

Clinical assessment

The following measures are collected during the clinical assessment:

- Demographic factors, including age, sex and education level
- Medical history, including history of TIA, stroke, cognitive impairment and vascular risk factors (i.e. hypertension, hyperlipidemia, diabetes, smoking, BMI and alcohol use)
- Physical activity (i.e. EPIC Physical Activity Questionnaire[12]) and physical performance (i.e. SPPB[13])
- Physical examination, including a National Institute of Health Stroke Scale (NIHSS) examination[14] and blood pressure measurements
- Current medication

Blood sampling

Laboratory investigations are performed in blood from a venipuncture in order to document the cardiovascular risk profile, including total cholesterol, HDL-cholesterol, LDL-cholesterol, triglycerides, HbA1c, and C-reactive protein. In women of childbearing age, a pregnancy test is performed as a screening measure before undergoing MRI.
In addition to these laboratory tests, blood is obtained in two 8ml cell preparation tubes with sodium citrate (BD, 362782). Directly after collection, peripheral blood mononuclear cells are isolated and stored at -80 degrees Celsius[15], with the aim to explore the contribution of immune cells to the severity of SVDs. This procedure is also performed in the other clinical studies of SVDs@target (i.e. INVESTIGATE-SVDs and TREAT-SVDs) and the analyses and findings will be combined for all three studies and addressed in separate work.

Blood pressure monitoring at home

At baseline, participants receive a telemetric blood pressure device to measure their blood pressure at home for seven days. The device (Tel-O-Graph® GSM Plus) has a CE 0044 label, has been validated according to the European standard ISO 81060-2:2009 and is graded A/A by the British Hypertension Society. Data are anonymously transferred via mobile phone networks (GPRS, General Packet Radio Service) to a central database for analysis. Participants measure the blood pressure three times daily: after waking, at noon and in the evening at bedtime. Participants are instructed to repeat the blood pressure measurements at each time point within 5 minutes. For data analyses, only

the 2nd blood pressure measurement is used. If only one reading at a time point is available, that data will be used for the analysis. In addition to blood pressure, a pulse wave analysis is automatically performed with each blood pressure measurement to assess pulse wave velocity.

Neuropsychological assessment

All participants undergo a standardized neuropsychological assessment battery in a fixed order. The battery includes the Consortium to Establish a Registry for Alzheimer's Disease (CERAD) battery[16], with the addition of the Trail Making Test[17], phonemic fluency[17], and digit span[18] to better assess processing speed and executive function (Table 3). The battery is consise, but still covers global cognition as well as specific cognitive domains. Individual test scores are standardized into *z*-scores using the control groups as a reference. Test *z*-scores are combined to represent specific cognitive domains (Table 3). Subsequently, global cognitive functioning is calculated as an average *z*-score across all domains. In addition, a clinical dementia rating scale (CDR) is obtained[19] and depressive symptoms are assessed with the Center for Epidemiologic Studies Depression Scale (CES-D).[20] The main cognitive outcome will be a compound score of the *z*-scores for the domains attention and processing speed, and executive function.

TABLE 3. Neuropsychological tests and questionnaires in fixed order.

Neuropsychological tests	Cognitive function	Cognitive domain
Category fluency (animals, 60s)	Verbal fluency, semantic memory	Executive function
Boston naming test (short version)	Word naming	Language
MMSE	Cognitive screening	-
Word List Learning		
Immediate recall	Episodic memory	Memory
Delayed recall	Episodic memory	Memory
Delayed recognition	Episodic memory	Memory
Constructional praxis		
Copy	Visuoconstruction	Visuoconstruction
Delayed recall	Visuospatial memory, visuoconstruction	Memory
Trail making test		
Part A	Attention and psychomotor speed	Attention and processing speed

Part B	Executive function	Executive function
Phonemic fluency (letter S, 60s)	Verbal fluency, executive function	Executive function
Digit span		
Forward	Attention and information processing speed	Attention and processing speed
Backward	Working memory	Executive function

Questionnaires	Scope
Clinical Dementia Rating scale	Cognitive screening questionnaire
CES-D questionnaire	Depressive symptoms questionnaire

MMSE= Mini-Mental State Examination, CES-D= Center for Epidemiological Studies Depression Scale

3T brain MRI

3T brain MRI data are acquired on a Philips Achieva 3T scanner with an 8-channel SENSE head coil at UMCU (patients with sporadic SVD and controls) and on a Siemens Magnetom Skyra 3T scanner with a 64 channel head coil at the LMU (patients with CADASIL and controls). The scan protocol includes a 3D T1-weighted gradient echo, a 3D T2-weighted turbo spin echo, a 3D T2*-weighted gradient echo, and a 3D fluid-attenuated inversion recovery (FLAIR) scan. These sequences serve to assess conventional markers of SVDs and global brain volumes. In addition, the scan protocol includes diffusion imaging to measure white matter integrity. Table 4 summarizes all sequences and technical details for both sites.

SVD markers – i.e. lacunes, microbleeds and perivascular spaces - are visually rated on the 3T MRI scans by two trained raters according to the STRIVE criteria[3]. Differences between raters are resolved by consensus.

Volumetric measures are determined with established protocols at the individual study sites, to ensure that the data are analyzed with the best suiting software for the scanner systems and participant populations. At the UMCU, white matter hyperintensities (WMHs) are automatically segmented from T1-weighted and FLAIR images[21,22], manually checked and, if necessary, edited. Lacunes are manually segmented using intensity-based seed-growing in an in-house built tool in MeVisLab (MeVis Medical Solutions AG, Bremen, Germany). T1-weighted images and FLAIR images are automatically segmented with the Computational Anatomy Toolbox (CAT12 http://www.neuro.uni-jena.de/cat/) to generate tissue probability maps from which gray matter (GM), white matter (WM) and cerebrospinal fluid (CSF) volumes are approximated. GM and WM volumes are

TABLE 4. 3 tesla brain MRI protocol information

MR sequence	Acquired resolution mm^3	Time min:s	Parameters
Utrecht			
T1-weighted GE	1.0x1.0x1.0	05:39	FOV 256x232x192 mm^3; TR 8 ms; TI 955 ms; shot interval 2500 ms; flip angle 7°
T2-weighted TSE	0.7x0.7x0.7	07:37	FOV 250x250x190 mm^3; TR 2500 ms; TE 298 ms
T2*-weighted GE	0.8x0.8x0.8	02:22	FOV 230x192x144 mm^3; TR 69 ms; TE 29 ms; flip angle 23°
FLAIR	1.0x1.0x1.0	06:15	FOV 250x250x180 mm^3; TR 5000 ms; TE 253 ms; TI 1700 ms
Diffusion MRI	2.5x2.5x2.5	06:49	FOV 220x220x120 mm^3; TR 8185 ms; TE 73 ms; b-values 0 and 1200 s/mm^2; directions 45
BOLD rs-fMRI	2.9x2.9x3.5	05:00	FOV 200x235x146 mm^3; TR 2500 ms; 3 echos at TE 9.1, 25.3, and 41.4 ms [44]
Qflow	1.2x1.2x2.0	00:19	FOV 150x103 mm^2; TR 14 ms; TE 3.7 ms; flip angle 25°; Venc 100 cm/s
ASL	3.0x3.1x7.0	06:00	FOV 240x240x133 mm^3; pCASL; label duration 1800 ms; postlabeling delay 1800 ms; 40 dynamics
Munich			
T1-weighted GE	1.0x1.0x1.0	05:08	FOV 256x256x192 mm^3; TR 2500 ms; TE 4.37 ms; TI 1100 ms; flip angle 7°
T2-weighted TSE	0.9x0.9x0.9	03:42	FOV 263x350x350 mm^3; TR 3200 ms; TE 408 ms
T2*-weighted GE	0.9x0.9x2.0	05:56	FOV 230x160x187 mm^3; TR 35 ms; TE 5-30 ms; flip angle 15°
SWI	0.6x0.6x3.0	04:02	FOV 240x156x195 mm^3; TR 28 ms; TE 20 ms; flip angle 9°
FLAIR	1.0x1.0x1.0	06:27	FOV 250x250x176 mm^3; TR 5000 ms; TE 398 ms; TI 1800 ms
Diffusion MRI	2.0x2.0x2.0	07:47	FOV 240x150x240 mm^3; TR 3800 ms; TE 104.8 ms; b-values 0, 1000 and 2000 s/mm^2; 90 diffusion directions (30 for b=1000 s/mm2 and 60 for b=2000 s/mm2)

3 tesla brain MRI protocol. GE= gradient echo; TSE= turbo spin echo; FLAIR= Fluid attenuated inversion recovery; DTI= diffusion tensor imaging; BOLD= Blood oxygenation level-dependent; rs-fMRI= resting state functional magnetic resonance imaging; Qflow = quantitative flow; (pC) ASL= (pseudoContinuous) Arterial spin labeling; SWI= susceptibility weighted imaging; FOV= Field of view; TE= Echo Time; TI= Inversion Time; TR= Repetition Time.

normalized for intracranial volume. At the LMU, volumetric measures are assessed as previously published.[23] In short, WMHs are automatically segmented using a deep learning algorithm[24,25], manually checked, and edited when necessary. Lacunes are manually segmented using intensity-based seed-growing in a custom 3D editing tool in MATLAB (R2016b, The MathWorks, Natick, MA). Total intracranial and brain volumes are approximated from tissue probability maps calculated from the T1-weighted images, using SPM (v12; Wellcome Department of Cognitive Neurology, London, UK; http://www.fil.ion.ucl.ac.uk/spm). GM and WM volumes are normalized for intracranial volume.

7T brain MRI

All 7T brain MRI data are acquired on a Philips 7T scanner at the UMCU (Philips Healthcare, Best, The Netherlands) using a 32-channel receive head coil in combination with a quadrature transmit coil (Nova Medical, MA, USA). 7T MRI offers three main advantages over regular field strength imaging for studying small vessel function[26]: (1) higher signal to noise ratio allowing for high spatial and temporal resolution measurements, (2) higher sensitivity to the magnetic susceptibility effect of deoxyhemoglobin responsible for the blood oxygenation level-dependent (BOLD) MR contrast and (3) improved ability to discern the BOLD signal in the small vessels from that in larger draining veins.

In ZOOM@SVDs, we use three dedicated 7T protocols that can inform about small vessel function:

1. Blood flow velocity and flow pulsatility are assessed in perforating arteries in the basal ganglia and semioval centre with dedicated 2D phase-contrast velocity mapping.[27-29] These measures assess flow in the perforating arterie sin a 2D slice at the level of the basal ganglia and semioval centre. The measures are influences by the state of the perforating arteries, but also by up- and downstream flow regulation.
2. Small vessel reactivity in the visual cortex in response to a visual stimulus (i.e. neurovascular coupling) is assessed by means of the BOLD hemodynamic response. This is an ROI based measure in the visual cortex that assesses the parenchymal microvasculature. Neuronal activation triggers neurovascular coupling and induces vasodilation through the capillaries in the feeding pre-cappilary, parenchymal and penetrating arterioles to increase blood flow to the activated visual cortex[30].
3. Whole-brain small vessel reactivity (cerebrovascular reactivity) to a hypercapnic stimulus (i.e. breathing 6% CO_2 in air) is measured with the BOLD response. This is a

whole-brain measure from which more specific ROIs can be defined to assess the local parenchymal microvasculature. The hypercapnic stimulus causes relaxation of the vascular smooth muscle cells at the level of the arterioles, thereby causing direct small vessel vasodilation[31].

The three protocols are complementary as they assess different small vessel populations in different ROIs, either at rest or during stimulation with two different types of stimuli. The next three paragraphs describe the methods of these three 7T MRI protocols.

Blood flow velocity and pulsatility index in perforating arteries

Perforating artery flow data are acquired using two single-slice 2D phase-contrast acquisitions. Slices are placed at the level of the basal ganglia and the semioval centre using predefined anatomical landmarks.[27] A peripheral pulse unit is used for retrospective cardiac gating (Table 5 summarizes technical details). For post-processing, the ROI in the basal ganglia slice is manually delineated from the 2D phase-contrast magnitude image. The ROI in the semioval centre slice is generated using an automatically delineated 2D white matter mask from a T1-weighted scan. The outside border of this mask (80 pixels = 14 mm) is excluded to be robust to subject motion between the acquisition of the T1-weighted and the 2D phase-contrast scan, which could lead to unsolicited inclusion of cortical vessels located in sulci. In these ROIs, perforating artery detection is performed with a previously developed method which automatically excludes perforating arteries in ghosting artefacts in the semioval centre [32] and perforating arteries in the basal ganglia that are oriented non-perpendicularly to the scanning plane. Additionally, apparent perforating arteries that are located within a 1.2mm radius from each other are excluded, as these mostly are 'false detections' of larger and non-perpendicular vessels. Subsequently, the perforating artery flow is assessed per subject as in earlier work.[27,29,33] The protocol is summarized in Fig. 1.

Outcome measures, assessed separately for the basal ganglia and the semioval centre, are cerebral perforating artery density (number of perforating arteries/cm^2), mean blood flow velocity (the averaged mean velocity per subject in cm/s) and flow pulsatility index (PI). To determine PI, the perforating arteries' velocities over the cardiac cycle are first normalized and averaged. Then PI is calculated per subject as $(V_{max}-V_{min})V_{mean}$ where V_{max}, V_{min} and V_{mean} are the maximum, minimum and mean of the normalized and averaged blood flow velocity over the cardiac cycle.[27,28] For ZOOM@SVDs we consider PI

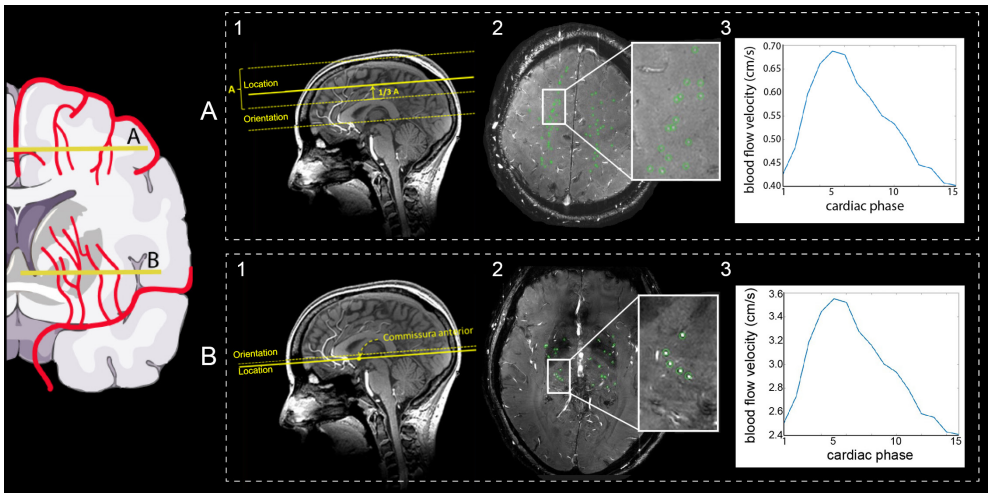

FIGURE 1. Overview figure of the single-slice 2D phase-contrast acquisitions. The schematic image on the left provides an impression of the perforating arteries that are assessed. Part A and B show examples of the (1) image acquisition, (2) 2D slice with the perforating arteries in green in the regions of interest, and (3) a blood flow velocity trace for the semioval centre (A) and the basal ganglia (B) respectively. From the blood flow velocity trace, an average blood flow velocity and flow pulsatility index are calculated.

TABLE 5. 7 tesla MRI protocol information

MR sequence	Acquired resolution mm^3	Time min:s	Parameters
T1-weighted	1.0x1.0x1.0	01:59	FOV 250x250x190 mm^3; TR 4.2 ms; TI 1297 ms; shot interval 3000 ms; flip angle 5°
2D-Qflow CSO	0.3x0.3x2.0	03:24*	FOV 230x230 mm^2; reconstructed resolution 0.18x0.18mm^2 ; TR 29 ms; TE 16 ms; Venc 4 cm/s
T1-weighted[a]	1.0x1.0x1.0	00:47	FOV 250x250x190; TR 4.1 ms; TI 1253 ms; shot interval 3000; flip angle 5°
2D-Qflow BG	0.3x0.3x2.0	03:47*	FOV 170x170 mm^2; reconstructed resolution 0.18x0.18mm^2 ;TR 28 ms; TE 15 ms; Venc 20 cm/s
2D-Qflow M1	0.5x0.5x3.0	01:47*	FOV 250x200 mm^2; TR 12 ms; TE 4.3 ms; Venc 100 cm/s
T2* whole brain	0.6x0.6x0.6	03:02	FOV 239x191x100 mm^3; TR 77 ms; TE 27 ms; flip angle 20°
T2* visual cortex	0.6x0.6x1.0	02:21	FOV 160x169x29 mm^3; TR 1250 ms; TE 16 ms; flip angle 40°

BOLD fMRI visual cortex[b]	1.3x1.3x1.3	10:05	FOV 140x140x11 mm^3; TR 880 ms; TE 25 ms
T1-weighted[a]	1.0x1.0x1.0	00:47	FOV 250x250x190 mm^3; TR 4.1 ms; TI 1253 ms; shot interval 3000; flip angle 5°
BOLD fMRI whole brain	2.0x2.0x2.0	10:00	FOV 224x256x101 mm^3; TR 3000 ms; TE 25 ms
BOLD fMRI whole-brain[c]	2.0x2.0x2.0	10:00	FOV 224x256x101 mm^3; TR 3000 ms; TE 25 ms

7 tesla brain MRI protocol in fixed order. CSO= Semioval Centre; BG= Basal Ganglia; M1= first segment of the middle cerebral artery; BOLD= Blood oxygenation level-dependent; fMRI= functional magnetic resonance imaging; FOV= Field of view; TE= Echo Time; TI= Inversion Time; TR= Repetition Time. * Total scan time for a heart rate of 80bpm.
a A fast version of the T1-weighted sequence was added multiple times to assess potential subject motion during the scan, particularly after repositioning for attaching the mask for the hypercapnic challenge.
b The participant is presented with a visual stimulus.
c The participant undergoes a hypercapnic challenge.

Small vessel reactivity to a visual stimulus

Participants are presented with a strong visual stimulus to activate the visual cortex, and the subsequent increase in oxygenated blood to the activated brain is measured through a BOLD contrast weighted sequence. By making a fit of the average hemodynamic response function (HRF) in response to the stimulus, we can study the amplitude, and timing of small vessel reactivity in the cortex.

BOLD MRI data are acquired in eight slices in the visual cortex during a 10-minute experiment (Table 5 summarizes technical details of the sequence). The visual stimulus is an 8Hz blue-yellow reversing checkerboard, presented with Presentation software (Presentation® version 18.1, Neurobehavioral Systems, Inc). The stimulus train compromises a block design part to determine the region of interest, and an event-related design part to derive the HRF[34]. The experiment starts with the event-related design which consists of a baseline period of 45.1 seconds (= 51 volumes), a trigger period of 413.6 seconds (= 470 volumes) and another baseline period of 59.8 seconds (= 68 volumes). During the baseline period, a black screen with two red dots is presented to serve as a fixation point. During the trigger period, a total of 51 stimuli of 500 ms each are presented (2x2 125 ms opposing checkerboard frames). The inter-stimulus interval range is 3.3-18.7 seconds, sampled from an exponential distribution, and uniform jittering of ¼*TR is applied (yielding a sub-TR temporal resolution of 220 ms)[34,35]. The block design consists of blocks of 16.72 seconds (=19 volumes) in which the fixation

screen and reversing checkerboard are alternated over three blocks (total of 100.32 seconds = 114 volumes). Within the ROI we disentangle signal from the small vessels and from larger draining veins based on signal properties: large draining veins have a low signal and high signal variability wherefore we can calculate a temporal noise-to-signal ratio per voxel and then apply a single fixed value threshold above which the voxel represents signal from a large vein. The protocol is visually summarized in Fig. 2A.

Outcome measures for the block design are ROI volume and BOLD amplitude. Outcome measures for the event-related design are four HRF characteristics: amplitude, full-width-at-half-maximum (FWHM), onset time and time-to-peak, separately for both the small vessels and the larger draining veins within the ROI. For ZOOM@SVDs we consider HRF amplitude and FWHM in the small vessels as primary outcome measures.

Small vessel reactivity to a hypercapnic stimulus

Whole-brain cerebrovascular reactivity was measured using BOLD contrast weighted MRI during a 10-minute experiment (Table 5 summarizes the sequence's technical details). The vasoactive stimulus is a hypercapnic challenge based on an earlier published protocol in SVDs[36]. In short, participants wear a face mask connected to a unidirectional breathing circuit. The participants breathe medical air and 6% CO_2 in air with a flow rate of 30L/min in alternating two-minute blocks: three two-minute blocks of medical air with two two-minute blocks of 6% CO_2 in air in between. Gasses are pre-mixed in medically graded cylinders (Linde Gas, The Netherlands). Monitoring equipment records pulse rate (sampling rate = 500Hz) and end-tidal CO_2 ($etCO_2$, 40Hz,; CD3-A AEI Technologies, Pittsburgh, USA). The protocol is visually summarized in Fig. 2B.

Outcome measures are the BOLD response amplitude in the cortical and subcortical GM, and total WM, NAWM and WMH. For ZOOM@SVDs, we consider the BOLD response amplitude in all these ROIs as primary outcome measures.

Follow up assessment

Two years after the baseline visit, all participants are invited for follow-up. During this visit, the clinical assessment, neuropsychological assessment (same test versions as at baseline) and 3T brain MRI scan are repeated (see Table 1 and respective sections above). If participants are not able to undergo a visit in the hospital, a short evaluation is performed via a telephone interview. If there is doubt about the reliability of the patient

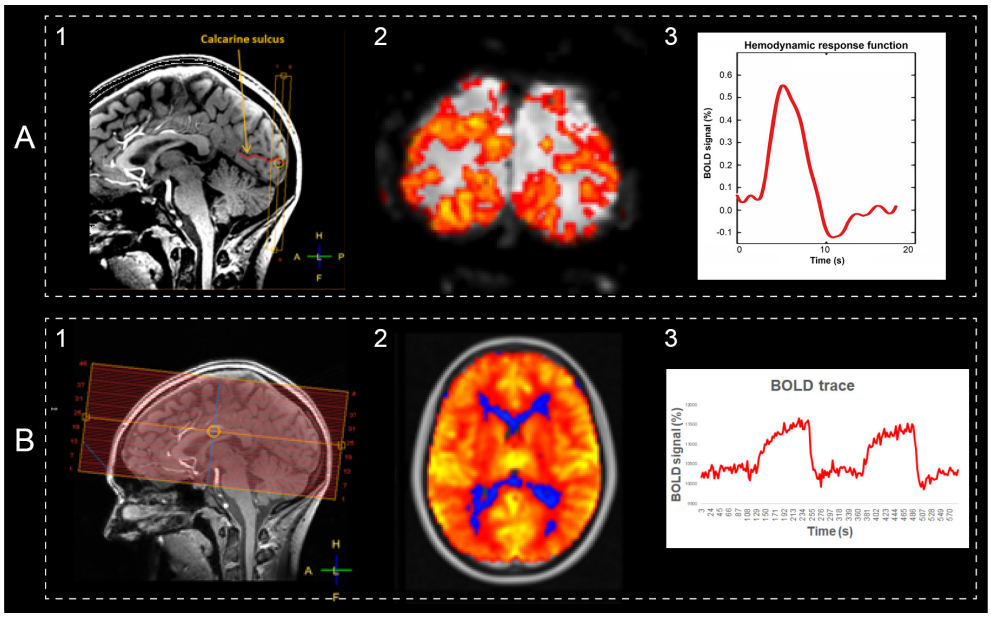

FIGURE 2. Overview figure of the BOLD acquisitions. Part A (visual stimulus) and B (hypercapnic stimulus) show examples of the (1) image acquisition, (2) voxelwise reactivity maps, and (3) BOLD signal curves over time for small vessel reactivity. For A, amplitude and full-width-at-half-maximum are extracted from the hemodynamic response function. For B, the average % of BOLD signal change to the hypercapnic stimulus is calculated, using the recorded etCO2 trace as the input model for analysis.

report because of cognitive problems, additional information is gathered from next of kin. Study participation finishes after the follow-up visit.

Sample size considerations

With a sample size of 60 patients with sporadic SVDs and 30 age and sex-matched controls, we can detect baseline abnormalities of small vessel function on continuous outcome measures with an effect size of 0.5 or more between groups with a power of 80% at a 5% significance level. At two-year follow-up, we expect that the dropout rate will not exceed 20%. This means that we can detect associations between baseline small vessel function and lesion progression or cognitive decline over two years if the determinant explains 16% or more variance with a power of 80% at a 5% significance level.

Regarding the 20 CADASIL patients with their 10 age and sex-matched controls, we can detect abnormalities of small vessel function with an effect size of 0.96 or more

between groups with a power of 80% at a 5% significance level. The average age of the CADASIL participants in the study is around 50 years. At this age, CADASIL patients already have marked manifestations of SVDs. In controls of this age, none or only very subtle manifestations of sporadic SVDs are to be expected. If CADASIL indeed manifests with abnormalities of small vessel function on 7T MRI, there should be substantial differences between the groups, for which the sample size should be sufficient.

Planned analyses

For the primary objective – to assess which aspects of small vessel function on 7T brain MRI are affected in patients versus controls –, cross-sectional analyses will be performed at baseline to compare patients with CADASIL or sporadic SVDs to their respective controls. Main outcome measures are compared between patients and controls with the appropriate parametric or non-parametric independent samples tests, adjusting for age and sex.

For the secondary objective – to assess how small vessel function relates to SVD disease severity at baseline and disease progression after two years –, analyses will primarily be performed within the patient groups. Measures of small vessel function will be related with baseline parenchymal SVD markers and cognitive functioning, and the progression of these indicators of disease severity at follow-up. Analyses will be performed with multiple regression and will be adjusted for age sex and vascular risk factors where approriate.

Timeline

The first participant was enrolled in March 2017. Participant enrolment for the CADASIL patients and their age and sex-matched controls was completed in July 2019. Enrolment for the patients with sporadic SVDs and controls is still ongoing. We expect to publish the first baseline results in 2021. Two-year follow-up visits are ongoing.

DISCUSSION

ZOOM@SVDs will provide novel functional biomarkers of SVDs at the level of the small vessels themselves. We will assess cerebral perforating artery flow, and vascular reactivity to a visual and a hypercapnic stimulus with 7T MRI in patients with hereditary (i.e. CADASIL) and sporadic SVDs and controls. The different protocols in ZOOM@SVDs capture complementary aspects of small vessel function; in different types of small

vessels, in different ROIs, both at rest and during stimulation with two different types of stimuli. We will determine which aspects of small vessel function are affected by SVDs and how this relates to disease severity and progression.

The small vessel functional measures in ZOOM@SVDs were chosen based on their relevance for SVDs and earlier research. We assess blood flow velocity and pulsatility index in perforating arteries in the basal ganglia and semioval centre. These perforating arteries are of particular interest given that, in SVDs, these are affected by arteriolosclerosis. We interpret pulsatility index as a measure of vascular stiffness, but the measure is also influenced by up- and downstream cerebral blood flow, pulse pressure and autoregulation. In earlier explorative work, we reported higher pulsatility in perforating arteries of patients with stroke attributable to SVD compared with controls, but similar blood flow velocity.[28] In ZOOM@SVDs, we will expand these observations in larger cohorts of highly phenotyped patients, including patients with CADASIL as a prototypic condition of pure and relatively severe SVD. In addition, we assess small vessel reactivity through neurovascular coupling in the visual cortex. Earlier studies with similar paradigms on 3T MRI have observed decreased vascular reactivity in response to a visual stimulus in patients with cerebral amyloid angiopathy (CAA).[37–41] In ZOOM@SVDs, we study CADASIL and sporadic SVDs that show largely subcortical lesions, but might have abnormal cortical small vessel reactivity as well. The strength of 7T MRI is that we will be able to carefully isolate the signal from the parenchyma, derived from changes in blood oxygen levels in the local capillaries and draining venules, in reponse to upstream arteriolar dilation. It is important to realize that, in order to represent neurovascular coupling and small vessel function, neuronal activation to the visual stimulus should be unaffected. We expect neuronal activation to be normal in CADASIL and sporadic SVD, as an earlier study reported normal cortical electrical potentials to a visual stimulus in patients with CADASIL and CAA.[39] Lastly, we assess small vessel reactivity with a hypercapnic stimulus that causes vasodilation in the arterioles.[31] Compared with the visual stimulus, the hypercapnic stimulus provides a whole-brain (rather than only cortical) measure of small vessel reactivity, that does not involve neurovascular coupling. Earlier studies used this paradigm on 3T MRI and observed that lower vascular reactivity was related to a higher burden of parenchymal SVD lesions in sporadic[42] and monogenic SVD.[43] In ZOOM@SVDs, we can capitalize on the high-resolution signal of 7T MRI to study local small vessel function, for example at the exact location of parenchymal lesions.

A strength of the ZOOM@SVDs study is that we will assess small vessel disease at its core, in the small vessels. By using three complementary measures across different brain regions we will be able to evaluate different aspects of small vessel function in different vessel subpopulations. By studying both monogenic and sporadic SVDs, we expect to find both shared and differential features of different forms of SVDs. Although downstream consequences of CADASIL and sporadic SVDs in the parenchyma show important similarities, there clearly are differences in the molecular and cellular pathways that affect the small vessels, likely with different signatures of vessel (dys) function. Moreover, in sporadic SVDs, vascular risk factors may differentially affect different vessel populations. Hypertension, for example, is known to most strongly affect the perforating arteries at the base of the brain, which are directly exposed to high pressure from the large arteries.[44] Finally, functional changes in different vessel populations may differentially affect the brain parenchyma. Therefore ZOOM@SVDs will also addess the interrelation between the nature of small vessel dysfunction and patterns of injury, also in longitudinal analyses. A limitation of ZOOM@SVDs is that, given the extensive protocol, there will likely be a relative overrepresentation of patients that are less affected (i.e. in earlier disease stages). Moreover, in order not to make the protocol too demanding, we prioritized detailed assessment of the primary parameters of interest. Consequently, some of the secondary clinical outcome measures are only assessed with screening tests with restricted sensitivity (e.g. assessment of motor performance and depression). Finally, 3T MRIs and their post-processing were performed at different centres for patients with CADASIL and sporadic SVDs. Importantly, the scans of the respective controls were always acquired on the same scanners as the patients. Although differences in scan acquisition and analysis may give rise to small differences in for example brain volume measurements, this should not impact the outcome of the study, because all primary analyses involving 3T parenchymal injury markers will be done within each patient group in comparison to their respective controls.

ZOOM@SVDs will characterize which small vessel function measures are affected in patients with CADASIL and sporadic SVDs compared with controls. Within the patient groups, we will establish which functional measures relate to disease severity (e.g. lesion burden and cognitive functioning). These markers could be well-suited to assist future etiological studies. In addition, the reversible nature of small vessel function makes the measures possibly potent outcome markers in intervention studies on candidate therapies that target the small vessels, thereby ultimately supporting the development of eagerly needed SVD treatment.

ACKNOWLEDGEMENTS

We would like to thank all participants who generously offer their time and energy for the purpose of this study. We acknowledge our colleagues at Diakonessenhuis for referring participants to the UMCU for study participation, and the help from Jenny Watchmaker and Annabel Groenenberg in initial steps of setting up processing pipelines for the BOLD hypercapnic stimulus data.

REFERENCES

1. Wardlaw, J. M., Smith, C. & Dichgans, M. Small vessel disease: mechanisms and clinical implications. Lancet Neurol. 18, 684–696 (2019).
2. Debette, S., Schilling, S., Duperron, M. G., Larsson, S. C. & Markus, H. S. Clinical Significance of Magnetic Resonance Imaging Markers of Vascular Brain Injury: A Systematic Review and Meta-analysis. JAMA Neurol. 76, 81–94 (2019).
3. Wardlaw, J. M. et al. Neuroimaging standards for research into small vessel disease and its contribution to ageing and neurodegeneration. Lancet Neurol. 12, 822–838 (2013).
4. Van Norden, A. G. W. et al. Diffusion tensor imaging and cognition in cerebral small vessel disease: The RUN DMC study. Biochim. Biophys. Acta - Mol. Basis Dis. 1822, 401–407 (2012).
5. Tuladhar, A. M. et al. White matter integrity in small vessel disease is related to cognition. NeuroImage Clin. 7, 518–524 (2015).
6. Baykara, E. et al. A Novel Imaging Marker for Small Vessel Disease Based on Skeletonization of White Matter Tracts and Diffusion Histograms. Ann. Neurol. 80, 581–592 (2016).
7. Duering, M. et al. Serum neurofilament light chain levels are related to small vessel disease burden. J. Stroke 20, 228–238 (2018).
8. Pantoni, L. Cerebral small vessel disease: from pathogenesis and clinical characteristics to therapeutic challenges. Lancet Neurol. 9, 689–701 (2010).
9. Dabertrand, F. et al. Potassium channelopathy-like defect underlies early-stage cerebrovascular dysfunction in a genetic model of small vessel disease. Proc. Natl. Acad. Sci. 112, E796–E805 (2015).
10. Joutel, A. et al. Cerebrovascular dysfunction and microcirculation rarefaction precede white matter lesions in a mouse genetic model of cerebral ischemic small vessel disease. J. Clin. Invest. 120, (2010).
11. Zwanenburg, J. J. M. & Van Osch, M. J. P. Targeting cerebral small vessel disease with MRI. Stroke 48, 3175–3182 (2017).
12. Pols, M. et al. Estimation of Reproducibility and Relative Validity of the Questions Included in the EPIC Physical Activity Questionnaire. Int. J. Epidemiol. 26, 181S – 189 (1997).
13. Guralnik, J. M. et al. A Short Physical Performance Battery Assessing Lower Extremity Function: Association With Self-Reported Disability and Prediction of Mortality and Nursing Home Admission. J. Gerontol. 49, M85–M94 (1994).

14. Ortiz, G. A. & Saaco, R. L. National Institues of Health Stroke Scale (NIHSS). in (2008).
15. Hamot, G., Ammerlaan, W., Mathay, C., Kofanova, O. & Betsou, F. Method Validation for Automated Isolation of Viable Peropheral Blood Mononuclear Cells. Biopreservation and Biobaking 13, 152–163 (2015).
16. Morris, J. C. et al. The Consortium to Establish a Eegistry for Alzheimer's Disease (CERAD). Part I. Clinical and Neuropsychological Assessment of Alzheimer's Disease. Neurology 39, 1159–1165 (1989).
17. Lezak, M. D., Howieson, D. B., Bigler, E. D. & Tranel, D. Neuropsychological Assessment. (NY: Oxford University Press, 2012).
18. Wechsler, D. Wechsler Adult Intelligence Scale-Fourth Edition. (Pearson, 2008).
19. Morris, J. C. The Clinical Dementia Rating (CDR): Current version and scoring rules. Neurology 43, 2412–2412 (1993).
20. Lewinsohn, P. M., Seeley, J. R., Roberts, R. E. & Allen, N. B. Center for Epidemiological Studies-Depression Scale (CES-D) as a screening instrument for depression among community-residing older adults. Psychol. Aging 12, 277–287 (1997).
21. Camarasa, R., Doué, C., de Bruijne, M. & Dubost, F. Segmentation of White Matter Hyperintensities with an Ensemble of Multi-Dimensional Convulational Gated Recurrent Units. (2018).
22. Kuijf, H. J. et al. Standardized Assessment of Automatic Segmentation of White Matter Hyperintensities and Results of the WMH Segmentation Challenge. IEEE Trans. Med. Imaging 38, 2556–2568 (2019).
23. Gesierich, B. et al. Alterations and test–retest reliability of functional connectivity network measures in cerebral small vessel disease. Hum. Brain Mapp. 41, 2629–2641 (2020).
24. Ronneberger, O., Fischer, P. & Brox, T. U-Net: Convolutional Networks for Biomedical Image Segmentation. in International Conference on Medical Image Computing and Computer-Assisted Intervention (2015).
25. Long, J., Shelhamer, E. & Darrell, T. Fully convolutional networks for semantic segmentation. in 2015 IEEE Conference onf Computer Vision and Patter Recognition (CVPR) (2015).
26. Siero, J. C. W., Bhogal, A. & Jansma, J. M. Blood oxygenation level-dependent/ Functional Magnetic Resonance Imaging: Underpinnings, Practice, and Perspectives. PET Clin. 8, 329–344 (2013).
27. Bouvy, W. H. et al. Assessment of blood flow velocity and pulsatility in cerebral perforating arteries with 7-T quantitative flow MRI. NMR Biomed. 29, 1295–1304 (2016).

28. Geurts, L. J., Luijten, P. R., Klijn, C. J. M., Zwanenburg, J. J. M. & Biessels, G. J. Higher Pulsatility in Cerebral Perforating Arteries in Patients With Small Vessel Disease Related Stroke, a 7T MRI Study. Stroke 50, 62–68 (2018).
29. Arts, T., Siero, J. C. W., Biessels, G. J. & Zwanenburg, J. J. M. Automated Assessment of Cerebral Arterial Perforator Function on 7T MRI. J. Magn. Reson. Imaging 53, 234–241 (2021).
30. Iadecola, C. The Neurovascular Unit Coming of Age: A Journey through Neurovascular Coupling in Health and Disease. Neuron 96, 17–42 (2017).
31. Ainslie, P. N. & Duffin, J. Integration of cerebrovascular CO2 reactivity and chemoreflex control of breathing: Mechanisms of regulation, measurement, and interpretation. Am. J. Physiol. - Regul. Integr. Comp. Physiol. 296, (2009).
32. Arts, T., Siero, J., Biessels, G. J. & Zwanenburg, J. Method for vessel selection effects the outcome and reproducibility of velocity and pulsatility measures in cerebral penetrating arteries. in Annual Meeting of the International Society of Magnetic Resonance #3264 (2019).
33. Geurts, L., Biessels, G. J., Luijten, P. & Zwanenburg, J. Better and faster velocity pulsatility assessment in cerebral white matter perforating arteries with 7T quantitative flow MRI through improved slice profile, acquisition scheme, and postprocessing. Magn. Reson. Med. 79, 1473–1482 (2018).
34. Siero, J. C., Petridou, N., Hoogduin, H., Luijten, P. R. & Ramsey, N. F. Cortical Depth-Dependent Temporal Dynamics of the BOLD Response in the Human Brain. J. Cereb. Blood Flow Metab. 31, 1999–2008 (2011).
35. Siero, J. C. W. et al. BOLD Specificity and Dynamics Evaluated in Humans at 7 T: Comparing Gradient-Echo and Spin-Echo Hemodynamic Responses. PLoS One 8, 1–8 (2013).
36. Thrippleton, M. J. et al. Cerebrovascular reactivity measurement in cerebral small vessel disease: Rationale and reproducibility of a protocol for MRI acquisition and image processing. Int. J. Stroke 13, 195–206 (2018).
37. Williams, R. J. et al. Identification of neurovascular changes associated with cerebral amyloid angiopathy from subject-specific hemodynamic response functions. J. Cereb. Blood Flow Metab. 0271678X1769105 (2017) doi:10.1177/0271678X17691056.
38. Dumas, A. et al. Functional MRI detection of vascular reactivity in cerebral amyloid angiopathy. Ann. Neurol. 72, 76–81 (2012).
39. Cheema, I. et al. Functional magnetic resonance imaging responses in CADASIL. J. Neurol. Sci. 375, 248–254 (2017).

40. Peca, S. et al. Neurovascular decoupling is associated with severity of cerebral amyloid angiopathy. Neurology 81, 1659–1665 (2013).
41. Opstal, A. M. Van et al. Cerebrovascular function in pre-symptomatic and symptomatic individuals with hereditary cerebral amyloid angiopathy: a case-control study. Lancet Neurol. 16, 115–122 (2017).
42. Blair, G. W. et al. Intracranial hemodynamic relationships in patients with cerebral small vessel disease. Neurology 94, e2258–e2269 (2020).
43. Moreton, F. C. et al. Vasoreactivity in CADASIL: Comparison to structural MRI and neuropsychology. J. Cereb. Blood Flow Metab. 38, 1085–1095 (2018).
44. Kundu, P., Inati, S. J., Evans, J. W., Luh, W. M. & Bandettini, P. A. Differentiating BOLD and non-BOLD signals in fMRI time series using multi-echo EPI. Neuroimage 60, 1759–1770 (2012).

Chapter 8

NOVEL 7T MARKERS OF SMALL VESSEL FUNCTION IN CADASIL

H. van den Brink*, T. Arts*, A. Kopczak*, L.P. Onkenhout, J.C.W. Siero, J.J.M. Zwanenburg, B. Gesierich, M. Duering, M.S. Stringer, J. Hendrikse, J.M. Wardlaw, M. Dichgans, G.J. Biessels. On behalf of the SVDs@target group.

*these authors contributed equally to this manuscript.

Manuscript in preparation for submission in JAMA Neurology

ABSTRACT

Background and purpose: Cerebral small vessel diseases (SVDs) are a major cause of stroke and dementia. To better understand underlying disease mechanisms, we need to study SVDs at their core, the small vessels. In this study we investigate cerebral small vessel function with 7T MRI in patients with Cerebral Autosomal Dominant Arteriopathy with Subcortical Infarcts and Leukoencephalopathy (CADASIL) and controls.

Methods: 23 patients with CADASIL and 13 age- and sex-matched controls were included and underwent clinical assessment, 3T brain MRI (for SVD lesions) and 7T brain MRI (for small vessel function). Primary focus was to investigate differences between patients and controls in small vessel function: (1) blood flow velocity and pulsatility in perforating arteries in the semioval centre and basal ganglia, (2) vascular reactivity in the visual cortex after visual stimulation, and (3) whole brain vascular reactivity to a hypercapnic stimulus. Secondary focus was to relate small vessel dysfunction with age and white matter hyperintensity volume in patients.

Results: Age and sex were similar for patients with CADASIL (age 51.1±10.1, 52% women) and controls (46.1±12.6, 46% women). Compared with controls, patients with CADASIL had decreased blood flow velocity in perforating arteries in the semioval centre (mean difference -0.09 cm/s, p=.03) and basal ganglia (mean difference -0.98 cm/s, p=.003), whereas pulsatility index was increased, both in the semioval centre (mean difference 0.19, p=.009) and basal ganglia (mean difference 0.17, p=.05). Compared with controls, small vessel reactivity to a visual stimulus in the visual cortex was decreased (BOLD mean difference -0.21%, p=.04) in patients, whereas reactivity to a hypercapnic stimulus was increased in the cortex (BOLD mean difference 0.42%, p=.05) and decreased in white matter hyperintensities (BOLD mean difference -0.13%, p=.04). Within the patient group, reactivity to hypercapnia in the cortex correlated with age (B -8.40, p=.02) and WMH volume (B -0.08, p=.03).

Conclusion: Abnormalities of small vessel function were observed in patients with CADASIL using multiple novel 7T MRI measures probing different vessel populations and different aspects of vascular physiology. These measures can be used to further explore disease mechanisms, also in sporadic SVDs.

INTRODUCTION

Cerebral small vessel diseases (SVDs) are a major cause of stroke and dementia[1]. SVD related lesions on brain MRI can be found in roughly 70% of 65-year-old individuals and in almost all 90-year-olds[2]. Despite the profound health impact of SVDs, specific treatment is lacking, which is likely attributable to our limited understanding of underlying disease mechanisms. Because of the small size of the arterioles, capillaries and venules where the disease originates, SVDs have thus far mostly been studied through markers of parenchymal injury (e.g. lacunes, white matter hyperintensities, microbleeds, enlarged perivascular spaces[3], microstructural white matter changes[4–6], blood based markers of neuro-axonal damage[7]). These markers are associated with important functional outcomes such as risk of stroke, cognitive decline and dementia. It is however important to realize that these lesions are a downstream consequence of SVDs. It is essential to also study SVDs at their core; at the level of the small vessels.

Cerebral Autosomal Dominant Arteriopathy with Subcortical Infarcts and Leukoencephalopathy (CADASIL) is a monogenic form of SVD, caused by a mutation in the *NOTCH3* gene for which changes in cerebral vessels have primarily been evaluated with autopsy studies[8,9]. Pathology in small penetrating cerebral and leptomeningeal arteries is an important feature, including degeneration of vascular smooth muscle cells and thickening of the arteriolar wall[8–10]. This likely impacts small vessel function, as has been observed in pial and parenchymal arteries in experimental animal models[11]. However, few previous studies have addressed such functional abnormalities in humans in vivo. High field imaging with 7T MRI now offers the possibility to zoom in on cerebral small vessel function[12,13].

Here we evaluate cerebral small vessel function in patients with CADASIL using 7T MRI. Specifically, we assess (1) which measures of small vessel function on 7T MRI are affected in patients with CADASIL relative to controls and (2) how small vessel dysfunction on 7T MRI relates with disease severity.

METHODS

Study design and participants

Participants in this study were recruited through the ZOOM@SVDs study, a prospective

observational cohort study[13]. The study, part of the SVDs@target collaborative program, is a collaboration between the Institute for Stroke and Dementia Research at Ludwig-Maximilians-Universität (LMU), Munich, Germany, and the University Medical Center Utrecht (UMCU) in the Netherlands. At LMU, a tertiary national referral centre for patients with CADASIL in Germany, 23 patients with CADASIL and 13 age- and sex-matched controls were recruited. CADASIL was either confirmed by mutation in the *NOTCH3* gene (n=21) or by skin biopsy (n=2). Controls were recruited among partners or relatives of the patients and through flyer advertisement. Participants underwent clinical assessment at the LMU and travelled to the UMCU to undergo 7T brain MRI. Detailed inclusion and exclusion criteria and study procedures are published in the protocol paper of ZOOM@SVDs[13].

The Medical Ethics Review Committees of the LMU and UMCU both approved the study. Written informed consent was obtained from all participants prior to enrolment in the study.

Clinical assessment

Demographics and vascular risk profile were recorded for all participants. Stroke, hypertension and diabetes mellitus were recorded based on presence in medical history. Current systolic and diastolic blood pressure were based on 7-day, three times daily, blood pressure measurements at home with a telemetric blood pressure device (Tel-O-Graph® GSM Plus, graded A/A by the British Hypertension Society). Smoking was based on self-report. Cognitive function was assessed with a standardized neuropsychological test battery which, among others, included tests for executive function and attention and processing speed[13].

3T brain MRI

Participants underwent 3T brain MRI at the LMU on a Siemens Magnetom Skyra 3T scanner with a 64 channel head coil. The scan protocol included a 3D T1-weighted gradient echo, a 3D T2*-weighted gradient echo, and a 3D fluid-attenuated inversion recovery (FLAIR) scan (sequence details see Supplemental table 1). Lacunes (on T1-weighted and FLAIR) and microbleeds (on T2*-weighted) were manually rated according to the STRIVE-criteria[14]. Volumetric measures and masks of white matter hyperintensities (WMH), lacunes, intracranial volume, total brain volume, white matter and grey matter were assessed as previously published[15].

7T brain MRI

Participants underwent 7T brain MRI at the UMCU on a Philips 7T scanner (Philips Healthcare, Best, The Netherlands) using a 32-channel receive head coil with a quadrature transmit coil (Nova Medical, MA, USA) (sequence details see Supplemental table 1). Three different measures of small vessel function were assessed:

1) Blood flow velocity and pulsatility were assessed in perforating arteries at the level of the basal ganglia (diameter 200-800µm) and semioval centre (100-300µm)[16–18] Flow data were acquired with two single-slice 2D-Qflow velocity mapping acquisitions, and a peripheral puls eunit was used for retrospective cardiac gating. From these data, mean blood flow velocity and pulsatility index in perforating arteries in the basal ganglia and semioval centre were calculated as main outcome variables.
2) Small vessel reactivity in response to a visual stimulus was assessed in the visual cortex with the blood oxygen level-dependent (BOLD) response. Participants were presented with a fixation screen alternated with very short (0.5s) and longer blocks (19s) of visual stimulation with a 8Hz blue-yellow reversing checkerboard, during a 10-minute experiment (for the detailed parameters of the stimulation protocol see13). Neuronal activation triggers neurovascular coupling and induces vasodilation through the capillaries in the feeding pre-capillary and parenchymal arterioles to increase blood flow to the activated cortex[19]. The increase in oxygenated blood was measured with BOLD contrast MRI that was acquired in the visual cortex. From these data, the region of interest (ROI) was determined based on the response to longer blocks of visual stimulation. Within that ROI, the average hemodynamic response function (HRF) in the visual cortex was fitted based on the short blocks of visual stimulations. BOLD % signal change and full-width-at-half-maximum of the HRF fit are considered main oucome variables.
3) Whole-brain small vessel reactivity to a hypercapnic stimulus was measured with the BOLD response. The participants wore a face mask to breath medical air and premixed 6% CO_2 in air in alternating blocks: three two-minute blocks of medical air with two two-minute blocks of 6% CO_2 in air in between. The hypercapnic stimulus causes relaxation of the vascular smooth muscle cells at the level of the arterioles, thereby causing direct small vessel vasodilation[20]. The increase in oxygenated blood to the arterioles is again measured with BOLD contrast MRI. Monitoring equipment recorded pulse rate and end-tidal CO_2 ($etCO_2$, 40Hz,; CD3-A AEI Technologies, Pittsburgh, USA) (for the detailed stimulation protocol see[21]). From these data, whole-brain cerebrovascular reactivity was assessed. The bold

% signal change in the cortical gray matter, the subcortical grey matter and white matter are considered main outcome measures.

These 7T MRI protocols assess different small vessel populations, in different ROIs, either at rest or during stimulation with two different types of stimuli. The detailed processing pipelines are described in the supplemental materials.

Statistics

Differences in characteristics between patients with CADASIL and controls were tested with an independent samples t-test for continuous normally distributed data, Mann-Whitney U test for non-parametric continuous data (i.e. WMH, lacunes and microbleeds) and chi-square for categorical data. Differences between patients and controls on the small vessel function measures were tested with ANCOVA, with a correction for age and sex. Pulsatility index was additionally corrected for mean blood flow velocity, and all BOLD hypercapnia comparisons were additionally corrected for change in $etCO_2$ in response to hypercapnia.

Within the patient group, mean blood flow velocity in the semioval centre (not in the basal ganglia, because of limited WMH volume) and BOLD % signal change to hypercapnia were compared in normal appearing white matter (NAWM) and WMH with a paired samples t-test. Pulsatility index in the semioval centre in NAWM versus WMH was tested with a repeated measures ANOVA, corrected for mean blood flow velocity. Also within the patient group we explored if small vessel function markers with a potential disease effect (defined as $p<0.1$) showed a relation with age and with WMH volume, as proxies of disease severity. This was tested with linear regression. We used the cube-root of the WMH volume, normalized to the intracranial volume. Given the collinearity of possible confounders (e.g. age, $etCO_2$) with the small vessel function measures, we did not correct these exploratory correlations.

All statistical analyses were performed in SPSS version 25 and $p<.05$ was considered significant.

RESULTS

The characteristics of the 23 patients with CADASIL and 13 controls are shown in Table 1. Age and sex were similar for patients (mean age 51.1±10.1, 52% women) and controls

(46.1±12.6, 46% women). As expected, patients significantly differed from controls on history of stroke and SVD lesion burden on 3T MRI. Supplemental Fig. 1 lists the number of scans included in the final analysis.

TABLE 1. Characteristics of patients with CADASIL and controls

	CADASIL n=23	Control n=13	*p*-value
Demographics			
Age, M±SD	51.1±10.1	46.1±12.6	0.20
Female sex, n (%)	12 (52)	6 (46)	1.00
Vascular risk profile			
Stroke, n (%)	7 (30)	0 (0)	**0.03**
Hypertension, n (%)	4 (17)	1 (8)	0.63
Current 7-day systolic BP, M±SD [mmHg]	118.4±10.1	120.9±10.2	0.48
Current 7-day diastolic BP, M±SD [mmHg]	76.0±8.9	79.0±10.6	0.37
Diabetes Mellitus, n (%)	1 (4)	1 (8)	0.67
Current/ever smoker, n (%)	15 (65)	6 (46)	0.31
3T MRI SVD markers			
WMH volume, median [IQR] [% of ICV]	4.5 [4.4]	0.01 [0.04]	**<0.001**
Lacune presence, n (%)	13 (57)	0 (0)	**0.001**
Lacune count[a], median [IQR]	4 [5]	0 [0]	
Microbleed presence, n (%)	13 (57)	0 (0)	**0.001**
Microbleed count[b], median [IQR]	3 [6]	0 [0]	
Brain volume, M±SD [% of ICV]	78.3±5.2	77.6±3.2	0.76

BP = blood pressure; M = mean; ICV = intracranial volume; IQR = interquartile range; SD = standard deviation; WMH = white matter hyperintensities;
[a] Count for participants with ≥ lacune(s).
[b] Count for participants with ≥ microbleed(s).

Small vessel function in patients with CADASIL and controls

Perforating artery density (i.e. number of perforating arteries per cm^2) was similar for patients and controls in the semioval centre (2.2±0.8/cm^2 and 2.2±1.0/cm^2 respectively, p=0.9) and the basal ganglia (0.9±0.3/cm^2 and 1.0±0.3/cm^2, p=0.5). Mean perforating artery blood flow velocity was lower (semioval centre p=.03; basal ganglia p=.003), and pulsatility index higher (semioval centre p=.009; basal ganglia p=.05) in patients with CADASIL than in controls (Table 2). Flow measures were also affected in the NAWM in patients compared to controls (velocity p=.05; pulsatility index p=.01; Supplemental Table 2). In patients, flow measures in the NAWM and WMHs of the semioval centre were similar (velocity p=.14; pulsatility index p=.12; Supplemental Table 3).

The fits of the average HRFs to the short visual stimulus in the visual cortex are shown in Fig. 1 for patients with CADASIL and controls. The BOLD % signal change was lower (p=.04) for patients than controls (Table 2). There was no difference in the timing of the response; the full width at half maximum (Table 2), onset time (CADASIL 2.1±0.5s versus controls 1.7±0.5s, p=0.07), and time to peak (CADASIL 4.6±1.0s versus controls 4.4±0.4s, p=0.5) were not significantly different between the groups. The size (i.e. number of activated voxels) of the participant-specific ROIs in which the HRFs were fitted were similar between patients and controls. The BOLD % signal change to the longer blocks of visual stimulation was also similar between groups (Supplemental Table 4).

The BOLD % signal change to the hypercapnic stimulus was higher (*p*=.05) in the cortical grey matter in patients than in controls, whereas there was no difference in the subcortical grey matter (Table 2). In contrast, in the total white matter, the BOLD response was lower (*p*=.04) in patients than in controls (Table 2). In patients, BOLD % signal change was lower (*p*=.002) in WMH than in NAWM (Supplemental table 3), with a paradoxical ***negative*** signal change to the hypercapnic stimulus within the WMHs. In the NAWM, BOLD % signal change was similar in patients and controls (Supplemental Table 2).

Small vessel dysfunction and disease severity in patients with CADASIL

For the 7T small vessel measures that differed between patients and controls, relations with disease severity were explored (Table 3, Supplemental table 5). Blood flow velocity in the semioval centre perforating arteries had a negative relation with WMH volume (*p*=.06), but not with age (Table 3; Fig. 2). Also, BOLD % signal change in the cortical grey matter showed a negative relation with both age (*p*=.02) and WMH volume (*p*=.03).

DISCUSSION

Cerebral small vessel function on 7T MRI proved to be abnormal in patients with CADASIL. Perforating artery flow and pulsatility, as well as reactivity to a visual or hypercapnic stimulus were different from controls. Moreover, among patients, cortical reactivity to a hypercapnic stimulus related with disease severity manifested in age and WMH volume.

Perforating artery flow has not been previously studied in patients with CADASIL, but increased pulsatility in perforating arteries has previously been reported in an

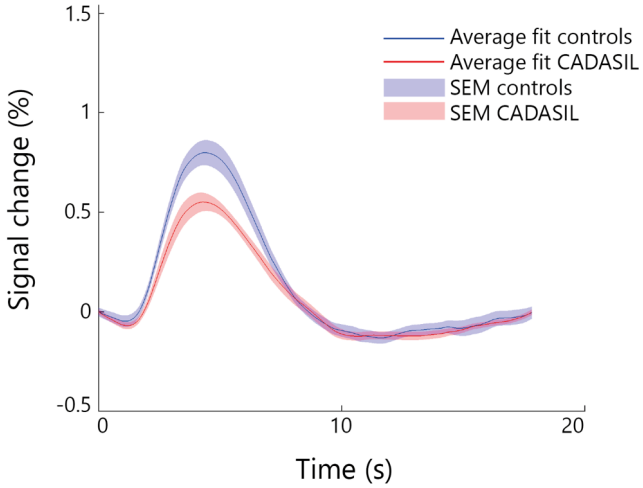

FIGURE 1. The average hemodynamic response function fit and standard errors of the mean (SEM) for patients with CADASIL and controls.

TABLE 2. Small vessel function on 7T MRI in patients with CADASIL and controls

	CADASIL	Control	*p*-value
2D-Qflow semioval centre[a]	n=22	n=10	
Blood flow velocity [cm/s]	0.54±0.06	0.63±0.13	**0.03**
Pulsatility index[b]	0.56±0.19	0.37±0.11	**0.009**
2D-Qflow basal ganglia[a]	n=21	n=9	
Blood flow velocity [cm/s]	3.07±0.67	4.05±0.83	**0.003**
Pulsatility index[b]	0.46±0.12	0.29±0.15	0.05
BOLD visual stimulus[c]	n=19	n=10	
BOLD % signal change	0.61±0.20	0.82±0.25	**0.04**
Full width at half max [s]	3.82±0.65	3.94±0.36	0.59
BOLD hypercapnic stimulus[d]	n=17	n=11	
CGM BOLD % signal change	2.18±0.72	1.76±0.62	0.05
SGM BOLD % signal change	2.38±0.77	2.40±0.90	0.96
WM BOLD % signal change	0.03±0.16	0.16±0.19	**0.04**

BOLD = blood oxygen level-dependent; CGM = cortical grey matter; SGM = subcortical grey matter; WM = white matter. Data are shown as mean ± standard deviation.

[a] The ROI is the entire semioval centre and basal ganglia excluding lacunes. Analyses are corrected for age and sex.

[b] Additional correction for blood flow velocity.

[c] Analyses corrected for age and sex.

[d] Analyses corrected for age, sex and change in end-tidal CO2 to hypercapnia.

exploratory study in patients with sporadic SVDs (i.e. with lacunar infarction or deep intracerebral haemorrhage).[17] In contrast to that previous study, we also observe decreased flow velocity in patients with CADASIL compared to controls, both in perforating arteries in the basal ganglia and semioval centre. Total blood flow in these perforating arteries is a product of flow velocity and arteriolar surface area. Surface area of individual perforating arteries cannot currently be measured with 7T MRI, because resolution is insufficient. Hence lower flow velocity may reflect preserved total blood flow with a larger surface area, and/or decreased total blood flow. The latter seems a more reasonable interpretation. With regard to the interpretation of increased blood flow pulsatility in patients with CADASIL, this may reflect changes in upstream vessels (generating a more pulsatile perfusion pressure), vascular stiffness in the perforating arteries themselves, and changes in the downstream vascular bed, including abnormal microvascular compliance. At autopsy, pathological vessel wall changes in CADASIL

TABLE 3. Relation of small vessel dysfunction with disease severity in CADASIL patients

	Age	WMH volume
2D-Qflow semioval centre[a]		
Blood flow velocity (cm/s)	B = -51.25 *p* = 0.15	B = -0.60 *p* = 0.06
Pulsatility index	B = -9.62 *p* = 0.42	B = -0.10 *p* = 0.36
2D-Qflow basal ganglia[a]		
Blood flow velocity (cm/s)	B = -1.44 *p* = 0.69	B = -0.04 *p* = 0.18
Pulsatility index	B = 26.23 *p* = 0.20	B = 0.16 *p* = 0.42
BOLD visual stimulus		
BOLD % signal change	B = -2.17 *p* = 0.87	B = -0.05 *p* = 0.62
BOLD hypercapnic stimulus		
CGM BOLD % signal change	**B = -8.40** ***p* = 0.02**	**B = -0.08** ***p* = 0.03**
WMH BOLD % signal change	B = -20.69 *p* = 0.19	B = 0.18 *p* = 0.23

BOLD = blood oxygen level-dependent; CGM = cortical grey matter; WMH = white matter hyperintensities

Tested with linear regression without corrections, and WMH volume was cube-root transformed and normalized for intracranial volume. Sensitivity analyses on non-transformed data, with Spearman correlations, produced similar results (data not shown).

[a] The ROI is the entire semioval centre and basal ganglia minus lacunes.

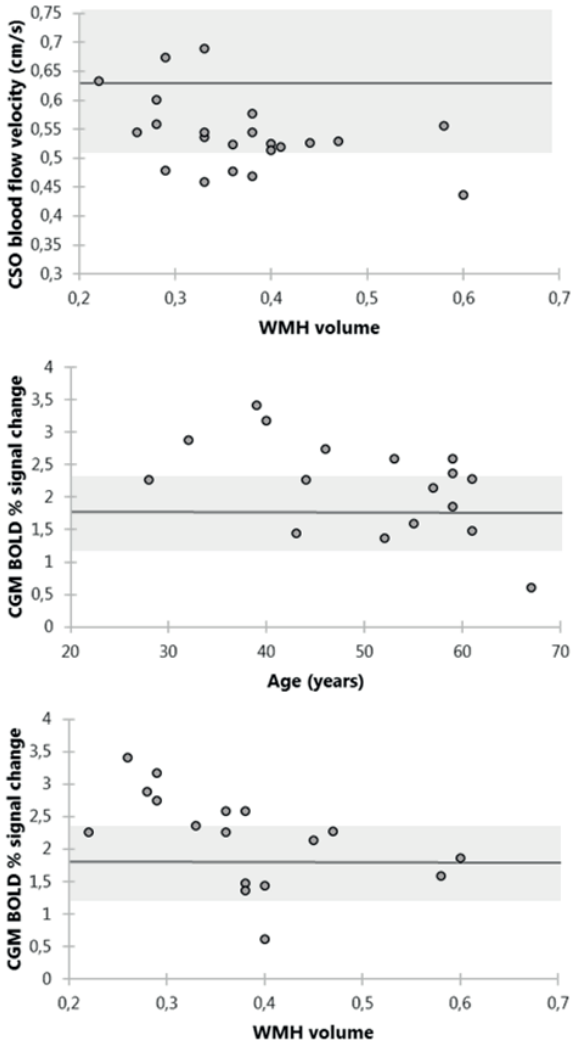

FIGURE 2. Negative relations of small vessel function measures with age and WMH volume in patients with CADASIL. This figure illustrates the three relevant relations from Table 4. As a reference, the average and standard deviations of the y-axis variables of the controls are added as a line with a shaded bar. WMH volume was cube-root transformed and normalized for intracranial volume.

have primarily been noted in arterioles, including narrowing due to intimal thickening and fibrosis and degeneration of smooth muscle cells, but vascular changes also

occur in capillaries and the venules.[22] Hence, although increased pulsatility could well reflect vascular stiffness of the perforating arteries that are probed with the 7T measurements, there could be alternative explanations. Of note, blood flow velocity and pulsatility index changes were similar in perforating arteries in NAWM and WMHs. Hence, the observed changes likely reflect generalized disease effects. Moreover, the 2D slices predominantly capture perforating arteries that are passing through the white matter at the site of measurement rather than arteries that specifically supply that part of the white matter. Importantly, despite the modest sample size of the study, we could demonstrate that blood flow velocity in the perforating arteries in the semioval centre seems to have a negative relation with WMH volume. This indicates that this measure may become progressively abnormal in patients as the disease evolves.

Small vessel reactivity was affected in patients with CADASIL compared with controls. In patients, reactivity to a very short visual stimulus in the visual cortex was lower than in controls, whereas reactivity to a hypercapnic stimulus in the cortex was higher. Moreover, while reactivity to hypercapnia in the NAWM was apparently unaffected in patients compared to controls, reactivity in WMHs was markedly disturbed, with a paradoxical flow ***decrease*** during hypercapnia. There are few previous studies on similar measures of small vessel reactivity in CADASIL, and they all use MRI with lower field strength. Two studies used hypercapnia and acetazolamide to induce reactivity responses and also reported reduced reactivity in WMHs compared with NAWM[23,24], while the one using acetazolamide reported no differences in reactivity in the cortex relative to controls.[24] In contrast to our findings with visual stimulation, a previous study found increased reactivity in the visual cortex in five patients with CADASIL compared with controls.[25] Stimulus duration may be a factor in these differential findings (previous study: 40s stimulation>increased response; our study: 19s>neutral response; 0,5s>decreased response). Fundamental differences in the nature and duration of the stimulus in our study may also explain the observed dissociation in the response to the short visual stimulus and the prolonged hypercapnic stimulus. Clearly, responses to these different stimuli involve different physiological pathways in different vessel populations. The BOLD signal to a short visual stimulus depends on activation of cortical neurons, which directly initiates a brief response of the local capillaries, so-called neurovascular coupling. By contrast, hypercapnia, as applied here, is a prolonged stimulus to the vasculature that is independent of neuronal activation and directly affects the smooth muscle cells in the arterioles throughout the brain.[20] Based on our

findings we could hypothesize that, in CADASIL, the vascular system seems unable to sufficiently respond to subtle and local demands in the cortex, whereas prolonged and global stimulation can still set vascular processes in motion, at least in the initial stages of the disease, resulting in a preserved response in the cortex. We could speculate that the increased response in the cortex to hypercapnia is a compensatory response, that fails with progression of disease, as suggested by the negative relation with age and WMH volume (Fig. 2). Moreover, vascular reactivity apparently fails, even with possible steal effects inducing a negative response in white matter areas that have been damaged as manifested in WMHs. Taken together, the findings of this study suggest that changes in small vessel reactivity in CADASIL have a dynamic nature, depending on the tissue type that is assessed, the type and extend of stimulation, and disease stage.

An important strength of this study is that small vessel function was assessed with three complementary measures, allowing to uncover dynamic small vessel functional changes. For this application 7T MRI not only provides higher spatial and temporal resolution, but the BOLD signal properties on 7T also permit separation of the signal in small vessels from that in larger draining veins.[26] A limitation of our study is possible selection bias that is inherent to the demanding protocol, which required travelling from Germany to the Netherlands for 7T brain MRI. Therefore, patients in this study are mostly in earlier disease stages, which limited the possibilities to study the relation of small vessel function with disease severity (e.g. cognition). On the other hand, the study shows that even in these early stages small vessel function changes are already apparent. A limitation of the use of the visual stimulus to induce reactivity is that, in order for the BOLD signal to represent vascular reactivity, neuronal activation to the visual stimulus should be unaffected, which was not tested. However, an earlier study confirmed that neuronal activation to a visual stimulus is similar in patients with CADASIL and controls.[25]

This study demonstrated abnormal small vessel function in patients with CADASIL compared with age- and sex-matched controls. We used multiple novel 7T MRI measures that probe different vessel populations and different aspects of vascular physiology, thereby unveiling dynamic small vessel function alterations in CADASIL. These alterations partly showed progressive abnormality with increasing disease severity. These findings help better understand CADASIL, but also serve as a model for the more prevalent sporadic SVDs, which we will study next.

REFERENCES

1. Wardlaw, J. M., Smith, C. & Dichgans, M. Small vessel disease: mechanisms and clinical implications. Lancet Neurol. 18, 684–696 (2019).
2. Debette, S., Schilling, S., Duperron, M. G., Larsson, S. C. & Markus, H. S. Clinical Significance of Magnetic Resonance Imaging Markers of Vascular Brain Injury: A Systematic Review and Meta-analysis. JAMA Neurol. 76, 81–94 (2019).
3. Wardlaw, J. M. et al. Neuroimaging standards for research into small vessel disease and its contribution to ageing and neurodegeneration. Lancet Neurol. 12, 822–838 (2013).
4. Van Norden, A. G. W. et al. Diffusion tensor imaging and cognition in cerebral small vessel disease: The RUN DMC study. Biochim. Biophys. Acta - Mol. Basis Dis. 1822, 401–407 (2012).
5. Tuladhar, A. M. et al. White matter integrity in small vessel disease is related to cognition. NeuroImage Clin. 7, 518–524 (2015).
6. Baykara, E. et al. A Novel Imaging Marker for Small Vessel Disease Based on Skeletonization of White Matter Tracts and Diffusion Histograms. Ann. Neurol. 80, 581–592 (2016).
7. Duering, M. et al. Serum neurofilament light chain levels are related to small vessel disease burden. J. Stroke 20, 228–238 (2018).
8. Chabriat, H., Joutel, A., Dichgans, M., Tournier-Lasserve, E. & Bousser, M. G. CADASIL. The Lancet Neurology vol. 8 643–653 (2009).
9. Di Donato, I. et al. Cerebral Autosomal Dominant Arteriopathy with Subcortical Infarcts and Leukoencephalopathy (CADASIL) as a model of small vessel disease: Update on clinical, diagnostic, and management aspects. BMC Med. 15, 1–12 (2017).
10. Hervé, D. & Chabriat, H. CADASIL. J. Geriatr. Psychiatry Neurol. 23, 269–276 (2010).
11. Joutel, A. et al. Cerebrovascular dysfunction and microcirculation rarefaction precede white matter lesions in a mouse genetic model of cerebral ischemic small vessel disease. J. Clin. Invest. 120, (2010).
12. Zwanenburg, J. J. M. & Van Osch, M. J. P. Targeting cerebral small vessel disease with MRI. Stroke 48, 3175–3182 (2017).
13. van den Brink, H. et al. Zooming in on cerebral small vessel function in small vessel diseases with 7T MRI: Rationale and design of the "ZOOM@SVDs" study. Cereb. Circ. - Cogn. Behav. 2, 1–9 (2021).
14. Gesierich, B. et al. Alterations and test–retest reliability of functional connectivity network measures in cerebral small vessel disease. Hum. Brain Mapp. 41, 2629–2641

(2020).
15. Bouvy, W. H. et al. Assessment of blood flow velocity and pulsatility in cerebral perforating arteries with 7-T quantitative flow MRI. NMR Biomed. 29, 1295–1304 (2016).
16. Geurts, L. J., Luijten, P. R., Klijn, C. J. M., Zwanenburg, J. J. M. & Biessels, G. J. Higher Pulsatility in Cerebral Perforating Arteries in Patients With Small Vessel Disease Related Stroke, a 7T MRI Study. Stroke 50, 62–68 (2018).
17. Arts, T., Siero, J. C. W., Biessels, G. J. & Zwanenburg, J. J. M. Automated Assessment of Cerebral Arterial Perforator Function on 7T MRI. J. Magn. Reson. Imaging 53, 234–241 (2021).
18. Iadecola, C. The Neurovascular Unit Coming of Age: A Journey through Neurovascular Coupling in Health and Disease. Neuron 96, 17–42 (2017).
19. Ainslie, P. N. & Duffin, J. Integration of cerebrovascular CO2 reactivity and chemoreflex control of breathing: Mechanisms of regulation, measurement, and interpretation. Am. J. Physiol. - Regul. Integr. Comp. Physiol. 296, (2009).
20. Thrippleton, M. J. et al. Cerebrovascular reactivity measurement in cerebral small vessel disease: Rationale and reproducibility of a protocol for MRI acquisition and image processing. Int. J. Stroke 13, 195–206 (2018).
21. Craggs, L. J. L., Yamamoto, Y., Deramecourt, V. & Kalaria, R. N. Microvascular pathology and morphometrics of sporadic and hereditary small vessel diseases of the brain. Brain Pathol. 24, 495–509 (2014).
22. Pfefferkorn, T. et al. Reduced Cerebrovascular CO2 reactivity in CADASIL: A Transcranial Doppler Sonography Study. 17–21 (2001).
23. Chabriat, H. et al. Cerebral hemodynamics in CADASIL before and after acetazolamide challenge assessed with MRI bolus tracking. Stroke 31, 1904–1912 (2000).
24. Cheema, I. et al. Functional magnetic resonance imaging responses in CADASIL. J. Neurol. Sci. 375, 248–254 (2017).
25. Siero, J. C. W., Bhogal, A. & Jansma, J. M. Blood oxygenation level-dependent/ Functional Magnetic Resonance Imaging: Underpinnings, Practice, and Perspectives. PET Clin. 8, 329–344 (2013).

Supplements

Supplemental Tables and Figures

SUPPLEMENTAL TABLE 1. Brain MRI scan parameters

MR sequence	Acquired resolution ($mm^{3)}$	Time (min:s)	Parameters
3T MRI			
T1-weighted GE	1.0x1.0x1.0	05:08	FOV 256x256x192 mm^3; TR 2500 ms; TE 4.37 ms; TI 1100 ms; flip angle 7°
T2*-weighted GE	0.9x0.9x2.0	05:56	FOV 230x160x187 mm^3; TR 35 ms; TE 5-30 ms; flip angle 15°
FLAIR	1.0x1.0x1.0	06:27	FOV 250x250x176 mm^3; TR 5000 ms; TE 398 ms; TI 1800 ms
7T MRI			
T1-weighted	1.0x1.0x1.0	01:59	FOV 250x250x190 mm^3; TR 4.2 ms; TI 1297 ms; shot interval 3000 ms; flip angle 5°
2D-Qflow CSO	0.3x0.3x2.0	03:24*	FOV 230x230 mm^2; reconstructed resolution 0.18x0.18mm^2 ; TR 29 ms; TE 16 ms; Venc 4 cm/s
2D-Qflow BG	0.3x0.3x2.0	03:47*	FOV 170x170 mm^2; reconstructed resolution 0.18x0.18mm^2 ;TR 28 ms; TE 15 ms; Venc 20 cm/s
BOLD fMRI visual cortex[a]	1.3x1.3x1.3	10:05	FOV 140x140x11 mm^3; TR 880 ms; TE 25 ms
BOLD fMRI whole-brain[b]	2.0x2.0x2.0	10:00	FOV 224x256x101 mm^3; TR 3000 ms; TE 25 ms

BG = basal ganglia; BOLD = Blood oxygen level-dependent; CSO = semioval centre; fMRI = functional MRI; FOV = field of view; TE = echo time; TI = inversion time; TR = repetition time.
* Total scan time for a heart rate of 80 bpm.
[a] The participant is presented with a visual stimulus.
[b] The participant undergoes a hypercapnic challenge.

SUPPLEMENTAL TABLE 2. Small vessel function in NAWM in patients with CADASIL versus controls

	NAWM CADASIL	NAWM Control	*p*-value
2D-Qflow semioval centre[a]	n=22	n=10	
Blood flow velocity (cm/s)	0.55±0.07	0.63±0.13	0.05
Pulsatility index[b]	0.62±0.24	0.37±0.11	0.01
BOLD hypercapnic stimulus[c]	n=17	n=11	
BOLD % signal change	0.13±0.29	0.16±0.19	0.41

BOLD = blood oxygen level -dependent; NAWM = normal appearing white matter; Data are shown as mean ± standard deviation.
[a] Lacunes were excluded from the ROI. Analyses are corrected for age and sex.
[b] Additional correction for blood flow velocity.
[c] Analysis corrected for age, sex and change in end-tidal CO_2 to hypercapnia.

SUPPLEMENTAL TABLE 3. Small vessel function in NAWM versus WMH in patients with CADASIL

	NAWM	WMH	*p*-value
2D-Qflow semioval centre[a] (n=15)			
Blood flow velocity [cm/s]	0.53±0.06	0.48±0.14	0.14
Pulsatility index[b]	0.60±0.28	0.85±0.45	0.12
BOLD hypercapnic stimulus[c] (n=17)			
BOLD % signal change	0.13±0.29	-0.11±0.18	0.002

BOLD = blood oxygen level-dependent; NAWM = normal appearing white matter; WMH = white matter hyperintensities. Data are shown as mean ± standard deviation.
[a] Lacunes were excluded from the ROIs. 84.6% of total white matter in 2D slice was NAWM and 15.4% were WMHs. NB: n=15 (not 22) because for 7 of the patients, no perforating arteries were detected within WMHs.
[b] Analysis corrected for blood flow velocity.
[c] 64.6% of total white matter was NAWM and 35.4% were WMHs

SUPPLEMENTAL TABLE 4. Activation to the block design visual stimulus in patients with CADASIL and controls

	CADASIL n=19	Control n=10	*p*-value
Activated voxels[a] [%]	32.7±13.3	30.4±12.7	0.67
BOLD % signal change	3.6±1.0	3.6±0.8	0.82

Data are shown as mean ± standard deviation.
[a] Calculated as number of activated voxels divided by the number of voxels in the scanning plane.

SUPPLEMENTAL TABLE 5. Relation of small vessel dysfunction with lacunes and cognition in patients with CADASIL

	Lacunes	Cognition[b]
2D-Qflow semioval centre[a]		
Blood flow velocity (cm/s)	r_s = -0.20 *p* = 0.38	r_s = -0.28 *p* = 0.22
Pulsatility index	r_s = 0.00 *p* = 1.00	r_s = 0.21 *p* = 0.35
2D-Qflow basal ganglia[a]		
Blood flow velocity (cm/s)	r_s = -0.01 p = 0.96	r_s = 0.35 *p* = 0.13
Pulsatility index	r_s = 0.21 *p* = 0.36	r_s = -0.08 *p* = 0.75
BOLD visual stimulus		
BOLD % signal change	**r_s = -0.47** ***p* = 0.04**	r_s = -0.29 *p* = 0.25
BOLD hypercapnic stimulus		
CGM BOLD % signal change	r_s = -0.37 *p* = 0.15	r_s = -0.24 *p* = 0.37
WMH BOLD % signal change	r_s = 0.19 *p* = 0.46	r_s = 0.10 *p* = 0.70

BOLD = blood oxygen level-dependent; CGM = cortical grey matter; WMH = white matter hyperintensities.

[a] The ROI is the entire semioval centre and basal ganglia minus lacunes.

[b] Compound score of executive function and attention and processing speed. All participants underwent a standardized neuropsychological test battery (full test battery reported in13) Individual test scores were standardized into z-scores using the control group as a reference. Test z-scores were then combined to represent specific cognitive domains. The executive function domain is composed of z-scores on category fluency, phonemic fluency, trail making test part B/A, and digit span backward. The attention and processing speed domain is composed of z-scores on TMT A and digit span forward. A compound score was calculated as the average of the two domain z-scores[13].

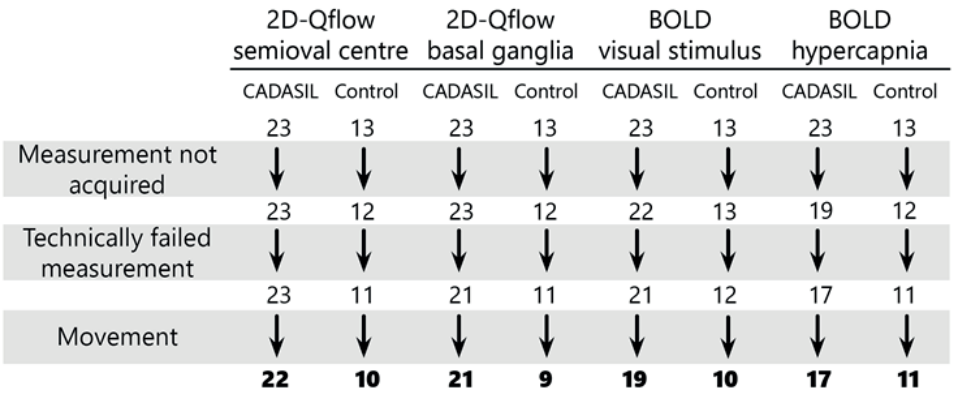

SUPPLEMENTAL FIGURE 1. Flowchart showing reasons for excluded scans per small vessel function measurement. Reasons for not acquired measurement are: technical failure on the scanner for the 2D-Qflow scans, glasses that would not fit in the head coil for the BOLD visual stimulus scan, and participants unwilling or unable to do the hypercapnia challenge after first trying it outside the scanner for the BOLD hypercapnia scan.

Processing pipelines for the three 7T measures that assess small vessel function

Blood flow velocity and pulsatility index in perforating arteries

To calculate mean blood flow velocity and pulsatility index in the perforating arteries in the basal ganglia and semioval centre, the post processing pipeline of the 2D-Qflow scans involved: (1) generating regions of interest (ROI) in the basal ganglia and semioval centre, (2) detecting individual perforating arteries, and (3) calculating mean blood flow velocity and pulsatility index from the flow data.

The ROI in the basal ganglia slice was manually delineated in the 2D-Qflow magnitude image. The ROI in the semioval centre was generated using an automatically delineated 2D white matter (WM) mask from a T1-weighted scan. The outside border of this mask (80 pixels = 14 mm) was excluded to be robust to small participant motion between the acquisition of the T1-weighted and the 2D-Qflow scan, which could lead to unsolicited inclusion of cortical vessels located in sulci. Separate ROIs were also generated for white matter hyperintensities (WMHs) (based on 3T WMH masks) and normal appearing white matter (NAWM) in the semioval centre. Lastly, lacunes were excluded from all ROIs, because no perforating arteries are expected in a cavity.

In the ROIs, perforating artery detection was performed with a previously developed method which automatically excludes perforating arteries in ghosting artefacts in the

semioval centre, and perforating arteries in the basal ganglia that are oriented non-perpendicularly to the scanning plane[16]. Additionally, apparent perforating arteries that are located within a 1.2 mm radius from each other were excluded, as these mostly are 'false detections' of larger and non-perpendicular vessels.

Cerebral perforating artery density was calculated (number of perforating arteries/cm^2). Perforating artery flow was then assessed per participant as in earlier work[14,16,19]. The blood flow velocity over the cardiac cycle was averaged per participant to calculate mean blood flow velocity in cm/s per participant. To calculate flow pulsatility index (PI), the velocities over the cardiac cycle were first normalized and averaged. PI was then calculated per participant as

$$PI = (V_{max} - V_{min})/V_{mean}$$

where V_{max}, V_{min} and V_{mean} are the maximum, minimum and mean of the normalized and averaged blood flow velocity over the cardiac cycle[14,15]. Mean blood flow velocity and pulsatility index are considered the primary outcome measures.

Small vessel reactivity to a visual stimulus

The visual stimulus experiment that was used to stimulate the visual cortex and induce an increase in BOLD signal compromised two parts. Block design stimulation was used to determine the region of interest (i.e. the voxels in the scanning plane that activate in response to the visual stimulus), and event-related design stimulation was used to make a fit of the average HRF in response to the visual stimulus in the participant-specific ROI. The BOLD MRI data that was acquired during the experiment was processed according to the following steps: (1) data cleaning, (2) generating a participant-specific ROI in the visual cortex based on BOLD MRI data from the block design, and (3) fitting an average HRF per participant based on BOLD MRI data acquired during the event-related design in the ROI.

Raw BOLD MRI data were motion corrected with the '2Dimreg' function of AFNI[20]. Data were spatially smoothed using a 2-mm full-width-at-half-maximum (FWHM) Gaussian kernel, and independent component analysis was performed with the MELODIC tool in FMRIB Software Library FSL (version 6.0., Oxford, UK)[21]. A maximum of 60 data components were computed and manually rated as signal or noise to delete noise components[22]. The dataset was then cut to create a separate dataset for the event-related and the block design parts, 589 and 129 volumes respectively (note 34 baseline volumes between the event-related and the block design parts were included in both

the event-related and block design datasets).

Generation of the participant-specific ROI was based on the block design data. Data were temporally filtered to remove slow signal drifts using a high-pass temporal filter with a cut-off at 1/100Hz. Cluster analysis was then performed using a time-series GLM approach as implemented in FEAT of FSL. The GLM included several regressors; the regressor of interest was the time-series model consisting of the task design convolved with a gamma hemodynamic response function. A temporal derivative regressor was added to correct for slice timing differences, and additional regressors for outlier time points (as detected with FSL Motion Outliers with standard settings) were added to remove the effects of outliers from the analysis. Estimates of brain activity magnitude in response to the stimulus were computed and converted to a z-statistic. The z-statistic images were non-parametrically thresholded using clusters determined by z>3.1 and a (corrected) cluster significance threshold of p=.05. The significantly activated clusters defined the starting point of the ROI. From this ROI, large vessels were removed in order for the ROI to represent the activated voxels in the parenchyma and be most specific to small vessel reactivity. On 7T MRI, large vessels have a low BOLD signal and high BOLD signal variability wherefore we could calculate a temporal noise-to-signal ratio per voxel and then apply a single fixed value threshold (of 3) above which the voxel represented signal from a large vessel.

Estimation of the HRF was performed with the event-related dataset, as in earlier published work[23]. In short, the fitting was done by means of conjugate gradients for deconvolution, after normalization of the voxel's signal time-series by the baseline signal (mean of the first 45 volumes) and 8-fold Fourier interpolation (images were acquired every 880 ms, thus yielding an effective temporal HRF resolution of 110 ms). This level of interpolation was chosen for the purpose of slice-timing correction, and thus equal to the number of slices (=8). Slice-timing correction was performed simultaneously with the HRF estimation by shifting the stimuli model for each slice according to the slice acquisition time. BOLD % signal change (i.e. maximum amplitude), full-width-at-half-maximum, time-to-peak, and onset time were calculated from the HRFs. Onset time was defined by the fit of a line to the slope between 20% and 80% of the peak of the HRF and computing the intercept with the baseline[24]. BOLD % signal change and full-width-at-half-maximum of the HRF fit are considered main outcome variables.

Small vessel reactivity to a hypercapnic stimulus

To determine cerebrovascular reactivity to a hypercapnic stimulus, the acquired BOLD

MRI data post-processing pipeline involved: (1) delineation of ROIs for cortical grey matter (GM), subcortical GM and WM (including separate masks for WMH and NAWM), and (2) a voxel-based analysis to calculate the amplitude of the reactivity response.
Several masks were used in order to make the ROIs. The WM and GM probability masks and the delineations of WMHs and lacunes were taken from the 3T images. Lacunes were dilated with a 2D 3mm kernel to include surrounding pathology. Lacunes and WMHs together constitute the lesion mask. With these masks, the ROIs were calculated. First, the subcortical GM ROI was defined using the FIRST tool in FSL[25] and consists of the thalamus, caudaute head and putamen. The lesion mask was subtracted from this subcortical GM ROI, the ROI was eroded with a cubic kernel of 3 voxels and binarized. The cortical GM ROI was defined by subtracting the subcortical GM and large vessels from the GM probability mask, thresholding the result at 0.5 and binarizing. The NAWM ROI was derived by subtraction of the lesions and large vessels from the WM probability mask, thresholding at 0.9 and binarizing. Large vessels were excluded from the WMH mask to obtain the WMH ROI. The WM ROI is a combination of both the NAWM and WMH ROI. Lastly, all ROIs are multiplied with a binary brain mask, and the pons and cerebellum were removed from all ROIs. The ROIs were registered from 3T space to 7T BOLD space to be able to obtain the regional BOLD response amplitudes.
To obtain BOLD % signal change to the hypercapnic stimulus, BOLD data were processed with FSL. The data were motion-corrected using FSL MCFLIRT[26] and smoothed (FWHM Gaussian = 3 mm), after which ICA-AROMA was applied (using the 'non-aggressive' setting) to identify and remove motion-related components from the data[27]. In addition, FSL Motion Outliers (with standard settings) was used to identify time points in the data that showed large motion, and slice time correction was performed. Using a general linear model in FSL FEAT, each participant's BOLD signal was regressed with the participant's $etCO_2$ trace (the envelope of the subject-specific $etCO_2$, derived and normalized between 0 and 1 using Matlab (R2020a, Mathworks, Natick, MA)), as well as the BOLD scan number (to account for linear signal drift), and the outlier time points added as confounders. This yielded a map of the response amplitude expressed as a percentage change in BOLD in response to the stimulus. Finally, we overlaid the ROIs on this map and performed voxel-wise averaging to obtain the ROI specific BOLD % signal change. The BOLD % signal change in the cortical GM, subcortical GM and WM ROIs are considered main outcome measures.

Chapter 9

SUMMARY, DISCUSSION, AND FUTURE PERSPECTIVES

Investigating the functioning of the cerebral small vessels is important, because these vessels play an essential role in the cerebral blood supply. In case of diseased cerebral small vessels there is high risk of stroke and dementia. However, as described in the introduction of this thesis, the cerebral perforating arteries could until recently not be investigated in-vivo in humans due to their small size. Nowadays, with 7 tesla (T) MRI, we have the ability to study the hemodynamics and functioning of the cerebral microvasculature.[1-3]

The overall goal of this thesis was to make the existing cerebral perforating artery flow measures more reliable and increase the applicability of these metrics. In addition, we aimed to apply these and other measures of microvascular function in cohort studies to explore factors relevant for small vessel functioning in healthy controls and patients. This chapter provides a summary and general discussion of all studies presented in this thesis. Also, future perspectives and challenges are discussed.

Part I: What else is in there?

Making small perforating artery detection more reliable and employable

To gain more knowledge of the cerebral small vessels it is important to be able to study the functioning of the small vessels in-vivo. This is currently achieved using a 2D phase contrast (PC) sequence on 7T MRI, after which perforating arteries are automatically detected and flow velocity and pulsatility can be measured.[2,4] These measurements are particularly valuable in elderly cohorts, since they are susceptible to small vessel hemodynamic changes. However, it is known that subject movement during scanning is more frequent in elderly patients compared to the young and healthy, resulting in more motion related ghosting artifacts in the 2D PC scans. This requires manual exclusion of the false positive perforating artery detections (i.e. the perforating arteries located in the artifacts), which is a subjective and time-consuming undertaking. Also, the availability of 7T MRI scanners is nowhere near that of 3T MRI scanners, limiting the use of 2D PC imaging for small vessel flow assessment. Therefore, it would be of great value if perforating arteries located in ghosting artifacts could be dealt with in an automated manner and if perforating artery blood flow velocity and pulsatility could also be measured on 3T MRI and. In this part of the thesis we looked to increase the potential of our perforating artery imaging and detection method by questioning "What else is in there?"

Subject motion during scanning mainly impacts the 2D PC MRI scans in the semi-oval centre (CSO), and results in ghosting artifacts, subsequently leading to false-positive vessel detection. These false positives make the subject's small vessel velocity and pulsatility measures less accurate. Our first attempt to exclude false positive-vessel detections focused on the velocity traces of the individual perforating arteries themselves to determine what constitutes a true positive and a false positive. However, defining what velocity trace appears as true and which does not, is not highly straightforward. The false-positive detections are mostly weak signals of large cerebral pulsating vessels, which makes the velocity trace appear as an actual small vessel trace. In addition, the individual velocity traces are relatively noisy, which creates a large 'gray area' between a true and false velocity trace. Hence, the approach presented in **Chapter 2** was based on the spatial location of the detection to allocate it as a true or false perforating artery. We showed that this exclusion method, based on the perforating arteries' spatial locations, has equal repeatability for blood flow velocity and improved repeatability for the pulsatility and the number of included perforating arteries compared to manual censoring. Also, good agreement is found between both methods. This automated method is not only more robust and objective than the previously used manual selection method, it also saves the user a substantial amount of time. However, besides ghosting, other artifacts can result from subject movement, and in case of severe subject motion scan quality is so poor that exclusion of the data cannot be avoided. Therefore, time and effort can be invested in either prevention or correction of subject motion. Motion prevention may be achieved during scanning by using a mouthpiece, though, motion is most common in the elderly[5,6] and elderly people (with potential cognitive decline) might be less willing to use it. So, alternatively, motion correction in k-space after data acquisition may be of help, with the use of equipment which records subject movement during scanning with either video, tactile sensors or magnetic field sensors.[7-9] A disadvantage of this method is that is makes data reconstruction more complicated due to the k-space corrections, disabling use of a fast fourier transformation. Finally, to shorten the scan time to acquire 2D PC images and reduce subject motion during scanning, compressed sensing can be used, which allows accurate data reconstruction with sparsely sampled k-space data.[10] With less k-space data to acquire, less time is required to fill k-space. Finally, some perforating arteries, particularly those in the deep gray matter of the basal ganglia (BG) have a relatively high level of tortuosity. This means that part of the vessels will not run perpendicularly to the 2D PC scanning plane, resulting in inaccurate flow measures. In

this thesis we tackled this issue by taking the perforating artery voxel and assessing the shape of the collection of surrounding high-intensity voxels. If the ratio of the smallest axis length to largest axis length of this shape was less than a set threshold, the shape was determined to be elliptical and the small perforating artery was excluded. Although most non-perpendicular perforating arteries were excluded with this method, a more refined option would be to scan multiple slices. An equal perforating artery location on all acquired slices then indicates a perpendicular vessel orientation. Future research could explore the implementation of multiband imaging for the 2D PC sequence at 7T MRI.[11] Research than particularly concerns the reduction of inflow effects. Scanning two CSO slices with a sufficient gap, followed by two BG slices would reduce inflow, but reduces the ability for vessel-to-vessel matching. Another option is to simultaneously image one CSO slice and one BG slice, and to repeat this for two adjacent slices. However, given the different flow velocities ranges in the CSO and BG, a multi-venc approach (or comparable) would have to adhered.

In **Chapter 3** we aimed to make the 2D PC sequence more widely employable, and investigated the ability to measure cerebral small vessel flow at 3T MRI in the BG. The agreement between the perforating artery measures of both scanning modalities, i.e. blood flow velocity and pulsatility, was investigated. Although results of this comparison showed little to no agreement of the flow measures between the two scanning modalities, 3T MRI did enable us to measure flow in the cerebral perforating arteries. Differences between 3T and 7T MRI were not unexpected and could be explained by the fact that both field strengths can measure only the proverbial tip of the iceberg of the perforating arteries, resulting in scanner-dependent biases. In addition, differences in the 2D slice planning impacted scanner modality agreement. This demonstrated the importance of using equal scanning protocols and field strengths, as well as a stringent planning protocol within future clinical studies. The scanner dependent biases also result in the detection of only one fifth of the vessels at 3T MRI compared to 7T MRI. This warrants the use of larger cohorts at 3T MRI to obtain a similar effect size as that at 7T MRI, though the larger availability of 3T MRI will aid in this matter.

Concerning future research, it is important to investigate repeatability of 2D PC imaging at 3T MRI in subject cohorts and validate group comparisons, in line with previous 7T MRI research.[12] With proven repeatability of flow measures at 3T MRI, the applicability of the 2D PC sequence for perforating artery flow determination will increase. Alternatively,

future studies can also resort to the use of large subject cohorts to obtain enough power. When using 3T MRI, one must take into account that the relatively larger cerebral vessels measured by this modality may have a different disease progression than the smaller vessels measured by 7T MRI. Similar findings at 3T and 7T MRI may therefore not have similar implications regarding health and disease. However, it is suggested that the effects of endothelial failure, which play an important role in cerebrovascular disease, are present at an earlier stage in larger perforating arteries compared to the smaller arteries.[13] This leads to arteriolar disease in the BG, in advance of arteriolar disease leading to white matter hyperintensities (WMHs) in the CSO. This is an advantage since early onset arterial deterioration is more prone to exist in the BG and can thus be investigated using 3T MRI.

So, what else is in there? A lot more is in there! Together, these studies increased the potential of perforating artery imaging and detection by improvement of the reliability of perforating artery flow assessment in a time-efficient manner and bringing small vessel research a step closer towards employability at 3T MRI. This not only eased the use of the 2D PC sequence for perforating artery detection, it also paved the way for perforating artery flow determination in large subject cohorts. Currently, alternative techniques to study the hemodynamics of the small cerebral arteries are scarce. Most techniques are still limited to hemodynamical measurements of cerebral vessels with larger diameters (often not much smaller than 1 mm) or use mathematical models based on data from published literature.[14,15] Consequently, research concerning the smaller arteries is frequently of an anatomical rather than functional nature.[16–18] Though, interesting developments occur in the field of ultrasound, in which ultra-fast ultrasound gives access to measurement of the small cerebral vessels and enables slow blood flow measurements. However, despite the fact that ultrasound is non-invasive and a portable and affordable technique, it is hampered by reduced signal due to the skull barrier. To avoid such and other hindrances of measuring (structural) properties of the small cerebral small vessels, some authors resort to measurements in the retina. Similarities between retinal vessels and cerebral small vessels have been shown, and relations between microvascular changes in the retina and SVD have been reported. Retinal optical coherence tomography for example enables an insight into SVD vessel pathology, which cannot be done using MRI, and Doppler flowmetry allows for retinal microvascular flow measurements. Though the fact remains that the retinal vessels serve as a proxy for the cerebral small vessels. In addition, as microvascular changes are often related

to lesions depicted and quantified using MRI, using MRI to determine microvascular properties is a logical extension. At the same time, PC imaging techniques are also under constant development. Methods using shared velocity encoding have been devised to increase temporal resolution[19] as well as radial and spiral sampling schemes to limit acquisition times.[20] In addition, methods using variable velocity encoding are being introduced, enabling optimal encoding of various flow velocities. This increases acquisition time, but does reduce measurement noise.[21] Given the advantages and challenges of the aforementioned techniques to measure small vessel blood flow, we believe that the 2D PC sequence presented in this thesis is a good method for the assessment of small vessel flow. With the improvements presented in our research 2D PC imaging holds promise for complementing other available techniques as well as the existing functional and anatomical knowledge of the (small) cerebral vasculature in health and disease.

Part II: What is out there?

Characterizing small vessel hemodynamics in relation to a range of cardiovascular factors

In this part of the thesis we assessed the cerebral perforating artery function as part of a bigger cardiovascular sytem. From the perspective of the small perforating arteries we asked ourselves "What is out there?" As the perforating arteries are part of the cardiovascular tree, they are part of an intricate network of interconnected blood vessels, which have their own vascular properties and interrelations.[22–24] In addition, cardiovascular risk factors have known associations with perforating arteries.[25,26] At the same time, various feedback mechanisms exist to control the cerebral blood flow and pressure in response to cardiovascular alterations and risk factors.[27–29] Here, we aimed to characterize small perforating artery flow measures in relation to a range of cardiovascular factors with known small vessel associations. We therefore investigated perforating artery flow in relation to a carotid occlusion, explored the phenomenon of damping in the small cerebral arteries in relation to proximal measures of pressure and arterial stiffness, and assess associations between small vessel flow and cardiovascular risk factors.

The small cerebral vessels in the CSO and BG are part of the anterior cerebral circulation, and are receive blood supply from the internal carotid arteries.[22] However, in patients with carotid occlusive disease (COD), one or both carotid arteries are stenotic or

blocked, changing local hemodynamics. Patients with COD are known to have cerebral hemodynamic alterations and slow-flow infarcts, mainly in border zone areas of the brain including the CSO and BG. In addition, they commonly have manifestations which are frequently present in small vessel disease.[30–33] In **Chapter 4,** we aimed to assess if small vessel hemodynamics of the cerebral perforating arteries is affected by a carotid occlusion. In addition, we investigated if perforating artery flow measures were related to lesions typically attributed to SVD, which are also more common in people with COD. Our results showed that, in a group of patients with COD without recent ischemic symptoms, although several measures of cerebral perforating artery flow were unaffected, there were indications of reduced perforating artery flow velocity, particularly in the watershed areas, and reduced perforating artery flow velocity tended to WMH volume These hemodynamic changes may be clinically relevant given their shown relation with a higher lesion burden in patients with COD. First, this study indicated altered flow measures in the cerebral perforating arteries in patients with COD. In future studies with less hemodynamically stable participants it is plausible that more pronounced results are obtained, as well as more proximal hemodynamical changes, for example in the M1. Longitudinal studies may be of greatest value, as changes in cerebral small vessel hemodynamics might predict lesion formation or the occurrence of symptoms. Currently, it is known that flow obstruction in large arteries supplying blood to the brain causes the cerebral vasculature to compensate for the altered hemodynamics, mainly with the aim to maintain sufficient cerebral blood flow (CBF).[34] Therefore, investigating small vessel flow in participants from the time of onset of plaque buildup in one or both carotid arteries can give insight into these compensatory mechanisms in response to the obstruction and can indicate when these mechanisms become insufficient. An important compensatory mechanism to take into consideration in future research is the presence and degree of collateral flow. In patients with COD, the circle of Willis is a major source of collateral flow and aims to redistribute blood flow and pressures in the cerebral vessels. The presence of collateral flow has shown to be associated with a low incidence of border zone infarcts in symptomatic patients.[35] It can be of interest to investigate how small vessel flow velocity and pulsatility relate to the presence and amount of collateral flow, to assess to what degree collateral flow prevents hemodynamic alterations in the microvasculature in patients with COD. Our assessment of hemispherical flow in patients with COD did not show any hemispherical differences, but the possibility exists that hemispherical differences only occur when collateral flow is unable to redistribute blood flow and pressure over hemispheres. In

literature, no consensus exists concerning the presence of hemispherical differences in CBF, CVR or the presence of lesions,[36] underlining the need for further research.
Second, this study indicated that the cerebral perforating arteries contribute to damage and possibly also clinical outcome in COD. Previous research on associations between the presence of cerebral damage or events and cerebral flow in patients with COD showed that cerebral cortical microinfarct burden was related to the severity of cervical arterial compromise.[37] Further, rosary-like infarctions in the borderzone regions appeared to be associated with hemodynamic failure due to COD.[38] This latter finding is supported by the fact that the absence of collateral flow, indicating more hemodynamic impairment, was shown to be related to a higher prevalence of border zone infarcts.[35] Together, this support the suggestion that altered cerebral hemodynamics due to COD is involved in the occurrence of cerebral damage and events. Though, to be able to relate hemodynamical changes to lesion formation over time, longitudinal studies are needed. In this study, assessment of the cerebral perforating artery flow in patients with COD is hindered by the fact that we cannot know whether the lower perforating artery flow and subcortical ischemic lesions in patients with COD are a direct consequence of hemodynamic changes at the level of the carotid artery, or rather reflect the co-occurrence of COD, as the latter can be due to shared risk factors between atherosclerosis and SVD.[36,39] The key in unraveling these disorders may lie in the assessment of structural vascular changes. Currently, retinal examination is performed due to shown associations between retinal microvascular changes and SVD.[40] This offers an opportunity for in-vivo investigation of vessel pathology in patients with COD, in order to assess possible similarities with known SVD-unique pathology.

In **Chapter 5** we explored the association of proximal measures of pressure and arterial stiffness with cerebral damping towards the perforating arteries. Pressure pulsations originate in the heart and propagate blood through the cardiovascular tree. Damping of the pressure pulsations created by the beating heart not only occurs in large arteries such as the aorta and circle of Willis, but also in the small arteries and microcirculation and aims to protect the vasculature from an excess of pulsatile energy, averting vascular damage. In this chapter we explored the phenomenon of damping of pressure pulsations between the first segment of the middle cerebral artery (M1) up to the small perforating arteries, with velocity pulsatility as a proxy for pressure pulsatility. Damping was assessed in association with proximal measures of pressure and arterial stiffness, i.e. left ventricular stroke volume, mean arterial pressure, pulse pressure and aortic

pulse wave velocity. Results not only indicate the presence of damping between the M1 and the perforating arteries of the CSO and BG, but also suggest that this distal damping increases when proximal pressure and arterial stiffness increase. Currently, prior measurements of cerebral damping are mainly performed in larger cerebral arteries (> 1 mm in diameter). Using MRI and transcranial Doppler, previous studies have found damping in vessels of the circle of Willis and larger segments of lenticulostriate arteries to decrease with age with and therefore pulsatility to increase with age.[41,42] The same was seen in whole brain pulsatility measures in the distal cerebral arteries of on average 1 mm in diameter.[15] With this study we showed the ability to measure the phenomenon of damping of pressure pulsations in the smaller cerebral arteries of healthy elderly subjects, and showed associations between cerebral damping and proximal measures of pressure and arterial stiffness. In the future, (longitudinal) studies performing similar measurements but focusing on young healthy subjects as well as older subjects with cardiovascular disease, can be of great value, as it may reveal how damping in small cerebral vessels deteriorates with age or disease. Further, studies in various cohorts and longitudinal studies may reveal how cerebral damping is related to cerebral lesion formation, such as the advance of white matter hyperintensities. Concerning future exploration of the contribution of cerebral vessels to pressure damping in disease, research into cerebrovascular diseases such as SVD can greatly benefit from the small vessel measures presented here, as it is believed that in SVD amplification of pressure pulsations in the small cerebral arteries lead to MRI manifestation commonly seen in patients with SVD, such as white matter hyperintensities.[39,43] However, due to the relative novelty of pulsatility measurements in the small cerebral perforating arteries, little is yet known about these topics. We therefore believe that the deployment of the 2D PC pulsatility measurements as presented in this thesis can help unravel the role of cerebral damping in aging and disease. Further, it is of great importance to complement small vessel hemodynamic studies as performed in this chapter with other hemodynamical as well as structural research. For example, pathological and animal studies are unravelling structural alterations in the cerebral microvasculature such as endothelial defects, loss of smooth muscle cells, and thickening of the vessels wall, either with aging or in disease.[44] It is plausible that these pathological changes result from or cause alterations in cerebral damping, making it valuable to bring pulsatility and pathological measurements together. Finally, as previously stated, damping between the heart and microvasculature occurs in many locations and vessels. Here, we specifically assessed damping of pressure pulsations between the M1 and cerebral

perforating arteries. It can be of great interest to assess damping in multiple vascular segments along this cardiovascular tree, using a similar 2D PC acquisition, and assess its relations with for example age and cerebrovascular conditions.

In **Chapter 6** we examined the role of risk factors, and studied whether relationships exist between small perforating artery function measures and common cardiovascular risk factors. Our subject cohort consisted of subjects aged > 50 with either COD, vascular cognitive impairment, or no cerebrovascular disease. Except for an inverse relation between diastolic blood pressure and pulsatility in the BG, we found no consistent relationships. Results therefore show that cerebral perforating artery blood flow velocity and pulsatility appear to be largely independent of common vascular risk factors in our participant population above the age of 50 with mixed vascular burden. This may imply that in these patients auto-regulatory mechanisms can maintain a stable flow in the cerebral perforating arteries, regardless of presence of an adverse vascular risk profile. This is in line with the results found in Chapter 5, where flow pulsations towards the small perforating arteries were regulated, in that case by damping mechanisms. Literature on the impact of common cardiovascular risk factors (e.g. hypertension, diabetes mellitus, obesity, hyperlipidemia and smoking) on the large as well as the small vessels is elaborate, and clearly allude that risk factors are involved in structural changes such as vessel rarefaction, endothelial remodeling, and lower vessel density, which are thought to render tissues more vulnerable to ischemia and hypoperfusion.[45] In addition, literature suggests microvascular hemodynamical changes, such as a decrease in CBF and changes resulting from a decrease in arterial compliance.[46] It is not yet clear how these structural and hemodynamical changes relate to one another, and if hemodynamical changes results from structural changes or vice versa. Nevertheless, it is beyond dispute that common cardiovascular risk factors affect the cerebral microvasculature. It therefore highly plausible that results differ in a more homogenous subject group with a more homogenous pathology (our subject group contained patients with vascular cognitive impairment as well as patients with COD), as well as in hemodynamically more compromised patients, for example those with severe atherosclerotic disease or with advanced cerebral small vessel disease. Particularly in the latter, perforating arteries or auto-regulatory mechanisms along the cardiovascular tree may function differently. Due to the suggested effect of risk factors on the microvasculature, and the important role of the resulting microvascular changes in ischemic events, lesion formation and cognitive decline, microvascular

flow measurements can be of great added value. Together with pathological research it can aid in understanding how risk factors impact the small cerebral vessels and might help in deciding which risk factors should be treated to prevent or halt cerebral degeneration. Over the past years, much progress has been made in unraveling and describing mechanisms which underlie the responses of the cerebral microvasculature to risk factors, and the flow measurements of the small perforating arteries are a valuable asset in this area of research as literature suggests microvascular blood flow impairments.

In the studies in this part of the thesis we gained insight into small vessel hemodynamics in relation to a range of external cardiovascular factors. In case of an obstructed carotid the small vessel hemodynamics appear to be affected by proximal flow obstruction as shown in Chapter 4, and in Chapter 5 the degree of damping changed in response to proximal changes in pressure and arterial stiffness. This characterizes the cerebral small vessels not only as an anatomical part of a larger whole, but also as a functional part of a larger whole. Though results of Chapter 6 suggest otherwise, future research in more severely vascular compromised and homogenous cohorts may show associations between risk factors and small vessel flow, as suggested by literature. Therefore, looking at "what is out there" appears to be worthwhile concerning small vessel flow assessment, as our research shows that external factors affect small vessel hemodynamics. This implies that small vessel research should not solely focus on the small vessels and one should not ascribe small vessel alterations merely to changes in their vicinity, but also take cardiovascular factors into account. Although this makes small vessel research more complex, it does aid in unraveling the interplay of the small vessels with the cardiovasculature and gain insight into the underlying causes of small vessel demise. In the light of possible treatment this also teaches us which cardiovascular factor has potential to be targeted for treatment to either diminish, halt or prevent microvascular damage.

Part III: What is happening?
Exploring microvascular (dys)function in SVD

In this part of the thesis we aimed to investigate the flow measures of the cerebral microvasculature in patients with SVD. It is known that patients with SVD exhibit on MRI lacunar infarcts, white matter hyperintensities, microbleeds and enlarged perivascular spaces and animal models show abnormalities in microvascular function.[47–49] However,

MRI pathology and symptoms of SVD often reflect the end-stage of the disease and not the anomalies in the microvasculature, which is suggested to be the substrate of onset of SVD.[13] So in this part of the thesis, we assessed with 7T MRI the functioning of the microvasculature in patient with SVD to gain more understanding of its role in this disease. The included study cohort involved patients with monogenic SVDs and was part of the ZOOM@SVDs study, a substudy of the European Union's Horizon 2020 funded research program SVDs@target. This variant of SVD is called Cerebral Autosomal Dominant Arteriopathy with Subcortical Infarcts and Leukoencephalopathy (CADASIL). These patients have a ~100% risk of developing the disease.[50]

Chapter 7 discussed the rationale and the design of ZOOM@SVDs, which contains three measures: i) blood flow velocity and pulsatility of the small cerebral perforating arteries; ii) cerebrovascular reactivity in response to a hypercapnic stimulus; iii) cerebrovascular reactivity through neurovascular coupling. This chapter also elaborated on the current knowledge of these three measures and the imaging sequences involved in the study.

In **Chapter 8** we presented the results of the three measures discussed in chapter 7 concerning the microvascular function in CADASIL patients. Comparison between patients and controls showed a decrease in perforating artery blood flow velocity in both the CSO and BG in patients. Additionally, blood flow pulsatility in the perforating arteries was increased in patients. The vasodilatory challenge showed a larger increase in cortical blood flow in patients compared to controls, which is a counterintuitive response. This may indicate a possible compensation or redistribution mechanism such as vascular steal, and results suggest this mechanism to disappear with increasing disease severity. In response to a short visual stimulus we observe a decrease in vascular reactivity in patients compared to controls, which is intuitive. However, the response to a longer (i.e. stronger) visual stimulus is similar between patients with CADASIL and controls.
Comparison within patients between normal appearing white matter and WMHs, showed no differences in perforating artery blood flow velocity and pulsatility. Vascular reactivity results show a decreased, and even negative vascular reactivity in WMHs in patients in response to the hypercapnic stimulus, indicating a decrease in blood flow in the WMHs in response to a vasodilatory challenge. Regarding associations between small vessel dysfunction and disease severity, a negative relation was found between blood flow velocity in the CSO and WMH volume.

In the introduction of this thesis we posed the question "What is happening?" These results indicate that in patients with CADASIL "a lot is happening", given that the cerebral vasculature in CADASIL patients expresses a versatile behavior, in which regional alterations seem to be associated with one another and multiple functional aspects of the microvascular seem altered. This study therefore showed the added value of combining diverse measurement techniques to measure vascular function in multiple brain regions and vessel populations, and with that capture the complex functional cerebral alterations in patients with CADASIL. Because, despite some differences, CADASIL and sporadic SVD closely resemble one another on a neuropathological and clinical level.[50,51] Therefore, research into CADASIL has immediate relevance to sporadic SVDs. As ZOOM@SVDs also includes a cohort of patients with sporadic SVD, future research will investigate the measures of microvascular function as discussed in this chapter in this patient cohort. As the study with patients with sporadic SVDs is a study with a 24 month follow-up, it also allows the assessment of relations between microvascular function and parenchymal lesion progression and cognitive decline. This is interesting because, as microvascular dysfunction is suggested to result in lesions and cognitive decline,[13] it enables us to investigate the role of the microvasculature in these SVD manifestations. If microvascular dysfunction is shown to be an important predictor of lesions progression and cognitive decline, microvascular dysfunction could serve as an outcome marker for treatment compounds that affect the small cerebral vessels. Concerning assessment of SVD, albeit sporadic or genetic, it is important to realize the complexity of SVDs. It impacts many aspects of the cerebral vasculature, which results in a range of cerebral abnormalities relating to, for example, the structural integrity of vessels and the blood-brain barrier, size of perivascular spaces, cerebral blood flow, cerebral reactivity and waste clearance.[44,49] This large variety of abnormalities requires a divers and complementary range of measurements and measurement techniques. This chapter has shown that 7T MRI enables us to study multiple aspects of the cerebral hemodynamics and that the high field strength allows focus on the smaller cerebral vessels. Therefore, MRI proved to be an indispensable tool to investigate the cerebral vasculature in humans in-vivo. However, we must realize that the MRI measures presented in this chapter cannot capture all aspects involved in SVD and that it is essential to complement them with other measures and techniques, such as computational tomography for lesion detection, and MR spectroscopy and positron emission tomography for metabolic imaging. A valuable multimodal approach is positron emission tomography combined with computed tomography (PET-CT), which can

combine functional PET information with high-resolution morphological information. However, this approach cannot perform PET and CT scans simultaneously, making organ/subject motion and differences in breathing patterns problematic. Contrary to PET-CT, PET-MRI is able to simultaneously perform hemodynamic as well as metabolic mapping and can therefore better link MRI derived anatomic and functional information with PET derived pathological information with perfect temporal correlation.[52] These multimodal approaches can also be of interest to investigate experimental therapeutics. Concerning the blood oxygen level-dependent (BOLD) signal, which is based on blood oxygenation changes, a disadvantage is that it reflects intra- and extravascular changes as well as changes in multiple vascular aspects such as the cerebral blood flow, cerebral blood volume, the cerebral metabolic rate of oxygen.[53] However, techniques to complement the composite BOLD signal are ASL-MRI with which CBF measurements can be performed,[54] and VASO fMRI which in 2001 was the first technique that was able to non-invasively assess cerebral blood volume in humans with results that agreed with other fMRI methods.[53] Besides the complementary use of various techniques, extensive research for new technical and physical improvements and advances is performed, especially to achieve a higher spatial and temporal resolution. These developments are very advantages for research into microvasculature, in which structures are small and processes often happen on short time scales. A disadvantage of techniques with higher spatial and temporal resolution is that they tolerate even less subject motion. Finally, animal models provide valuable information concerning pathological research and are indispensable when it comes to the evaluation of pharmacological treatments.[55–57] This is what makes research collaborations, such as the SVDs@target consortium, so valuable, as it combines pathological, clinical, and neuroimaging measurements to better understand the mechanisms underlying SVD. It is my believe that it is the key to achieving future developments in diagnosis, care and treatment of SVDs.

Conclusion

This thesis explored the assessment of microvascular function using 7T MRI. Examination of the method to image and detect cerebral small vessels improved the method, making it faster and more objective, and revealed proven feasibility on lower field strengths, amplifying its value for microvascular research. More sophisticated methods can further improve small vessel detection, for example with motion correction or prevention, or with compressed sensing. We assessed the characteristics of these small vessel flow measures by investigating associations with a range of cardiovascular factors.

This showed the wide range of applications for 2D PC small vessel flow assessment. Further, by using 2D PC imaging together with complementary MRI methods to assess microvascular flow, 7T MRI proved to be indispensable to investigate function of the smaller cerebral vessels in patients with SVD. I believe that by combining the small vessel functional measurements presented in this thesis with pathological and clinical (small vessel) measurements, 7T MRI can be of great value for a better understanding of the cerebral microvasculature in health and disease.

REFERENCES

1. Geurts, L. J., Luijten, P. R., Klijn, C. J. M., Zwanenburg, J. J. M. & Biessels, G. J. Higher Pulsatility in Cerebral Perforating Arteries in Patients With Small Vessel Disease Related Stroke, a 7T MRI Study. Stroke 50, 62–68 (2018).
2. Geurts, L., Biessels, G. J., Luijten, P. & Zwanenburg, J. Better and faster velocity pulsatility assessment in cerebral white matter perforating arteries with 7T quantitative flow MRI through improved slice profile, acquisition scheme, and postprocessing. Magn. Reson. Med. 79, 1473–1482 (2018).
3. Geurts, L. J. et al. Vascular reactivity in small cerebral perforating arteries with 7 T phase contrast MRI – A proof of concept study. Neuroimage 172, 470–477 (2018).
4. Arts, T., Siero, J. C. W., Biessels, G. J. & Zwanenburg, J. J. M. Automated Assessment of Cerebral Arterial Perforator Function on 7T MRI. J. Magn. Reson. Imaging 53, 234–241 (2021).
5. Zeng, L.-L. et al. Neurobiological basis of head motion in brain imaging. Proc. Natl. Acad. Sci. 111, 6058–6062 (2014).
6. Pardoe, H. R., Kucharsky Hiess, R. & Kuzniecky, R. Motion and morphometry in clinical and nonclinical populations. Neuroimage 135, 177–185 (2016).
7. Andersen, M. et al. Measuring motion-induced B0-fluctuations in the brain using field probes. Magn. Reson. Med. 75, 2020–2030 (2016).
8. Boer, V. O., Vd Bank, B. L., Van Vliet, G., Luijten, P. R. & Klomp, D. W. J. Direct B0 field monitoring and real-time B0 field updating in the human breast at 7 tesla. Magn. Reson. Med. 67, 586–591 (2012).
9. Mattern, H. et al. Prospective motion correction enables highest resolution time-of-flight angiography at 7T. Magn. Reson. Med. 80, 248–258 (2018).
10. Lustig, M., Donoho, D. & Pauly, J. M. Sparse MRI: The application of compressed sensing for rapid MR imaging. Magn. Reson. Med. 58, 1182–1195 (2007).
11. S. Park, Chen, L., Townsend, J., Lee, H. & Feinberg, D. A. Simultaneous Multi-VENC and Simultaneous Multi-Slice Phase Contrast Magnetic Resonance Imaging. IEEE Trans. Med. Imaging 39, 742–752 (2020).
12. Geurts, L., Biessels, G. J., Luijten, P. & Zwanenburg, J. Better and faster velocity pulsatility assessment in cerebral white matter perforating arteries with 7T quantitative flow MRI through improved slice profile, acquisition scheme, and postprocessing. Magn. Reson. Med. 79, 1473–1482 (2018).
13. Wardlaw, J. M., Smith, C. & Dichgans, M. Mechanisms underlying sporadic cerebral

small vessel disease : insights from neuroimaging. Lancet Neurol. 12, 70060–7 (2013).
14. Blanco, P. J., Müller, L. O. & Spence, J. D. Blood pressure gradients in cerebral arteries: A clue to pathogenesis of cerebral small vessel disease. Stroke Vasc. Neurol. 2, 108–117 (2017).
15. Vikner, T. et al. Characterizing pulsatility in distal cerebral arteries using 4D flow MRI. J. Cereb. Blood Flow Metab. 40, 2429–2440 (2020).
16. Chen, Y. C. et al. Correlation between the number of lenticulostriate arteries and imaging of cerebral small vessel disease. Front. Neurol. 10, 1–8 (2019).
17. Liem, M. K. et al. Lenticulostriate Arterial Lumina Are Normal in Cerebral Autosomal-Dominant Arteriopathy With Subcortical Infarcts and Leukoencephalopathy A High-Field In Vivo MRI Study. (2010) doi:10.1161/STROKEAHA.110.586883.
18. Kang, C. K. et al. Imaging and analysis of lenticulostriate arteries using 7.0-Tesla magnetic resonance angiography. Magn. Reson. Med. 61, 136–144 (2009).
19. Lin, H. Y. et al. Shared velocity encoding: A method to improve the temporal resolution of phase-contrast velocity measurements. Magn. Reson. Med. 68, 703–710 (2012).
20. Nayak, K. S. et al. Cardiovascular magnetic resonance phase contrast imaging. J. Cardiovasc. Magn. Reson. 17, 71 (2015).
21. Nilsson, A., Markenroth Bloch, K., Carlsson, M., Heiberg, E. & Ståhlberg, F. Variable velocity encoding in a three-dimensional, three-directional phase contrast sequence: Evaluation in phantom and volunteers. J. Magn. Reson. Imaging 36, 1450–1459 (2012).
22. Purves, D. et al. Neuroscience. (Sinauer Associates Inc., 2001).
23. Chandra, A., Li, W., Stone, C., Geng, X. & Ding, Y. The cerebral circulation and cerebrovascular disease I: Anatomy. Brain circulation, 3(2), 45. Brain Circ. 3, 45–56 (2017).
24. Djulejić, V. et al. Common features of the cerebral perforating arteries and their clinical significance. Acta Neurochir. (Wien). 157, 743–754 (2015).
25. Granger, D. N., Rodrigues, S. F., Yildirim, A. & Senchenkova, E. Y. Microvascular responses to cardiovascular risk factors. Microcirculation (2010) doi:10.1111/j.1549-8719.2009.00015.x.
26. Pase, M. P., Grima, N. A., Stough, C. K., Scholey, A. & Pipingas, A. Cardiovascular disease risk and cerebral blood flow velocity. Stroke (2012) doi:10.1161/STROKEAHA.112.666727.
27. Guyton, A. C. Blood pressure control - Special role of the kidneys and body fluids. Science (80-.). 252, 1813–1816 (1991).
28. Delicce, A. V, Basit, H. & Makaryus, A. N. Physiology, Frank-Starling Law. In: StatPearls. Treasure Island (FL): StatPearls Publishing; 2020. (StatPearls Publishing LLC, 2020).

29. Cipolla, M. J. Control of Cerebral Blood Flow. in The Cerebral Circulation (Morgan & Claypool Life Sciences, 2010).
30. Kandiah, N., Goh, O., Mak, E., Marmin, M. & Ng, A. Carotid stenosis: A risk factor for cerebral white-matter disease. J. Stroke Cerebrovasc. Dis. 23, 136–139 (2014).
31. Ammirati, E. et al. Relation between characteristics of carotid atherosclerotic plaques and brain white matter hyperintensities in asymptomatic patients. Sci. Rep. 7, 1–11 (2017).
32. Lin, M. P. et al. Collateral Recruitment Is Impaired by Cerebral Small Vessel Disease. Stroke 51, 1404–1410 (2020).
33. Mathiesen, E. B. et al. Reduced neuropsychological test performance in asymptomatic carotid stenosise. Neurology 62, (2004).
34. Gordon, A. L., Goode, S., Souza, O. D', Auer, D. P. & Munshi, S. K. Cerebral misery perfusion diagnosed using hypercapnic blood-oxygenation-level-dependent contrast functional magnetic resonance imaging: a case report. J. Med. Case Rep. 4, (2010).
35. Hendrikse, J., Hartkamp, M. J., Hillen, B., Mali, W. P. T. M. & Van Der Grond, J. Collateral Ability of the Circle of Willis in Patients With Unilateral Internal Carotid Artery Occlusion Border Zone Infarcts and Clinical Symptoms. Stroke 32, 2768–2773 (2001).
36. Klijn, C. J. M., Kappelle, L. J., Tulleken, C. A. F. & Van Gijn, J. Symptomatic carotid artery occlusion: A reappraisal of hemodynamic factors. Stroke vol. 28 2084–2093 (1997).
37. van den Brink, H. et al. Does cerebral hemodynamic compromise contribute to cerebral cortical microinfarcts: A proof of concept study in patients with internal carotid artery occlusion. Alzheimer's Dement. 16, e040256 (2020).
38. Krapf, H., Widder, B. & Skalej, M. Small rosarylike infarctions in the centrum ovale suggest hemodynamic failure. Am. J. Neuroradiol. 19, 1479–1484 (1998).
39. Wardlaw, J. M., Smith, C. & Dichgans, M. Mechanisms of sporadic cerebral small vessel disease: Insights from neuroimaging. Lancet Neurol. 12, 483–497 (2013).
40. Abdelhak, A. et al. Optical coherence tomography-based assessment of retinal vascular pathology in cerebral small vessel disease. Neurol. Res. Pract. 2, 13 (2020).
41. Schnerr, R. S. et al. Pulsatility of lenticulostriate arteries assessed by 7 Tesla flow MRI-Measurement, reproducibility, and applicability to aging effect. Front. Physiol. 8, 1–10 (2017).
42. Lefferts, W. K., DeBlois, J. P., Augustine, J. A., Keller, A. P. & Heffernan, K. S. Age, sex, and the vascular contributors to cerebral pulsatility and pulsatile damping. J. Appl. Physiol. 129, 1092–1101 (2020).

43. Webb, A. J. S. et al. Increased Cerebral Arterial Pulsatility in Patients With Leukoaraiosis Arterial Stiffness Enhances Transmission of Aortic Pulsatility. 43, 2631–2636 (2012).
44. Pantoni, L. Cerebral small vessel disease: from pathogenesis and clinical characteristics to therapeutic challenges. Lancet Neurol. 9, 689–701 (2010).
45. Hainsworth, A. H. & Markus, H. S. Do in vivo experimental models reflect human cerebral small vessel disease? A systematic review. Journal of Cerebral Blood Flow and Metabolism vol. 28 1877–1891 (2008).
46. Friedman, J. I. et al. Brain imaging changes associated with risk factors for cardiovascular and cerebrovascular disease in asymptomatic patients. JACC: Cardiovascular Imaging vol. 7 1039–1053 (2014).
47. Dabertrand, F. et al. Potassium channelopathy-like defect underlies early-stage cerebrovascular dysfunction in a genetic model of small vessel disease. Proc. Natl. Acad. Sci. 112, E796–E805 (2015).
48. Joutel, A. et al. Cerebrovascular dysfunction and microcirculation rarefaction precede white matter lesions in a mouse genetic model of cerebral ischemic small vessel disease. J. Clin. Invest. 120, (2010).
49. Wardlaw, J. M. et al. Neuroimaging standards for research into small vessel disease and its contribution to ageing and neurodegeneration. Lancet Neurol. 12, 822–838 (2013).
50. Joutel, A. & Faraci, F. M. Cerebral Small Vessel Disease (SVD): insights and opportunities from mouse models of collagen IV-related SVD and CADASIL. Stroke 45, (2014).
51. Chabriat, H., Joutel, A., Dichgans, M., Tournier-Lasserve, E. & Bousser, M. G. CADASIL. The Lancet Neurology vol. 8 643–653 (2009).
52. Pichler, B. J., Wehrl, H. F., Kolb, A. & Judenhofer, M. S. Positron Emission Tomography/Magnetic Resonance Imaging: The Next Generation of Multimodality Imaging? Seminars in Nuclear Medicine vol. 38 199–208 (2008).
53. Lu, H. & van Zijl, P. C. M. A review of the development of Vascular-Space-Occupancy (VASO) fMRI. NeuroImage vol. 62 736–742 (2012).
54. Calamante, F., Thomas, D. L., Pell, G. S., Wiersma, J. & Turner, R. Measuring cerebral blood flow using magnetic resonance imaging techniques. Journal of Cerebral Blood Flow and Metabolism vol. 19 701–735 (1999).
55. Heiss, W. D. The additional value of PET in the assessment of cerebral small vessel disease. J. Nucl. Med. 59, 1660–1664 (2018).
56. Stringer, M. S. et al. A Review of Translational Magnetic Resonance Imaging in Human and Rodent Experimental Models of Small Vessel Disease. Translational Stroke

Research vol. 12 15–30 (2021).
57. Mok, V. et al. Transcranial doppler ultrasound for screening cerebral small vessel disease: A community study. Stroke 43, 2791–2793 (2012).

Appendices

NEDERLANDSE SAMENVATTING

Onderzoek naar de kleine vaatjes in het brein is van grote waarde, omdat deze vaatjes een belangrijke rol spelen in de bloedvoorziening van de hersenen. Als deze kleine vaatjes door ziekte of veroudering zijn aangedaan, verhoogd dat de kans op beroertes en dementie. Onderzoek naar deze kleine vaatjes werd tot recentelijk bemoeilijkt omdat deze vaatjes meestal nog geen millimeter groot zijn. Sinds kort kunnen we met 7 tesla (T) MRI de hemodynamiek van de vaatjes onderzoeken en daarmee ook het functioneren van de cerebrale microvasculatuur.
Het algemene doel van het werk beschreven in deze thesis is om de bestaande flow metingen van de kleine vaatjes, i.e. bloedsnelheids- en pulsatiliteitsmetingen, betrouwbaarder te maken en de toepasbaarheid ervan te vergroten. Tevens onderzoeken we welke factoren van invloed kunnen zijn op deze metingen, en passen we deze en andere metingen van microvasculaire functie toe in een cohort van patiënten met small vessel disease (SVD).

De detectie van kleine cerebrale vaatjes betrouwbaarder maken en breder inzetbaar

De techniek om flow metingen van de kleine vaatjes mogelijk te maken is een snelheidsgecodeerde fase contrast (PC) sequentie op 7T MRI, waarna de kleine perforerende arteriën automatisch worden gedetecteerd en de bloedstroomsnelheid en pulsatiliteit kunnen worden berekend, zoals eerder is gedaan in de centrum semi-ovale (CSO) en de basale ganglia (BG). Deze maten zijn vooral van belang voor cohorten bestaande uit oudere mensen, omdat zij vatbaar zijn voor hemodynamische veranderingen in de kleine vaatjes. Echter, uit onderzoek is gebleken dat oudere mensen en patiënten meer bewegen tijdens MRI acquisities ten opzichte van jongere en gezonde mensen. In het geval van de 2D PC sequentie resulteert dat in de CSO in zogenaamde 'ghosting artefacten', wat tot gevolg heeft dat de gedetecteerde perforerende arteriën gelegen in de artifacten (i.e. de vals positieven) manueel geëxcludeerd moeten worden. Dit is niet alleen een tijdrovende, maar ook subjectieve handeling. Het zou daarom van grote toegevoegde waarde zijn als perforerende arteriën gelegen in ghosting artifacten automatisch geëxcludeerd kunnen worden. Daarnaast is de beschikbaarheid van 3T MRI scanners vele malen groter dat die van 7T MRI scanners, waardoor de inzet van 3T scanners de metingen voor bloedstroomsnelheden en pulsatiliteit breder inzetbaar kan maken.

Beweging van mensen in de MRI tijdens de 2D PC sequentie heeft vooral gevolgen

voor metingen in de centrum semi-ovale. Dit komt ten eerste doordat de perforerende arteriën in de CSO kleiner zijn dan in de BG, en ten tweede omdat er in de CSO meer grote vaten in het scanvlak liggen die bij beweging van het hoofd artefacten geven. In **Hoofdstuk 2** is een automatische methode gepresenteerd waarmee de perforerende arteriën gelegen in ghosting artefacten kunnen worden verwijderd. We hebben laten zien dat, vergeleken met de manuele methode, deze automatische exclusiemethode gelijke herhaalbaarheid heeft voor metingen van bloedstroomsnelheid en verbeterde herhaalbaarheid voor metingen van pulsatiliteit en het aantal geïncludeerde vaatjes. Ook vertoonden de methoden goede overeenstemming. Het gebruik van de automatische methode maakt de detectie en metingen van flow van de kleine vaatjes niet alleen robuuster en objectiever, maar het bespaard de gebruiker ook veel tijd.

In **Hoofdstuk 3** hebben we 2D PC data geacquireerd in de BG op zowel 3T als 7T MRI en de overeenstemming tussen de bloedstroomsnelheids- en pulsatiliteitsmetingen bepaald. Hoewel de resultaten weinig tot geen overeenstemming lieten zien tussen de twee scanmodaliteiten, hebben de metingen wel aangetoond dat flow in de cerebrale perforerende arteriën gemeten kan worden met 3T MRI. De verschillen tussen de modaliteiten waren niet geheel onverwacht, en konden worden verklaard door het feit dat beide modaliteiten alleen het spreekwoordelijke topje van de ijsberg van de perforerende arteriën kunnen meten, wat betekent dat ze alleen de arteriën meten met de hoogste bloedstroomsnelheid meten. Dit resulteert in scanner-afhankelijke bias. Deze bias was ook de reden waarom er op 3T MRI vijf maal minder kleine vaatjes werden gedetecteerd dan op 7T MRI. Tevens bleken verschillen in de planning van de 2D PC slice invloed te hebben op de overeenstemming tussen de twee veldsterktes. Deze constateringen benadrukken het belang van het gebruik van een gelijke scanprotocollen en gelijke MRI veldsterkten in toekomstige klinische studies.

Karakteriseren van de hemodynamiek van de kleine cerebrale vaatjes in relatie tot diverse cardiovasculaire factoren

De kleine cerebrale vaatjes zijn onderdeel van een groter geheel, namelijk de cardiovasculaire boom, die bestaat uit een complex netwerk van onderling verbonden bloedvaten, met ieder hun eigen vasculaire eigenschappen en onderlinge relaties. Daarbij is bekend dat vasculaire risicofactoren associaties vertonen met kleine cerebrale vaatjes. Het is daarom interessant de flow in de kleine perforerende arteriën te onderzoeken in relatie tot factoren die daarop van invloed kunnen zijn.

In **Hoofdstuk 4** onderzochten we een cohort van mensen met een eenzijdige of tweezijdige afsluiting van de halsslagader (i.e. carotis), ook wel een carotis occlusie genoemd. In dit cohort kijken we naar de invloed van een carotis occlusie op de flow in de cerebrale perforerende arteriën in de CSO en BG. Hiervoor vergeleken we de flow in de perforerende arteriën in oudere mensen met een carotis occlusie (COD) met die van controles. Tevens onderzochten we relaties tussen flow van de perforerende arteriën en laesies die typerend zijn voor small vessel disease. Hoewel verscheidene metingen van flow in de kleine vaatjes niet bleken te zijn aangedaan in patiënten met COD in vergelijking met controles, duiden resultaten wel op verminderde bloedstroomsnelheid in de kleine vaatjes, voornamelijk in de waterscheidingsgebieden, en lijkt deze verminderde bloedstroomsnelheid gerelateerd te zijn aan het volume van de witte stof hyperintensiteiten (WMHs) in patiënten met COD. Deze studie suggereert daarom dat de kleine cerebrale perforerende arteriën bijdragen aan hersenschade en mogelijk ook aan de klinische uitkomst in patiënten met COD.

In **Hoofdstuk 5** onderzochten we de relatie tussen proximale maten van druk en arteriële stijfheid en cerebrale demping van flow richting de perforerende arteriën. Drukpulsaties ontstaan in het hart en propageren bloed van het hart door de cardiovasculaire boom. Demping van deze drukpulsaties gebeurt niet alleen in de grote(re) vaten zoals de aorta en de vaten van de circle van Willis, maar ook in de kleinere arteriën en de microcirculatie. Deze demping heeft als doel de vaten te beschermen van een overvloed aan pulsatiele energie, en daarmee schade aan de vaten te voorkomen. In dit hoofdstuk hebben we proximale maten van druk en arteriële stijfheid, namelijk het linker ventrikel slagvolume, gemiddelde arteriële druk, polsdruk en de aortapulsgolfsnelheid, gerelateerd aan bloedstroomsnelheid en pulsatiliteit tussen het eerste segment van de middelste hersenslagader (M1) en de kleine perforerende arteriën in de CSO en BG. Dit hebben we onderzocht in een cohort van gezonde ouderen. Resultaten suggereerden niet alleen de aanwezigheid van demping tussen de M1 en de kleine arteriën van de CSO en de BG, maar ook dat deze demping toeneemt bij een toename van proximale druk en arteriële stijfheid.

In **Hoofdstuk 6** hebben we gekeken naar de relaties tussen cardiovasculaire risicofactoren en flow in de kleine cerebrale perforerende arteriën in de CSO en BG. Het onderzochte cohort bestond uit personen ouder dan 50 met ofwel COD, een vasculaire cognitieve stoornis, of geen van beide aandoeningen. Behalve een negatieve relatie

tussen diastolische bloeddruk en pulsatiliteit in de BG, vonden we geen relaties. Deze studie suggereert daarmee dat bloedstroomsnelheid en pulsatiliteit van de kleine cerebrale arteriën grotendeels onafhankelijk zijn van cardiovasculaire risicofactoren in deze populatie ten tijde van de scan. Toekomstig onderzoek kan nog kijken of blootstelling aan vasculaire risicofactoren in het verleden nog samenhangt met de functie van de kleine cerebrale arteriën.

Microvasculaire (dys)functie in SVD

Het is bekend dat patiënten met SVD op MRI lacunaire infarcten, WMHs, microbloedingen en vergrote periventriculaire ruimten vertonen en dat diermodellen functionele afwijkingen laten zien in de microvasculatuur. Echter, pathologie op MRI en symptomen van SVD weerspiegelen vaak een relatief laat stadium van de ziekte en niet de afwijkingen in de microvasculatuur, terwijl wordt gesuggereerd dat de microvasculatuur de locatie is waar SVD aanvangt. Het is daarom interessant om de kleine cerebrale vaatjes te onderzoeken in verschillende populaties die zijn getroffen door SVD, om meer inzicht te krijgen in de rol van deze vaatjes in deze veelvoorkomende ziekte.

In de studie besproken in de volgende hoofdstukken werd de flow van de kleine vaatjes onderzocht in een cohort van patiënten met een erfelijke vorm van SVD, namelijk CADASIL. Deze studie is onderdeel van ZOOM@SVDs, een substudy van SVDs@target, gefinancierd door de Horizon 2020 van de Europese Unie, waarin wij met verschillende onderzoeksgroepen uit Europa samenwerkten. CADASIL staat voor Cerebral Autosomal Dominant Arteriopathy with Subcortical Infarcts and Leukoencephalopathy. Mensen die deze erfelijke vorm van SVD bij zich dragen, hebben 100% kans om deze ziekte te krijgen. Ondanks enkele verschillen tussen deze vorm van SVD en sporadische (niet-genetische) SVD, hebben CADASIL en sporadische SVD veel overeenkomsten op neuropathologische en klinisch niveau. Onderzoek naar CADASIL is daarom ook relevant voor een beter begrip van de sporadische variant van SVD.

In **Hoofdstuk 7** presenteerden we de rationale en het design van ZOOM@SVDs, die drie metingen bevat: i) bloedstroomsnelheid en pulsatiliteit van de kleine cerebrale perforerende arteriën; ii) cerebrovasculaire reactiviteit (CVR) als reactie op een hypercapnische stimulus; iii) cerebrovasculaire reactiviteit door neurovasculaire koppeling. In dit hoofdstuk wordt tevens besproken welke MRI sequenties voor deze metingen zijn gebruikt en wat de huidige kennis is van deze maten.

In **Hoofdstuk 8** presenteerden we de resultaten van de metingen geïntroduceerd in hoofdstuk 7 betreffende de microvasculaire functie in een cohort van patiënten met CADASIL en vergeleken de resultaten met die van gezonde controles. Resultaten toonden verschillen aan tussen deze groepen, zoals een grotere verhoging van de bloedstroomsnelheid als reactie op de hypercapnische stimulus in patiënten ten opzichte van controles, en een lagere reactiviteit tijdens een visuele stimulus in patiënten. Tevens zagen we dat patiënten een lagere bloedstroomsnelheid en hogere pulsatiliteit hebben in de kleine cerebrale perforerende arteriën dan controles. Vergelijking binnen patiënten tussen normaal uitziende witte stof en WMHs, toonden geen verschillen in bloedstroomsnelheid en pulsatiliteit. Wel zagen we een verminderde, en zelfs negatieve vasculaire reactiviteit in WMHs in respons op de hypercapnische stimulus. Betreffende associaties tussen van microvasculaire dysfunctie en ziekte-ernst in patiënten, werd een negatieve relatie gevonden tussen bloedstroomsnelheid in de kleine perforerende arteriën in de CSO en het volume van de witte stof hyperintensiteiten.

Deze studie toont aan dat de cerebrale microvasculatuur in patiënten met CADASIL allerlei verschillen vertoont ten opzichte van controles, waarbij regionale afwijkingen gerelateerd lijken te zijn aan elkaar en meerdere functionele aspecten van de microvasculatuur veranderingen vertonen. Dit onderstreept de toegevoegde waarde van het combineren van meerdere 7T MRI technieken om de functie van de microvasculatuur te meten in verschillende breingebieden en vaatbedden, en daarmee de complexe functionele aspecten in kaart te brengen die een rol spelen in SVD.

Dit proefschrift onderzocht de functie van de cerebrale microvasculatuur met 7T MRI. Door verbeteringen aan te brengen aan de methode om de kleine cerebrale vaatjes in beeld te brengen en te detecteren, en te laten zien dat dit ook kan op 3T MRI, hebben we de waarde van de 2D PC metingen van bloedstroomsnelheid en pulsatiliteit in de kleine perforerende arteriën vergroot. Onderzoek naar de factoren die van invloed kunnen zijn op de functie van de perforerende arteriën, toonde het brede scala aan toepassingen voor de 2D PC sequentie om bloedstroomsnelheid en pulsatiliteit in de perforerende arteriën te meten. Ten slotte hebben we aangetoond dat 7T MRI onmisbaar is in het onderzoek naar kleine cerebrale vaatjes in patiënten met SVD.

ABOUT THE AUTHOR

236

Tine Arts was born on June 20th 1989 in Boxmeer, The Netherlands. Here she grew up with her parents, Hans and Brenda, and her sister Anne. She attended the Elzendaal College in Boxmeer, where her interest in physics as well as biology grew. After obtaining her diploma she enrolled in the Physics & Astronomy program at the Radboud University Nijmegen. During her bachelor she completed her internship at the department of Medical Physics and Biophysics and discovered her interest in medical physics. So after her bachelor, she said goodbye to the stars and continued with the physics master Experimental Neuroscience. After having followed MRI and cognition courses, she was inspired and determined to work on the interface of physics and healthcare. This lead to a master internship at the Minimally Invasive Healthcare department of Philips, and she moved to Eindhoven. Here, she worked on the use of functional MRI as an objective measure for well-being of subjects during MRI scanning. In 2014 she received her master's degree cum laude.
After a succesfull application she filled a research position at the Daniel den Hoed Clinic of the Erasmus MC in Rotterdam and moved to the small village of Rhenoy and later to Rotterdam. During this time she worked on comparing photon radiotherapy and proton radiotherapy treatments for the Holland Proton Therapy Center. This novel research sparked Tine's enthusiasm to do a PhD, and in 2016 she successfully applied for a PhD position in the 7 Tesla group at the UMC Utrecht. Here she worked on finding markers for cerebral small vessel disease with high-field MRI under the supervision of Prof. dr. Geert Jan Biessels, Dr. Jeroen Hendrikse, Dr. ir. Jaco Zwanenburg and Dr. ir. Jeroen Siero.

Currently, Tine is working as a Medical Affairs Specialist in Radiation Oncology at Quirem Medical in Deventer.

PUBLICATIONS

Peer-reviewed publications

In this thesis

T. Arts, J.C.W. Siero, G.J. Biessels, J.J.M. Zwanenburg - Automated assessment of cerebral arterial perfator function on 7T MRI. *Journal of Magnetic Resonance Imaging.* 53, 234-241 (2021).

T. Arts, T.A. Meijs, H.B. Grotenhuis, M. Voskuil, J.C.W. Siero, G.J. Biessels, J.J.M. Zwanenburg - Velocity and pulsatility measures in the perforating arteries of the basal ganglia at 3T MRI in reference to 7T MRI. *Frontiers in Neuroscience.* 15, 665480 (2021).

H. van den Brink, A. Kopczak, **T. Arts**, L.P. Onkenhout, J.C.W. Siero, J.J.M. Zwanenburg, M. Duering, G.W. Blair, F.N. Doubal, M.S. Stringer, M.J. Thrippleton, H.J. Kuijf, A. de Luca, J. Hendrikse, J.M. Wardlaw, M. Dichgans. G.J. Biessels - Zooming in on cerebral small vessel diseases with 7T MRI: Rationale and design of the "ZOOM@SVDs" study. *Cerebral Circulation - Cognition and Behavior.* 2, 100013 (2021).

Other

T. Arts, S. Breedveld, M.A. de Jong, E. Astreinidou, L. Tans, F. Keskin-Cambay, A.D.G. Krol, S. van de Water, R.G. Bijman, M.S. Hoogeman - The impact of treatment accuracy on proton therapy patient selection for oropharyngeal cancer patients. *Radiotherapy and Oncology.* 125, 520-525 (2017)

R.G. Bijman, S. Breedveld, **T. Arts**, E. Astreinidou, M.A. de Jong, P.V. Granton. S.F. Petit, M.S. Hoogeman - *Impact of model and dose uncertainty on model-based selection of oropharyngeal cancer patients for proton therapy.*
Acta Oncology (Madr). 56, 1444-1450 (2017)

Submitted manuscripts

T. Arts*, L.P. Onkenhout*, D. Ferro E.A. Oudeman, M.J.P. van Osch, J.J.M. Zwanenburg, J. Hendrikse, L.J. Kapelle, G.J. Biessels - Perforating artery flow velocity and pulsatility in patients with carotid occlusive disease. A 7 tesla MRI study. *Submitted in Cerebral Circulation - Cognition and Behavior.*

T. Arts, L.P. Onkenhout, R.P. Amier, R. van de Geest, T. van Harten, L.J. Kapelle, S. Kuipers, M.J.P. van Osch, E.T. van Bavel, G.J. Biessels, J.J.M. Zwanenburg - Non-

invasive assessment of damping of blood flow velocity pulsatility in cerebral arteries with 7T MRI. *Submitted in the Journal of Magnetic Resonance Imaging.*

In preparation

L.P. Onkenhout*, **T. Arts**, D. Ferro, S. Kuipers, E.A. Oudeman, T. van Harten, M.J.P. van Osch, J.J.M. Zwanenburg, J. Hendrikse, GJ. Biessels, L.J. Kapelle. *In preparation for submission in the Cerebral Blood Flow & Metabolism.*

H. van den Brink*, **T. Arts***, A. Kopczak*, L.P. Onkenhout, J.C.W. Siero, J.J.M. Zwanenburg, B. Gesierich, M. Duering, M.S. Stringer, J. Hendrikse, J.M. Wardlaw, M. Dichgans, G.J. Biessels. *In preparation for submission in JAMA Neurology.*

Conference proceedings (first author only)

T. Arts, J.C.W. Siero, J.J.M. Zwanenburg - *Targeting potential pulsatility in the cerebral microcirculation with BOLD fMRI at 7T.*
Poster presentation, ISMRM Benelux 2017, Tilburg, The Netherlands.

T. Arts, L.P. Onkenhout, J.C.W. Siero, J.J.M. Zwanenburg, G.J. Biessels - *Pulsatility and velocity in cerebral penetrating arteries in patients with carotid occlusive disease.*
Poster presentation, ISMRM Benelux 2018, Antwerp, Belgium.

T. Arts, L.P. Siero, J.J.M. Zwanenburg, J. Hendrikse, G.J. Biessels - *Velocity and pulsatility of small perforating arteries in hemispheres of patients with a carotid occlusion.*
E-poster presentation, ISMRM 2018, Montreal, Canada.

T. Arts, J.C.W. Siero, J.J.M. Zwanenburg, G.J. Biessels - *Method for vessel selection affects velocity and pulsatility measures and their reproducibility in cerebral penetrating arteries*
Poster presentation, ISMRM Benelux 2019, Leiden, The Netherlands.

T. Arts, J.C.W. Siero, J.J.M. Zwanenburg, J. Hendrikse, G.J. Biessels - *Automated vessel selection and its reproduciblity in velocity and pulsaltility measures.*
E-poster presentation, ISMRM 2019, Paris, France.

241

T. Arts, H. van den Brink, A. Kopczak, M. Dichgans, J. Hendrikse, J.C.W. Siero, J.J.M. Zwanenburg, G.J. Biessels - *Velocity and pulsatility in small cerebral perforators of CADASIL patients compared to healthy controls.*
Oral presentation, ISMRM Benelux 2020, Arnhem, The Netherlands
E-poster presentation, ISMRM 2020 (virtual conference).

T. Arts, L.P. Onkenhout, D. Ferro, E.A. Oudeman, L.J. Kapelle, M.J.P. van Osch, J.J.M. Zwanenburg, J. Hendrikse, G.J. Biessels - *The relationsship between cerebral arterial perforator function on 7Tesla MRI and carotid occlusive disease.*
E-poster presentation, ISMRM 2020 (virtual conference).

DANKWOORD

Al zit je tijdens een promotie veelal op een figuurlijk eilandje te werken, promoveren doe en kun je zeker niet alleen. Daarom bedank ik hier graag iedereen voor het mede tot stand brengen van dit proefschrift.

Allereerst wil ik **alle deelnemers** bedanken die voor mijn onderzoek vrijwillig tijd hebben doorgebracht in de 7T MRI scanner. Het was geweldig om te zien hoeveel mensen hiertoe bereid waren en ik heb met de deelnemers de mooiste gesprekken gevoerd. Deze ontmoetingen deden mij keer op keer beseffen waarom dit onderzoek zo ontzettend belangrijk is.

Prof. dr. G.J. Biessels. Beste Geert Jan, toen ik in 2016 kwam solliciteren werd me al snel duidelijk dat het SVDs@target project een prachtig en uitdagend project was om op te werken. Na mijn werk op het gebied van radiotherapie moest ik wel even schakelen, want wat was small vessel disease nu precies? Al snel kwam ik terecht in de wereld van de cerebrale hemodynamiek en de kleine vaatjes, en leerde ik iedere ontmoeting met jou weer iets nieuws. Je wist altijd de juiste vragen te stellen en vaak waren dat de vragen waarop ik zo snel geen goed antwoord wist. Jij leerde me met regelmaat een stapje terug te doen om na te denken over de essentie van mijn onderzoek met in het achterhoofd altijd de toegevoegde waarde voor de patiënt. Dank voor je tijd in je toch vaak drukke agenda, je heldere uitleg van voor mij ingewikkelde zaken en je aanmoediging.

Prof. dr. Hendrikse. Beste Jeroen, dank voor je betrokkenheid bij het SVDs@target project. Ik heb veel bewondering voor je positiviteit en al vonden onze meetings niet met grote regelmaat plaats, je was altijd op de hoogte van de nieuwste bezigheden en bevindingen binnen mijn onderzoek. Tevens heb ik grote waardering voor je bezoekjes aan ons kantoor om even te vragen hoe het ervoor stond. Uiteraard ook dank voor de schrijfdagen die je organiseerde in de meest inspirerende zalen van het Academiegebouw en voor de aanbevelingen voor boeken om meer uit het leven te halen. Zo heeft wellicht het boek "Make Time" het schrijven van dit proefschrift tot een efficiënte bezigheid gemaakt.

Dr. ir. Zwanenburg. Jaco, jij was mijn dagelijkse begeleider omtrent alles wat met de cerebrale microvasculatuur te maken heeft. Al snel leerde ik dat de drempel om bij je binnen te lopen laag was en dat ben ik erg gaan waarderen. Mijn vragen over

bloedsnelheden, flip angles, echotijden en k-space reconstructies werden altijd met groot enthousiasme beantwoord. Je organiseerde een schrijfretraite en mini-symposia om je PhD-groep wat hechter te maken en ik hoop van harte dat je dat voortzet. Vaker dan ik op twee handen kan tellen heb je mij en mijn directe collega's uit de brand geholpen bij de 7T als de paniek toesloeg, omdat sequenties maar niet wilden starten. Dank voor je aanmoediging, je luisterende oor als het glas voor mij weer eens half leeg leek te zijn en het overdragen van je grote enthousiasme voor al dat met kleine cerebrale vaatjes van doen heeft.

Dr. ir. J.C.W. Siero. Beste Jeroen, dank voor je hulp, je tomeloze en aanstekelijke enthousiasme bij mijn onderzoek en je vele ideeën. Je ondersteuning bij de analyse van de BOLD CVR data is mijns inziens onmisbaar geweest en ik had me daarbij geen betere begeleider kunnen wensen. Bij vragen over bash scripting of bijbehorende errors kroop jij met plezier achter mijn computer om de codes te verfijnen en binnen no-time werkende te krijgen. Tevens heb ik grote waardering voor het feit dat je me geregeld liet nadenken over mijn rol binnen mijn promotietraject en me liet doen wat voor mij het meest waardevol was. Ook luisterde je naar mijn strubbelingen en adviseerde je bij de dilemma's die ik daarbij soms ervaarde. Dank voor je inspiratie, je luisterende oor en je motiverende woorden.

De leescommissie, prof. dr. D.W.J. Klomp, prof. dr. P.A. de Jong, prof. dr. G.J. de Borst, prof. dr. R.M. Dijkhuizen en prof. dr. M.W. Vernooij, hartelijk dank voor de tijd en energie die jullie hebben gestoken in het beoordelen van dit proefschrift.

Beste Sylvia, toen je hoorde dat ik naar Ede was verhuisd, had ik er meteen een carpoolmaatje bij. Je was net zo'n vroege vogel als ik: lekker op tijd beginnen, voor de files uit, om op tijd weer thuis te zijn. Ik leerde al snel dat jij onmisbaar bent op de 7T afdeling met alle kennis en vaardigheden die je in huis hebt. Ik wil je bedanken voor alles dat je voor mij en mijn directe collega's van de neurologie hebt gedaan om onze onderzoeksprojecten qua 7T planning en timeslots draaiende te houden. Ik hoop dat we nog lang blijven bijpraten tijdens onze wandelingen in Ede.

Also many thanks to **the roommates** I have had over the years: **Arjan, Lisa, Carlo** and **Mario**. It was always a welcome distraction to chat several times a day, sometimes about heavy subjects such as the meaning of life (which we never managed to figure out), but

also on many (correction: almost all) occasions about food with Carlo (or his everlasting wish to diet), about books, music and work-related excitements and frustrations, with Mario about Netflix, bad Mexican music, and taco's. To you I say houdoe, arrivederci and adios. I will miss you!

Ook alle **collega's van de 7T groep**: dank voor de gezelligheid tijdens lunchpauzes, wandelingetjes, sightseeing en diners tijdens congressen en ook dank dat jullie me bleven meevragen voor de koffietrein ondanks dat ik negen van de tien keer 'nee' zei. En **Hans** en **Fredy**, volgens mij sloeg de angst en paniek toe als jullie Hilde en mij bij de 7T zagen zitten ("dit keer géén problemen meiden...?") maar dank dat jullie altijd pijlsnel te hulp schoten wanneer de 7T weer dienst weigerde. Daarvoor ook dank aan de collega's in het coil lab.

Alle **collega's van het SVDs@target consortium**, dank voor het prachtige onderzoek dat we samen tot stand hebben gebracht en voor de ontzettend leerzame, motiverende, maar zeker ook leuke meetings. Het was ieder jaar een groot plezier jullie weer te zien, bij te kletsen, en nieuwe steden te verkennen.

Hilde en Laurien, mijn MRI scanmaatjes door dik en dun, jullie waren ontzettend gezellige collega's. **Laurien**, jou leerde ik de eerste paar dagen van mijn promotie al kennen bij de 7T voor de CVON studie en op de VasCog. Je was ontzettend geduldig om mij alles over de CVON studie te leren en ik wist al snel dat we naast hard werken ook heel gezellig konden babbelen en lachen tijdens gezamelijke scansessies. Toen we eenmaal begonnen aan onze manuscripten was onze samenwerking subliem en hebben we mooie papers neer kunnen zetten waar we trots op mogen zijn. **Hilde**, ik leerde je kennen op de VasCog in de tijd dat je nog stagiair was. Toen je daar vertelde over je onderzoek naar micro-infarcten straalde je van enthousiasme. Twee jaar later zat ik in jouw sollicitatiecommissie en werd besloten dat jij een PhD plek mocht invullen. Jouw blijdschap voorspelde dat je die positie met verve zou vervullen en dat is zeker gebleken. De samenwerking met jou heb ik als geweldig leuk ervaren. In de afgelopen jaren hebben we samen gelachen, gehuild, gebaald en relatietherapie geopperd omdat een vechtscheiding met de 7T aanstaande was. Ik ben trots dat jij vandaag als paranimf naast me staat. Ook onze tripjes zal ik niet vergeten: Laurien, met jou heb ik Kopenhagen verkend (wat was het daar toch koud), met jou Hilde heb ik Split (wat was het daar toch warm) en Edinburgh (wat een regen) verkend, en met z'n drieën hebben we in Parijs genoten. Dames, zonder jullie was dit proefschrift niet geworden tot wat het is. Ik ga jullie missen!

Lieve vrienden**, Tim**, **Eline**, **Maartje**, **Britt** en **Anne Charlotte**. We zien elkaar niet altijd even vaak, maar als we samenkomen delen we lief en leed met elkaar. Dank voor jullie steun, en voor de vele goede gesprekken en adviezen. Maar ook dank voor de heerlijke sushi, taart, cake en nog meer ontelbaar lekkers. En dank dat ik met blijdschap, verdriet, frustratie en sarcasme altijd bij jullie terecht kon. En Tim, jij kunt als geen ander rust in mijn hoofd brengen als dat nodig is, en ik ben ontzettend blij dat ook jij vandaag mijn paranimf bent.

Lieve schoonfamilie, **Jan, Ellie** en **Bart**. Bij jullie in het verre zuiden kon ik altijd heerlijk onthaasten en kon ik het drukke PhD leven even achter me laten. Dank voor de liefde en warmte die jullie me de afgelopen jaren gegeven hebben.

Lieve **familie**, jullie zijn mijn grote steun en toeverlaat. **Ine**, hoe ouder ik word, hoe meer ik op jou ben gaan lijken en daar ben ik trots op. Dank voor de gesprekken als ik het even moeilijk had, de praatjes over de kleine, maar mooie dingen in het leven en voor de vele film- en boekentips die mij de nodige afleiding bezorgden. **Anne**, jij hebt mij de afgelopen jaren geleerd niet altijd zo irritant rationeel te zijn, maar ook wat vaker naar mijn gevoel te luisteren om geluk en rust te vinden. **Papa** en **mama**, oneindig dank voor jullie onvoorwaardelijke steun, liefde en toewijding. Jullie stonden altijd voor me klaar als ik even niet meer wist hoe ik verder moest. Ik weet zeker dat ik zonder jullie nooit zo ver gekomen zou zijn.

Lieve **Koen**, ook zonder jou was dit proefschrift nooit tot stand gekomen. Bedankt voor je oneindige steun en liefde. Jij gaf me rust wanneer ik panikeerde om de kleinste dingen en trok me na uren werken achter mijn laptop vandaan om het werk even los te laten. Je kon me na de slechtste werkdagen altijd weer laten lachen en me het gevoel geven dat het allemaal weer goed kwam. Ik verheug me op alle avonturen die we in de toekomst nog gaan beleven samen met ons komische konijnenduo Tommie en Doortje (en hopelijk later nog vele huisdieren meer).

WEES TROTS OP WAT JE HEBT BEREIKT,
AL HEB JE NOG DUIZEND DROMEN.

EN ZORG DAT JE AF EN TOE OOK KIJKT,
NAAR HOE VER JE AL BENT GEKOMEN.